# Multitechnique Characterization of Binary Asteroids

Myriam Pajuelo

# THÈSE DE DOCTORAT

de l'Université de recherche Paris Sciences et Lettres
PSL Research University

**Préparée à l'IMCCE - Observatoire de Paris**

# CARACTÉRISATION MULTITECHNIQUES DES ASTÉROÏDES BINAIRES

**École doctorale n°127**

ASTRONOMIE ET ASTROPHYSIQUE,

**Spécialité** SYSTÈME SOLAIRE, ASTÉROÏDES

**COMPOSITION DU JURY :**

Pr. Bruno SICARDY
LESIA, Président

Dr. Jessica AGARWAL
Max Planck Institute, Rapporteur

Dr. René DUFFARD
Inst. Astrofísica de Andalucía, Rapporteur

Pr. Philippe ROUSSELOT
Observatoire de Besançon, Examinateur

Dr. Alin NEDELCU
Astron. Inst. Romanian Academy, Examinateur

Soutenue par **Myriam PAJUELO**
le 26 septembre 2017

Dirigée par **Benoît CARRY**
et par **Mirel BIRLAN**

l'Observatoire de Paris

PSL RESEARCH UNIVERSITY PARIS

"Animula, vagula, blandula
Hospes comesque corporis
Quae nunc abibis in loca
Pallidula, rigida, nudula,
Nec, ut soles, dabis iocos."
—P. Aelius Hadrianus Imp. (138 AD)

Para
Luchefrén
el zurdo memorable
casi secular
&
Shaheem
el niño de mis ojos

# Remerciements

En premier lieu, ma profonde reconnaissance va à mes directeurs de thèse, qui ont œuvré à ce que ce travail doctoral arrive à bon port : A Benoît Carry, pour son appui constant, pour sa patience, sa générosité et sa motivation, pour m'avoir toujours guidée, partageant avec moi son enthousiasme et son immense connaissance sur les astéroïdes (et plus encore), et à Mirel Birlan, qui avec gentillesse et patience, m'a aussi guidée dans ce monde, particulièrement pour l'obtention de données spectrales, leur traitement et analyse; et qui, quand il me voyait perdre espoir avait toujours une solution en main pour me redonner du courage: *nici o problemă*.
Je remercie aussi Frédéric Vachier et Jérôme Berthier, qui généreusement m'ont aidée et entraîné pendant ces années avec les observations et programmes pour obtenir la précieuse information dont j'avais besoin pour mon travail et qui en plus m'ont accueillie dans leur bureau en me faisant sentir comme à la maison. J'ai eu la chance de les avoir à mes côtés. J'espère que nous aurons l'ocassion de poursuivre notre collaboration pendant longtemps.

A mon jury, Bruno Sicardy, Alin Nedelcu, René Duffard, Philippe Rousselot, et en particulier à Jessica Agarwal qui m'a fait de précieux commentaires sur le manuscrit de la thèse.

à l'Observatoire de Paris et particulièrement à mon lab: l'IMCCE où je remercie l'appui et l'accueil de Pascal Descamps, François Colas, Jérémie Vaubaillon, Florent Deleflie, William Thuillot, Lucie Maquet, Jonathan Normand, Sylvie Lemaître, Rachida Amhidez, Siegfred Eggl, Maria Kudryashova, Daniel Hestroffer, Amélie Muslewski, Sem Bendjeddou, Djamila Houibi, Yohann Gominet, Agnès Patu, et Mickaël Gastineau. Et d'une façon particulière je remercie Maïder Bugnon Olano qui a toujours été là, m'aidant et m'encourageant et me guidant dans le labyrinthe des papiers et de la bureaucratie française.
A mes compagnons doctorants de l'ED 127 : Auriane Egal, Melaine Saillenfest, Eléonore Saquet, William Polycarpe, Bogdan Dumitru, et en particulier Fatoumata Kebe, ma *space girl*, pour les joies partagées et pour sa solidarité.

A Michael Marsset, Pierre Vernazza, Regina Rudawska, Sylvain Bouley, Rafael Sfair, Juan Quintanilla, Elisa Rojas et María Candelaria, mes amies mexicains: Monica Rodriguez et Brisa Mansillas.
A ma famille en France : Yola Gloaguen, Isabelle Berman, Hervé Gloaguen et Regina de Oliveira. Merci pour leur appui et leur tendresse.

A mon université la PUCP, j'apprécie le soutien, a mes amis et collégues là-bas: Alberto Gago, Patrizia Pereyra, Francisco de Zela, Jorge Moreno, Jorge Urquiaga, Casio Oré, Carlos Argüelles. Et d'ailleurs: Nobar Baella, Mario Zegarra, Julio C.Tello et José Ishitsuka.
A toutes ces personnes qui m'ont beaucoup influencée, peut-être sans s'en rendre compte et depuis longtemps : Bruno Sicardy, Gonzalo Tancredi, Tabaré Gallardo, Ricardo Gil-Hutton, Marcela Cañada Assandri, Mark Showalter, Rick Binzel, Francesca DeMeo, et Petr Pravec.
A ceux de l'OCA: Morby, Paolo Tanga, Aurélien Crida, Seth Jacobson, Federica Spoto, Michiel Lambrechts, Patrick Michel, Jean-Pierre Rivet, Stefan Ast, Ali, Kaled et avec une affection particulière à Rafael Ribeiro (Rafinha). Merci de m'accueillir parmi vous à Nice, merci encore Ben-sama.
Aux artifices de *la Silla Social*: Lenka Badriyah et Rémy Joseph qui rendirent amusantes les nuits d'observation.

A la France et aux français, pour leur savoir-faire et la liberté, l'égalité et la fraternité transformées en actions. A Paris, bien sûr, où toujours je voudrais revenir...A Nissa la bella, pour son bleu infini. A France Inter, qui me tenait compagnie et en particulier à Jean Claude Ameisen avec son émission *"Sur les épaules de Darwin"* et Fabrice Drouelle avec *"Affaires sensibles"*. Et en particulier à *Marianne*, la vraie, celle de l'esprit français, qui surgit une nuit sombre et me sauva à temps pour que je puisse faire la soutenance. Merci infiniment.

Aux observateurs amateurs et professionnels, de part et d'autre de ce monde. Aux gens qui maintiennent les bases de données et les programmes, pour leur temps et leur passion pour l'observation et qui obtiennent toujours de meilleures données.

Enfin, et tout aussi important, je remercie l'appui de ma famille, qui malgré la distance a toujours été à mes côtés : Luchefrén (mi querido pá, el mejor), Lucía, Ana, Amelia, Luchi, Carlos et Enrique. Ainsi qu'à mon cher Shaheem.

*Paris, le 25 Septembre 2017* M. P.

# Abstract

Binary asteroids represent a natural laboratory to gather crucial information on small bodies of the Solar System, providing an overview of the formation and evolution mechanisms of these objects. Their physical characterization can constrain the processes that took part in the formation and evolution of planetessimals in the Solar System. The characteristics assessed in this work are: mass, size, shape, spin, density, surface composition, and taxonomy.

One of the most important characteristics that can be obtained of binaries -if the system can be resolved- is their mass through their mutual gravitational interaction. From the mass and the size of the asteroid we determine its density, which provides insight on its internal structure.

For this purpose, data mining has been done for high-angular resolution images from HST and ground-based telescopes equipped with adaptive optics (VLT/NACO, VLT/SPHERE, Gemini/NIRI, Keck/NIRC2) in the visible and near infrared. Having reduced the images and determined the satellite positions for over many epochs, the genetic algorithm Genoid algorithm is used to determine the orbit of the companion, and mass of the primary. This improves the ephemerides of binary companions, which in turn allows to stellar occultations by asteroids for future occultation campaigns.The occultation technique is the most fruitful for observing small diameter Solar System objects. As for the size and shape determination, KOALA multidata inversion algorithm is used.

Concerning photometry, light curves and SDSS colors have been obtained for binary asteroids from T1M at Pic du Midi & 1.20m telescope at Haute Provence Observatory, aiming at determining and refining their properties. I remotely acquired spectra of binary asteroids using Spex/IRTF system based on 3m at Mauna Kea (Hawaii), to determine their taxonomic class for the first time. Additionally, I collected spectra of small binaries from the SMASS collaboration database, modelled it, and found their taxonomy. I compare the now larger sample of classified binaries to the population of NEAs and Mars Crossers, and found a predominance of Q/S types. This is in agreement with a formation by YORP spin-up and rotational disruption.

Finally, I developed a taxonomic classification for asteroids in general, based on infrared large band photometry, and applied it to 30,000 asteroids from VHS survey at the ESO's telescope VISTA.

Key words: minor planets, asteroids, properties, asteroids techniques, spectra, taxonomy

# Résumé

Les astéroïdes binaires représentent un laboratoire naturel pour recueillir des informations cruciales sur les petits corps du Système Solaire, fournissant un aperçu des mécanismes de formation et d'évolution de ces objets. Leur caractérisation physique nous aide à comprendre les processus qui ont pris part à la formation et l'évolution des planétesimaux dans le Système Solaire.

Les caractéristiques qui sont évaluées dans ce travail sont : la masse, la taille, la forme, la rotation, la densité, la composition et la taxonomie. L'une des plus importantes caractéristiques que l'on puisse obtenir avec les objets binaires -si le système peut être angulairement résolu- est leur masse grâce à l'interaction gravitationnelle mutuelle. Avec la masse et la taille du corps, nous pouvons déterminer sa densité, qui peut nous donner un aperçu de sa structure interne.

A cet effet, l'exploration de données a été faite à partir d'images à haute résolution angulaire du télescope spatial Hubble et les télescopes au sol avec optique adaptative (VLT/NACO, VLT/SPHERE, Gemini/NIRI, Keck/NIRC2) dans le visible et proche infrarouge. Ayant réduit les images et mesuré les positions des satellites á de nombreuses époques, l'algorithme génetique Genoid est utilisé pour déterminer l'orbite de compagnons et la masse du corps central. Ceci est utile pour améliorer les éphémérides des satellites des binaires, qui à leur tour seront utiles pour prédire des occultations stellaires pour les futures campagnes d'occultation ; la technique d'occultation étant la plus fructueuse pour l'observation des objets de faible diamètre du Système Solaire. En ce qui concerne la taille et la détermination de la forme, l'algorithme KOALA d'inversion multidonnées est utilisé.

En ce qui concerne la photométrie, courbes de lumiere et couleurs SDSS ont été obtenues depuis le télescope de 1m au Pic du Midi et de 1.20m de l'observatoire de Haute Provence dans le but de déterminer et affiner leurs propriétés. J'ai egalement acquis à distance des spectres d'astéroïdes binaires en utilisant le spectrographe Spex sur le télescope IRTF de 3m au Mauna Kea (Hawaii), afin de déterminer leur classe taxonomique pour la première fois.

De plus, j'ai fait le modelisation de spectres de binaires sans taxonomie dans la base de données du SMASS collaboration. Ce plus grand échantillon, j'ai la comparez avec la population du NEAs et de Mars Crossers, en trouvant une prédominance dans le taxonomie Q/S. Cela est consistant avec la formation de binaires petits par effet YORP et perturbation rotationnelle.

Finalement, j'ai développé une classification taxonomique générale, basée sur la photométrie large bande dans l'infrarouge, et je l'ai appliquée aux données de 30,000 astéroïdes provenant du survey VHS conduit par le télescope VISTA de l'ESO.

Mots clefs : astéroïdes, propietes, spectra, taxonomie

# Resumen

Los asteroides binarios representan un laboratorio natural que nos sirve para obtener información importante sobre los cuerpos menores del Sistema Solar, brindándonos un panorama de los mecanismos de evolución y formación de estos objetos. Su caracterización ayuda a restringir los procesos que tomaron parte en la formación y evolución de los planetesimales en el Sistema Solar. Las características estudiadas en esta tesis de doctorado son: la masa, el tamaño, la forma, el spin, la densidad, la composición y taxonomía.

Una de las características más importantes que se puede obtener en el caso de los binarios -si el sistema puede ser resuelto angularmente- es su masa, aprovechando su interacción mutua. Con la masa y la estimación del tamaño del cuerpo podemos determinar su densidad, lo que nos da una mejor comprensión de su estructura interna.

Para este propósito, se ha colectado imágenes de gran resolución angular de las bases de datos del telescopio espacial Hubble y de telescopios con óptica adaptativa en Tierra (VLT/NACO, VLT/SPHERE, Gemini/NIRI, Keck/NIRC2) tanto en el visible como en el infrarojo cercano. Habiendo reducido las imágenes y determinado las posiciones de los satélites para varias épocas, se ha utilizado el algoritmo genético Genoid para determinar la órbita del satélite, sus parámetros y la masa de su cuerpo central. Esto ayuda a mejorar las efemérides de los satélites de binarios lo que a su vez será útil para predecir ocultaciones estelares para las futuras campañas de ocultaciones; siendo la técnica de las ocultaciones una de las más fructíferas para observar objetos pequeños del Sistema Solar. Para la determinación del tamaño y forma se ha usado el algoritmo KOALA que permite la inversión de datos de diferente tipo.

En cuanto a la fotometría, he obtenido curvas de luz y colores SDSS para algunos asteroides binarios usando el T1M de Pic du Midi y el telescopio de 1.20m del observatorio de Haute Provence (OHP) con el propósito de determinar y refinar sus propiedades. Además adquirí de manera remota, espectros de asteroides binarios usando Spex/IRTF de 3m. en el Mauna Kea (Hawaii), con el fin de determinar su clase taxonómica por vez primera.

Adicionalmente hice el modelamiento de espectros de binarios sin taxonomía obtenidos de la base de datos de la colaboracion SMASS. Esta muestra más grande la comparé con la población de NEAs y Mars Crossers, hallando una predominancia en la taxonomía Q/S. Esto es consistente con la formación de binarios pequeños via efecto YORP y disrupción rotacional.

Y los más importante, desarrollé una clasificación taxonómica para asteroides en general, basada en fotometría de larga banda en el infrarojo cercano, y la apliqué a los datos de 30,000 asteroides provenientes del survey VHS, conducido por el telescopio VISTA de la ESO.

Palabras clave: asteroides, propiedades, espectros, taxonomía

# Contents

**Acknowledgements (Français)** **i**

**Abstract (English/Français/Español)** **iii**

**List of figures** **xiii**

**List of tables** **xvii**

**1 Introduction** **1**

1.1 Asteroids *Do* have satellites . . . 4
1.2 Why study binary asteroids? . . . 6
1.2.1 Nomenclature . . . 8
1.2.2 On the size of binary asteroids . . . 9
1.2.3 Where are the binaries in the Solar System? . . . 12
1.3 Formation mechanisms of binary asteroids . . . 19
1.3.1 Mutual Capture . . . 19
1.3.2 Collisions . . . 19
1.3.3 Tidal Breakup . . . 20
1.3.4 Rotational Disruption . . . 21
1.4 Properties of binary asteroids . . . 21
1.4.1 Orbital elements . . . 21
1.4.2 Spin and 3-D Shape . . . 23
1.4.3 Mass and Bulk Density . . . 25
1.4.4 Surface Properties . . . 27
1.4.5 Absolute Magnitude and Albedo . . . 28
1.5 Methods to study asteroids . . . 28
1.5.1 Lightcurves . . . 29
1.5.2 High Angular Resolution and High Contrast Imaging . . . 30
1.5.3 Stellar Occultations . . . 30
1.5.4 Spectroscopy . . . 32
1.5.5 Other methods . . . 32

**2 Data & reduction** **35**
2.1 Basic Concepts of Photometry . . . 35
2.2 Telescopes . . . 39
2.2.1 Mobile telescope for stellar occultations . . . 39
2.2.2 Observatoire de Haute-Provence (OHP) / 1.20 m Telescope . . . 40
2.2.3 Pic du Midi Observatory / 1 meter Telescope (T1M) . . . 40
2.2.4 La Silla Observatory / New Technology Telescope (NTT) . . . 40
2.2.5 Infra Red Telescope Facility - IRTF . . . 42
2.2.6 Large facilities for high angular resolution . . . 42
2.2.7 Sky surveys and Catalogs . . . 44
2.2.8 Additional resources . . . 45
2.3 Data Reduction . . . 47
2.3.1 Adaptive Optics . . . 49
2.3.2 Electronic Detectors . . . 49
2.3.3 Filters . . . 54
2.3.4 Fringes in red filters . . . 54
2.4 The case of spectroscopy . . . 55

**3 Spectroscopic survey of binary asteroids** **57**
3.1 On asteroid classification and meteorites . . . 58
3.2 Reflectance Spectra . . . 62
3.3 Near infrared Spectra (NIR) . . . 62
3.4 Why determine binaries taxonomy? . . . 62
3.5 Binaries NIR Spectra Observed with Spex . . . 63
3.6 Observing method and data reduction . . . 64
3.7 Methods used to analyze data . . . 64
3.8 Results on individual targets . . . 67
3.8.1 (2691) Sersic . . . 67
3.8.2 (4383) Suruga . . . 68
3.8.3 (7187) Isobe . . . 70
3.8.4 (8373) Stephengould . . . 71
3.8.5 (76818) 2000 $RG_{79}$ . . . 72
3.9 Data through The MIT-UH-IRTF Joint Campaign for NEO Spectral Reconnaissance 74
3.9.1 (88710) 2001 $SL_9$ . . . 74
3.9.2 (162483) 2000 $PJ_5$ . . . 75
3.9.3 (190208) 2006 AQ . . . 77
3.9.4 (348400) 2005 $JF_{21}$ . . . 77
3.9.5 (374851) 2006 $VV_2$ . . . 78
3.9.6 (399307) 1991 $RJ_2$ . . . 79
3.9.7 (399774) 2005 $NB_7$ . . . 80
3.9.8 1994 XD . . . 80
3.9.9 2007 $DT_{103}$ . . . 81

3.9.10 (8306) Shoko . . . 82
3.9.11 (185851) 2000 $DP_{107}$ . . . 82
3.9.12 2014 $WZ_{120}$ . . . 83
3.9.13 (410777) 2009 FD . . . 83
3.9.14 (452561) 2005 AB . . . 83
3.9.15 (162000) 1990 OS . . . 84
3.9.16 (66063) 1998 $RO_1$ . . . 84
3.10 Discussion . . . 84

**4 A new taxonomy based on NIR photometry** **89**
4.1 Rationale for a taxonomy based on NIR colors . . . 89
4.1.1 Introduction . . . 89
4.1.2 Large surveys as data sources . . . 90
4.1.3 Motivation . . . 91
4.2 Definition of a new taxonomic scheme for NIR colors . . . 91
4.2.1 Method . . . 91
4.2.2 Data retrieval . . . 92
4.2.3 Learning sample . . . 93
4.2.4 Taxonomy scheme . . . 95
4.3 Spectral classification of asteroids serendipitously observed by VISTA . . . 96
4.3.1 Classification . . . 96
4.3.2 Validation . . . 97
4.3.3 Results . . . 102
4.3.4 Conclusions . . . 104
4.4 Other Photometric Data . . . 105

**5 Physical, spectral, and dynamical properties of (107) Camilla's triple system** **109**
5.1 Introduction . . . 109
5.2 Observations . . . 110
5.2.1 Optical lightcurves . . . 110
5.2.2 High-angular resolution imaging . . . 110
5.2.3 High-angular resolution spectro-imaging . . . 111
5.2.4 Stellar occultations . . . 111
5.2.5 Near-infrared spectroscopy . . . 112
5.3 Dynamical properties . . . 112
5.3.1 Data processing . . . 112
5.3.2 Orbit determination with `Genoid` . . . 113
5.3.3 Orbit of *S/2001 (107) 1* . . . 114
5.3.4 Orbit of *S/2016 (107) 1* . . . 114
5.4 Surface properties . . . 116
5.4.1 Data processing . . . 116
5.4.2 Spectrum of (107) Camilla . . . 117
5.4.3 Spectrum of *S/2001 (107) 1* . . . 118

5.5 Physical properties . . . 118
5.5.1 Data processing . . . 118
5.5.2 3-D shape modeling with KOALA . . . 119
5.5.3 Spin and 3-D shape of (107) Camilla . . . 119
5.5.4 Diameter of *S/2001 (107) 1* . . . 121
5.6 Discussion . . . 123
5.6.1 Density . . . 123
5.6.2 Craters . . . 124
5.7 Conclusions . . . 124

**6 Conclusions and Perspectives** **127**

**A An appendix** **129**
A.1 Asteroid spectra vs meteorites spectra . . . 129
A.2 Asteroid Band parameters . . . 134
A.3 (8373) Stephengould spectrum Analysis . . . 136
A.4 Details on the observing data sets of (107) Camilla . . . 138
A.5 Previous determinations of mass and diameter of (107) Camilla . . . 146

**Bibliography** **175**

# List of Figures


1.1 Asteroid belt in $\epsilon$ Eridani system . . . 2
1.2 Distribution of asteroids in the Inner Solar System . . . 3
1.3 Asteroid composition. . . . 4
1.4 Galilean moons . . . 4
1.5 Ida and Dactyl . . . 6
1.6 2014 JO25 . . . 9
1.7 Possible evolutionary paths of asteroids after fission . . . 10
1.8 Size of an asteroid from optical and infrared observations. . . . 11
1.9 Asteroid sizes. . . . 12
1.10 Known binary population. . . . 15
1.11 Asteroids population classes definition. . . . 16
1.12 Discovery statistics of PHAs. . . . 16
1.13 Binaries in ASTORB population in the Solar System . . . 17
1.14 Planetary migration on the asteroid belt . . . 18
1.15 Possible formation of satellites from large impacts. . . . 20
1.16 Shoemaker Leavy-9 comet breakup . . . 21
1.17 Mars doublet crater . . . 22
1.18 Itokawa rubble. . . . 22
1.19 Orbital elements . . . 23
1.20 Kirkwood gaps . . . 24
1.21 Asteroids spin rate vs. diameter from light curves. . . . 29
1.22 Binaries-AO . . . 30
1.23 Asteroids spin rate vs. diameter from light curves. . . . 31
1.24 Occultation geometry. . . . 33
1.25 Chords from an occultation. . . . 33
1.26 Polarization of asteroids. . . . 34

2.1 Atmospheric windows. . . . 36
2.2 Diffraction . . . 38
2.3 Portable telescope for occultations. . . . 39
2.4 Galilean moons . . . 40
2.5 T1M at Pic du Midi. . . . 41
2.6 NTT: New Technology Telescope. . . . 41

2.7 IRTF: Infra Red Telescope Facility . . . 42
2.8 Very Large Telescope . . . 43
2.9 Gemini Telescope . . . 43
2.10 Keck Telescope . . . 44
2.11 Hubble Space Telescope . . . 45
2.12 The SDSS telescope. . . . 46
2.13 The VISTA telescope on Paranal. . . . 47
2.14 Raw and corrected images of (4666) Dietz . . . 48
2.15 Adaptive Optics concept. . . . 50
2.16 CCD scheme . . . 51
2.17 Bias and flat frames. . . . 53
2.18 SDSS and VISTA transmission filters . . . 54
2.19 Interference fringes and clean image. . . . 55
2.20 The SDSS telescope. . . . 56

3.1 Summary of Bus DeMeo Taxonomy. . . . 58
3.2 Comparison of the different taxonomies. . . . 60
3.3 Undifferentiated and differentiated asteroids. . . . 61
3.4 Binary asteroids without taxonomy . . . 63
3.5 NIR spectra of Sersic, Suruga, Isobe, Stephengould and 2000 RG79 . . . 66
3.6 (4383) Suruga Mineralogical analysis. . . . 69
3.7 Mineralogical analysis results for (88710) 2001 $SL_9$. **Top** Linear continuum tangential to spectral curve of spectrum obtained after merging visible spectrum [Lazzarin et al., 2004] and NIR spectrum of (88710) 2001 $SL_9$. **Middle** Wavelength position of the centers of the two absorption bands. The regions enclosed correspond to the band centers computed for the H, L, and LL chondrites. **Bottom** Band area ratio (BAR) versus band I center. The regions enclosed by continuous lines correspond to the values computed for basaltic achondrites (BA), ordinary chondrites (OC), and olivine-rich meteorites (Ol) [Gaffey et al., 1993]. . . . 76
3.8 Plot of binaries with known taxonomy (light green dots), and all-binary population (black dots) among the total asteroid population on the background. . . . 85
3.9 SMASS binaries colaboration spectra . . . 87
3.10 Contributed taxonomy - histogram . . . 87
3.11 Taxonomies founded in this work with background small asteroid taxonomy . . . 88

4.1 Degeneracy classes. . . . 92
4.2 Error cumulative histograms for defining cuts. . . . 93
4.3 Histograms of G2V colors. . . . 94
4.4 Definition of cluster for classification in color-color space . . . 96
4.5 Results of spectral classification . . . 98
4.6 VISTA MOVIS asteroid classification in J-Ks vs H-Ks . . . 99
4.7 VISTA validated with DeMeo . . . 100
4.8 Fraction of VISTA-DeMeo validation. . . . 101

4.9 Match between SDSS and VISTA taxonomies. . . . . 102
4.10 Plot of classified objects with VISTA. . . . . 103
4.11 Relative distribution of asteroid types . . . . . 103
4.12 Gradie and Tedesco distribution . . . . . 104

5.1 Examples of AO images of Camilla . . . . . 113
5.2 Residuals on predicted positions of *S/2001 (107) 1* . . . . . 115
5.3 Residuals on predicted positions of *S/2016 (107) 1* . . . . . 115
5.4 Near-infrared spectra of Camilla and its largest moon *S/2001 (107) 1* . . . . . 117
5.5 Optical lightcurves of Camilla . . . . . 120
5.6 Disk-resolved profiles of Camilla . . . . . 120
5.7 Stellar occultations by Camilla . . . . . 120
5.8 Topography of (107) Camilla . . . . . 121
5.9 Magnitude of *S/2001 (107) 1* with respect to Camilla . . . . . 122
5.10 Magnitude of *S/2016 (107) 1* with respect to Camilla . . . . . 122
5.11 Mass estimates of (107) Camilla gathered from the literature. . . . . 125
5.12 Diameter estimates of (107) Camilla gathered from the literature. . . . . 126

A.1 Reflectance spectrum of (2691) Sersic and meteorites . . . . . 130
A.2 Reflectance spectrum of (4383) Suruga and meteorites . . . . . 131
A.3 Reflectance spectrum of (7187) Isobe and meteorites . . . . . 132
A.4 Reflectance spectrum of (8373) Stephengould and meteorites . . . . . 133
A.5 Band parameters of (2691) Sersic . . . . . 134
A.6 Band parameters of (4383) Suruga . . . . . 135
A.7 Merged spectra of visible and NIR spectra of (8373) Stephengould . . . . . 136
A.8 (8373) Stephengould linear fit of spectra . . . . . 137

# List of Tables


3.1 Spex - Observational circumstances for each asteroid . . . . . 63
3.2 Some characteristics of the asteroids observed with Spex . . . . . 65
3.3 Slopes and mineralogical parameters of binary spectra . . . . . 72
3.4 Matching asteroid spectra with RELAB spectra . . . . . 73
3.5 Synthesis of asteroids characterized during this work with no previous taxonomy. These are all small asteroids. In the table are presented: dynamical type (DT), absolute magnitude (H), geometric albedo ($p_v$), diameter in Km (D), previous taxonomy, assigned taxonomy from this work, meteorite class and meteorite analogue. Physical characteristics of the binary asteroids: absolute magnitude, albedo, diameter, previous taxonomical class, this work taxonomical class, suitable meteorite analogue class, and best match analogue. . . . . 85

4.1 G2V Colors . . . . . 95
4.2 Case one color . . . . . 97
4.3 Colors Pic du Mid . . . . . 106

5.1 Orbital elements of the satellites of Camilla . . . . . 116
5.2 Orbital and physical parameters of Camilla obtained with KOALA . . . . . 123

A.1 Lightcurves of Camilla . . . . . 138
A.2 AO images of Camilla . . . . . 140
A.3 Comparison of Camilla shape model with stellar occultations . . . . . 142
A.4 Astrometry of *S/2001 (107) 1* . . . . . 142
A.5 Astrometry of *S/2016 (107) 1* . . . . . 144
A.6 Diameter estimates of (107) Camilla . . . . . 146
A.7 Mass estimates of (107) Camilla . . . . . 147

# 1 Introduction

Some 4.6 billion years ago, the Solar System was forming from the dust and gas left by dead stars, that formed a planetary nebula with diverse composition, that transformed in a distribution of matter with different type of content and a thermal gradient (Fig. 1.1) [1] that depended on a star: the Sun. The seeds that later became planets and moons, and the world as we know it, had transformed due to different processes from that initial "debris". We know that because astronomy has the tools that permit us to unveil the mysteries of asteroids and comets, which are some *relatively* unchanged remnant debris from the formation of the solar system. How did all that occur? Like detectives, we can look and see in what we have in our near cosmic neighborhood, in that rocks of different sizes that orbits our Sun: in asteroids.

What we can see now is what has survived. But all of this debris has experienced numerous collisional, dynamical, and thermal events that had shaped their present-day physical and orbital properties. The task is to interpret this record by observation, studying meteorites, -which are the chunks of them that had also survived to arrive on Earth- by doing experimentation, and using theoretical models to understand how all this happened.

The total mass of asteroids is ~ 1/15 that of the Moon. But even though this represents a tiny fraction of the total mass of planets, their large numbers, their diverse compositions from a variety of materials -mostly rock, some metallic- (Fig. 1.3), and their orbital distributions, provide powerful constraints for planet formation models.

Around ~ 90% reside in a zone known as the asteroid belt (Fig. 1.2) between Mars and Jupiter, and are strongly influenced by the gravity of the latter. But they are not uniformly distributed through the asteroid belt, there exists certain zones with very few of them, noted by Daniel Kirkwood in 1868. These are gaps in the distances of these bodies orbits from the Sun. Located at positions where their period of revolution about the Sun is an integer fraction of Jupiter orbital period (Fig. 1.20). The inner, middle, and outer sections of the main belt, ranging from 2.0–2.5, 2.5–2.82, and 2.82–3.2 AU[2] respectively, are separated by the 3:1 and 5:2 mean motion

[1] in a similar way as currently is being investigated in $\epsilon$ Eridani system.

[2] AU -Astronomical Unit: the mean distance of Earth from the Sun = $1.496 \times 10^{11}$ m

Figure 1.1 – Artist's illustration of $\epsilon$ Eridani system showing $\epsilon$ Eridani b. A Jupiter-mass planet is shown orbiting its parent star at the outside edge of an asteroid belt. In the background can be seen another narrow asteroid or comet belt plus an outermost belt similar in size to our Solar System's Kuiper Belt. The similarity of the structure of this system -the closest debris disk around a star similar to the early Sun- to our Solar System is remarkable. Observations by the NASA *Stratospheric Observatory for Infrared Astronomy* (SOFIA) confirmed the existence of the asteroid belt adjacent to the orbit of the Jovian planet [Su et al., 2017]. (Credits: NASA/SOFIA/Lynette Cook).

resonances.

We can say that the only constant in the Universe is the change. What we can see now in asteroids is a stage of their evolution. Binary asteroids let us have a deeper insight in that evolution in a shorter time scale.

There has been a long way since the first innocent sights of asteroids. Before, there was no data, astronomers were free to speculate how that might look like. For example the idea that small bodies would not be able to hold on regolith like the Moon does. Wouldn't any impact ejecta just get blasted away, never to return, thanks to the lack of gravity? Nowadays the images of Deimos show that even a 15 km body could retain regolith, even more it seemed that the debris has slid downhill from Deimos' equatorial ridge. "One of the early prejudices was that, in presence of very low gravity, downslope movement wouldn't be effective," As Joseph Veverka said fascinated by what tiny worlds showed "As it turned out, efficiency of moving stuff downhill is independent of gravity" [Small is not Dull, Veverka, 2013]. The images of these small worlds are now increasing, showing more complexities. What would have thought

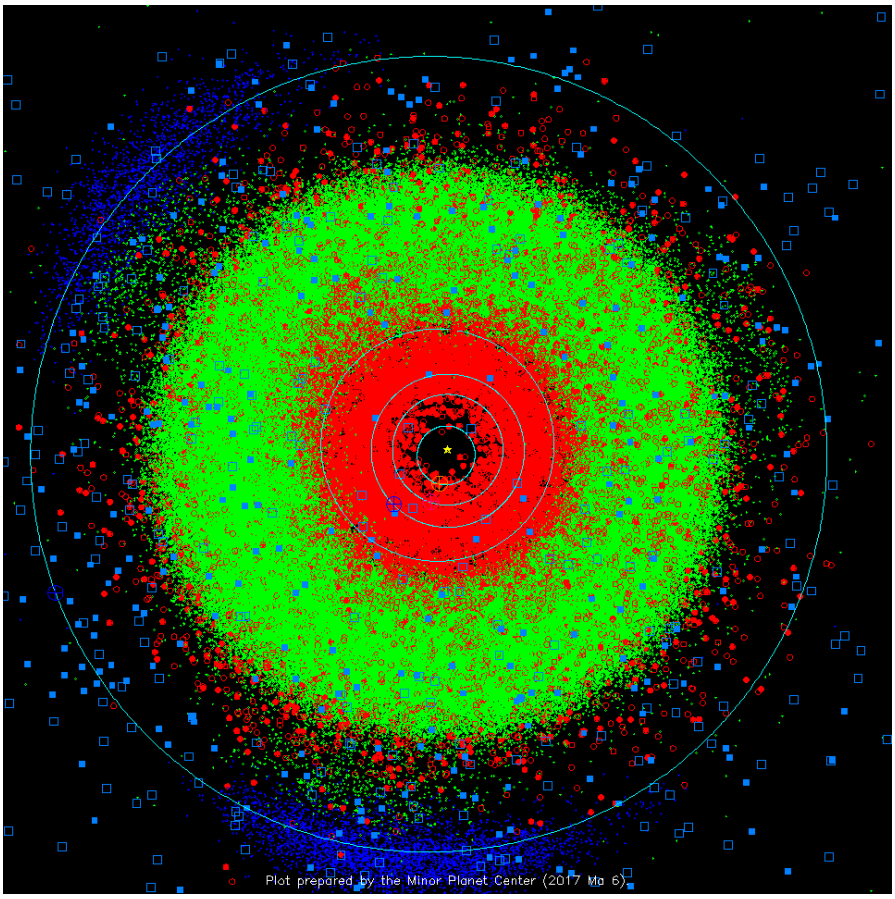


Figure 1.2 – The asteroid population of the Solar System interior to the orbit of Jupiter. Main-belt asteroids between Mars and Jupiter are shown in green, near-earth asteroids (NEA) are shown in red, comets are shown as blue squares, and Jupiter trojans are shown as clusters of blue dots. (Image: the Minor Planet Center.)

Veverka on Itokawa?

We are in a golden era for planetary research. Today we have different methods to question nature, a large amount of data, ground and space telescopes, adaptive optics (AO), detectors in the UV, visible, and IR, spacecraft that had already descend on minor bodies and collect samples, plans to impact them, ongoing space missions to asteroids... so even thought we can't test nature like is usual in labs on Earth "controlling" the experiment, we can serendipitously follow objects according to their natural cycles to obtain information.

As Richard Binzel said at *ACM 2017* [Advances in Understanding physical properties of small bodies, Binzel, 2017] the conference on asteroids, comets and meteors, held in Montevideo - Uruguay on April 2017, the study of planetary bodies has moved on a first stage from astronomical to geological, the next stage is to move from geological to geophysical.

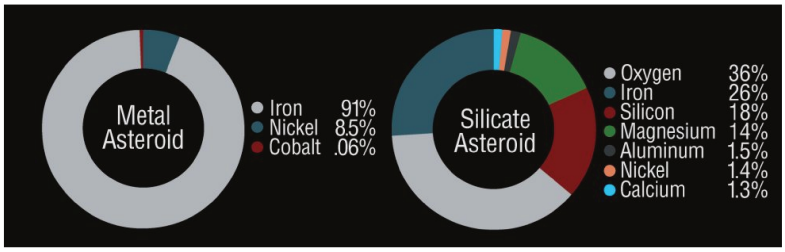


Figure 1.3 – Asteroid composition. Image adapted from NASA/Osiris-REx

## 1.1 Asteroids *Do* have satellites

This was the name of the chapter in *Asteroids III* by Merline et al. [2002] were it was at last included the existence of satellites of asteroids in the Decadal review on asteroids published by the University of Arizona Press after many years of suspecting their existence.

Since 1610, when Galileo Galilei [1610] observed with his telescope that Jupiter has satellites ("carried stars" with it) and was like a mini-Solar System (Fig. 1.4), the awe -as the Aristotelean universe collapsed- has increased and we as humans have wondered of other worlds. At the time of writing this manuscript it is hot news the discovery of a "close" simile of our Solar System with 7 sisters of Earth near Trappist-1 [Gillon et al., 2017]. Asteroids with satellites in fact offer the opportunity to investigate how this systems came to be from the primordial blocks.

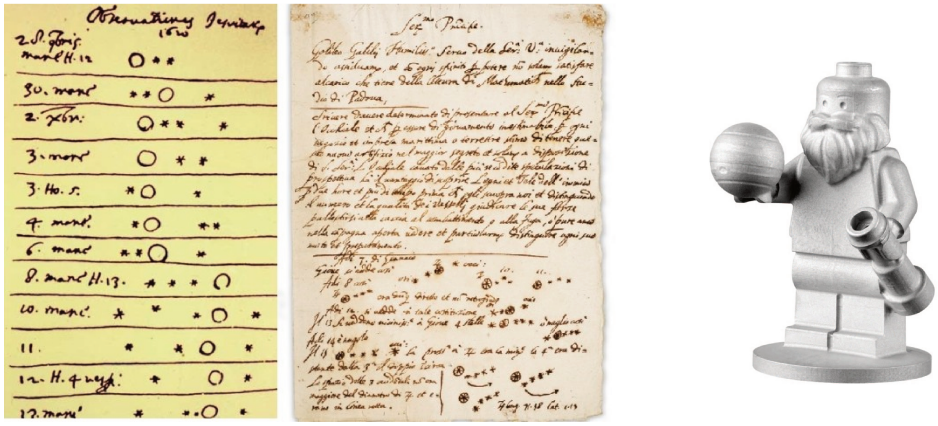

Figure 1.4 – **Left:** Galileo drawings of the moons discovered by him around Jupiter. **Right:** Lego aluminum minifigure of Galileo in Juno spacecraft (Credit: Lego.com).

Giussepe Piazzi discovered Ceres, the first asteroid, on January 1, 1801 from a brand new observatory at the Royal Palace in Palermo [Foderà Serio et al., 2002], which at the time had the most accurate instruments like the 5-foot Palermo Circle and the 5-foot circular-scale altazimuth telescope. Ceres was considered at the time as "the missing planet" that should be wandering between the orbits of Mars and Jupiter as suggested by Johannes Kepler in his *Mysterium Cosmographicum* [Kepler et al., 1596], an idea that was motivated by his thoughts

on, *"Why had God been motivated mathematically to select the planetary orbits in the way He had?"*. The huge gap between Mars and Jupiter was especially difficult to explain for him. Kepler tried a bold approach placing a new planet between Jupiter and Mars[3] [Foderà Serio et al., 2002].

The name *Asteroids* was first used by Herschel [1802] to denote the *star like* bodies Ceres and Vesta, after thoroughly observing them, estimating their sizes, and make a digression on the nature of these two stars that were nor planets, nor comets. A new name was needed. Herschel asked for help (urged by the publication of a paper) in between his friends and acquaintances to propose a name for these objects. It was a greek scholar, Charles Burney Jr., who coined the word [Cunningham, 2013, 2016].

Interestingly, Herschel [1802] himself had also search for satellites around these asteroids, and conclude *"...there can be no great reason to expect that they should have any satellites. The little quantity of matter they contain, would hardly be adequate to the retention of a secondary body..."*.

In 1901, Charles Andre suggested that the lightcurve of Eros had imprints of a satellite around it. In the 70's, anomalous lightcurves suggested satellites; in the 80's several observations supported the idea that binary asteroids existed: from observing asteroids with slow and fast rotation and the image of double craters on the Moon and even on the Earth. Several efforts were done searching for them without success. More and more lightcurves were acquired from different asteroids with no positive result (Nysa, Ophelia, Hebe, Pallas, etc) [Weidenschilling et al., 1989, 1987, Gehrels et al., 1987].

It was not until 1993 that, on its tour to the jovian system, the Galileo spacecraft made the first detection of a satellite around an asteroid, in a rather serendipitous way. The images taken by the probe showed that (243) Ida (31km), has a moon, [Belton and Carlson, 1994] (Fig. 1.5) officially named Dactyl (1.4km) now. That event boosted the observational search and theoretical research on binary asteroids, including numerical simulations to understand the processes that could form such systems.

The first detections from lightcurves shapes of Near Earth Asteroids (NEAs) were made by Petr Pravec et al. and Stefano Mottola et al., these includes: 1994 $AW_1$ [Pravec and Hahn, 1997], 1991 VH [Pravec et al., 1998b], 3671 Dionysus [Mottola et al., 1997], and 1996 $FG_3$ [Pravec et al., 1998a].

The first confirmed detection of an asteroid satellite from a ground-based telescope was that of Petit-Prince (13km), the moon of (45) Eugenia (215km) by direct imaging assisted by adaptive optics (AO) in 1998 [Merline et al., 1999]. This was the first positive detection from a dedicated survey with the capability to search for faint companions ($\Delta m \sim 7$ mag) as close as a few tenths of an arcsecond from the primary. With this survey were also detected the binaries: (762) Pulcova and (90) Antiope [Merline et al., 2000].

[3] and also another between Venus and Mercury

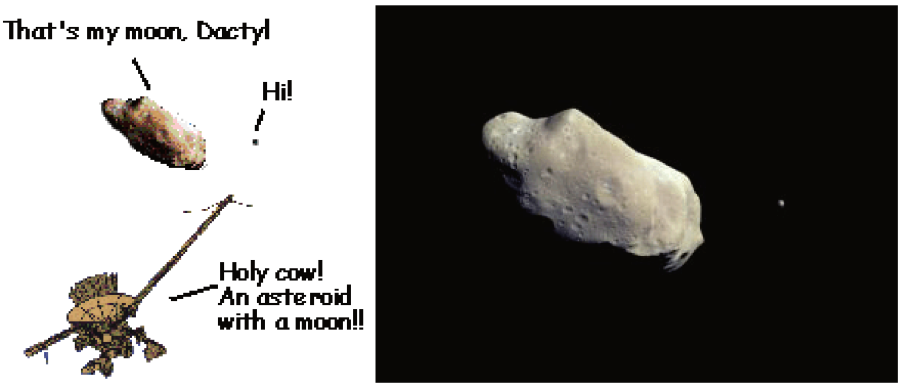


Figure 1.5 – Left: Galileo probe made asteroid (243) Ida flyby on August 1993, on its way to the Jovian system. Image credit: Sue Kientz. Right: Ida and its satellite Dactyl, the first binary system discovered by the Galileo Imaging Team on February 1994. Photo credit: NASA

The first two Near Earth Asteroids (NEAs) binaries detected by radar were: 2000 $DP_{107}$ [Ostro et al., 2000, Margot et al., 2000, Pravec et al., 2000] and 2000 $UG_{11}$ [Nolan et al., 2000].

Since then, the discovery of many binaries and a handful of multiples has been well sustained, mostly by lightcurves and by radar. The majority of these binaries are NEAs.

## 1.2 Why study binary asteroids?

This question is answered almost with the same answer to "why study asteroids?" just that in this case we have the advantage of the interaction between the parts, that, as was said in the beginning, gives the mass of the system, on formation processes of minor bodies and planets and on the origin of the Solar System.

How planet formation occurred can be addressed with a better comprehension on how asteroids form and evolved.

Binary asteroids represent an important population for the study of the Solar System. Their mutual interaction gives us clues on the dynamics of minor bodies, and besides, if the system can be resolved, a direct way to estimate the mass of the asteroid (which is the most productive method) [Carry, 2012]. In that sense, it is relevant to refine the orbits of these bodies in order to compute their mass more precisely. If in addition we can determine the shape of the body, we can have a better estimation of its density -a fundamental property- with more precision.

With comets, asteroids are the most direct remnants of the original building bricks that formed bigger bodies as planets, containing the record of pristine conditions that existed at the beginning of the formation of the Solar System. Asteroids don't experience erosion by wind or water, or tectonic plates activity, they don't usually experience volcanism; and unless they

are massive enough, they don't become differentiate bodies. Their evolution is determined by its environment. Things happen when they approach a planet, when there is a collision, or because of the solar wind or when interplanetary particles impinge on them. As such, they evolve differently from planets and being in a way pristine, carry with them the imprints of their birth from the solar nebula, this is why they can serve as tracers of the evolution of the Solar System.

Asteroids, -and mostly binary asteroids- can give us a window of the processes involved in the evolution of the Solar System and a time-scale that shows how the composition of the Solar System was varying with time.

The scope of this manuscript will be dedicated to binary asteroids in the inner regions of the Solar System, the Kuiper belt population that apparently have different physical, dynamical and evolutionary properties, will not be considered here. In general, I will refer to binaries, but in fact the population I am considering includes triples like (45) Eugenia, and (87) Sylvia.

Binaries can also help to constrain our knowledge of the collisional evolution of asteroids.

**On designation of asteroids and binaries**

At the beginning, asteroids were unique objects, they were given names of notable personages: Ceres, Pallas, Juno, Vesta[4], etc. But, little by little and then, abruptly the frequency of discoveries began to grow and boost and it was needed a more suitable way to name them. Currently, an asteroid is given a provisional designation with four numbers, 2 capital letters, and a subscript number related to its discovery, composed in this way: first four numbers are the year of discovery, then the first letter is the half-month period during which the object was discovered, the second letter with a subscript number gives the order of discovery within that period. For example: the binary 1991 $RJ_2$ was discovered in 1992 in the first fortnight of September[5].

When the orbit of the asteroid becomes well enough determined, the asteroid receives a permanent number issued sequentially by the Minor Planet Center. On the other hand, names for minor bodies like asteroids can be proposed to the Committee on Small Body Nomenclature (CSBN) of the IAU http://www.ss.astro.umd.edu/IAU/csbn/, the one who will decide according to several rules [6].

In the case of binaries, when one satellite is discovered, a provisional name is also given, the letter code is replaced by the asteroid number in parentheses. For example, the satellite of (45) Eugenia was named S/1998 (45) 1, being 1998 the year of the moon discovery, the discoverers

[4] now numbered in order of discovery: (1) Ceres, (2) Pallas, (3) Juno, (4) Vesta, all women!...not anymore

[5] The first 25 asteroids discovered during the half month period September 1–15 in 1991 will be numbered 1991 RA to 1991 RZ. The next 25 will be numbered 1991 $RA_1$ to 1991 $RZ_1$, subsequent discoveries in that period the subscript number will be 2, 3, 4,... etc.

[6] https://www.iau.org/public/themes/naming/#minorplanets

proposed Petit Prince [7] as permanent name for this satellite, which was accepted. In 2004, a second satellite was discovered, it still has a provisional name, S/2004 (45) 1, but it's informally well known as Petit Princesse. Where more than one moon has been discovered, the discovery sequence is specified by roman numerals, so that Eugenia's moon would be: (45) Eugenia I Petit Prince, and (45) Eugenia II Petit Princesse.

The discovery of new binaries has been increased as technology and methods improved. Although the techniques used defines also biases on the knowledge of binaries population. Lightcurves permits the detection of close satellites around small asteroids, not of distant companions. With radar, satellites widely separated from the asteroid can be detected, but there is a limit for the detection for distant MBAs. High resolution imaging is suitable for finding distant companions of large MBAs.

The reports on discovery of asteroid satellites are sent to the Central Bureau for Astronomical Telegrams (CBAT) which is responsible for the dissemination of information on transient astronomical events. Confirmed discoveries are published as "telegrams" by CBET (Central Bureau Electronic Telegrams)[8] and can be consulted at the **Satellites and Companions of Minor Planets** page of the IAU [9].

There exists dedicated programs for the discovery of satellites like, Petr Pravec's group Ondrejov Asteroid Photometry Project [10], Raoul Behrend Light curves program [11].

Dedicated decadal publication on Asteroids (Asteroids, Asteroids II, Asteroids III, Asteroids IV) by University of Arizona Press refer from the first volume to the possibility, and then when confirmed, to the existence of binary asteroids.

It also exist Binaries Asteroid's Workshop (the first one celebrated in 2007, the last one -4th- in 2016) where specialists gather to discuss ideas on detection, characterization, formation, and implications of binary and multiple objects among the NEO, main-belt, Trojan, Centaur and TNO populations.

### 1.2.1 Nomenclature

The scenario of binaries is a bit diverse, some definitions to clear the panorama, according to Jacobson and Scheeres [2011], Walsh and Jacobson [2015] are useful to group them in order to define better the objects of this work.

- **Binary asteroids**: A couple of asteroids that are gravitationally bound are called binaries (in case they are three they are known as triples). The larger component is the primary,

[7] http://www.boulder.swri.edu/merline/petitprince.name.txt
[8] Not actual telegrams, the name was kept for historical reasons.
[9] http://www.cbat.eps.harvard.edu/minorsats.html
[10] http://www.asu.cas.cz/ ppravec/
[11] https://obswww.unige.ch/~behrend/page_cou.html

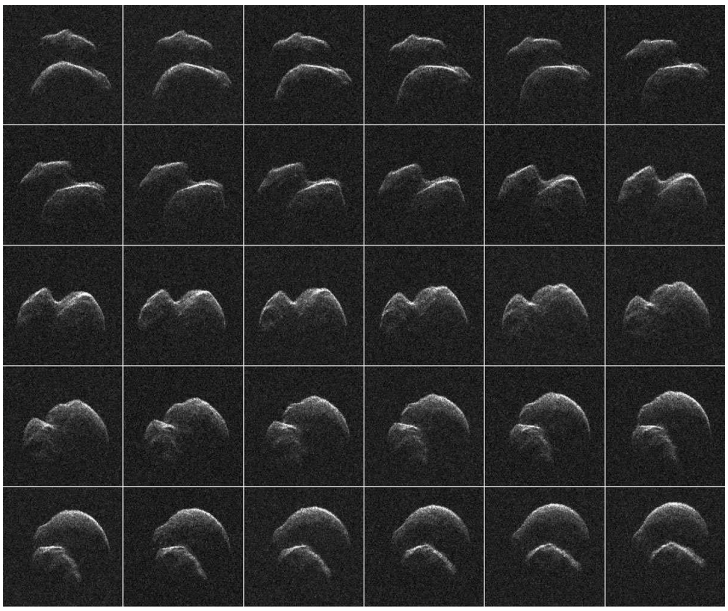

Figure 1.6 – 17-April-2017 Arecibo Radar images from contact binary 2014 JO25. Credit: JPL/NASA.

and the smaller component is called the secondary.

- **Asteroid Pairs**: These denote a couple of asteroids that are genetically related but not gravitationally bound. Recently was discovered the youngest pair P/2016 J1. Remarkably, each member went active after splitting [Moreno et al., 2017].

- **Contact Binaries**: These are two asteroids in contact that look as a double-lobed object. As for today, there are a handful of confirmed contact binaries like 2014 $JO_{25}$ (which just happen to pass close to the Earth on April 19 of this year, Fig. 1.6), and several suspected. On the other hand, comets like 67P/Churyumov–Gerasimenko and 8P/Tuttle are contact binaries.

- **Split Pairs**: These systems are inferred from dynamical models having their heliocentric orbits closely link but they are not actual binaries, although some of its members are binaries.

### 1.2.2 On the size of binary asteroids

At the beginning, asteroids had been considered to be spherical, since the first spacecrafts like NEAR sent the images of (433) Eros it was first viewed how different from round can asteroids be. This complicates the determination of the volume, and with that the density. It is necessary to determine as accurate as possible the volume. Several techniques can be used for that.

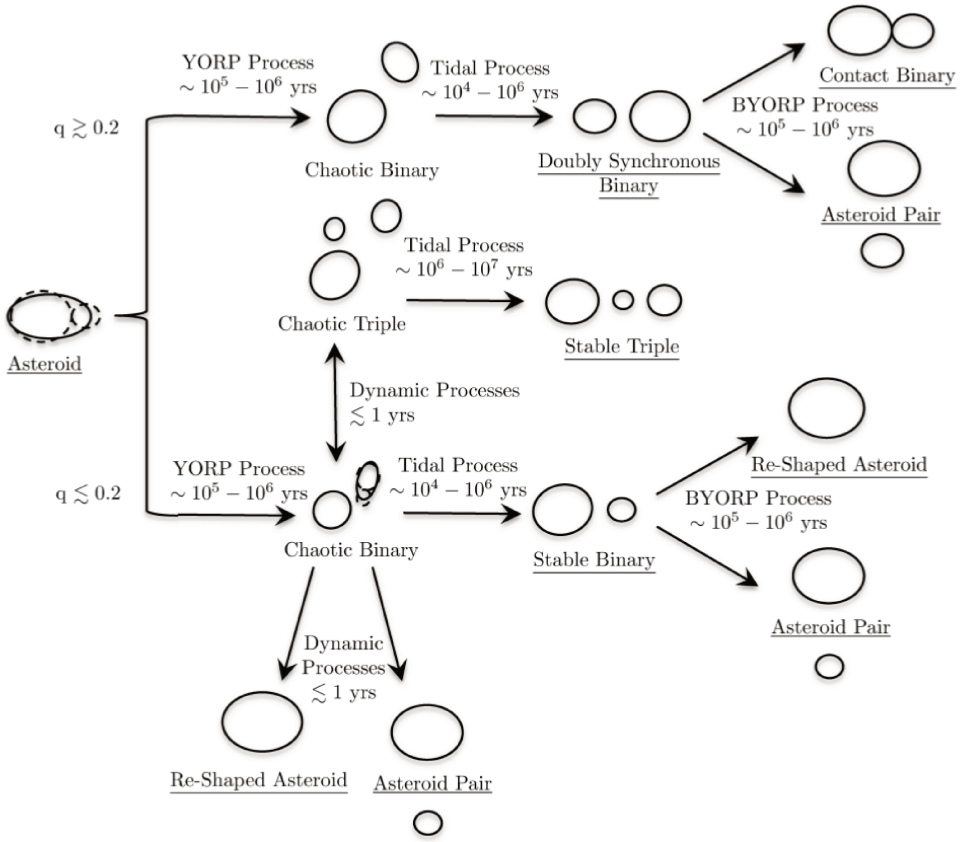


Figure 1.7 – Flowchart showing the possible evolutionary paths for an asteroid after it undergoes rotational fission and the different outcomes of that processes. Figure from Jacobson and Scheeres [2011].

Infrared light is widely used to determine an asteroid's size because visible-light from the sun reflects off the surface of the rocks. The more reflective the object is, or the more albedo the object has, the more light it will reflect as can be see in Fig. 1.8, three asteroids doesn't look the same in both ranges of wavelengths. that means that the brightness of an asteroid in visible light is the result of both its albedo and size. Combined measurements in visible and infrared light are used to calculate asteroids albedos.

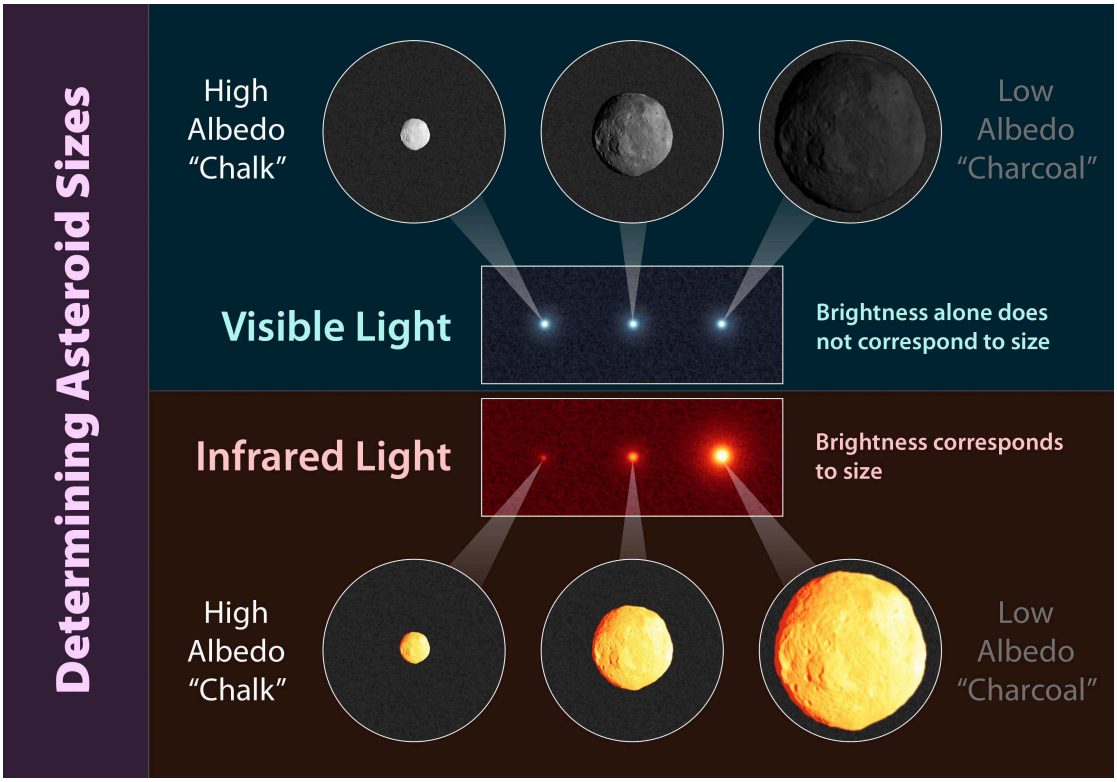


Figure 1.8 – Size of an asteroid from optical and infrared observations. (Credit: NASA)

Small and large asteroids behave differently. That is why in general they are divided in small and large, the dividing line is approximately set by Jacobson et al. [2014] to a diameter of about 20 km. The small ones are affected by the YORP effect (non gravitational effect) along their lifetime (Fig. 1.7). For low sizes, very small asteroids are defined as asteroids with diameters less than 200 m. (Fig. 1.9). Among small asteroid about 15 ± 4% are binary asteroids [Margot et al., 2015]. We currently know 213 systems.

The secondary-to-primary size ratio $Ds/Dp$ is an important quantity in binary systems. Pravec et al. [2006] identified two effects limiting sizes of binary system components. One effect is that Ds/Dp ratios appear to concentrate below Ds/Dp = 0.5. Satellites larger than 0.5 Dp appear rare in asynchronous binary NEA systems. Binary systems with Ds/Dp > 0.18 appear to concentrate among NEAs with Dp < 2 km.

This apparent lower abundance of binaries with larger primaries/satellites might be related with mechanism preferring creation/stability of satellites among asteroids with Dp < 2 km, or there is a mechanism that limits secondary size to Ds < 1 km.

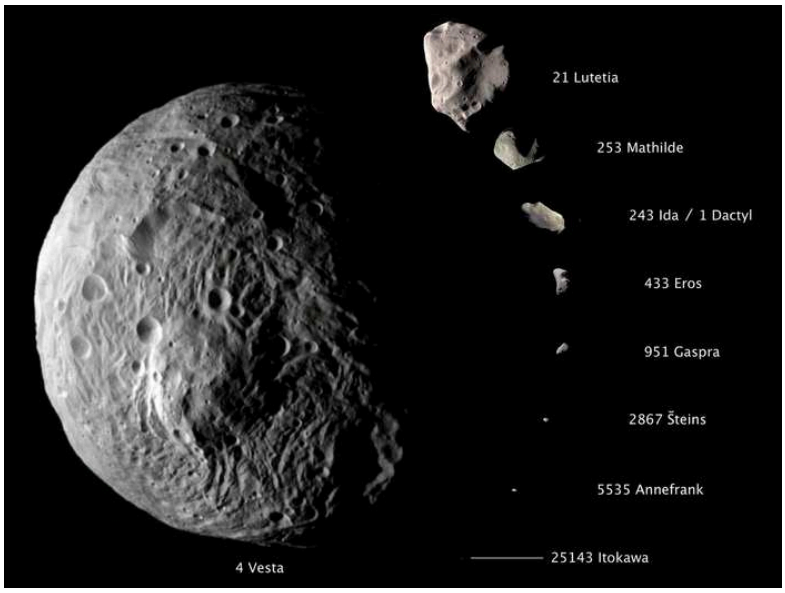


Figure 1.9 – Composite image showing the comparative sizes of nine asteroids from Vesta (~530 km) to Itokawa (~0.5 km). Image from NASA.

Smaller sizes typically indicate a younger surface age, so it is possible the difference is due to weathering effects. In general, the characterization of asteroids is biased to large or interesting cases due to the resources implied in their observation.

### 1.2.3 Where are the binaries in the Solar System?

Asteroids are not homogeneously distributed in the Solar System as can be seen in Fig. 1.2, there are denser regions. The crowded zones were defined by different type of interactions and are a snapshot in the evolution of the Solar System.

Dynamically, asteroids are grouped in the following populations (Fig. 1.11):

- **NEAs** the Near Earth Asteroids are the asteroids with perihelion distance $q$ less than 1.3 AU. This group is subdivided according to their perihelion distance $q$, aphelion distance $Q$ ($Q = a(1+e)$) and their semi-major axes $a$ [12].
  - **Atiras** are those whose orbits are contained entirely within the orbit of the Earth $Q$< 0.983 AU (named after asteroid 163693 Atira).

[12] https://cneos.jpl.nasa.gov/about/neo_groups.html

  - **Atens** are Earth-crossing NEAs with semi-major axes smaller than Earth's and $Q$>0.983 AU (named after asteroid 2062 Aten).
  - **Apollos** are Earth-crossing NEAs with semi-major axes larger than Earth's (named after asteroid 1862 Apollo) and $q$<1.017 AU.
  - **Amors** are Earth-approaching NEAs with orbits exterior to Earth's $a$> 1AU, but interior to Mars 1.017<$q$<1.3 AU (named after asteroid 1221 Amor).
  - **PHAs** the Potentially Hazardous Asteriods are NEAs whose *Minimum Orbit Intersection Distance* (MOID) with the Earth is 0.05 AU or less, and whose absolute magnitude $H$ is 22.0 or brighter. In principle these could possibly impact the Earth within the next century, producing major damage. About 1800 PHAs are known as for 14 May 2017 from an estimation of 4700±1500 [13] (Fig. 1.12).

- **Mars Crossers** these asteroids have an orbit that crosses the orbit of Mars. Due to secular perturbations, Mars eccentricity varies substantially over million-year time scales; thus, this population fluctuates over time.
- **MBA** the Main Belt Asteroids occupy the Main asteroid belt between Mars and Jupiter 2.2 <$q$< 3.3 AU (the most asteroid-populated zone in the Solar System). These asteroids are grouped according to their orbits as: Hungarias (HUN), Inner Main Belt (IMB), Middle Main Belt (MMB), Outer Main Belt (OMB), Cybeles, and Hildas.
- **Jupiter Trojans** trojans in general are asteroids that have stable orbits in the $L_4$ and $L_5$ Lagrangian points of a planet, in this case, Jupiter. They share Jupiter's orbit at 5.2 AU but lead or trail the giant by ~60°in longitude.
- **TNOs** Trans Neptunian Objects, actually not considered asteroids, but included in the list for completion.

There are binary asteroids all over in the Solar System! The last census[14] gives:

- 61 near-Earth asteroids (2 with two satellites each),
- 22 Mars crossing asteroids (1 with two satellites),
- 128 main-belt asteroids (8 with two satellites each),
- 4 Jupiter Trojans
- 81 Trans-Neptunian Objects (TNO)

Clues can be obtained from binary asteroids prevalence in a population. As noted by [Polishook and Brosch, 2008], binarity is a very common phenomenon for NEAs, specially for

[13] http://www.minorplanetcenter.net/iau/lists/t_phas.html
[14] http://johnstonsarchive.net/astro/asteroidmoons.html

Atens, perhaps even more than for other NEA groups among which 15% are assumed to be binaries [Bottke and Melosh, 1996b]. This may indicate that Atens suffer more disruptions caused by planetary encounters than do Apollos or Amors. One possible explanation could be their higher likelihood of tidal interactions with Earth and Venus, causing stronger tidal forces. According to numerical models by Scheeres and Ostro [2004] Aten asteroids are more prone to spin up and three times more likely to disrupt than Apollo and Amor asteroids. Another possibility is that the much closer distance of small Atens to the Sun enhances the effect of thermal reemission due to the YORP effect. Thus, the Atens can rotate faster and could eventually disrupt.

In this work I will concentrate in binaries in the internal part of the Solar System (Fig. 1.13), but I also have observed TNOs (Ch. 4).

Asteroids in the main belt were thought to have formed essentially where they are now [Gradie and Tedesco, 1982]. Early measurements in the 80's showed that the inner main belt was redder and the outer main belt was bluer. Distinct color groupings of asteroid types group were found, the difference seemed a function of distance from the Sun. At the time, that was interpreted as the remanent of the temperature gradient across the Main Belt from the time of planetesimal formation, supporting the idea of a static Solar System. But that idea has changed dramatically, now we know there has been many variations and a lot of mixing, the main belt of asteroid and the Kuiper Belt- are no longer considered primordial.

Planetary migration models like Nice Model [Tsiganis et al., 2005, Gomes et al., 2005, Morbidelli et al., 2005, Levison et al., 2011] and Grand Tack Model [Walsh et al., 2011] recreate the structure of the Solar System (Fig. 1.14). Late-stage migration modeled by Levison et al. [2009] helps to support a Dynamic Solar System. With the measure of the composition predicted by Levison et al. [2009] we can see now that the mixing is the norm in the MBA [DeMeo and Carry, 2013].

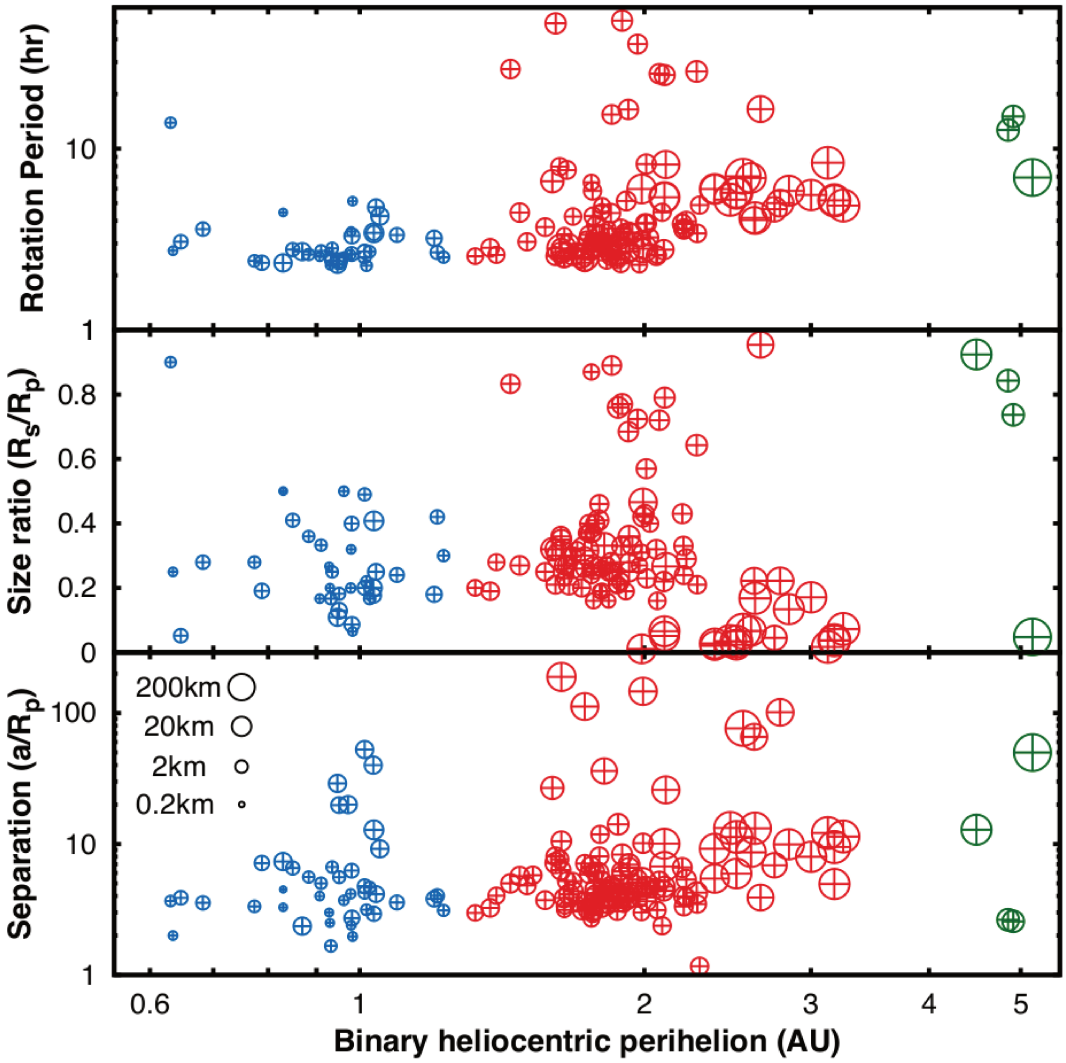


Figure 1.10 – The known population of binary asteroids. Panels shown: (Bottom) the component separation in terms of the primary radius, (Middle) the size ratio of the two components, and (Top) the rotation period of the primary all plotted as a function of the system's heliocentric orbit's pericenter. The size of the symbol indicates the size of the primary body. Figure from Walsh and Jacobson [2015].

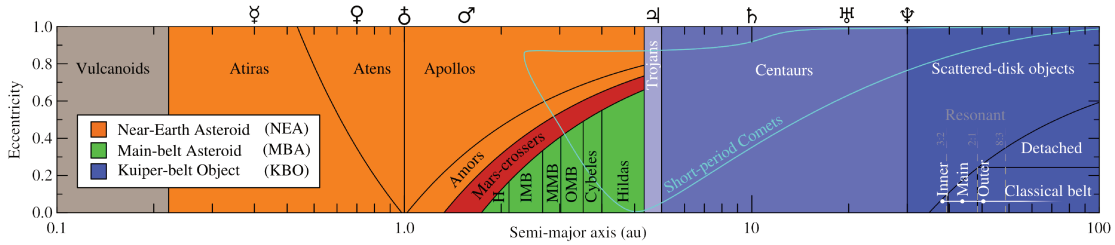


Figure 1.11 – Graphical representation of the definition of population classes of small bodies in SkyBoT (IMCCE).

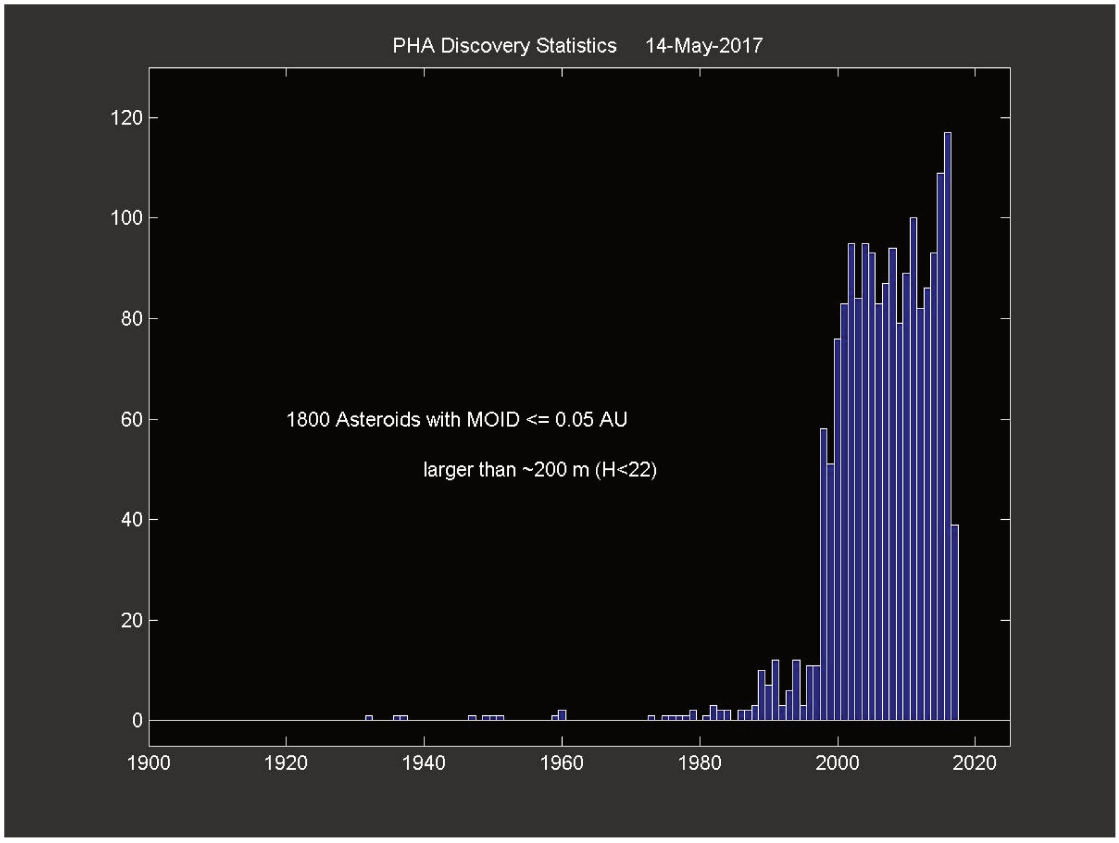


Figure 1.12 – Discovery statistics of Potentially Hazardous Asteroids as for May 2017. Image: European asteroid research node (EARN).

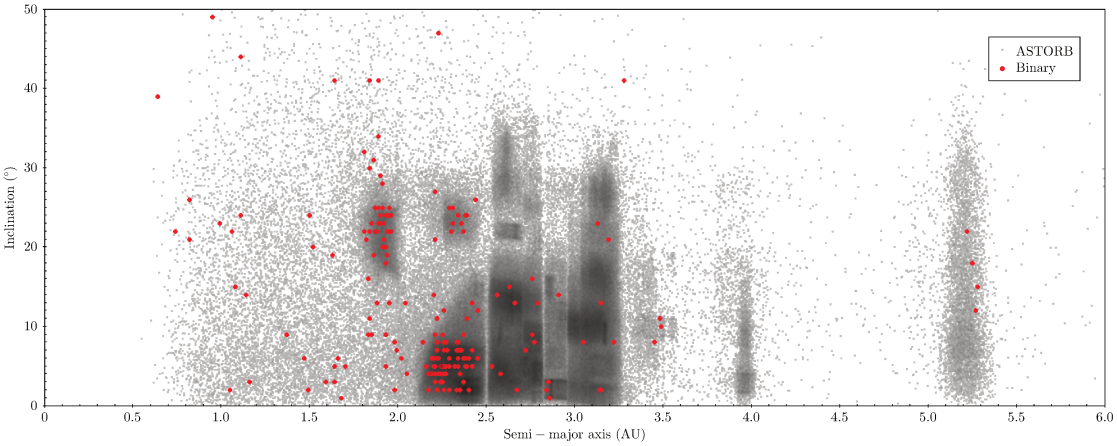


Figure 1.13 – Binaries in ASTORB (the Asteroid Orbital Elements Database, generated by Edward Bowell at Lowell Observatory with NASA funding) population in the Solar System.

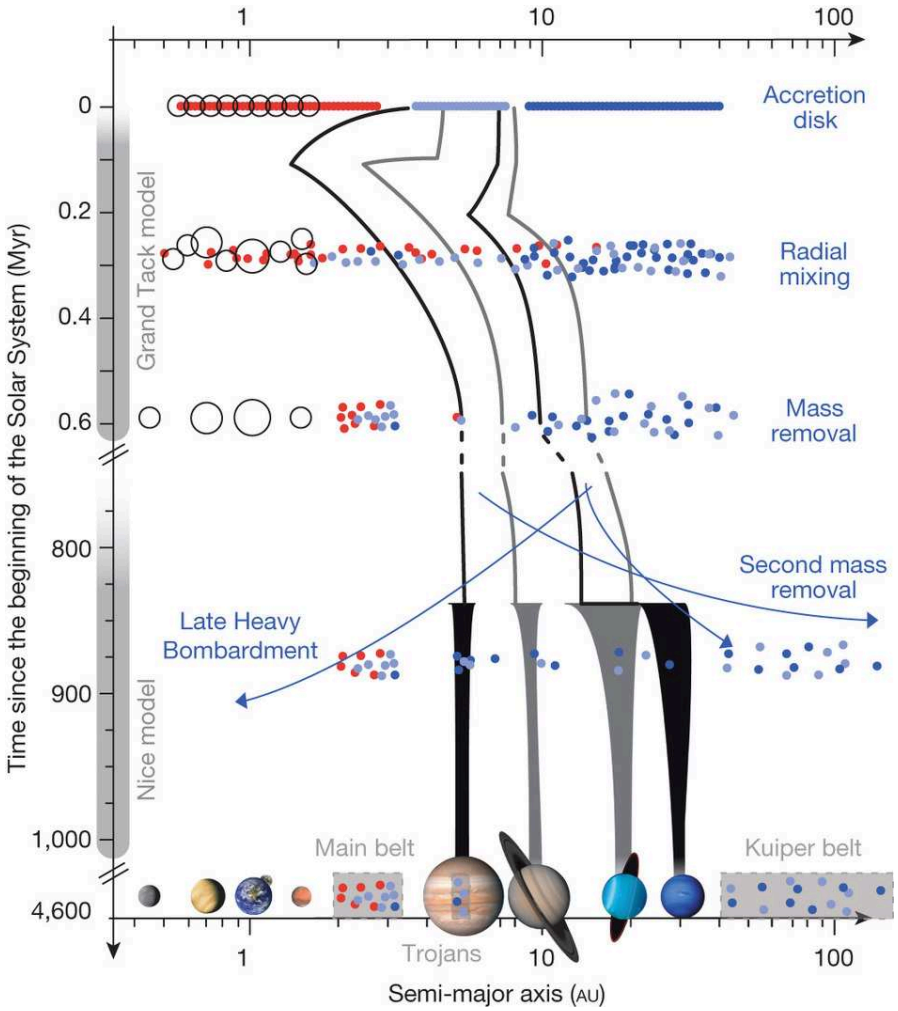


Figure 1.14 – Cartoon of the effects of planetary migration on the asteroid belt based on Nice and Grand Tack models which depicts periods of radial mixing, mass removal and planet migration ultimately arriving at the current distribution of the inner Solar System. Figure from DeMeo and Carry [2014].

## 1.3 Formation mechanisms of binary asteroids

One of the remarkable aspects of binaries is their diversity (Fig. 1.7). When studying them, we are decoding the differences in their formation and evolution mechanisms that act as a function of size, distance from the Sun, and the properties of their nebular environment at the beginning of Solar System history and their dynamical environment over the next 4.5 billions of years. Binaries are the laboratory where we can study numerous types of physical processes acting on asteroids, testing physical properties otherwise possible only with spacecraft. Several scenarios are considered for the formation of binaries.

### 1.3.1 Mutual Capture

In this scenario, the two components of the binary system become mutually bound by virtue of having relative speeds at encounter below their mutual escape speeds. This is a possible origin of Mars moons Phobos and Deimos (still an open question). Escape speeds of asteroids are of order m/s, while encounter speeds are of order km/s [Bottke et al., 1994]. The chances of direct capture are really small in the present-day populations of these bodies. However if a third body is present within the Hill sphere, the encounter speed can be reduced, allowing the capture [Goldreich et al., 2002].

It must be considered that given the short dynamical lifetime of NEAs and the relatively short collisional lifetime of MBAs, the mutual capture mechanism is not favored for those groups (any binaries formed in this fashion have long been destroyed).

### 1.3.2 Collisions

Since collisions are the dominant evolutionary process affecting asteroids, it is plausible that these satellites are by-products of cratering and/or catastrophic disruption events.

If a close encounter between two minor planets results in a collision, binaries may be formed by virtue of interactions between the debris pieces and/or between the debris and the largest remnant [Scheeres, 2002]. Following Newton's laws, material ejected from the surface of a spherical body either escapes, reimpacts, or enters orbit.

There are implications of the system transferring energy and angular momentum between rotational and translational motion, while conserving the total system energy and angular momentum. From results Scheeres [2002] developed a set of sufficient conditions for stability against escape and impact. With these he delineate several classes of final outcomes for a binary asteroid system, each of which may have implications for asteroid observations.

Durda et al. [2004] performed numerical simulations of impacts with smooth-particle hydrodynamics considering the formation of SMAshed Target Satellite (SMATS, Fig. 1.15). which applies for large asteroids like Camilla (Ch. 5).

Families of asteroids are also formed from collisional events, their study gives us information on the physics of catastrophic collisional breakup. The family members are the outcome of an experiment that was performed by nature.

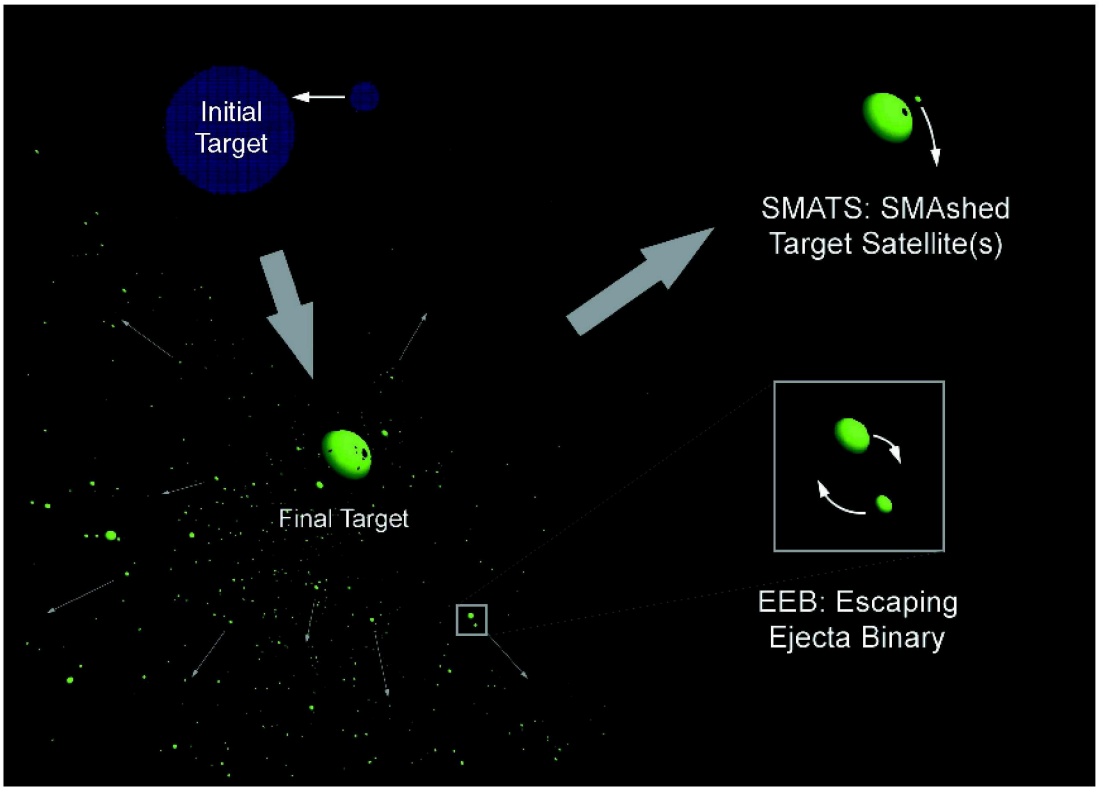


Figure 1.15 – Satellites resulting from large impacts according to simulations by Durda et al. [2004]. SMAshed Target Satellites (SMATS) form from impact debris that enters into orbit around the remaining target body, which is a gravitationally reaccreted rubble pile (Fig. 1.18). Smaller escaping fragments with similar trajectories become gravitationally bound to one another.

### 1.3.3 Tidal Breakup

After having observed that 10% of the impact craters on Venus and Earth (Fig. 1.17) are doublets (simultaneous formation) and with the use of numerical models, Bottke and Melosh [1996a,b] proposed that some fast rotating rubble-pile contact binary asteroids [15] (Fig. 1.18), undergo tidal breakup (they were well separated before impact) and split into multiple co-orbiting fragments after experiencing a close approach with a planet, in similar way as comet Shoemaker-Levy 9 fragmented as it passed by Jupiter before crashing on the planet [Asphaug and Benz, 1994](Fig. 1.16). This mechanism may cause the binary component to escape,

[15] Rubble-pile asteroids are defined as a collection of gravitationally self-bound components ranging in size from micrometers to kilometer size fragments.

but secondary satellites may form continuously during close encounters. This determines a steady-state distribution of binary asteroids in the Near Earth region.

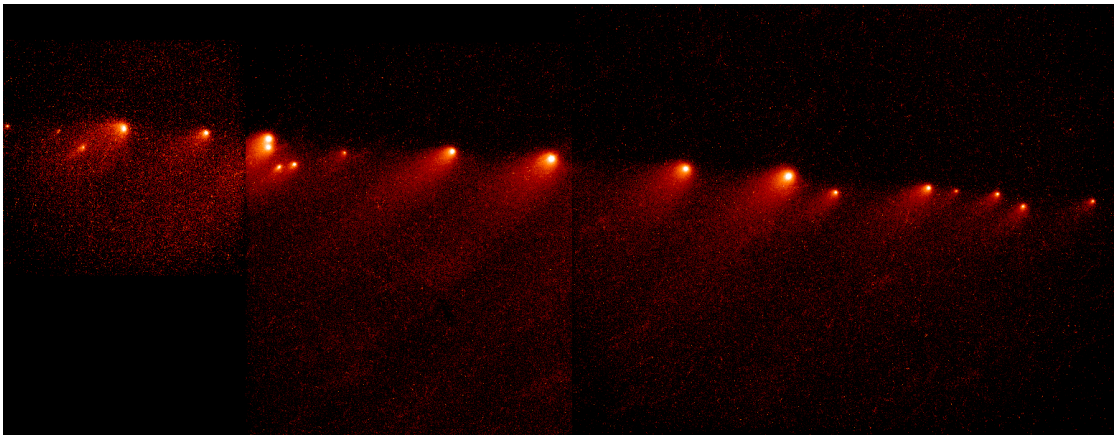

Figure 1.16 – Shoemaker Leavy-9 comet breakup

### 1.3.4 Rotational Disruption

The median dynamical lifetime of NEAs (before ejection from the Solar System or collision with a planet or the Sun) is ~10 Myr [Gladman et al., 1997]. There must be some efficient mechanism that can form binaries operating presently in the NEA region. A rotational disruption mechanism such as tidal disruption may be viable for the formation of binary NEAs. This requires that the progenitor have low tensile strength, i.e. that the object cannot resist being stretched (such as by centrifugal forces). Richardson et al. [2002] describe the evidence for the existence in the minor planet population of these so-called gravitational aggregates (of which "rubble piles" are a special case of loosely consolidated bodies with very low tensile strength and moderate porosity). The low bulk densities of primitive asteroids, many of which were measured by virtue of a natural satellite, are suggestive of this kind of interiors: Bulk porosities of 40%–60% are required if such bodies are the parent bodies of chondritic material that falls to Earth in the form of meteorites. It is currently thought that most binaries with D<20km were formed by rotational fission because of their short rotation periods [Margot et al., 2015].

## 1.4 Properties of binary asteroids

### 1.4.1 Orbital elements

The keplerian elements that define the orbit of an asteroid are (Fig. 1.19):

- $a$ **semimajor axis** 1/2 of the major axis of the elliptical orbit (the mean distance from the Sun). Describes the dimensions of its orbit around the Sun, its value determine its orbit period $T$.

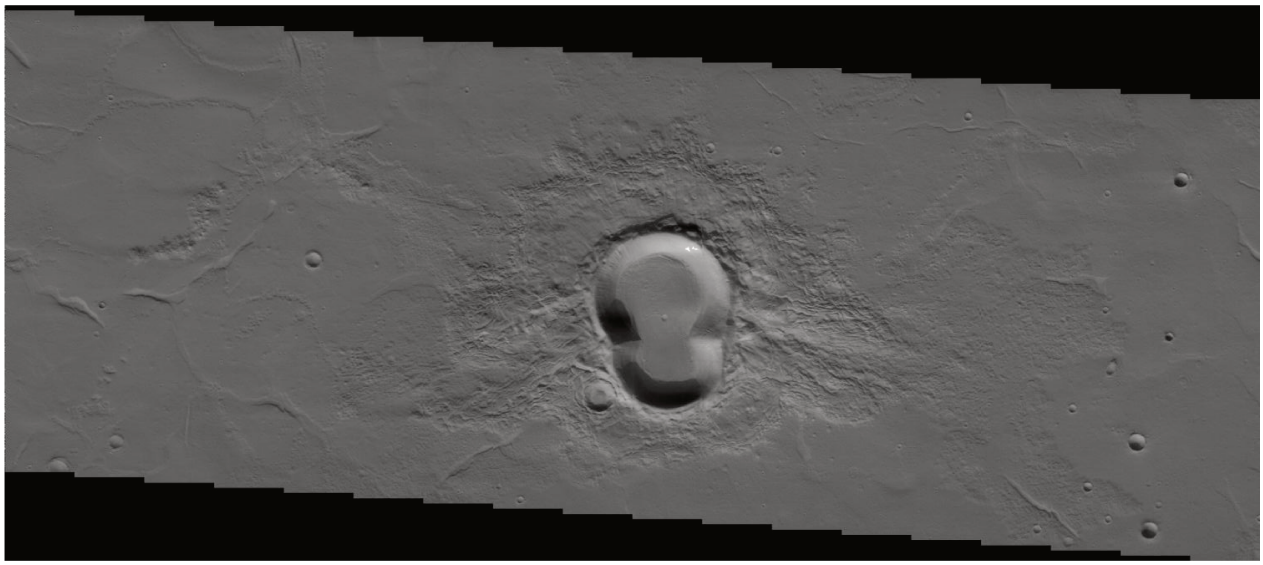

Figure 1.17 – Mars doublet crater. Image credit: NASA/JPL/ASU

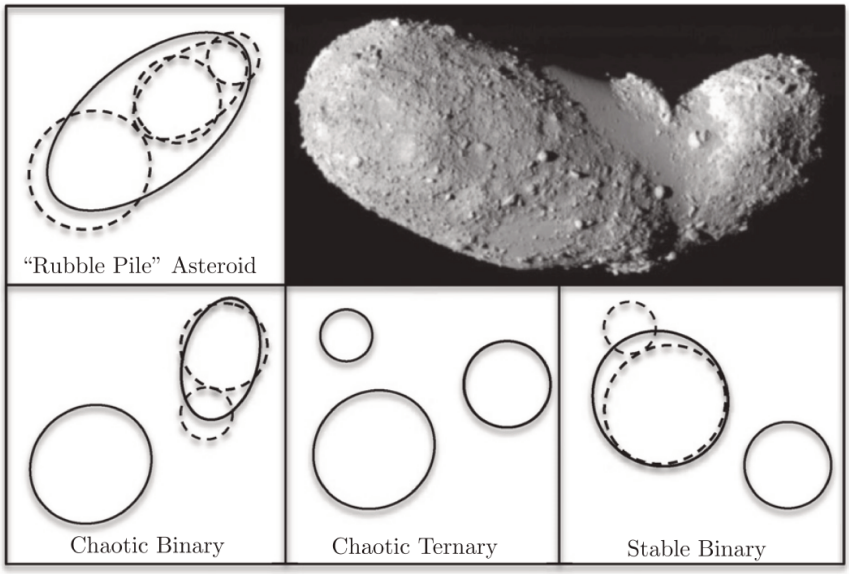


Figure 1.18 – **Upper right** image of Itokawa taken by the Hayabusa spacecraft (Image: ISAS/-JAXA) which motivates cartoons showing the low mass ratio evolutionary model from Jacobson and Scheeres [2011]. Solid lines indicate surfaces, dashed lines indicate "rubble pile" internal substructure. The "rubble pile" asteroid evolves from the upper left to bottom left chaotic binary panel via a YORP-induced rotational fission event. A secondary fission occurs between the lower left and lower middle panels creating a chaotic ternary system. On the right lower panel is seen a less energetic, more stable binary system, which results from the impact of one of the components on the primary.

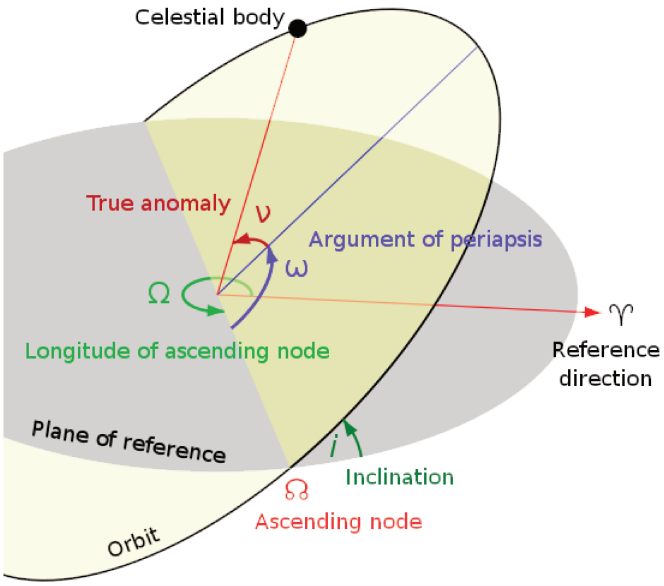


Figure 1.19 – Diagram of the orbital elements. (Credit: Wikipedia)

- $e$ **eccentricity** is the amount by which the orbit deviates from circularity
- $i$ **inclination** is the angle between the orbit plane and the ecliptic plane.
- $\Omega$ **longitude of ascending node** is the angle in the ecliptic plane between the inertial-frame x-axis and the line through the ascending node.
- $\varpi$ **argument of periapse** is the angle in the orbit plane between the ascending node and the perihelion point.
- $\nu$ **true anomaly** is the angle in the orbit plane between the perihelion point and the position of the orbiting object.

Proper elements are quasi-integrals of motion (i.e they are nearly constant in time) and are used for millions of years simulations. They are of critical use in identifying families. Orbital elements includes perturbations (has osculating changes).

### 1.4.2 Spin and 3-D Shape

Pravec and Harris [2000] had already analyzed the distribution of asteroid spin rates vs. size and found fast and slow rotators specially among that of $D < 40$ km, founding interesting characteristics between small fast rotators that would imply they are rubble piles (Fig. 1.23).

Spin of asteroids can be detected by radar, from this facilities for example was detected the changes of spin state on NEA Toutatis and there are predictions for increasing number of

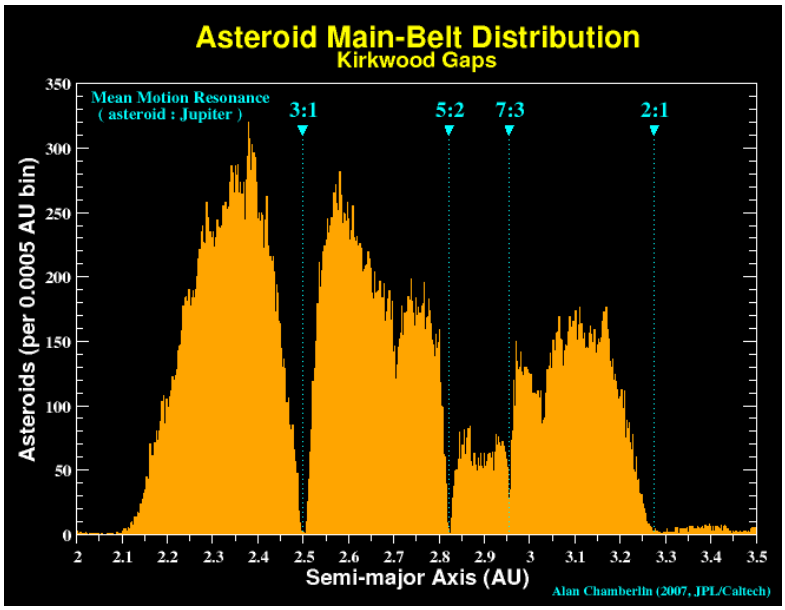


Figure 1.20 – Kirkwood gaps. (Credit: JPL/NASA)

NEAs, it is even predicted spin-state changes for (99942) Apophis after its close encounter with Earth on 2029 [Scheeres et al., 2005].

Asteroids with diameters larger than ~ 200 m rarely spin with periods less than ~ 2.2 h, which corresponds with the critical disruption spin rate of self-gravitating, "rubble pile" bodies [Pravec and Harris, 2007], a possible mechanism of formation of binaries.

The majority of NEA binary systems are found with a rapidly rotating primary, with rotation periods between 2.2 and 3.6 h, which are among the most rapid rotations found for NEAs [Pravec et al., 2006], this supports the theory for formation of small binaries by rotational fission.

Unfortunately, currently no clear test exists to help differentiate between the lightcurve of an elongated asteroid to a lightcurve of a synchronous binary asteroid. Ďurech and Kaasalainen [2003] showed that contact binaries or near contact binaries can be modeled as single bodies with almost the same lightcurves. Asteroids that were suspected as binaries, such as (216) Kleopatra, exhibit their true bifurcated-elongated shape only by radar and high angular resolution observations [Ostro et al., 2000] and asteroids that were considered as an elongated asteroid, such as (90) Antiope, were found to be binaries using direct imaging with high angular resolution observations. Moreover, the features in the asteroid's lightcurve, that support the binary scenario depend on observation geometry: the amplitude of the lightcurve is changing with increasing phase angle, The shape of the curve (V-shaped minima/U-shaped maxima) change with the aspect angle of the asteroid rotation axes.

From photometry of Atens asteroids throughout the Solar System were discovered as binaries:

(69230) Hermes, a NEA with rotation and orbital periods of 13.89 h [Pravec et al., 2003]; (854) Frostia, (1089) Tama, (1313) Berna and (4492) Debussy are main belt asteroids with periods of 37.73, 16.44, 25.46 and 26.61 h, respectively [Behrend et al., 2006]; (90) Antiope is an almost-synchronous binary system of equal-size components.

#### Angular momentum content

The angular momentum is a fundamental characteristic of asteroid rotation. Both the angular momentum vector $\vec{L}$ and the inertia tensor $\hat{I}$ changes during the evolution of asteroids through collisions and other processes, $\vec{L}$ is defined as: $\vec{L} = \hat{I}\vec{\omega}$ were $\vec{\omega}$ is the spin angular velocity of the asteroid. The total angular momentum in a binary asteroid is:

$$\vec{L} = \vec{L_1} + \vec{L_2} + \vec{L_{orb}} \tag{1.1}$$

where $\vec{L_i}$ is the rotational angular momentum of the $i$th body and $\vec{L_{orb}}$ is the orbital angular momentum.

Pravec and Harris [2007] considered the ratio between the mass equivalent sphere total angular momentum of the system and the angular momentum of a critically spinning equivalent sphere[16]. The angular momentum of the equivalent sphere spinning at the critical spin rate is $L_{eqsph}$ . The normalized total angular momentum of the binary system is expressed as:

$$\alpha_L \equiv \frac{L_1 + L_2 + L_{orb}}{L_{eqsph}} \tag{1.2}$$

Applying the above considerations to a data set of binaries, Pravec and Harris [2007] obtained the angular momentum content in binaries. They found that small asteroid binaries have the total angular momentum close to critical. For systems originating from critically spinning rubble piles, e.g., by a spin fission, $\alpha_L$ is close to 1. This suggests that the small binaries formed from parent bodies spinning at the critical rate (sufficient to overcome gravity) (Fig. 1.23).

### 1.4.3 Mass and Bulk Density

The determination of the mass of an asteroid is not a trivial task. One of the ways this can be done is by means of gravitational perturbation: (on a natural or artificial body) asteroid-asteroid or asteroid-spacecraft. This can be done from determining the trajectory of the perturbed body after the close encounter. Needless to say that this kind of encounters are scarce, in the first case ruled by nature and the second by budget, although nowadays with past

[16] a sphere of the same total mass and volume as the two components of the binary system

and current missions flybys and rendezvous has been more frequent, and now even asteroid dedicated.

Other gravitational perturbation is the one that is produced from the interaction between an asteroid and its satellite which is what we consider in the binaries of this manuscript. By means of Kepler's third law [deduced from observations Kepler, 1619], it can be determined the mass of the primary body knowing the orbital period $P$ and the semimajor axis of the satellite:

$$\frac{P^2}{a^3} = \frac{4\pi^2}{GM} \tag{1.3}$$

with $M$ the mass of the system (mass of primary and secondary) $M = M_p + M_s$ and $a$ the mean separation of the bodies (orbital semimajor axis), where the components are considered as point masses and $G$ is the gravitational constant.

The first determination of this kind came of course from the first confirmed satellite of an asteroid: Dactyl, the satellite of (243) Ida. From spatially resolved images taken by the Galileo spacecraft of this binary Belton et al. [1995] were able to estimate the mass, volume and bulk density of Ida.

In principle, measuring any two of the quantities yields the third; generally, $P$ and $a$ are obtained from observations, and $M$ is deduced. To obtain masses of the individual components requires an assumption that either $M_p \gg M_s$ (so that $M \simeq M_p$), or, if reliable estimates of the sizes of either component are available, that they have the same bulk density which is what is generally assumed (although may not be necessarily true). Measured sizes and masses may be combined to estimate the **density** ($\rho$, the mass per unit volume of a substance), a fundamental property indicative of composition (see Carry [2012] for an extensive study).

**Grain density** is the mass of an object divided by the volume occupied by a grain. On the other hand, the term **bulk density** is referred to the mass of an object divided by its total volume. It is the density measured by spacecrafts.

The **porosity** is the ratio between grain and bulk density and it gives the percentage of the bulk volume of a solid occupied by empty space. It is the non solid or pore volume fraction and as such, dimensionless. The porosity may also be inferred if a likely analog material (such as a meteorite with similar spectral signatures to an asteroidal component) with known bulk density is available this can provide a clue to the internal structure, such as whether large void spaces may be present [Consolmagno et al., 2008].

Most asteroids have significant porosity. This property can be large enough to affect the internal structure of asteroids, their gravity field, impact dynamics, collisional lifetimes. It also can affect their physical properties which include thermal diffusivity, seismic velocity, cosmic

ray exposure and dielectric permeability. Thermal and seismic effects can affect asteroid internal evolution, metamorphism, shock dissipation and elastic properties which in turn can determine whether colliding asteroids accrete or disrupt [Britt et al., 2002].

High porosity attenuates shock propagation, affecting the nature of cratering and lengthening the collisional lifetimes of porous asteroids. From density trends analysis, asteroids are divided in 3 groups:

1. monolithic asteroids
2. asteroids with macroporosities
3. rubble piles

In case of collisions, it has been discovered by experiments and porosity models that porosity helps to dissipate a portion of the impact energy into the crushing of pores, which result in compaction. As such, porous asteroids are more resistant to collisional disruption.

Comparing masses of asteroids, Ceres has over one-third of the estimated total mass of all the asteroids in the asteroid belt. Kuchynka and Folkner [2013] estimate asteroid masses from planetary range measurements. The mass of the Main Belt of Asteroids is estimated in 30 $\times 10^{20}$ kg [Kuchynka and Folkner, 2013].

### 1.4.4 Surface Properties

The reflectivity of the light on an asteroid depends on the light impinged, the composition of the surface, and the size of the grain on the surface.

Because of continuous bombardment of ions from solar wind and interplanetary particles, atmosphereless and magnetosphereless bodies like asteroids are exposed to these fluxes.

Meteorites are samples of planetary bodies that have survived passage through our atmosphere and reached the Earth, as such, they are cosmochemical time capsules from the Solar System's birth, encoding clues about how our cosmic neighborhood came to be. Coming mainly from asteroids, they serve as evidence of the nature of these bodies. This gives us clues about composition, bulk density and porosity of their parent bodies. Identification has been made for the Moon, Mars, Vesta [Prettyman et al., 2012], and Itokawa [Nakamura et al., 2011].

But in meteorite collections there is not yet positive identification of all asteroid types, there are some missing meteorite to link with all the parent bodies known at the moment so we can piece together the full picture. There are several international efforts to recover fresh meteorites short after they arrive on Earth. Networks with cameras and radars are surveying the sky in order to detect meteors and put alerts so meteorite recovery can be organized. Some of the networks are: FRIPON (France), Australia, The NASA All-sky Fireball Network, Saskatchewan Fireball Camera Network (USA), Brasil etc.

Part of the aims of this work was to assess the taxonomy of binary asteroids with unknown spectral classification to determine their composition for the first time (Ch.3). The characterization of binaries physical properties from the ground is possible by spectroscopy in both visible and infrared spectral regions. When possible, mineralogical composition can be established.

Experiences in labs explain the spectral differences observed between the most populated class of meteorite the ordinary chondrites OC and the surface of their supposed parent bodies (S-type asteroids). It has been simulated in labs the ionic bombardment of ion fluxes.

### 1.4.5 Absolute Magnitude and Albedo

The absolute magnitude of an asteroid $H$, is a measure of its intrinsic mean brightness in the visual if the asteroid were placed at a distance of 1 AU from Earth, at 1 AU from the Sun, and at zero phase angle. This is estimated from measurements of its apparent magnitudes at the occasions it has been observed, meaning that it had different configurations: heliocentric distance, phase angles and aspect, although in first approximation that last quantity is assumed to be spherical.

## 1.5 Methods to study asteroids

Basically all the information we have from asteroids come in form of light, to collect it we use detectors in telescopes. In our era we have them on ground and also in space. We can detect also signals from different ranges of wavelength namely UV, visible, IR and radio. In this work we will use only visible and near Infrared (NIR) that at the end give complimentary information.

Regarding telescopes, although size matters, actually there's a wide variety of telescopes that observers uses to collaborate with the aims to better determine the nature of asteroids. From amateur "little" telescopes gathering light for lightcurves (LC) and occultations, to the biggest ones in super professional observatories that include AO and state of the art optics and mechanics and even space telescopes and space probes with sensitive instruments.

The detection of light from asteroids comes from different programs, which includes large surveys that were originally planned to detect other sources like stars, galaxies and cosmological objects, were it happens to pass by some of these minor bodies in the Field of View, the detection is serendipitously made.

"We are now on the threshold of a new era of asteroid studies," wrote Tom Gehrels in the introduction of *Physical studies of minor planets*, [Gehrels, 1971][17] having at the time the completion to magnitude ~14, and detected magnitude 16 in extended program. Since then,

[17] Recalled in *Asteroids III* and *Asteroids IV*

the work done on asteroids has come a long way, now magnitudes reach ~20–24.

### 1.5.1 Lightcurves

Photometric observations are the classical method for obtaining information on objects with a complex shape and structure. Lightcurves are one of the most fruitful and classical methods to discover and characterize binaries. It consists in gathering light from astronomical objects, following them as to see the differences in the amount of light received. From that light record, one can confirm if some asteroid is not single by the different peaks in the lightcurve, it serves also to determine the periods of each component and their poles [Pravec et al., 2016] (Fig. 1.21). Due to eclipses and the mutual occultations of components, the amplitude of the light curve of the asteroid can change. In order to find specific features, it is necessary to perform photometric observations over a long time interval which depends on the particular system.

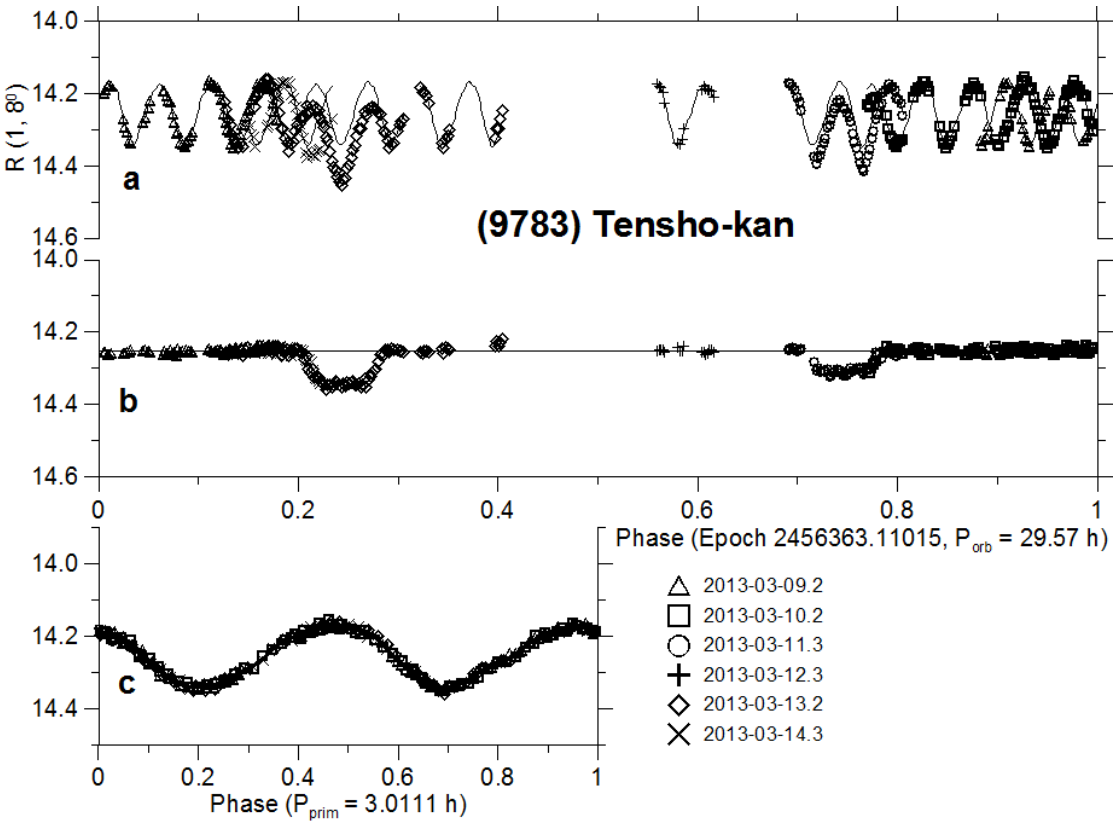


Figure 1.21 – Lightcurve of (9783) Tensho-kan. (a) Full lightcurve, (b) after substraction of the primary lightcurve, can be identified mutual events, eclipses/occultations. (c) primary rotational ligtcurve (enlarged). (Credit image:P. Pravec)

### 1.5.2 High Angular Resolution and High Contrast Imaging

New challenges appeared in recent times to imaging extrasolar planets and discs. This requires dedicated instruments and strategies to overcome two main challenges:

1. the tiny angular separation between the star and the planet or disc. The projected separation is below $0.1''$ for a planet orbiting at 10 AU from a star distant of 100 pc.

2. the contrast between a star and its planet ranges between $10^{-4}$ for a young giant planet to $10^{-10}$ for an Earth shining in reflected light. Discs are also very tenuous, with contrasts ranging from $10^{-4}$ for the brightest debris discs down to $10^{-10}$.

New designs for extreme AO , high contrast cameras, design of new coronographs allowed the detection of dimmest objects around stars like exoplanets. This state of the art instruments applied to imaging binary asteroids permit also discover and characterize them. That kind of instruments (NIRC2, SPHERE, NIRI) can be used to image and resolve asteroids, like the study of 107 Camilla I present in Ch. 5.

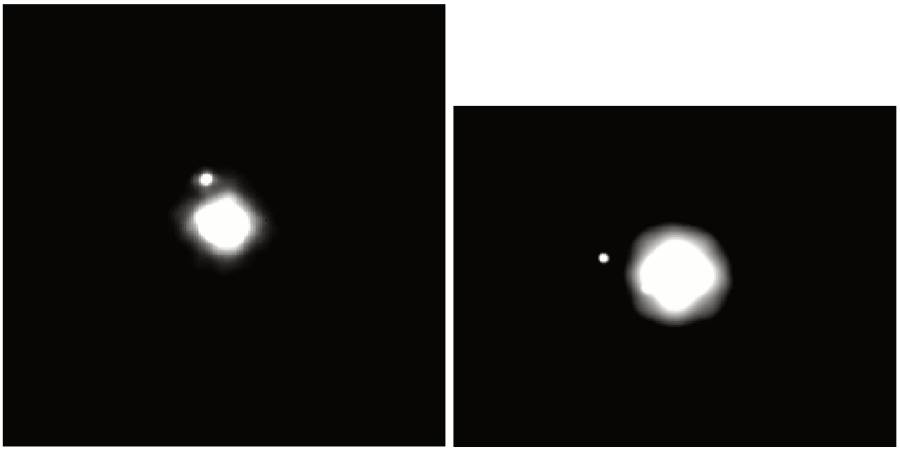

Figure 1.22 – Reduced AO images of binary asteroids taken at VLT. (Left) (762) Pulcova on the 1st of May, 2012. (Right) (107) Camilla on July 31, 2004.

### 1.5.3 Stellar Occultations

Occultations are one of the best sources of accurate information about the position, shape, and nature of the surface of asteroids. The concept is quite simple: an asteroid passes between a star and the Earth, and the total light received by a ground telescope -that is pointing the star- is dimmed (Fig. 1.24). Observed from different points on the surface of the Earth, these events can be used to determine the size and shape of the asteroid, if its speed and distance to the Earth are known.

As simple as it is, the technique permits to determine very valuable data on asteroids with

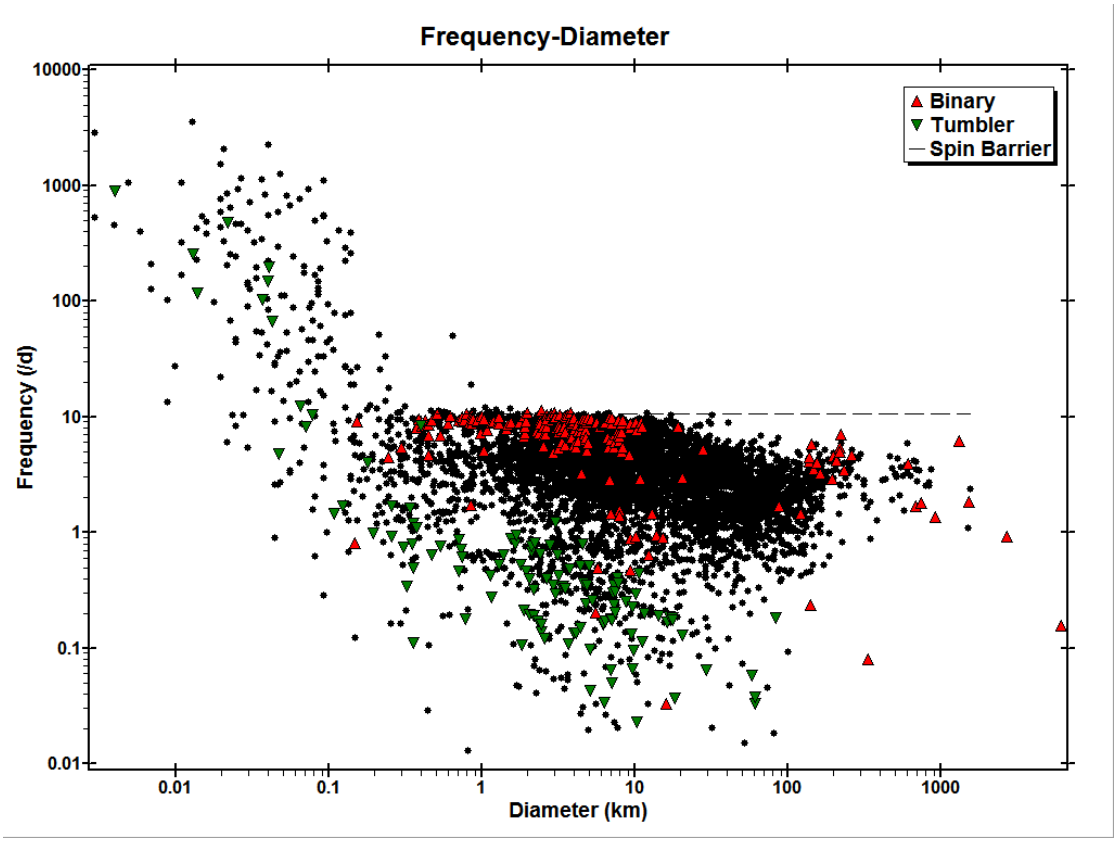


Figure 1.23 – The rotation rate of asteroids can be determined from lightcurves. The periods are plotted as frequency (cycles/day) vs. size (km) in this plot from the Asteroid Light Curve Photometry Database, binary asteroids in red, tumbler in green [a].

[a] http://alcdef.org/

modest equipment (depending on the magnitude of star and asteroid). For this reason there are several groups dedicated to observe occultations, many of them, amateur astronomers, some of which had made valuable contributions to the knowledge of asteroids. In fact, occultations, alike asteroid lightcurve detections, gives opportunity for collaboration between professional and amateur astronomers, something that is happening more often nowadays.

For each detection, the time of the occultation can be converted in a distance called *chord*. Only one of these chords is not enough, the more chords the better, the more events recorded for the same object, the better, because this allows to constrain the shapes of asteroids (Fig. 1.25). For this reason, when an occultation is known to happen, alerts are diffused and observation campaigns organized in order to involve and display observers over the predicted path of the shadow that will be projected on the earth by the passage of the asteroid in front of the star. That shadow will move quickly, at ~ 30000 km/h, meaning that for the observers, a typical event can be of only several seconds (depending on the size of the asteroid).

By the reliable registration of the time of the beginning and end of the occultation by each observer, it will be possible to rebuild the profile of the asteroid (for the plane projected on the earth) and estimate it dimensions. Occultations lightcurve profiles have allowed to detect atmospheres, and even the first system of rings around centaur Chariklo [Braga-Ribas et al., 2014]). In the case of binary asteroids, with the predicted path of the shadow from ephemeris of the asteroid and the star to be occulted, it is possible to determine information of satellite, a very difficult task by other means. In this *Gaia era*, more precise ephemeris are beginning to be released, this will evidently boost the detection of occultations [Tanga and Delbo, 2007].

### 1.5.4 Spectroscopy

Astronomy became physics when at last the composition of the first celestial bodies were revealed through spectroscopy, this began with the first spectroscope invented by Joseph Fraunhofer in 1814. Since then, the advance in knowledge of composition of bodies has improve hand in hand with better instruments, techniques, and methods. In the case of asteroids, that reflect light, it is performed reflectance spectroscopy in the visible and NIR for this work.

### 1.5.5 Other methods

#### Radar

Radar is a suitable technique for objetcs close to the Earth. Although some Main Belt asteroids have been observed there are not many suitable MBAs targets because the SNRs are much lower than for NEAs (echo power goes as distance to the power -4).

Radar is suitable to detect the surface structure of asteroids on grain size scales which can be

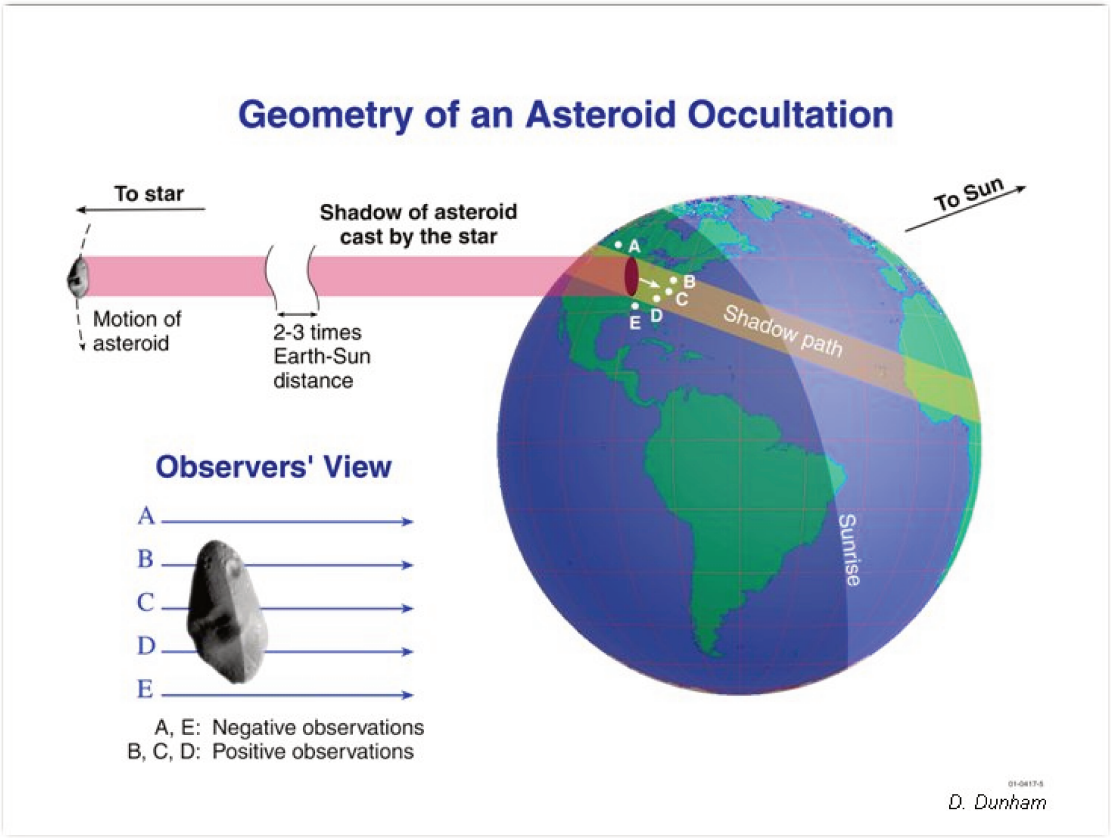


Figure 1.24 – Geometry of an asteroid occultation Image Credits: David Dunham

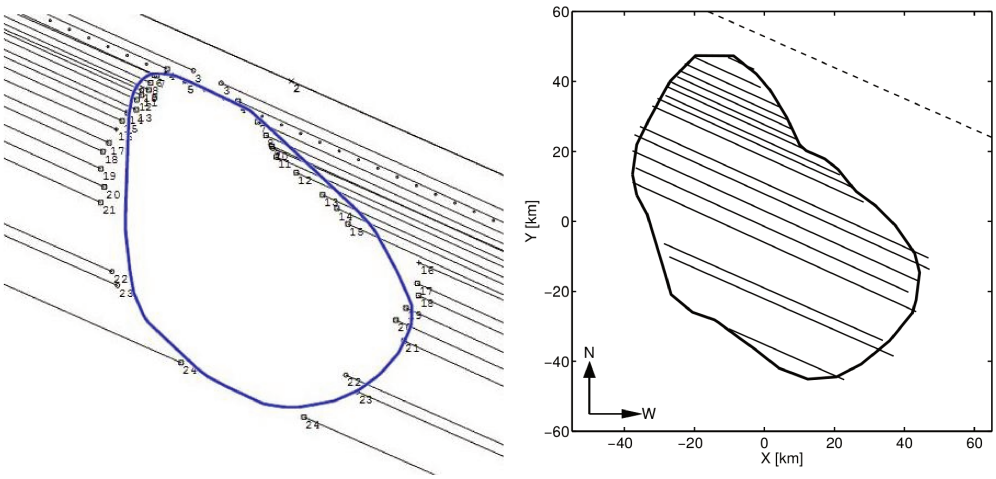


Figure 1.25 – (*(Left)* Occultation outline for (135) Hertha in December 2008, with light curve inversion model in blue [Timerson et al., 2009]. *(Right)*. Chords for the same occultation, now the model includes lightcurve information. The dashed line is a negative observation [Ďurech et al., 2015].

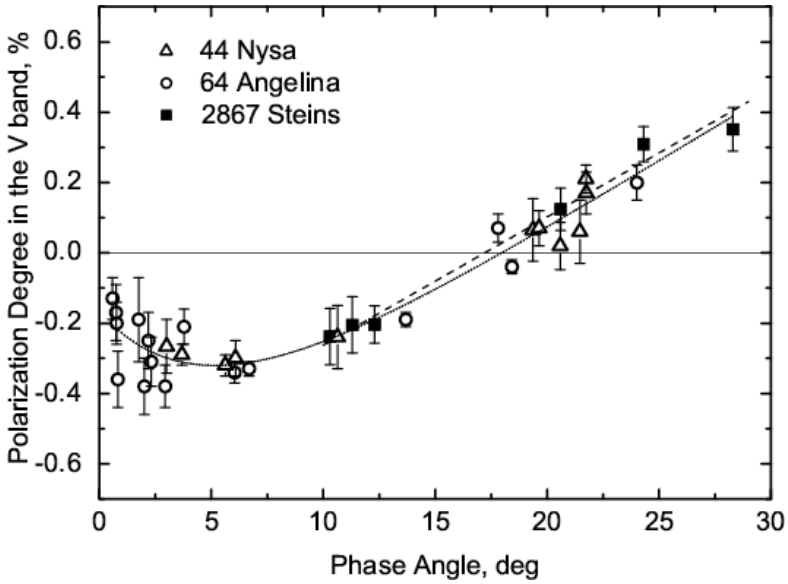


Figure 1.26 – Polarization degree versus phase angle in the V and R bands for (2867) Šteins. Image from Fornasier et al. [2006].

deduced from the variation of reflectivity with phase angle. Radar provide knowledge about the size, shape, metal content, and surface roughness of asteroids.

The highest resolution that can be achieved is 3.75 m/pixel. Radar observations benefit greatly from optical observations, especially lightcurves and taxonomic classification.

Radar observations provide unambiguous detections of binary asteroids because images at decameter resolution can resolve the individual components.

### Polarimetry

Polarimetry can be used to define the diameter, albedo, compositional class and surface structure of an asteroid. This measurement depends on the variation of linear polarization of the sunlight reflected from the asteroid with phase angle. The plot of polarization as a function of the phase angle defines the curve of polarization of an asteroid, which is negative at small angles and rise linearly at angles greater than 15°. The inversion angle is where the polarization changes sign. It is known an experimental relationship between the albedo and the slope of the polarimetric curve at the inversion angle (Fig. 1.26).

# 2 Data & reduction

In this section I will present technical details on instruments for data collection and data treatment.

When detecting light for astronomy, there are several procedures to be performed because the signal must be reliable for research purposes.

## 2.1 Basic Concepts of Photometry

Photometry is a photon-counting technique that gives us information about the brightness of a body, in the case of asteroids, its shape and the scattering properties of its surface. When a time series of brightness measurements are combined, we can have a lightcurve which shows the variations in brightness as the body rotates upon itself and move around the Sun.

The measure of photometric quantities is affected by several effects. This is why images must be corrected.

#### Photometric sky

This is the best sky for observing astronomic objects: no visible clouds, transparency variations under 2%, only assessable from the analysis of photometric standard stars. Unfortunately, when observing even at large facilities, nothing assures that the weather will be good enough, Luckily, for some not very dim targets, it is possible to work with a clear sky, even with a fraction of the Moon. If relative photometry is performed, the weather is not so stringent, one compares the instrument magnitude of the object to a known comparison object, and then corrects the measurements.

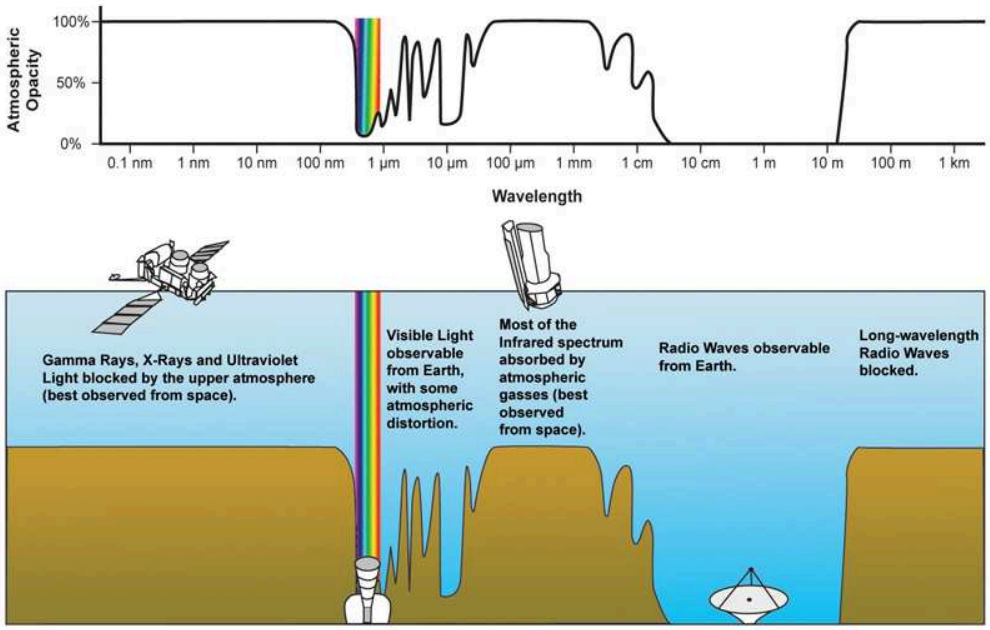


Figure 2.1 – Atmospheric electromagnetic transmittance. Earth atmosphere is transparent to visible light and some radio waves and is absorbing in most parts of the IR. UV, X and gamma rays don't pass through it. Credit: NASA.

### Magnitude

For celestial objects, the brightness is referred to as the *magnitude*, a scheme defined by Hipparchus in 120 BC based on the appearance of stars to the naked eye, with higher numbers indicating fainter objects. Originally it reaches until magnitude 6 (the dimmest seen with the eyes). The scheme is still used nowadays adapted to the observations with instruments and detectors covering negative quantities until magnitudes bigger than 20. But human vision is logarithmic, apparent brightness (flux) and magnitudes are related by the difference in magnitude defined by Norman Pogson in the 1850s.:

$$m_1 - m_2 \approx 2.5 \log\left(\frac{F_2}{F_1}\right) \tag{2.1}$$

where $m_1$ and $m_2$ are magnitudes, and $F_1$ and $F_2$ are fluxes for two objects.

### Magnitude systems

As stated, the definition of magnitude is relative, addressing the magnitude difference between two objects. To be able to compare astronomical sources observed with different telescopes, there is a need to standardize the measure. This is why there are standardized sets of filters

which includes the Johnson, Cousins, SDSS, 2MASS, VISTA filters, etc. (Fig. 2.18).

An important concept for absolute calibration, is the comparison to standard and field stars. For moving objects like asteroids, it is also important to correct for the varying heliocentric and geocentric distance, and the phase angle.

#### Atmospheric Absorption

Depending on the wavelength of light, Earth's atmosphere can be transparent or opaque due to the composition of the atmosphere. Some near infrared (NIR) light can reach observatories on high altitudes. There are infrared (IR) windows centered at certain wavelengths as 1.25. 1.65, 2.2, 3.5 and 4.8 $\mu$m (Fig. 2.1).

#### Optical Diffraction

The image of a point source of light (like a star) formed by a circular aperture is fundamentally limited by diffraction, which causes a point source of light to be surrounded by a series of bright and dark rings. At a critical angle $\theta_c = 1.22\lambda/D$, where $D$ is the telescope diameter and $\lambda$ is the wavelength, both in meter. The first dark ring in one object's pattern falls into the central bright spot of the other object's and one can not distinguish the two objects (Fig. 2.2). The angular resolution in radians is $\theta$

$$\theta = \frac{\lambda}{D} \tag{2.2}$$

Depending on the wavelength, this can be improved with bigger diameters, but diffraction will never disappear.

#### Seeing and image quality

The seeing is the blurring of the images due to the turbulence in Earth's atmosphere. It is an inherent property of the atmospheric turbulence, independent of the telescope that is observing through the atmosphere.

The image quality, on the other hand, is defined as the full width at half maximum (FWHM) of long-exposure images, is a property of the images obtained in the focal plane of an instrument mounted on a telescope observing through the atmosphere. It is therefore a quantity measured at a certain airmass and wavelength of observation. The image quality in a large telescope is always better than the seeing at the same wavelength and airmass [Martinez et al., 2010].

The point spread function, or **PSF** is the function that describes how the image from a point source is degraded in the focal plane of a telescope due to seeing and optics.

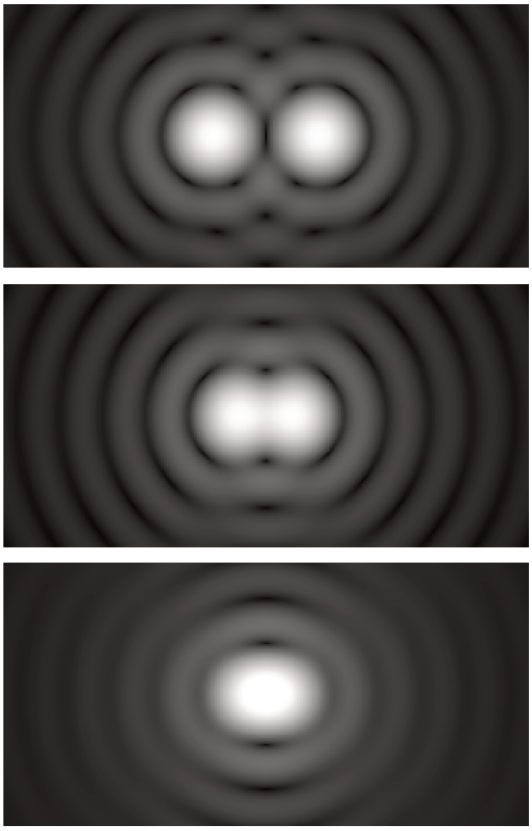

Figure 2.2 – Diffraction patterns generated by light from two points sources passing through a circular aperture (the pupil of the eye, a telescope aperture, etc.). Top: Points far apart can be distinguished; (middle) points meeting the diffraction limit began to fuse; (bottom) points closer can not be distinguished. Image credit: Spencer Bliven

Figure 2.3 – Portable telescope for occultations

## 2.2 Telescopes

I have used myself different telescopes, from mining databases I have collected images of large telescopes some with AO systems, and even one space telescope. I will give a brief description of all of them.

### 2.2.1 Mobile telescope for stellar occultations

I was trained with a small (D<30cm) commercial telescope for observing occultations. For this it was important to set up the instrument as quickly and efficiently as possible (trained with stopwatch). I learned how to perform the polar alignment as fast as possible, this is the aligning of the mount so that moving the telescope in right ascension precisely mimics the motion of the sky.

The reason for this is that occultations are detected from the parts of the Earth where the shadow of the asteroid passes, the path of the shadow and the duration of the occultation can be predicted (with uncertainties), thus, one only has to go chase the shadow. This can happen in the middle of nowhere, often the predictions are updated and the observer has to install the telescope hoping that it is in the correct place in the correct time because the events can last a few seconds only. Precise time and position are required, the occultation kit includes a Global Positioning System (GPS), and a fast camera, in this case I used a Watec camera. I participate, and went to observe in four stellar occultation of binary asteroids. (Fig. 2.3).

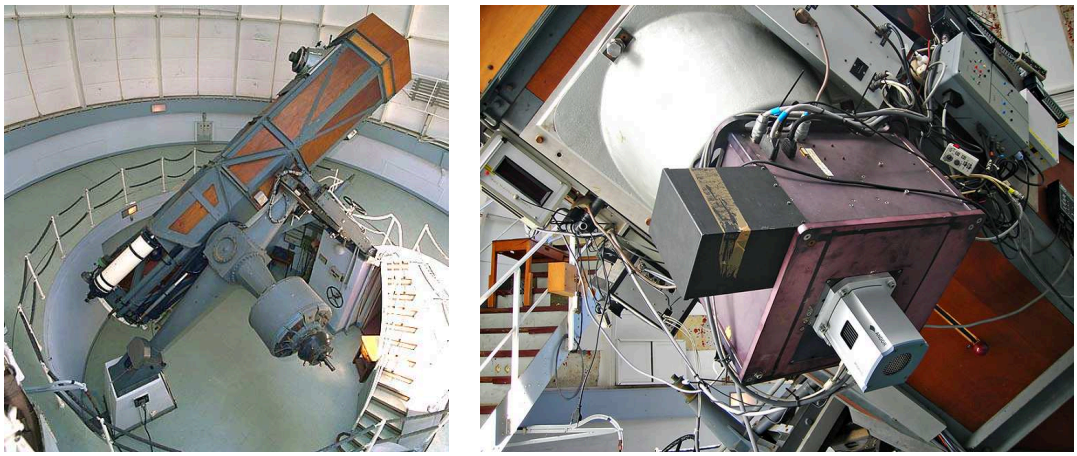

Figure 2.4 – **Left:** Telescope 1.20m at the Observatoire Haute Provence (OHP). **Right:** Camera Andor Ikon L 936 at the telescope 1.20m.(Credit: Ministère de la Culture - France).

### 2.2.2 Observatoire de Haute-Provence (OHP) / 1.20 m Telescope

I performed observations at the Observatoire de Haute-Provence (OHP), located in the south-east of France (IAU code: 511). Here I used the 1.20m newtonian telescope, f/6 ($f$ = 7.232m) equipped with an Andor Ikon L 936 camera which has a CCD 2048×2048 and a Field of view (FoV) = 13.1'×13.1'. (Fig. 2.4). I used the filter wheel with SDSS filters to collect photometric data for colors and lightcurves of binaries (Ch. 4).

### 2.2.3 Pic du Midi Observatory / 1 meter Telescope (T1M)

Pic du Midi is a facility in the French Pyrenees (IAU code: 586). I used the 1 meter telescope (T1M), D=1,05m F/D=5. This tool is equipped with a CCD camera with a sensor Marconi DZ936BV with a resolution arcsec/ pixel = 0.21. I used the filter wheel with SDSS filters (Fig. 2.5) to collect photometric data for colors and lightcurves of binary asteroids (Ch. 4).

### 2.2.4 La Silla Observatory / New Technology Telescope (NTT)

The New Technology Telescope (NTT), has an Alt-Az mounting, and is a 3.58m Richey-Chretien telescope that was the prototype of active optics (AO), its parameters are: f/2.2, D=3.58m. Its primary mirror can be slightly deformed. This Observatory is located at the outskirts of the Atacama Desert in Chile and is a complex of several telescopes, large and small (IAU code: 809, Fig. 2.6). Here I used the ESO Faint Object Spectrograph and Camera 2 (EFOSC2) with the Gunn filters ($griz$) for colors and lightcurves of KBOs and the comet 67P/Churyumov (Ch. 4).

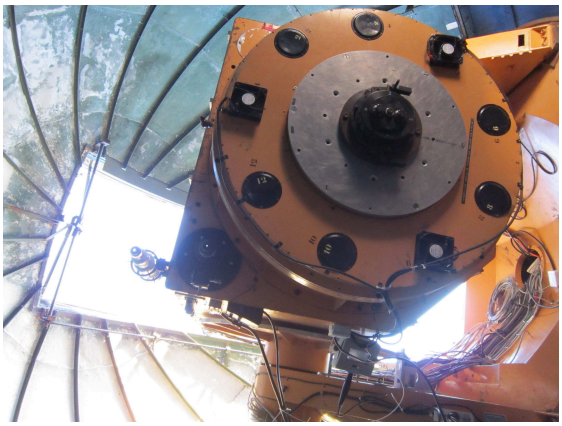

Figure 2.5 – Primary mirror and the slit of 1 meter telescope at Pic du Midi.

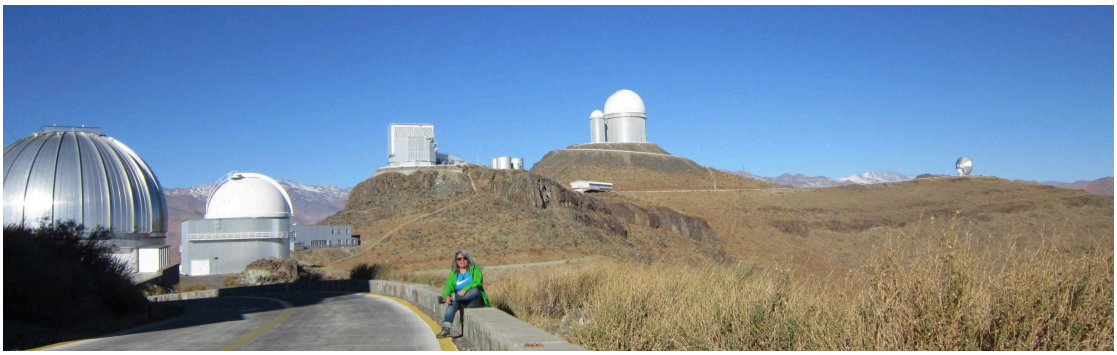

Figure 2.6 – Image of NTT (New Technology Telescope) in between the complex of telescopes at ESO's La Silla Observatory (the third telescope from left to right.)

Figure 2.7 – Image of NASA Infra Red Telescope Facility (IRTF) Credits: NASA.

### 2.2.5 Infra Red Telescope Facility - IRTF

This is NASA telescope at the summit of Mauna Kea, designed for IR observations (IAU code: 568, Fig. 2.7). Its primary mirror has 3m. Here I used the spectrometer Spex to acquire spectra of binaries without taxonomy (Ch. 3). In this case I observed remotely from CODAM, Observatoire de Paris at Meudon.

### 2.2.6 Large facilities for high angular resolution

I have collected data from several large telescopes, most of them AO images from the archives of the The Canadian Astronomy Data Centre (CADC) http://www.cadc-ccda.hia-iha.nrc-cnrc.gc.ca/ to study the orbit of the satellite of binary asteroid (107) Camilla (Ch. 5).

- **Very Large Telescope (VLT)**

  This ESO telescope is located at Cerro Paranal at the Atacama desert near Antofagasta, Chile (IAU code: 309, Fig. 2.8). The VLT is a complex of 4 identical 8.2-m Unit Telescopes (UT) Ritchey–Chrétien style. The four telescopes can be operated separately or combined in interferometric mode (there are also other 4 auxiliary telescopes) and can detect from UV to mid-IR.

  The AO images of Camilla were detected with both the NACO and SPHERE, first and second generation Adaptive Optics instruments respectively. In the case of SPHERE, with the Infra-Red Dual-beam Imager and Spectrograph (IRDIS) camera with the integral Field Spectrometer (IFS) in IRDFIS mode (IRDIS and IFS observing simultaneously).

Figure 2.8 – Very Large Telescope. Image: ESO.

Figure 2.9 – Gemini Telescope. Image: www.gemini.edu.

- **Gemini North**

  This telescope is located in Hawaii[1]. It is a 8.1 m Cassegrain reflector telescope that can work in the optical and near-infrared, employing sophisticated adaptive optics technology. The images I used from here were detected with NIRI (Near InfraRed Imager and spectrograph). It can work in the wavelength range 1-5 $\mu$m with Natural Guide Star (NGS) Adaptive Optics (AO), or Laser Guide Star (LGS) AO imaging (IAU code: 568, Fig. 2.9).

- **Keck Observatory**

  The Keck observatory consist in two-telescope KeckI & KeckII near the summit of Mauna Kea, Hawaii (IAU code:568, Fig. 2.10). The telescopes are reflector style and the diameter of the mirrors is 10m each. It can work from optical to near-infrared wavelengths. The images I obtained were detected with the Near Infrared Camera (NIRC2) that works with the Keck Adaptive Optics system to produce the highest-resolution ground-based

[1] it has a twin -Gemini South- in Cerro Pachón, Chile

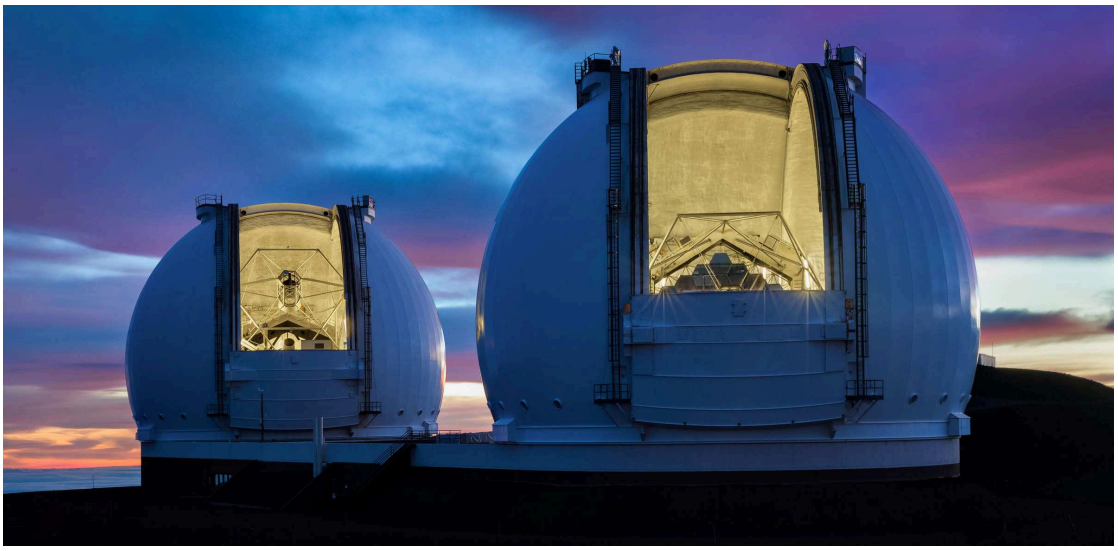

Figure 2.10 – Keck Telescope. Image: Keck Observatory.

images and spectroscopy in the 1–5 $\mu$m range. The detector is a 1024x1024 Aladdin-3 array with 27 $\mu$m pixels. The observation was in imaging mode.

- **Hubble Space telescope - HST**

  The HST is a Cassegrain reflector of Ritchey–Chrétien design. With a diameter 2.4 m, Focal length 57.6 m, focal ratio f/24, and a collecting area of 4.5 $m^2$. It can detect in different wavelengths: NIR, visible light, and UV, and being at the space, has the great advantage that it is not seeing limited, but it is diffraction limited (as opposed to non-AO ground-based facilities). (IAU code: 250, Fig. 2.11).

### 2.2.7 Sky surveys and Catalogs

In current times there exist a wealth of data that has increased tremendously if compared with the past decade (not to mention the time before). Sometimes data is reserved to the groups involved in the projects, but often it is released after some time. I will explain how one can get data from several servers or databases.

There are several survey catalogs of asteroids based on optical to near-infrared observations: the 2MASS Asteroid Catalog [Sykes et al., 2000] compiles near-infrared colors of 1054 asteroids based on the *Two Micron All Sky Survey - 2MASS*; the *Subaru Main Belt Asteroid Survey (SMBAS)* [Yoshida and Nakamura, 2007] gives the size and color distributions of 1,838 asteroids observed with the Subaru telescope; the SDSS Moving Object Catalog, described above.

Data on solar system objects are often ancillary results from surveys designed primarily to investigate astrophysical sources beyond the Solar System. From different surveys -in general

Figure 2.11 – Image of the HST as seen from the Space Shuttle Discovery during its second servicing mission. Credits: Hubblesite.org.

dedicated to distant objects- there has been observed also *moving objects* like asteroids. Two of the most important surveys gathering these data are:

1. The *Sloan Digital Sky Survey Moving Object Catalog* SDSS - MOC [Ivezić et al., 2001, Parker et al., 2008] provides accurate astrometric and 5-band photometric measurements. Now in its fourth release (MOC4), it has produced the largest available catalog of multi-color photometric measurements for asteroids [Ivezić et al., 2002, Juric et al., 2007] and has done in total ~450,000 observations (until March 2007) with 100,000 unique and identified asteroids out of 250,000 observations, and 200,000 unidentified objects. I have use data from this release in Chapter 3.
2. The *Visible and Infrared Survey Telescope for Astronomy* VISTA Hemisphere Survey (VHS) MOVIS catalog. Which so far has identified 39,947 objects from the Data Release 3 (DR3) in near infrared [Popescu et al., 2016]. VISTA is equipped with astounding capabilities from state of the art optics, it is already giving us precious information on Solar System objects like asteroids. I had use data from this release in Chapter 4.

### 2.2.8 Additional resources

Data volume is increasing dramatically in astronomy as detectors and telescopes become more advanced and powerful. Solar System objects data has been collected in sky surveys providing more and more accurate measures and in the coming future this will be increasing more. First and foremost of course the NASA's Astrophysics Data System Abstract Service (ADS) and Data Archive is the place to look for data and information in astronomy.

For this work I have used several online compilations. My sincere gratefulness to the persons

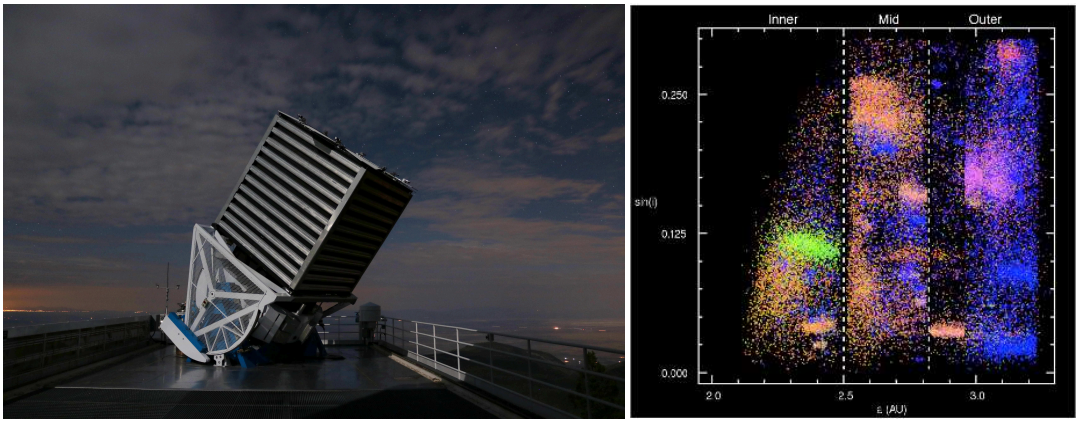


Figure 2.12 – **Left:** The SDSS telescope at night. Image Credit: Patrick Galume. **Right:** A plot of the proper $a$ vs. $sin(i)$ for 45,087 objects. The color of each dot is representative of the object's color measured by SDSS. The three main regions of the belt, defined by strong Kirkwood gaps are marked. Image from Parker et al. [2008]

who do this work of compiling and putting on line this information.

- Asteroids with Satellites http://www.johnstonsarchive.net/astro/asteroidmoons.html
- Ondrejov Asteroid Photometry Project http://www.asu.cas.cz/~ppravec/
- Minor Planet Bulletin http://minorplanet.info/minorplanetbulletin.html
- Brian Warner Database http://alcdef.org/

To access catalogs and online resources, the virtual observatory offers convenient tools. During this project I have used extensively Miriade [Berthier et al., 2009], which is part of the more general IMCCE-VO Solar System portal in the Virtual Observatory (VO) framework. The IMCCE ephemeris service on the web[2] provides positional and physical ephemerides of planets and small bodies of the Solar System, as well as some physical data. Miriade features several functions (SSODNET, SKYBOT, AstroId, etc), of them I have used extensively SKYBOT.

SKYBOT[3] is a service developed by Berthier et al. [2006] at IMCCE. The core of SkyBoT is a database of pre-computed ephemeris of all of the known Solar System objects (asteroids, planets, natural satellites and comets) over a period of years that extends from 1889 to 2060. The ephemerides provided by SkyBoT are J2000 astrometric geocentric or topocentric equatorial coordinates (right ascension and declination) at the requested epoch. It also provides position and motion vector at a specified epoch. The right ascension and declination of the targets are computed by numerical integration of the 8 bodies pertubed problem, taking into

[2] http://vo.imcce.fr/webservices
[3] http://vo.imcce.fr/webservices/skybot/index.php

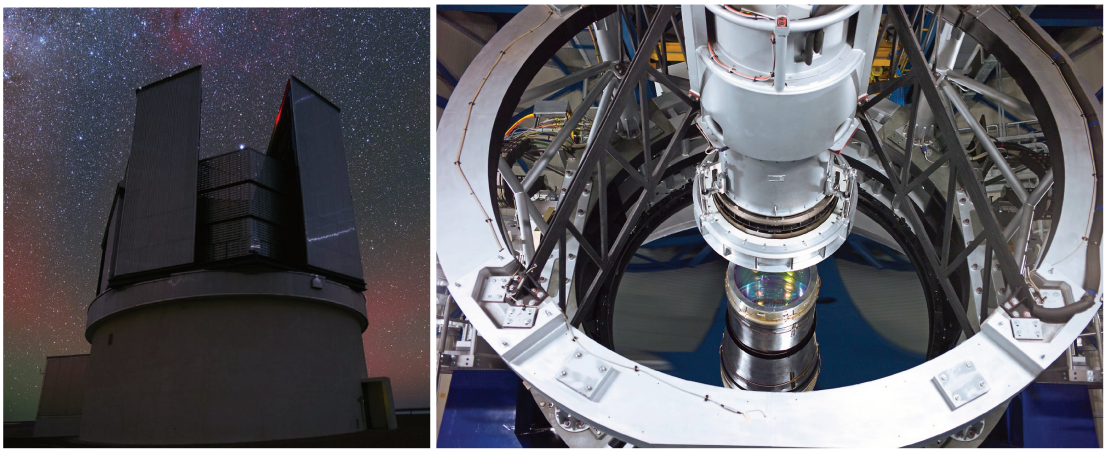

Figure 2.13 – **Left:** The VISTA telescope in Paranal. Image Credit: Y. Beletsky (LCO)/ESO. **Right:** Image of the 4.1 metre mirror of the telescope. The entrance lens of VIRCAM (VISTA InfraRed CAMera), the giant infrared camera, is visible at the centre, under the structure that supports the secondary mirror. Credit: ESO.

account relativistic perturbations (post-newtonian approximation). The pre-computed orbits are also calculated with the same algorithm, with a sampling step of 1 day and a storage step in the SkyBoT database of 10 days. For asteroids the dynamical properties are issued from the ASTORB database (Lowell Observatory), for comets from the IMCCE cometary database. Ephemeris of the planets are computed using the INPOP[4] planetary theory. Skybot provides ephemerides with an accuracy of few tens of milli-arcseconds (depending on how accurate is the body orbit).

## 2.3 Data Reduction

Data collected at telescopes have several issues to solve, that depends on the wavelength, the telescope, the camera, the detector, the filters used, if there is AO involved and so on.

### Visualizing the Data

Astronomical images are usually stored using the FITS standard (Flexible Image Transport System). In order to see the image in the process of correction and analysis, it should be used some tool that can handle the FITS images. The one I used was `ds9`, an astronomy FITS file viewing and analysis software from the Smithsonian Astrophysical Observatory (SAO)[5]. It is extremely useful for rescaling intensities of an image, fitting the intensities to a particular function (squared, logarithmic...), binning images, applying filters and color maps, etc.

[4] Intégrateur Numérique Planétaire de l'Observatoire de Paris
[5] http://hea-www.harvard.edu/RD/ds9/

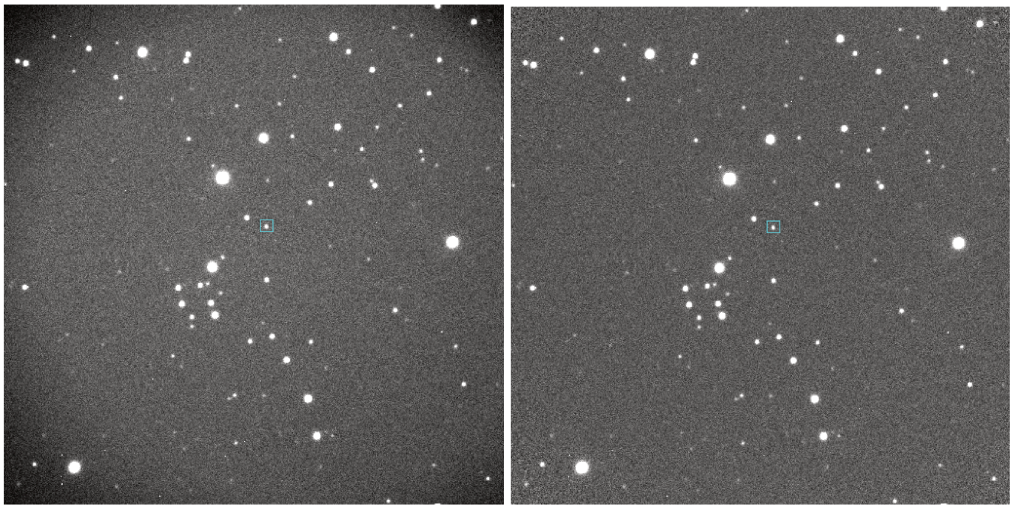

Figure 2.14 – **Left:** Raw image, vignetting can be observed in the corners. **Right:** the same image after correction. Inside blue light square is binary asteroid (4666) Dietz. Images were taken with SDSS filter *g* at the T1M Pic du Midi Observatory in January 25, 2017.

### *Audela*

For this work, I made an extensively use of *Audela*, an open source astronomy software[6] developed by both amateur and professional astronomers [Klotz et al., 2012] -many of them french- in their spare time. *Audela* is intended for digital observations and can handle large amount of data. It is robust; under the philosophy of open source software it is flexible, fully customizable, always improving. Its features include advanced image processing and acquisition functions. It enables the control of cameras and telescopes, and has been used to robotize several telescopes (e.g T60 at Les Makes- La Reunion Island and the TAROT robotic telescopes[7]) and to control the image acquisition in telescopes like the `T1M` (1 meter telescope) at Pic du Midi.

### Raw to Calibrated Data

The data obtained with a telescope needs corrections, before doing these, the data is known as raw (Fig. 2.14). The procedures depends on the instrument and detector used and in some cases, observatories provide software for doing this. However, there are standard steps to do this: detection and removal bad pixels in the data, background subtraction (including bias, dark), correction for non-linear effects or relative variations in sensitivity of the detector system (called flat field), and correction for geometric distortions in the imaging device.

In several facilities the image data (usually FITS) is registered with a text that contains all

[6] http://audela.org/
[7] Télescope à Action Rapide pour les Objets Transitoires

the information regarding the image: how it was obtained, and, in some cases, how it was processed, this is called a *header*. Headers contain: name of object, date, exposure time, number of bins, filters used, etc.

### 2.3.1 Adaptive Optics

Before entering the atmosphere, light from a distant source comes as a plane wave. The speed of light varies as the inverse of the refractive index $n$. Earth atmosphere is not homogeneous, it has different layers that fluctuates. Fluctuations in $n$ are proportional to the fluctuations in the atmospheric temperature. As light passes through the different layers, speed changes and the original plane wave is deformed. This also depends on the wavelength, since the wave vector $\mathbf{k}$ is related to it in this form: $|\mathbf{k}| = 2\pi/\lambda$.

Adaptive optics is a technology that corrects in real time for the blurring effects of atmospheric turbulence by means of monitoring the wavefront distortions and compensating for it using different mechanisms like deformable mirrors or tip-tilt correction[8]. In this way the wavefront is turned planar again; thus, the image can be obtained at the diffraction limit (Fig. 2.15).

Large ground-based telescopes like Keck, Gemini, VLT, count with AO systems.

### 2.3.2 Electronic Detectors

Astronomical detectors may be different in nature, for this work I had used Charge Coupled Devices (CCD) detectors for all the observations at visible wavelengths, and Aladdin Arrays for the NIR wavelengths. These detectors have several advantages compared with others like ancient photographic plates. They have also some limitations.

- **CCD**

  A CCD consists of an array of semiconductor capacitor elements called "wells" or pixels. When a photon strikes a pixel, then, with a certain probability, an electron is freed from the semiconductor and stored in the well. In that way, CCDs convert optical images into electronic images (Fig. 2.16). When the exposure is finished, the stored electron charges are transferred from well to well, and finally past an amplifier and a analog-to-digital converter (ADC) that converts the charges into analog data units ("ADUs") which are stored electronically.

  Because the efficiency of CCDs is not 100%, not all the pixels which are read out from the CCD chip represent the data we are interested in. Occasionally a cosmic ray strikes a pixel, and leaves some signal that will appear in the raw image.

  Among the many advantages that CCDs have, we can mention:

[8] mirror is tilted at the tip in order to correct the distorted wavefront.

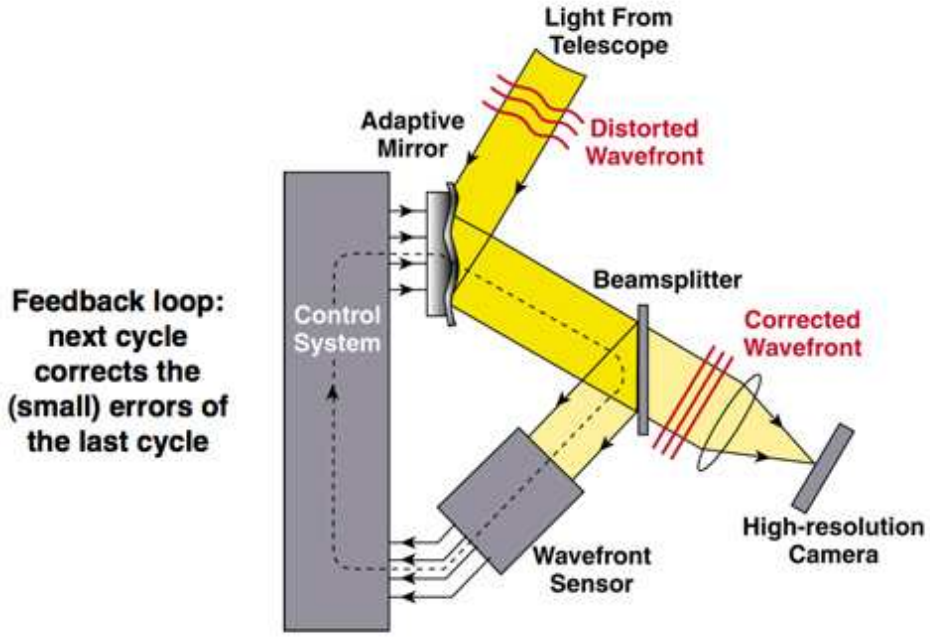


Figure 2.15 – Adaptive Optics concept. Image credits: Lawrence Livermore National Laboratory and NSF Center for Adaptive Optics.

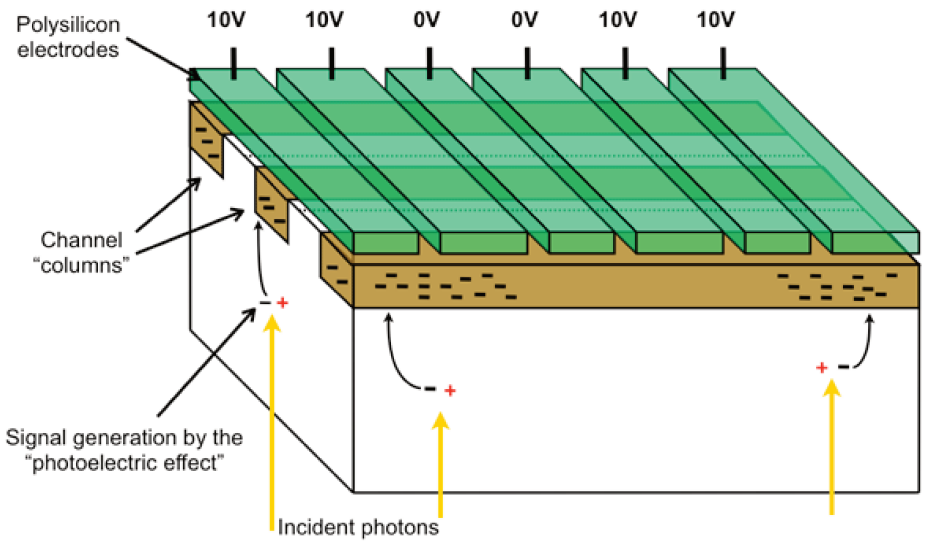


Figure 2.16 – Scheme of a CCD. Photons are converted into electrons via the photoelectric effect and being attracted to the potential wells under electrodes with positive voltage applied. (Copyright: Oxford University Press).

1. Great detector quantum efficiency. CCD's detects a great fraction of photons (~ 90%) compared with other detectors like photographic plates (~ 10%), or the eye retina[9]. This means about an order of magnitude improvement in sensitivity between photographic plates and CCDs.

2. CCDs count photons. For each photon detected, an electron is produced and counted, thus these are linear detectors. But because each detector pixel has a finite size, above a certain number of counts, linearity breaks down, meaning that for very bright sources, the fluxes are unreliable (the detector is saturated).

3. CCDs are digital detectors, so the data is more easily handled, stored and as so, it can stand more reliable for further analysis, something very important in astronomy due to the long term analysis that has to be carried on with almost all kinds of astronomical objects.

- **ALADDIN arrays**

  In the case of NIR detection, the cameras NIRI (Gemini), NACO (VLT), SPHERE(VLT), SPEX (IRTF), NIRC2 (Keck) and VIRCAM (VISTA) all of them use *Advanced Large Area Detector Developments in InSb* or ALADDIN arrays, which are detectors of InSb, sensitive in the IR ranges.

[9] which is strongly dependent on many stimulus parameters and is determined from behavioral measurements 0.03-0.06%, and from direct estimates: 0.1-0.3%

### Signal to Noise Ratio or *S/N*

The signal to noise ratio ($S/N$) for a point or extended source depends on both the Poisson noise[10] of the object, and on noises associated with the background. Sources of background noise include "read noise" of the CCDs, and Poisson noise in the dark current, sky background, and any intrusive light superposed on the target.

The equation for the $S/N$ of a measurement with a CCD is given by the formula [Howell, 2006]:

$$\frac{S}{N} = \frac{N_*}{\sqrt{N_* + n_{pix}(N_S + N_D + N_R^2)}} \tag{2.3}$$

where:

$N_*$ is the total number of photons (signal) collected from the object of interest.

The “noise” terms in the above equation are the square roots of $N_*$

$n_{pix}$ is the number of pixels under consideration for the $S/N$ calculation,

$N_S$ is the total number of photons per pixel from the background or sky,

$N_D$ is the total number of dark current electrons per pixel,

$N_R^2$ is the total number of electrons per pixel resulting from the read noise.

### Calibration frames

1. BIAS frames

   The amplifier that increases the signal before the ADC, has a built-in offset or bias, which ensures that the ADC always receives a positive signal. This offset must be removed if the data values are to be truly representative of the counts recorded per pixel. Thus, the first step in reducing CCD images is to remove the bias from all digital images. To achieve this we obtain BIAS frames. This is a zero seconds exposure with the shutter closed so that no photons fall on the chip. In theory these frames contain only bias numbers and some readout noise. By subtracting one frame, or the average of several frames, from each subsequent image the bias is removed (Fig. 2.17).

2. Flat field frames: FLAT

   This refers to correcting the CCD throughput at each pixel so that each one would respond equally to a source with the same photon flux. This is necessary because there

[10] or photon noise, which is an uncertainty associated with the measurement of light inherent to its quantized nature. It has a Poisson distribution.

are pixel-to-pixel sensitivity variations across the array. This also corrects the effect of dust or scratches on the CCD window, and the vignetting by the telescope or camera lens optics. The flat-field are obtained by taking images of an evenly illuminated surface (DOME FLATs) or by shooting a part of the sky without visible stars near dusk or dawn (SKY FLATs). It is advised to take several FLATs (at least ten) and average them to reduce the photon noise (Fig. 2.17).

3. Thermal count frames or DARK frames

   During long integrations at moderate cooling or in the NIR, a significant amount of charge can accumulate in the CCD pixels due to thermal excitation. The purpose of producing dark or thermal count images is to subtract the contribution from thermally generated charge in the image. (this can be avoided by cooling the CCDs e.g. at T120 OHP, the temperature < 50°).For long integrations (depending on the chip), the dark count will begin to appear in certain pixels on the CCD which have particularly high dark currents; these are known as "hot-pixels" which can be as bright as some of the dim stars in the image or even saturate. Many dark count images may be obtained and averaged and the same dark frame can be applied to all images, regardless of what filters or optics were used to produce the image.

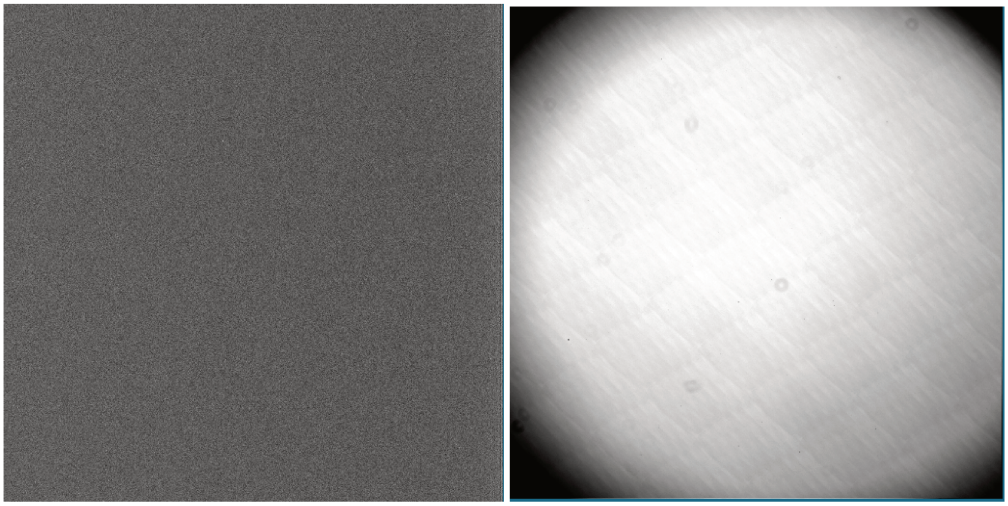

Figure 2.17 – Two calibration frames: **Left:** Bias frame. **Right:** Flat frame in *g* filter.

The use of the basic set of calibration images in the reduction of CCD object frames is as follows. First, subtract a mean bias frame (or dark frame if needed [11]) from your object frame. Then, divide the resulting image by a (bias or dark subtracted) mean flat field image. With these steps the object frame is corrected for bias level, dark current (if needed), and nonuniformity within each image pixel. During the analysis of your object frames, it is likely that the background or sky contribution to the image will need to be removed or accounted for in some manner.

[11] This depends on the level of dark current expected. Or the sky in NIR.

This correction for the background sky level in your image frames is performed as part of each specific analysis step using “sky” regions in the object frame itself and is not removed or corrected for with some sort of separate “sky” frame. In equational form, the calibration process can be written as:

$$\text{Reduced Object frame} = \frac{\text{Raw frame - Bias frame}}{\text{Flat field frame}} \tag{2.4}$$

in where, the flat field has already been bias subtracted and the bias frame would be replaced by a dark frame when appropriate [Howell, 2006].

### 2.3.3 Filters

A filter is a device that blocks all unwanted light waves and lets only the specified wavelength pass through for observation. There are different kinds of filters defined by the magnitude allowed to pass and with very specific characteristics for each telescope system (to don’t overlap). In this work I had used Sloan Digital Sky Survey (SDSS) and Visible and Infrared Survey Telescope for Astronomy (VISTA) filters, covering a wide part of the visible and near infrared part of the spectra (Fig. 2.18).

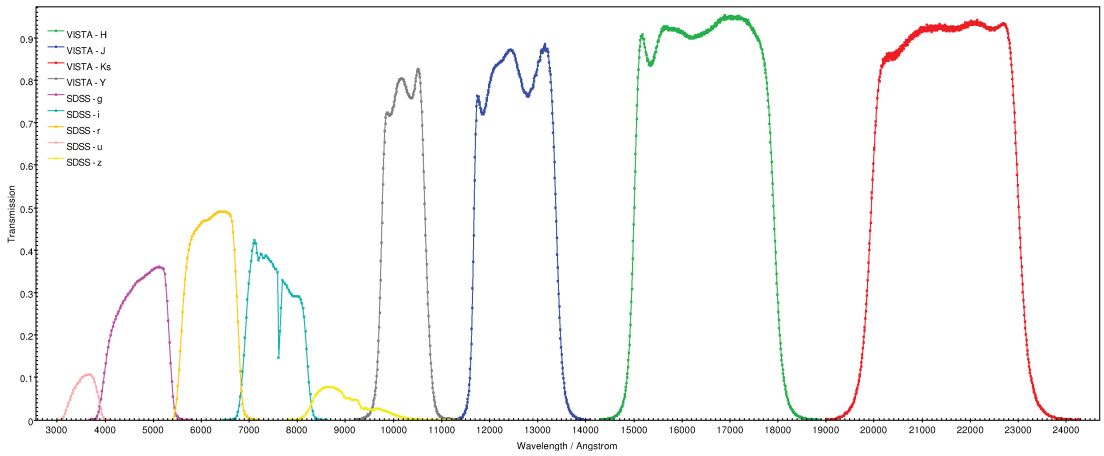


Figure 2.18 – SDSS and VISTA Transmission filters used in this work photometry (Ch. 4). A wide part of the visible and near IR spectra is covered.

### 2.3.4 Fringes in red filters

In this case, for some CCDs, fringes appear from the interference of monochromatic light within the CCD, like in the case of EFOSC2 at NTT (La Silla) or the camera at the telescope at Pic du Midi Observatory (Fig. 2.19). For moving targets like asteroids it can be critical to

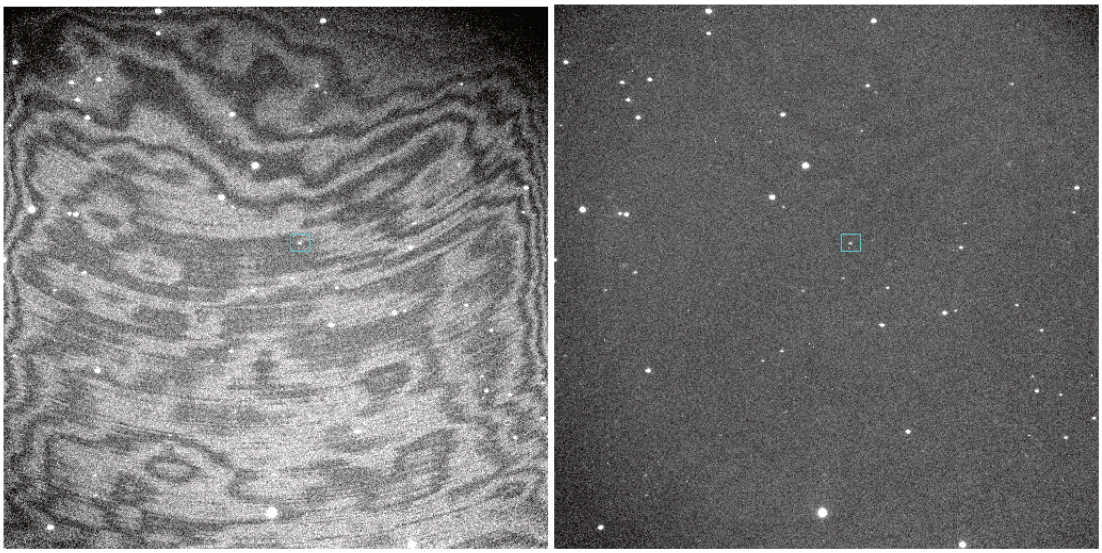

Figure 2.19 – **Left:** Interference fringes in image of (17365) 1978 $VF_{11}$, a trojan binary asteroid (inside the blue light square) in $z$ SLOAN filter obtained at Pic du Midi 1M telescope in 25 January 2017. **Right:** The same image after data processing.

remove the fringes to provide uniform photometry. Fringes must be scaled and subtracted from each image. Snodgrass and Carry [2013] developed a simple technique that I used to automatically remove them.

## 2.4 The case of spectroscopy

Spectra give true physical information about the composition of asteroids. This technique consists in the dispersion of light as a function of wavelength; in this case, the CCD image has one spatial dimension and one spectral (wavelength) dimension. With spectra, the composition of objects can be derived (it can also be studied atmosphere's characteristics). The resolving power $R_\lambda$ is given by $R_\lambda \equiv \lambda/\Delta\lambda$ ($\Delta\lambda$ is the spectral resolution).

CCD spectra need also to be reduced and calibrated in a similar way as mentioned before for images. In addition, the spectrum must be calibrated in wavelength. This is done observing a lamp with well known emission lines. Also, the obtained spectrum of the asteroid must be divided by a solar-like spectrum, also known as solar analogue (G2-type star) to obtain the reflectivity of the asteroid. In Fig. 2.20 are explained the four steps in the reduction of asteroid spectra according to Bobby Bus et al. [2002] in Asteroids III .

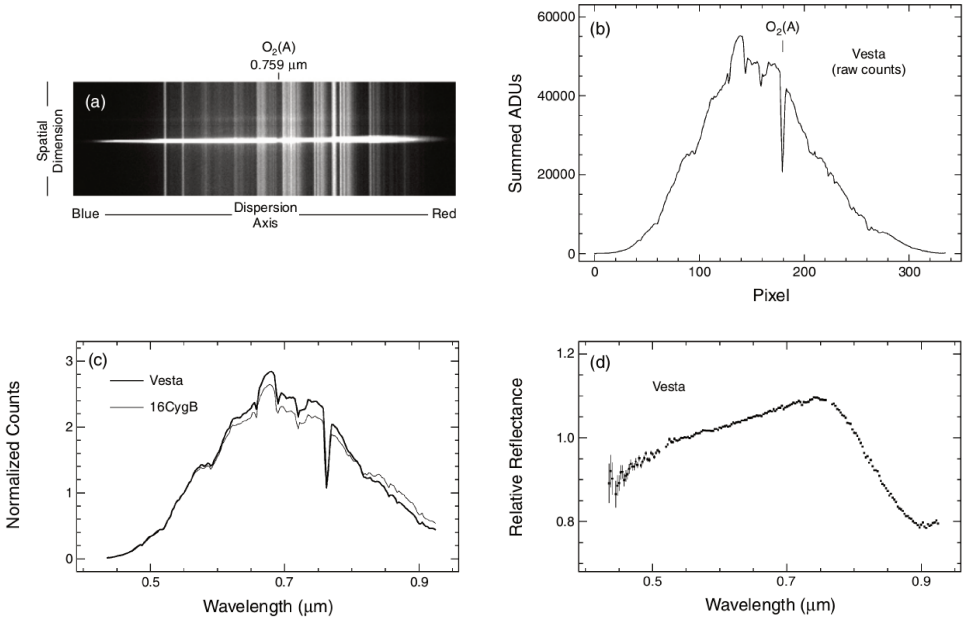


Figure 2.20 – The four steps in the reduction of asteroid spectra according to Bobby Bus et al. [2002]: (a) Spectral image of Vesta, which has been bias and flat-field corrected. The bright vertical stripes are night-sky emission lines. The strong $O_2$(A) atmospheric absorption band is labeled. (b) Extracted one-dimensional spectrum obtained by summing the object counts (ADUs) along each column within the extraction aperture and subtracting the fitted sky level. Sensitivity falls at both ends of the spectrum. (c) Spectrum for both Vesta and the solar-analog star 16CygB after each has been calibrated for dispersion (wavelength correction) and atmospheric extinction. The counts in both spectra have been normalized to 1.0 at 0.55 $\mu$m. (d) Vesta divided by solar analog, normalized at 0.55 $\mu$m. Image from Bus et al. [2002].

# 3 Spectroscopic survey of binary asteroids

In nature, the various observed characteristics that objects shows, allow us to group them. This classification is a first step of study which can be very exhaustive if we can find ways to identify the more fundamental properties of objects, like spectra. Spectra of planetary bodies shows differences which gives us information on the surface of the body and with that, of the processes that this body has experienced (heating, aqueous alteration, weathering...). They present different shapes, slopes, some of them absorptions features. Thus, Solar System objects are grouped according to the similarity of their spectra.

This of course has improved as a wider wavelength range has become available, showing processes hidden in the visible part of the spectrum.

In an intuitive way, the tendency has been to establish a relation between the taxonomic classes and mineralogies, comparing asteroid reflectance spectra with those obtained from meteorites and different minerals in the laboratory. The first rigorous asteroid taxonomy was developed by Chapman et al. [1975] based on a synthesis of polarimetry, radiometry, and spectrophotometry for a sample of 110 asteroids, in it, only two classes were formally recognized: C and S, with other unusual spectra labeled U. Similar was the one developed by Bowell et al. [1978] in which classes were denominated according to the mineral associated with the spectrum: the C class was associated to carbonaceous chondrites, the S class to stony-iron meteorites, the E class to enstatite achondrites, and the M class to the metallic iron-nickel meteorites. Subsequent taxonomies by Tholen [1984] taxonomy based on results from the Eight-Color Asteroid Survey [ECAS, Zellner et al., 1985] with 14 recognized classes. This system takes advantage of the wealth of information that can be gathered with CCDs even to obtain information from spectra of small asteroids [Barucci et al., 1987, Tedesco et al., 1989, Bus and Binzel, 2002].

Tholen [1984] uses principal components analysis (PCA), which is an attempt to reduce the dimensionality of the problem of classification, of the eight-color data, but this changed little by little as the observations improved in quantity and quality and classification algorithms turned better. Also, differences were recognized in spectra and the number of classes increased

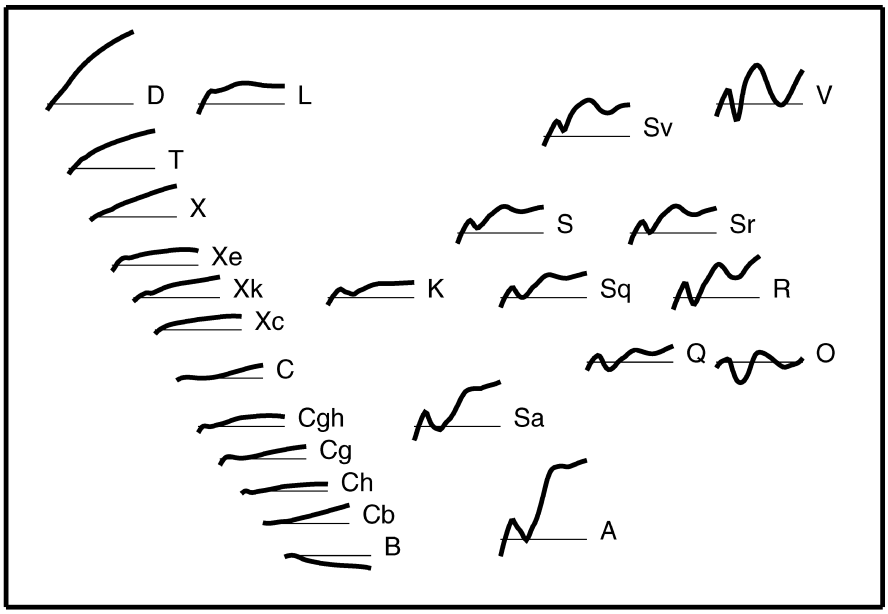


Figure 3.1 – Summary of Bus DeMeo Taxonomy. Image from DeMeo et al. [2009].

as large as 26 in Bus and Binzel [2002], to be later redefined to 24 classes when including Near Infrared reflection spectra in the taxonomy developed by DeMeo et al. [2009] using PCA (Fig. 3.1).

Part of the aims of this work was to assess the taxonomy of binary asteroids with unknown spectral classification to determine their composition for the first time and study how taxonomic class distributes among binaries. The characterization of binaries physical properties from the ground is possible by spectroscopy in both visible and infrared spectral regions. When possible, mineralogical composition can be established.

## 3.1 On asteroid classification and meteorites

The goal of asteroid classification is to group them according to their compositional -mainly superficial- resemblances obtained from spectroscopic observations, and to identify the samples that arrive on Earth, and whose spectra are obtained in laboratories, as coming from some common origin or asteroid parent bodies (this includes other bodies like planets or the Moon). Nowadays, geologic studies plays an important role in the groupings of meteorites according to petrologic, mineralogical, bulk-chemical, and isotopic properties. This suggest the existence of 100–150 distinct parent bodies. The diverse composition found in meteorites gives clues on the processes that these bodies went through and besides information of their parent body formation processes, they can reveal also collisional processes that can reveal the interior of differentiated bodies which in turn can give insights on the age and mass of the parent body (Fig. 3.2).

- **Asteroid classes** There are several classification schemes that appeared since the 1970's, they employs single-letter designations. This began with C, and S types, each letter relates to the -at the time- inferred composition of an asteroid: C (carbonaceous), S (stony), M (metallic), F (flat), R (red), etc. This has changed progressively with a better understanding of these minor bodies. The current standard is Bus-DeMeo taxonomy with 24 classes. A comparison of the evolution of these systems can be seen in Fig. 3.2 taken from *Asteroids IV* DeMeo et al. [2015]. The most abundant classes or complex are S, C and X.

- **Meteorite classifications** Meteorites are classified according to their structure and mineralogy, using different analysis: chemical, isotopic, and structural. Three very broad categories are recognized: stones, irons and stony-irons. There are also various subcategories. The most basic separation of meteorites is into unmelted (chondrites) and melted ones (non-chondrites). The chondrites are generally assumed to come from parent bodies that were smaller and/or formed later that those of the non-chondrites, although some chondrites may be the unmelted crusts of differentiated bodies. For further subdividing meteorites, the most useful classification tools reflect the meteorites nebular (primary) and parent body (secondary) characteristics. A significant number of meteorites do not fit into the established groups. The convention is that groups must be composed of five or more members, so these meteorites are classified as ungrouped.

- **Types of minerals involved** The relevant minerals in asteroids are determined from spectrum analysis and also the retrieval of some samples (with spatial missions). For the S-complex, the minerals involved are olivine and pyroxene. In the C-complex: opaques, carbon, phyllosilicates, and according to their spectrum, they can have also olivine and pyroxene. In the case of the X-complex which includes asteroids with different albedos, the minerals are opaques, carbon, low-Fe pyroxenne, enstatite, oldhamite. In the case of the other classes (end members and outliers) the composition can include pyroxene, olivine and also organics, plagioclase feldspar, pallasite, brachinite, etc. Anhydrous pyroxene-rich from interplanetary dust particles (IDPs) have been proposed also as surface analogs for about two- thirds of all C-complex asteroids.

| Taxonomic System | Tholen (1984) | Gaffey (1993) | Bus (2002) | Bus-DeMeo (2009) (B-D) | Taxonomy Notes | Relevant Minerals and Possible Meteorite Analogs |
|---|---|---|---|---|---|---|
| Wavelength Range | 0.33–1 μm | 0.35–2.50 μm | 0.45–0.90 μm | 0.45–2.45 μm | | |
| S-complex |  S | SI<br>SII<br>SIII<br>SIV<br>SV<br>SVI<br>SVII | S<br>Sa<br>Sq<br>Sr<br>Sk<br>Sl | 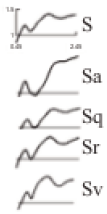 S<br>Sa<br>Sq<br>Sr<br>Sv | Tholen: Defined only S.<br>Gaffey: 7 mineralogic classes based on Band I center and Band II/Band I area ratio. Primarily separates olivine to orthopyroxene ratio.<br>Bus: Separates based on strength of 0.9-μm drop, indicative of 1-μm band.<br>B-D: Definition largely preserved from Bus. Now includes full 1- and 2-μm feature in near-IR. Sl, Sk, and Ld are removed, Sv is added. | Minerals: olivine, pyroxene<br>Meteorites:<br>S(I): pallasites?, R chondrites, brachinites<br>S(IV): many are ordinary-chondrite-like<br>S(V): primitive achondrites?<br>S(VII): basaltic achondrites |
| C-complex | 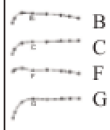 B<br>C<br>F<br>G | | B<br>C<br>Cb<br>Cg<br>Cgh<br>Ch | 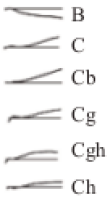 B<br>C<br>Cb<br>Cg<br>Cgh<br>Ch | Tholen: Primarily distinguished by the 0.3–0.5-μm UV dropoff region. Bus and B-D do not cover this region, thus do not make these distinctions.<br>Bus: Defined by UV dropoff and/or by 0.7-μm Cgh, Ch feature.<br>B-D: Definition largely preserved from Bus. Near-IR is largely degenerate. | Minerals: opaques, carbon, phyllosilicates, some have weak features indicating olivine, pyroxene<br>Meteorites: carbonaceous chondrites (except CV), possibly impact melts from ordinary chondrites and HEDs? |
| X-complex |  E<br>M<br>P | | X<br>Xc<br>Xe<br>Xk | 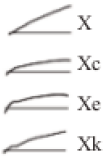 X<br>Xc<br>Xe<br>Xk | Tholen: EMP are spectrally degenerate. Distinguished by high (E), med (M), and low (P) albedo.<br>Bus: X class defined by shape of curve and/or 0.49-μm Xe feature.<br>B-D: Definition largely preserved from Bus. Near-IR is largely degenerate. | Minerals:<br>M,P: opaques, carbon, low-Fe pyroxene.<br>E: enstatite, oldhamite<br>Meteorites:<br>M,P: carbonaceous chondrites (not CV).<br>M w/high radar albedo: irons, CB chondrites, silicate-rich irons<br>E: enstatites |
| Other: End members, outliers | 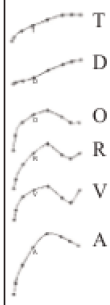 T<br>D<br>O<br>R<br>V<br>A | | T<br>D<br>Q<br>O<br>R<br>V<br>A<br>K<br>L<br>Ld | 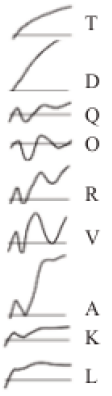 T<br>D<br>Q<br>O<br>R<br>V<br>A<br>K<br>L | Definitions for each of these classes are relatively consistent among taxonomies as they are each spectrally distinct. | D: opaques, organics<br>Q: mostly LL OCs<br>O: pyroxene, olivine<br>R: olivine, pyroxene<br>V: HEDs, pyroxene, plagioclase feldspar<br>A: pallasite, brachinite, R chondrites, olivine<br>K: CO, CV, olivine<br>L: CAI-rich, spinel-rich |

Figure 3.2 – Comparison and explanation of the progression of spectral taxonomies with the description of relevant minerals and meteorites for each class. Table from DeMeo et al. [2015].

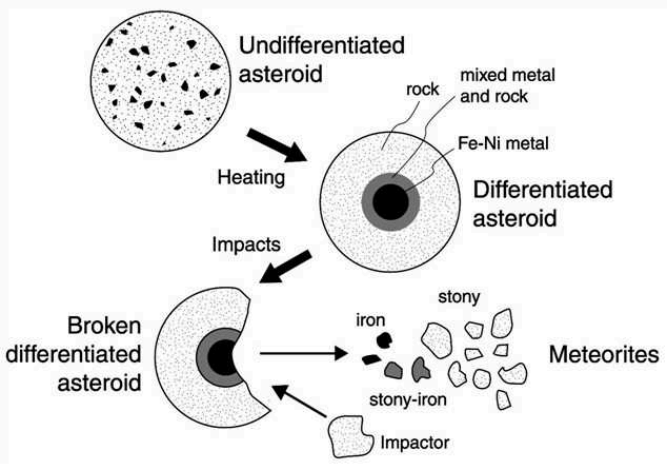


Figure 3.3 – Comparison scheme between undifferentiated and differentiated asteroids. For example, (4) Vesta survives with its original basaltic surface. When differentiated asteroids experience collisions, their crusts are stripped away and their densest Fe cores are exposed. In other cases the crusts are partially stripped away, and the exposed surfaces may be such as those visible today on the less abundant A-, E-, and R-class asteroids. Image from http://www.cefns.nau.edu/geology/naml/Meteorite/Book-GlossaryA.html.

## 3.2 Reflectance Spectra

Reflection spectra provides information about the top-most layers of the surface of asteroids. Mineral compositions of asteroids are inferred from visible and near-infrared reflectance spectroscopy.

$$\text{Reflectance}_\lambda(\text{object}) = \frac{\text{Flux}_\lambda(\text{object})}{\text{Flux}_\lambda(\text{standard})} \tag{3.1}$$

Here, the standard is a telluric standard star, of which observations are required for all NIR spectroscopic observations to cancel telluric (atmospheric) strong and variable absorption features due to the Earth's atmosphere in the data obtained. This star must be near in both time and sky position (air mass) to the object.

## 3.3 Near infrared Spectra (NIR)

Statistical work on spectral data allows the construction of taxonomic systems, a first step in studies of comparative planetology. The current taxonomy for asteroids by DeMeo et al. [2009] underlines the importance of both visible and near-infrared spectral data in asteroid classification statistics. This is quite understandable as the characteristic absorption bands for regoliths on asteroid surfaces are located in the 0.4-3.6 $\mu$m spectral region[1]. Also, with few exceptions, this spectral region is accessible from the ground, the atmosphere being mostly transparent to these wavelengths.

NIR spectra of S type asteroids are dominated by two bands, a broad band at about 1 $\mu$m caused by pyroxene and olivine absorptions, and a broad band at about 2 $\mu$m caused predominantly by pyroxene. The variations in the compositions of these minerals and the presence of minor minerals such as metal and plagioclase affect the position and width of these two bands (Fig. 3.1).

## 3.4 Why determine binaries taxonomy?

There are about 700,000 known asteroids, most of them belonging to the Main Belt. Among small asteroids (up to 10–15 km), about 15 ± 4% are binary asteroids [Margot et al., 2015]. We currently know 213 systems. Unfortunately, spectral classification is missing for 127 (60%) of them [Johnston, 2016], and the density has been estimated for only 54 systems (25%). It is crucial to gather spectral classifications of these minor bodies, as well as to monitor the relative position of the satellites around them to derive their density [Carry, 2012]. This will help us to better constrain the properties of these minor bodies such as internal structure, and

[1] We refer here only to the reflection spectral behaviors.

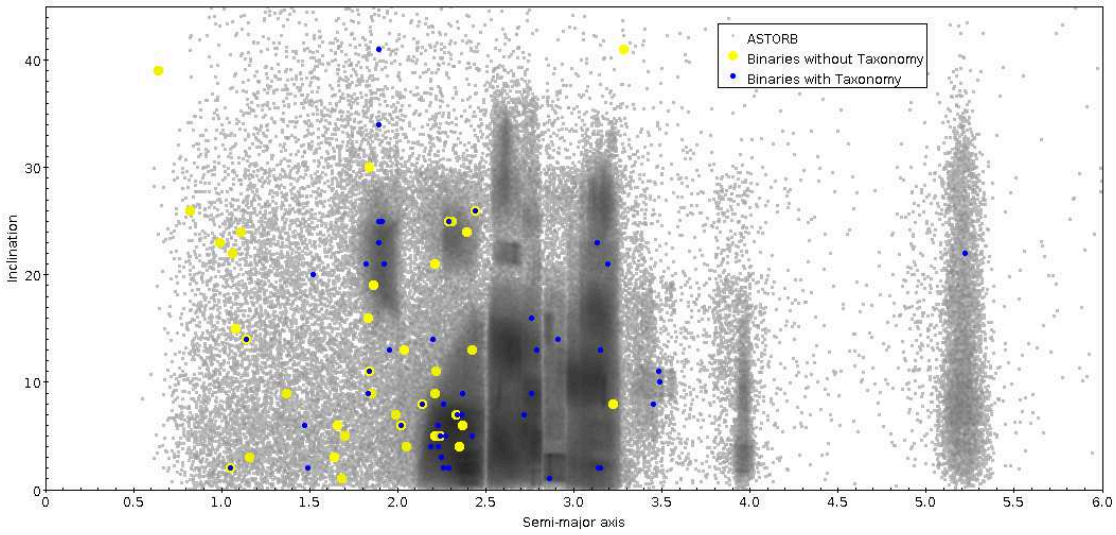


Figure 3.4 – Binary asteroids without taxonomy before current work.

Table 3.1 – Observational circumstances for each asteroid. Asteroid designations, mid-date of observation (UT), apparent magnitude (V), phase angle ($\alpha$), heliocentric distance ($\Delta$), airmass (AM), the integration time for each spectrum (IT), and the number of cycles of each observation are presented. The last two columns describe the solar analogs (SA) used for data reduction as well as their airmass at the observing time ($AM_{SA}$).

| Asteroid | Date (UT) | V (mag) | $\alpha$ (°) | $\Delta$ (AU) | AM | IT (s) | Cycles | SA | $AM_{SA}$ |
|---|---|---|---|---|---|---|---|---|---|
| (2691) Sersic | 2015-09-30T10:10:00.00 | 16.33 | 8.69 | 2.34 | 1.04 | 120 | 6 | HD 377 | 1.21 |
| (4383) Suruga | 2015-09-30T12:30:00.00 | 15.8 | 5.64 | 2.30 | 1.25 | 120 | 6 | HD 7983 | 1.41 |
| (7187) Isobe | 2015-09-30T14:10:00.00 | 16.78 | 30.92 | 1.77 | 1.10 | 120 | 13 | HD 232824 | 1.22 |
| (8373) Stephengould | 2015-09-29T14:38:51.64 | 17.94 | 31.20 | 1.88 | 1.26 | 120 | 3 | HD 60298 | 1.20 |
| (76818) 2000 RG79 | 2015-09-29T14:38:51.64 | 17.94 | 31.20 | 1.88 | 1.26 | 120 | 3 | HD 60298 | 1.20 |

formation processes.

Our aim is also to investigate whether small binaries -as is the case of the sample in this work- are more frequent among some kind of taxonomic class or not and if this is consistent with a binary formation mechanism that involves YORP-induced spin-up and rotational fission and mass shedding [Walsh et al., 2008, Walsh and Jacobson, 2015, Margot et al., 2015].

## 3.5 Binaries NIR Spectra Observed with Spex

In this first part of the chapter, I present spectroscopic results for one Mars Crosser and four Main Belt asteroids (Fig. 3.5) in the 0.8-2.5 $\mu$m spectral region. These objects were observed during the night of September 29, 2015 granted by the NASA Infrared Telescope Facility (IRTF). In Section 3.6, I describe the observation method and the data reduction process. In section 3.7

I present the methods that we use to model and analyze the data and interprete the obtained spectra to assess the composition and mineralogy of the asteroids. In Section 3.8, I present the current available information on these binaries with the results of the spectral analysis for each body.

## 3.6 Observing method and data reduction

I observe the asteroids and the solar analogs (for telluric corrections and removal of the solar continuum) alternatively during the run. In order to have the least amount of airmass, we scheduled the observations of all asteroids as close to the meridian as possible, preceded by the observation of their solar analogs. The search for these stars was done with the star locator on the IRTF webpage[2]. The photometrical G2V standards were chosen, with the following stars used as solar analogs: HD 377, HD 7983, HD 232824, each of them close to their respective asteroid (see details in Table 3.1).

The asteroids were observed in the 0.8 - 2.5 $\mu$m spectral region with SpeX the low-to medium-resolution near-IR spectrograph and imager [Rayner et al., 2003], on the 3-meter NASA IRTF located on Mauna Kea, Hawaii. Observations were performed remotely from the Centre d'Observation à Distance en Astronomie à Meudon [CODAM, Birlan et al., 2004, 2006] using the low resolution Prism mode ($R$ = 100) of the spectrograph. We used a 0.8×15 arcsec slit oriented North-South. The spectra for the asteroids and the solar analog stars were obtained alternatively on two separated locations on the slit denoted A and B using the $nodding$ procedure [Nedelcu et al., 2007][3]. We follow the *SpeX Observing Manual* [Rayner, 2015] throughout the run and for the reduction of the data, we used Spextool (SPectral EXtraction TOOL), an Interactive Data Language (IDL)-based data reduction package written by Cushing et al. [2004] to reduce data obtained with SpeX.

The circumstances of observations are presented in Table 3.1. All the asteroid spectra were obtained taking images with an integration time (IT) of 120s in the nodding procedure for several cycles, in order to increase the signal to noise ratio ($S/N$). For asteroids (2691) Sersic and (8373) Stephengould, the atmospheric conditions and their low brightness imply a poor $S/N$. The weather conditions of the night were: seeing 0.6 arcsec, humidity (at the beginning of the run) 16%, we note the presence of clouds during the run and temperature of 4.5°C.

## 3.7 Methods used to analyze data

For the analysis, I gather information of all previously published physical and dynamical properties of the asteroids observed. Table 3.2 summarizes some parameters of the sample, and also the taxonomic classification given in this work.

[2] http://irtfweb.ifa.hawaii.edu/cgi-bin/spex/find_a0v.cgi
[3] A cycle commands a beam-switch sequence, in case AB, 2 images are taken.

Table 3.2 – Some characteristics of the observed asteroids: dynamical type (DT), semi-major axis (a), eccentricity (e), inclination (i), absolute magnitude (H), geometric albedo ($p_v$), and taxonomic classification determined in the present study.

| Object | DT | a (AU) | e | i (°) | H | $p_v$ | Type |
|---|---|---|---|---|---|---|---|
| (2691) Sersic | MB | 2.24459579 | 0.11243958 | 3.594182 | 13.2 | 0.261[a] | Sr |
| (4383) Suruga | MB | 2.42449137 | 0.06338279 | 7.153714 | 13.0 | 0.32[a] | V |
| (7187) Isobe | MBI | 1.93746414 | 0.08610948 | 21.78856 | 14.0 | 0.134[a] | K |
| (8373) Stephengould | MC | 3.28021862 | 0.55469871 | 40.79090 | 14.2 | – | X[b] |
| (76818) 2000 RG79 | HUN | 1.92991672 | 0.09576145 | 18.1352629 | 13.7 | – | Xc |

[a] From Masiero et al. [2011]

[b] The composite V+NIR spectrum was used.

The only visible spectral counterpart available for this analysis was for (8373) Stephengould. For the other cases, were the visible range was lacking, the slope was computed for the spectra normalized to 1.25 $\mu$m. I also found Sloan Digital Sky Survey (SDSS) colors for (4383) Suruga, which were included in the analysis.

For analyzing the spectra, I used `M4AST` (Modeling for asteroids), a public software tool developed at the IMCCE by Popescu et al. [2012] and proposed as a centralized database for all published data that currently contains more than 7,000 spectra of asteroids, including SMASS MIT's database [Binzel et al., 2004] and libraries such as RELAB [Pieters, 1983]. `M4AST` also proposes methods and routines to achieve taxonomy classification, spectral comparison using Cloutis et al. [1986] model to compute spectral parameters, and space weathering effects model proposed by Brunetto et al. [2006] in order to model spectra and extract several mineralogical parameters [Birlan et al., 2016]. `M4AST` is free and available via a web interface.[4] Variables like the grain size, packing state, or the viewing geometry are mostly ignored, though these variables can affect the spectral slope and bands [Perna et al., 2016].

All NIR spectra are normalized to 1.25 $\mu$m and are plotted in Fig. 3.5 with error bars. In the case of (8373) Stephengould, we joined the visible counterpart available in the literature [de León et al., 2010] with the NIR part of this work for the analysis (Fig. A.7).

The discussion about taxonomic type of each object is made with reference to Fig. 3.5. The results for taxonomic classification of spectra are synthesized in Table 3.2 to allow a comparison with the physical properties.

Table 3.4 summarizes the comparison of asteroid spectra with those of meteorites from RELAB spectral database[5]. The corresponding figures are in Appendix A.1.

[4] http://m4ast.imcce.fr/

[5] http://www.planetary.brown.edu/relab/

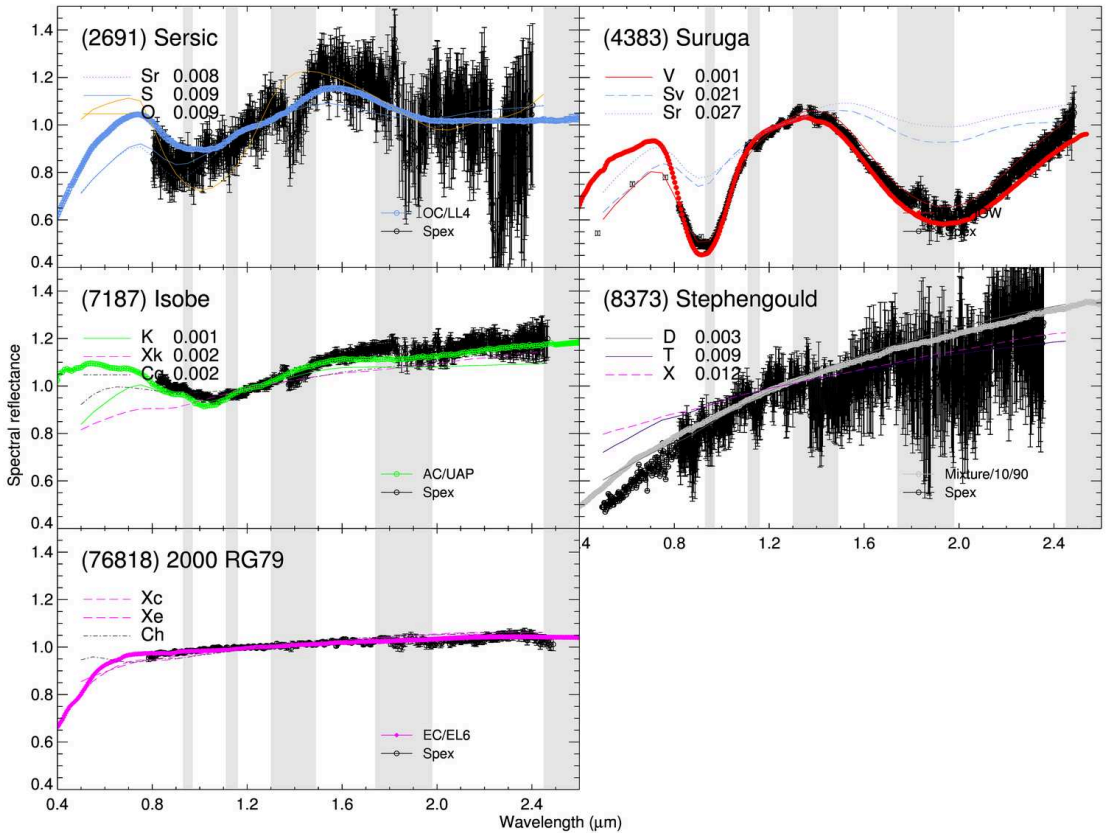


Figure 3.5 – NIR spectra of (2691) Sersic, (4383) Suruga, (7187) Isobe, (8373) Stephengould and (76818) 2000 RG79 with error-bars. Classification was made using DeMeo et al. [2009] taxonomical system, and we report the best three matches, with their $\chi^2$. For (4383) Suruga spectrum, five points from SDSS photometry were converted to reflectance [using the transformation by Bilir et al., 2005, Rodgers et al., 2006] and added. Shaded in light grey are wavelength ranges affected by atmospheric absorption [Lord, 1992]. All spectra are normalized to unity at 1.25 $\mu$m. Light blue corresponds to the best match spectra from RELAB library for each asteroid.

## 3.8 Results on individual targets

### 3.8.1 (2691) Sersic

This asteroid was discovered on May 18, 1974 from Felix Aguilar Observatory, El Leoncito, Argentina. Its companion was revealed from photometric observations by Oey et al. [2011] on June 2011. With an absolute magnitude of $H$ = 13.4, and a geometric albedo of $p_v$ = 0.261 ± 0.062 [Masiero et al., 2011], this object has an estimated diameter of 5 ± 0.11 km [from the effective diameter of the system, its albedo, and the combined $H$, Johnston, 2014].

Sersic is an inner main belt asteroid, next to the Flora family, near the $\nu_6$ secular resonance, a source region of near-Earth asteroids [Binzel et al., 2004]. Average properties of this family are: taxonomic class S [mainly obtained from visible spectroscopy, Florczak et al., 1998] and $p_v$ = 0.305 ± 0.064 [Masiero et al., 2015].

From spectroscopic observations of Flora members combined with analyses of meteorite samples, Vernazza et al. [2008], de León et al. [2010], and Dunn et al. [2013] had linked LL chondrite meteorites to the Flora family. No spectrum has been published for (2691) Sersic previously.

With M4AST online tool, using $\chi^2$ method with Bus-DeMeo taxonomy [DeMeo et al., 2009] system, this asteroid was classified as Sr-type [with a reliability factor [6] of 78.0%, Popescu et al., 2012] with a close fit with S and O type using standard error and mean square methods respectively. The spectrum shows a shallow absorption feature around 1$\mu$m. Owing to the paucity of known O-type asteroids, and the fact that S-types dominate the inner main belt population [DeMeo and Carry, 2013, 2014], the probability is higher for it to be an S-type classification for Sersic, over a less-likely O-type (Fig. 3.5).

Comparison with Relab database from the M4AST tool, shows that using $\chi^2$ method, the best spectral fit is obtained with Los Angeles meteorite (stone 1) (Sample ID:MT-JLB-006-C, This corresponds to a Shergottite, a martian meteorite (basaltic to lherzolitic igneous rocks) with chip natural texture. This doesn't match well with this asteroid, since Shergotittes have estimated time of formation of $1\times10^6$years [Jagoutz and Wanke, 1986] while the Flora family lifetime is $1\times10^9$years [Nesvorný et al., 2002]. For this reason we are considering the other closer analogues. The second match is for meteorite Hamlet (Sample ID OC-TXH-002-A20), an LL4 ordinary chondrite; the third match is for another sample of Los Angeles meteorite (Sample ID MT-JFM-005) again a Shergottite. The fourth, fifth and sixth matches are all Ordinary Chondrites, meteorites: Soko-Banja (OC/LL4, Sample ID MR-MJG-070), Barratta (OC/L4, Sample ID MH-CMP-002), and Bjurbole unshaken (OC/L4, Sample ID MP-FPF-027).

The poor $S/N$ makes the analysis very hard to do. Only the NIR part of the spectrum is available, therefore we can compute only the band minima. The first minimum is at 0.9161 ±

[6] Defined as the ratio of the number of points of the asteroid spectrum over the total number of points defined for the taxonomic type.

0.0054$\mu$m (Fig. A.5). The spectrum exhibits spectral variations around 1.45 $\mu$m and 1.9 $\mu$m due to the influence of telluric water that remained even after the data reduction.

Being (2691) Sersic an Sr-type asteroid, no attempt to model space weathering was conducted due to the low $S/N$. Better $S/N$ NIR spectra are thus needed, together with visible counterpart, to understand the reflectance properties of Sersic.

### 3.8.2 (4383) Suruga

Suruga, a Vestoid [i.e., a fragment of asteroid (4) Vesta, Binzel and Xu, 1993], was discovered in December 1989 from Gekko, Japan by Y. Oshima. Its companion was detected on February 2013 using lightcurve observations. The rotation period of the primary is 3.4068 ± 0.0003 h with an amplitude of 0.14 ± 0.01 mag, indicating a nearly spheroidal shape. The orbital period of the satellite is 16.386 ± 0.001 h [Warner, 2013b]. The ratio $Ds/Dp \geq 0.21 \pm 0.02$ [7]. This object has a geometric albedo $p_v$ = 0.320 ± 0.038 [Masiero et al., 2011]. The diameter of the primary is 6.33 ± 0.09 km and has been derived from lightcurves [Johnston, 2014]. A NIR spectrum has been published by de Sanctis et al. [2011]. We will compare the present results with theirs data. This is the only asteroid from the sample that had a previous taxonomy, it was identified as V-type; the `M4AST` online tool for taxonomy also classified this object as belonging to V-class (Fig 3.5).

This spectrum shows two prominent absorption features at 1 and 2 $\mu$m, typical of V-class asteroids. When comparing with spectra from Relab database, we found spectral matches with the achondrite meteorite Pavlovka, a howardite achondrite (Sample ID:MR-MJG-094). These type of meteorites are thought to have originated from the crust of the asteroid Vesta (Table 3.4, Fig. A.2). Other spectra that fits Suruga NIR spectrum corresponds to samples of particulates (0-25 $\mu$m) of the meteorites Le Teilleul (Sample ID:MP-TXH-093-A), Frankfort howardite (Sample ID:MP-TXH-085-A), and "Y-7308,142" (Sample ID:MP-TXH-097-A) all of them Howardite-Eucrite-Diogenite (HED). This matches suggests that the asteroid might be covered by a fine regolith layer. Two other matches corresponds to meteorites Kapoeta P11410 (Sample ID: SN-CMP-012) an achondrite HED Breccia and “GRO95574,9” (Sample ID: MP-TXH-125) a basaltic HED regolith breccia.

This spectrum was acquired with a high $S/N$ which ensures a small error in computing the position and depth of the band minima. The first minimum is at 0.9254±0.0007 $\mu$m and the second minimum is at 1.9710±0.0042 $\mu$m which implies a band separation of 1.0456 $\mu$m (Fig. A.6). It can also be seen a weak ~1.2 $\mu$m feature. For basaltic achondrites this is indicative of the presence of feldspar. The feature is weak in the spectra of howardites [Hardersen et al., 2004]. The normalization of this spectrum was made for the wavelength: 1.250 $\mu$m.

Because, only the NIR part of the spectrum is available, and as such solely the band minima can be computed, we look at data in SDSS catalog [Ivezić et al., 2010] and found the magnitudes in

[7] $Ds$: Diameter of secondary, $Dp$: Diameter of primary

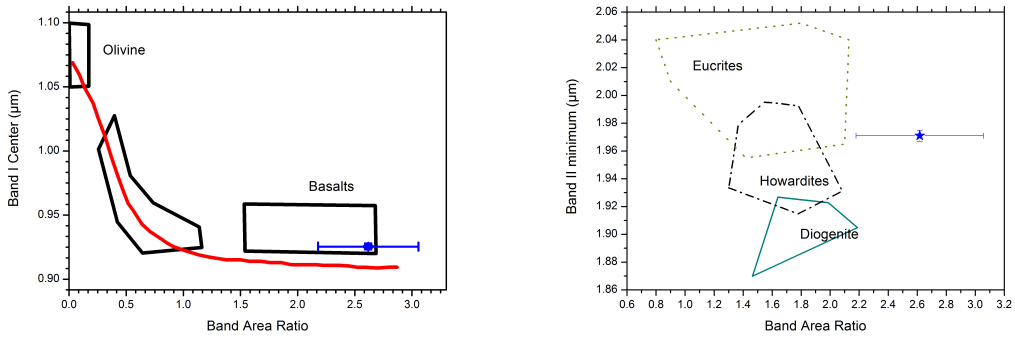


Figure 3.6 – (4383) Suruga Mineralogical analysis: *(Left)* Band Area Ratio (BAR) versus band I centers. The regions enclosed by continuous lines correspond to the values for basaltic achondrites, ordinary chondrites (OC), and olivine-rich meteorites (Ol) according to Gaffey et al. [1993]. *(Right)* Suruga spectrum (blue star) placed into BAR versus Band II minimum HED diagram of Moskovitz et al. [2010]. The BAR of Suruga is larger than those represented by HED's, similarly as V-type asteroids BARs in Moskovitz et al. [2010].

$ugriz$ filters. We converted them into spectral reflectance [Zellner et al., 1985]:

$$\log R_\lambda = \pm 0.4 c_\lambda$$

(where $c_\lambda$ is the tabulated color index and the negative sign is chosen for wavelengths shorter than visual) and the transformations for the colors of the Sun into reflectance using the Bilir, Karaali, and Tuncel transformation for $g$ filter [Bilir et al., 2005, Rodgers et al., 2006]. With these new "reflectance points" we complete the visual part of the spectrum we got (Fig. 3.5), and compute the Band Area Ratio BAR=2.6±0.4 and then compute the mafic mineral composition according to [Gaffey et al., 2002] (Fig. 3.6). We found $W_{O_7}$ and $F_{S_{45}}$ and the mineral abundances in the olivine-orthopyroxene mixture Ppx/(Opx)+ Ol = 1.1±0.2. We note, however, that although the band I area is uncertain owing to the poor sampling of the visible part, the BAR we derive is consistent with those of V-type asteroids [Moskovitz et al., 2010].

Using `M4Ast` analysis with de Sanctis et al. [2011] spectrum of Suruga: the first minimum is at 0.9023±0.0018 $\mu$m and the second minimum is at 1.8770±0.0072 $\mu$m which implies a band separation of 0.9747 $\mu$m (Fig. A.6). Comparing with the present work values, there is a notorious difference with the second minima value. This is understandable because De Sanctis spectrum values under `M4Ast` scheme are slightly noisy around 1.9$\mu$m. In the original work by de Sanctis et al. [2011], BII minimum is 1.91±0.005$\mu$m. In conclusion, this is a V-type asteroid.

### 3.8.3 (7187) Isobe

Asteroid (7187) Isobe was discovered by E. F. Helin in January 30, 1992 from Palomar Observatory, California, USA. It orbits in the Hungaria region[8], owing to its small size it might have been drifted by Yarkovsky effect and get trapped by secular resonances [McEachern et al., 2010]. Isobe has been studied by extensive lightcurve observations since 2004 [Warner, 2005, 2008, 2011, 2013a]. Warner also discovered its companion in August 26, 2012, using ligthcurve observations from Palmer Divide Observatory (PDO) under the PDO observing program, which concentrates on Hungaria asteroids. More recently, lightcurves published by Stephens [2016] do not make any evidence of mutual event into the binary system of Isobe.

The period of the primary is 4.2427±0.0002h [Warner, 2013a], while for the secondary, Warner found two possible solutions from which the longer one of 33.22±0.04 h, seems more probable since the "events" are about equally spaced in the overall curve, which may indicate that the satellite is on a circular orbit. In that case, the system is old enough to have evolved by tides because torques from mutual body tides dissipate energy circularize the orbit and affect the rotation rates [Jacobson and Scheeres, 2011, Murray and Dermott, 1999].

This asteroid has a magnitude $H$=13.89, a diameter 6.05±1.46 km, and a geometrical albedo $p_v$=0.134±0.104 [Masiero et al., 2012].

No spectrum has been published previously for (7187) Isobe. With `M4AST` Classification tool using $\chi^2$ approach we find that (7187) Isobe fits a K-type asteroid with a clear absorption band around 1 $\mu$m (Fig. 3.5). The reliability of the classification is 80.4%. The local minimum around 1$\mu$m was found at 1.0707 $\mu$m adjusting a second degree polynomial with $R^2$ = 0.8532. The fits with Xk and Cg types do not show very well this 1$\mu$m feature (Fig. 3.5).

The Relab meteorite sample that best fits is a Particulate Ground Dry-Sieved, Almahata Sitta #4 <125$\mu$m meteorite (sample ID: MT-PMJ-093-C), an Achondrite Ureilite Anomalous Polymict (0-125 $\mu$m)). Another fit is with a sample of Allende: HC-10 dark inclusion meteorite, a carbonaceous chondrite (sample ID: MT-TJM-073). Allende meteorite is olivine-rich, and contain an abundant matrix that is relatively featureless in the near infrared which explains why the 1$\mu$m absorption feature is subtler than in ordinary chondrite spectra [Vernazza et al., 2011]. Meteorite Tsarev (sample ID: MA-ATB-053 OC) an ordinary chondrite, also fits this spectrum. Other meteorite spectra found with `M4AST` were "LEW87009,16" (sample ID: LM-LAM-011), "EET90021,10" (sample ID: MP-TXH-043), and "LEW87148,15" (sample ID: MP-TXH-016); all of them carbonaceous chondrite. Of the last four spectra the one of "LEW87009,16" fits better the absorption around 1$\mu$m.

With the error bar of (7187) Isobe geometrical albedo, it is hard to favor one solution if CC, OC and ureilite are together. However, there is a clear dichotomy between ureilitic and chondritic materials. (Table 3.4, Fig. A.3). Regarding ureilites, this is consistent with the weak mafic iron silicate absorption bands that this spectrum presents in the 1$\mu$m and 2$\mu$m region according

[8] Using the dynamical class in vo.imcce.fr

to Cloutis et al. [2010]. The visible counterpart of the spectrum is needed to complete the analysis. With Nimura et al. [2006] method we can try to put constraint in the olivine band around 1$\mu$m in the Modified Gaussian Model.

### 3.8.4 (8373) Stephengould

Stephengould was discovered the 1$^{st}$ of January 1992 from Palomar Observatory, California, USA by C. S. Shoemaker and E. M. Shoemaker. Its companion was discovered in January 2010 by Krugly et al. [2010] using lightcurve observations (reexamination of previous observations shows what appears to be an event overlooked in the original analysis by Warner [2004]).

Stephengould is a Mars Crosser with an absolute magnitude $H$=13.8. From the lightcurves, the orbital period of the secondary is 34.15 ± 0.1 hr and the primary rotation period is 4.435 ± 0.001 hr. From mutual events, Krugly et al. [2010] obtained a lower limit on the secondary-to-primary mean-diameter ratio of 0.27.

This spectrum is featureless (Fig. 3.5), although it shows some artifacts. The bad $S/N$ does not permit to draw more conclusions. A composite VNIR spectrum by de León et al. [2010] was found in the literature and the NIR spectrum in this work has similar trends with it. Into our analysis we used the visible spectrum of de León et al. [2010], merge it with our NIR data, and compare the results of these two composite spectra. The composite spectral slope is 0.262 with a correlation of 0.8 which is in agreement with the one of de León et al. [2010], we can observe a similar positive slope in the spectrum (Fig. A.8).

With `M4AST` classification tool using $\chi^2$ approach based on Bus-DeMeo taxonomy [DeMeo et al., 2009] we find that the taxonomic type that best fit this spectrum is X-type followed by T and D type with a reliability of 75.6%. The normalization of this spectrum was made for the wavelength: 1.250 $\mu$m (Fig. 3.5).

Comparison of the asteroid spectrum with Relab samples, the best fits of the spectra were for the mesosiderite Veramin (Sample ID: MR-MJG-084), rock meteorite “Finest Octahedrite, Plessitic(0.15mm) IRANOM" Butler (Sample ID: MR-MJG-081), ordinary chondrite Pervomaisky (Sample ID: RS-CMP-064), carbonaceous chondrite Tagish Lake ET01-B (Sample ID: MT-MEZ-011), rock Medium Octahedrite IIIAB Chulafinnee (Sample ID: MR-MJG-082), and sulfide Mundrabilla troilite (Sample ID: MB-CMP-006-P2) (Fig. A.4).

D-type asteroids are characterized by low albedos [Fulchignoni et al., 2000], and are scarce in the inner Solar System [see DeMeo et al., 2014, Carry et al., 2016]. T-type asteroids seems to be also not so representative for the entire asteroidal population [DeMeo and Carry, 2014] and could be interpreted as an end-member class. Having no albedo information for Stephengould, and due to the more abundant X type asteroids [DeMeo and Carry, 2013]; this asteroid is more akin to the X-complex, although fits better to D-type (Fig. 3.5).

Table 3.3 – Slopes and mineralogical parameters of the spectra of binaries obtained (when possible) using Cloutis model.

| Object | Band I ($\mu$m) | Band II ($\mu$m) | Band II-Band I ($\mu$m) | Slope (Refl/$\mu$m) |
|---|---|---|---|---|
| (2691) Sersic | 0.9161 | - | - | 0.0633 |
| (4383) Suruga | 0.9254 | 1.9710 | 1.0456 | 0.0616 |
| (7187) Isobe | 1.0707 | - | - | 0.1571 |
| (8373) Stephengould | - | - | - | 0.2624 |
| (76818) 2000 RG79 | - | - | - | 0.0395 |

### 3.8.5 (76818) 2000 $RG_{79}$

This asteroid was discovered on September 8, 2000, by the *Lincoln Near-Earth Asteroid Research (LINEAR)* program at Socorro, New Mexico. Its companion was discovered by Warner et al. [2005] from photometric observations obtained during August 7-28, 2005 at Palmer Divide Observatory (PDO) (published in Warner and Stephens [2009]). Additional observations in 2008 and 2013 [Warner et al., 2011, Pravec et al., 2012, Warner, 2014a] helped refine the system parameters.

This is an Hungaria asteroid (a = 1.929 AU) with an absolute magnitude $H$=13.7, it has an estimated geometric albedo $p_v$ = 0.43. From the lightcurves, the primary rotation period is 3.1669 ± 0.0002 h and the orbital period of the secondary is 14.134 ± 0.002 h [Warner, 2014a]. From mutual events, the ratio $Ds/Dp$ is 0.32± 0.02 according to Warner [2014a] and $Ds/Dp \geq$ 0.35 according to Pravec et al. [2012]. The estimated diameter of the primary is 3.6 km [Pravec et al., 2006].

No spectrum has been published previously for (76818) 2000 RG79. The NIR spectrum obtained with Spex (Fig 3.5) has no features, only a very slight absorption at 2$\mu$m and a shallow slope that turns slightly negative around 2.37$\mu$m until the end of the spectrum at longer wavelengths. With `M4AST` Classification tool using $\chi^2$ approach based on Bus-DeMeo taxonomy [DeMeo et al., 2009] we find that the taxonomic types that best fit this spectrum are Xc, Xe and Ch types (Fig. 3.5). The reliability of the classification is 82.9%. From inspection of these classification, and comparing with Bus DeMeo MITs classification tool, the match that resembles best the spectrum of the asteroid is Xe type, which are numerous among hungarian [DeMeo and Carry, 2014].

When comparing the asteroid spectrum with Relab samples, the best fits of the spectra were for enstatite chondrite “ALHA81021,89 (EL6) <25um” (Sample ID: MT-PFV-119-B), Achondrite Mayo Belwa (Sample ID:TB-TJM-046), enstatite chondrite "QUE93372,13 (EH5) <25um” (Sample ID:MT-PFV-129-B), enstatite chondrite "ALH84206,25 (EH3) <45um” (Sample ID:MT-PFV-118-A) and enstatite chondrite "KLE98300,33 (EH3) <45um” (Sample ID:MT-PFV-122-A). The estimated geometric albedo of the featureless spectra of (76818) 2000 RG79 is compatible with enstatite chondrite meteorites [Vernazza et al., 2009].

Table 3.4 – Summary of results obtained by matching the asteroids spectra with spectra from RELAB database. The comparison was made using a $\chi^2$ method and a selection of the obtained results was done based on spectral features (band, band-gap, concavity) positions and albedo value. The figures for this comparison can be found in Appendix A.1

| | Matching results for asteroids spectra | | | | |
|---|---|---|---|---|---|
| Spectrum | Meteorite | Sample ID | Type | Texture | Size [ $\mu$m] |
| (2691) Sersic | Los Angeles (stone 1) | MT-JLB-006-C | SHE | Chip Natural | - |
| | Hamlet | OC-TXH-002-A20 | OC/LL4 | Chip | - |
| | Los Angeles | MT-JFM-005 | SHE | Particulate | 0-1000 |
| | Soko-Banja | MR-MJG-070 | OC/LL4 | - | - |
| | Barratta | MH-CMP-002 | OC/L4 | Slab | - |
| | Bjurbole unshaken | MP-FPF-027 | OC/L4 | Particulate | 0-1000 |
| (4383) Suruga | Pavlovka | MR-MJG-094 | AC/AHOW | - | - |
| | Le Teilleul | MP-TXH-093-A | AC/HED | Particulate | 0-25 |
| | Frankfort howardite | MP-TXH-085-A | AC/HED | Particulate | 0-25 |
| | "Y-7308,142" | MP-TXH-097-A | AC/HED | Particulate | 0-25 |
| | Kapoeta P11410 | SN-CMP-012 | AC/HED Breccia | Thin Section | - |
| | “GRO95574,9” | MP-TXH-125 | Basaltic HED Howardite | Particulate Ground | 0-125 |
| | (Howardite) <125$\mu$m | | Regolith Breccia | Dry-Sieved | |
| (7187) Isobe | Almahata Sitta #4 | MT-PMJ-093-C | AC/UAP | Particulate Ground | 0-125 |
| | <125$\mu$m | | | Dry-Sieved | |
| | Allende: HC-10 | MT-TJM-073 | CC/CV3 | Particulate Ground | 0-38 |
| | dark inclusion | | | Dry-Sieved | |
| | Tsarev | MA-ATB-053 | OC/L5 | Particulate Ground | - |
| | >300$\mu$m (ground) | | Laser Irradiated | Sorted | |
| | "LEW87009,16 " | LM-LAM-011 | CC/CK6 | Thin Section | - |
| | "EET90021,10 " | MP-TXH-043 | CC/C2 | Particulate | 0-125 |
| | "LEW87148,15 " | MP-TXH-016 | CC/CM2 | Particulate | 0-125 |
| (8373) Stephengould | Veramin | MR-MJG-084 | Rock/MES EC | - | - |
| | Butler | MR-MJG-081 | Iron/IRANOM | - | - |
| | Pervomaisky | RS-CMP-064 | OC/L6 | Slab | - |
| | Tagish Lake ET01-B | MT-MEZ-011 | CC/CI | Particulate Ground | 0-125 |
| | | | | Dry-Sieved | |
| | Chulafinnee | MR-MJG-082 | Iron/IIIAB | - | - |
| | Mundrabilla troilite | MB-CMP-006-P2 | Sulfide/Troilite | Particulate | 25-45 |
| (76818) 2000 RG79 | “ALHA81021,89 (EL6) | MT-PFV-119-B | EC | Particulate Ground | 0-25 |
| | <25um” | | | Dry-Sieved | |
| | Mayo Belwa | TB-TJM-046 | AC/AEA | Particulate Ground | 0-125 |
| | "QUE93372,13 (EH5) | MT-PFV-129-B | EC/EH5 | Particulate Ground | 0-25 |
| | <25 um" | | | Dry-Sieved | |
| | "ALH84206,25 (EH3) | MT-PFV-118-A | EC/EH3 | Particulate Ground | 0-45 |
| | <45 um" | | | Dry-Sieved | |
| | "KLE98300,33 (EH3) | MT-PFV-122-A | EC/EH3 | Particulate Ground | 0-45 |
| | <45 um" | | | Dry-Sieved | |

## 3.9 Data through The MIT-UH-IRTF Joint Campaign for NEO Spectral Reconnaissance

The previous binary asteroids were observed after the submission and approbation of a proposal sent to IRTF. The second time my proposal was accepted, I was granted the double amount of time. Unfortunately, on the date of the observation a snow storm happened in Hawaii and we could not observe. This is something that happens but of course, research has to continue, I needed more targets to analyze. With that in mind, I looked for data from the *MIT-UH-IRTF Joint Campaign for NEO Spectral Reconnaissance* collaboration.There, I found several spectra of binaries that were in my observing list. Obviously, these binaries were small, mostly NEAs, some of them were being observed as potential threats to Earth civilization, others, as potential targets to be investigated by space missions; being small and close to the Earth, some of them were tracked in order to detect BYORP effect. These objects are included in this work and as before, with the previous 5 binaries, spectra was classified using `M4Ast` tool, and I search for matching corresponding meteorite spectra in RELAB. Below I present the results, and in Table 3.5 is the synthesis of all the binaries characterized.

Although taxonomic classification had been performed previously for some of them, I classify all these spectra again with the same protocol as described above in the previous Section 3.8 for consistency.

### 3.9.1 (88710) 2001 $SL_9$

Asteroid (88710) 2001 SL9 was discovered in September 18, 2001 from Palomar Observatory, California, USA by *Near Earth Asteroid Tracking (NEAT)* [Helin et al., 1997], the autonomous celestial observatory developed by the Jet Propulsion Laboratory/NASA[9]. This is an Apollo type near-Earth asteroid. Its companion was discovered in October 2, 2001 by Pravec et al. [2001] from Ondrejov observatory and Palmer Divide Observatory.

The rotation period of the primary is 2.4004±0.0002 h and the orbital period of the secondary is 16.40 ± 0.02 h [Pravec et al., 2006]. This asteroid has a magnitude $H$=17.6 (JPL). Pravec et al. [2006] get an estimate for the diameter of the primary of 0.8 km (uncertain to a factor of two) and $Ds/Dp$ = 0.28±0.02. Warner [2014b] observed also this binary in September 2013.

The NIR spectrum obtained with SpeX (Fig. 3.5) shows the typical S-type curve. We find that the taxonomic types that better fits this spectrum are Sr, S, and Sq types with a reliability in the classification of 80.4%. From inspection, the match that resembles best the spectrum is Sr-type.

This asteroid was classified by Lazzarin et al. [2004, 2005] as Sr and Q types, they also determined an analog meteorite with VNIR data from *Spectroscopic Investigation of Near Earth*

[9] https://neat.jpl.nasa.gov/

*Objects* SINEO [Lazzarin et al., 2008][10]. de León et al. [2010] classify it as Q-type. [Lazzarin et al., 2008] NIR data has low $S/N$, for this work we had use their visible spectrum (available in MAst libraries) and join it with the NIR spectrum to perform the analysis. Fig. 3.7 shows the VNIR composite spectrum we used to analyze with Cloutis model.

The position of the centre of the two absorption bands were computed, their values are: BI min[$\mu$m] = 0.9246 ± 0.0038, BII min[$\mu$m] = 1.8727 ± 0.0087, Band separation[$\mu$m] = 0.9481. The band centers are: BI center[$\mu$m] = 0.9357 ± 0.0042, BII center[$\mu$m] = 1.8721 ± 0.0086, and the Band area ratio: 0.5858 ± 0.0019.

From the analysis, the resultant mineralogy is OPX/(OPX+OL)[$\mu$m] = 0.2976 (Fig. 3.7). This means that 2001 $SL_9$ is an ordinary chondrite, more akin to L subtype.

When comparing the asteroid VNIR spectrum with RELAB samples, the best fits of the spectra are all for ordinary chondrites: OC/LL4 Hamlet (LL4) <125 $\mu$m (Sample ID: OC-TXH-002-C), OC/L6 Chateau Renard (L6) <125 $\mu$m pellet irradiated with 5 mJ + 10 mJ laser (Sample ID: OC-TXH-011-D15), OC/H3.4 Chondrule M-H3.4-2149C (Dhajala H3.4) chondrules <125 $\mu$m (Sample ID: DP-JNG-012), OC/L5 Tsarev 15384,3-2 (Sample ID: RS-CMP-065-T) and OC/L4 Saratov (Sample ID: MB-CMP-028-B).

### 3.9.2 (162483) 2000 $PJ_5$

This Aten asteroid was discovered on August 4, 2000, by the *Lincoln Near-Earth Asteroid Research (LINEAR)* program at Socorro, New Mexico [Stokes et al., 2000]. Its binary behaviour was noticed due to their asynchronous rotation from photometric observations obtained by Polishook and Brosch [2008] in July, 2005 from Wise Observatory.

Polishook and Brosch [2008] obtained all the characteristics of this Aten, they even estimate its taxonomy from phase curve parameters, using the correlation between phase and albedo found by Belskaya and Shevchenko [2000]. This Aten has an absolute magnitude $H$=18.41± 0.05, a geometric albedo $p_v$ = 0.2 ± 0.05. Primary rotation period is 2.642 ± 0.001 h and the orbital period of the secondary is 14.16 ± 0.04 h. The estimated diameter of the primary is 0.6 ± 0.1 km and the ratio $Ds/Dp$ is 0.5.

Even though the NIR SMASS spectrum (Fig 3.9) is a bit noisy, the curves clearly shows absorption features at 1 and 2 $\mu$m. With `M4AST` classification tool using $\chi^2$ approach based on Bus-DeMeo taxonomy [DeMeo et al., 2009] we find that the taxonomic types that best fit this spectrum are Q, K and S. (Fig. 3.9). The reliability of the classification is 82.9%. From inspection of these classification, the match that resembles best the spectrum of (162483) 2000 PJ5 is a Q type.

The first minimum is at 0.9591±0.0034 $\mu$m and the second minimum is at 1.9669±0.1805 $\mu$m which implies a band separation of 1.0078 $\mu$m.

[10] http://www.astro.unipd.it/planets/sineo.html

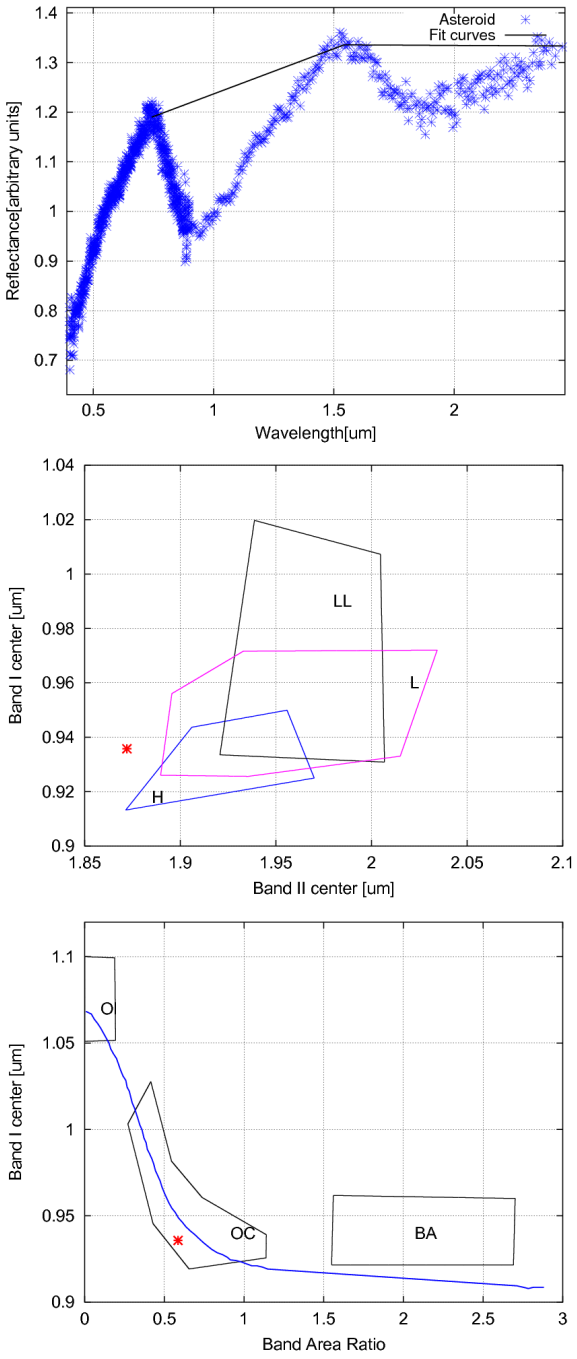


Figure 3.7 – Mineralogical analysis results for (88710) 2001 $SL_9$. **Top** Linear continuum tangential to spectral curve of spectrum obtained after merging visible spectrum [Lazzarin et al., 2004] and NIR spectrum of (88710) 2001 $SL_9$. **Middle** Wavelength position of the centers of the two absorption bands. The regions enclosed correspond to the band centers computed for the H, L, and LL chondrites. **Bottom** Band area ratio (BAR) versus band I center. The regions enclosed by continuous lines correspond to the values computed for basaltic achondrites (BA), ordinary chondrites (OC), and olivine-rich meteorites (Ol) [Gaffey et al., 1993].

When comparing the asteroid spectrum with RELAB samples, the best fits of the spectra were for the ordinary chondrites: Quenggouk (Sample ID: MR-MJG-042), Bandong (Sample ID: TB-TJM-067), Jelica (Sample ID: MR-MJG-072), Leedey (Sample ID: MR-MJG-060) and the silicate A-881757 (Sample ID: MB-CMP-029-M2).

### 3.9.3 (190208) 2006 AQ

This asteroid was discovered on 2006 January 2, from Mauna Kea Observatory, Hawaii, USA by D. J. Tholen. Its satellite was discovered by Warner [2015b] on 2014-2015 using lightcurve observations. This NEA type Amor is a so-called *wide binary*, an unusual binary type (fully asynchronous system,Warner [2015a]). In these kind of binaries the primary has a long period, ~hundreds of hours, and the satellite has a short period, with a low amplitude lightcurve; both are well separated, thus the orbital period is long and chances to see mutual events are low. this makes difficult its characterization, only some of the system parameters have been estimated so far. The rotation period of the primary is 182±2 h This asteroid has a magnitude $H$=18.1 (MPC), an estimated diameter of 1.06 km.

$S/N$ of this NIR SMASS spectrum (Fig 3.9) is low, but it can be noticed a slight absorption feature at 1$\mu$m. With `M4AST` Classification tool using $\chi^2$ approach based on Bus-DeMeo taxonomy [DeMeo et al., 2009] we find that the taxonomic types that best fit this spectrum are K, Cg and Ch. (Fig. 3.9). The reliability of the classification is 80.4%. From inspection of these classification, the match that resembles best the spectrum of (190208) 2006 AQ is a K type.

When comparing the asteroid spectrum with RELAB samples, the best fits are of different type of meteorites: Igneous meteorite Los Angeles (stone 1) (Sample ID: MT-JLB-006-B), Carbonaceous Chondrite meteorites Murchison (Sample ID: MR-MJG-109), Ordinary Chondrite meteorites Athens (LL6) chip (Sample ID: OC-TXH-013-A), Chondrite meteorites NWA753 (Sample ID: TB-TJM-114), and Chondrite meteorites A-881988,70 (Sample ID: MP-TXH-059) is obtained.

### 3.9.4 (348400) 2005 $JF_{21}$

This asteroid was discovered on May 4, 2005 from Kitt Peak Observatory, Arizona, USA by Spacewatch Program. Its satellite was discovered by Naidu et al. [2015] with Goldstone radar (8560 MHz, 3.5 cm) delay-Doppler images and echo power spectra, obtained on August 10, 2015. From the images with range resolutions of 150 m, the range extent of the primary is 0.3 km. They found that the two components were separated ~ 5.4 km in range with no obvious change in the separation during ~2 hours. They also found a persistent second narrow spike in the echo power spectra consistent with the presence of another satellite that still needs confirmation.

With an absolute magnitude of $H$ = 17.1, and a derived geometric albedo of $p_v$ = 0.59, this object has an estimated diameter of 0.6km [from the effective diameter of the system, its

albedo, and the combined $H$, Johnston, 2014]. This NEA is an Amor type and due to its orbital characteristics, it's a Potentially hazardous asteroid (PHA).

The NIR spectrum obtained from SMASS (Fig 3.9) shows two prominent absorption features at 1 and 2 $\mu$m, typical of V-class asteroids. Evidently, using `M4AST` Classification tool with $\chi^2$ approach based on Bus-DeMeo taxonomy [DeMeo et al., 2009] the best match is for V type followed by Sv and Sr types (Fig. 3.5). The reliability of the classification is 82.9%. When computing band minima, the first minimum is at 0.9332±0.0008 $\mu$m, and the second minimum at 1.9117±0.031 $\mu$m which implies a band separation of 0.9785 $\mu$m. Only the NIR part of the spectrum is available, and as such solely the band minima can be computed.

Comparing the asteroid NIR spectrum with RELAB meteorite database, all the best matches are Achondrites of varied subtypes: meteorite Kapoeta (ID: MP-TXH-053) subtype Basaltic HED Howardite; mateorite "MIL07001 <45 um" (ID: MT-AWB-168-A) subtype Basaltic HED Diogenite Harzburgitic and meteorite "GRA98108,26 chip" (ID: RM-REM-125) subtype Basaltic HED Olivine-Diogenite are the three best matches.

### 3.9.5 (374851) 2006 $VV_2$

This Apollo asteroid was discovered on November 11, 2006 from Socorro, New Mexico, USA, by the *Lincoln Near-Earth Asteroid Research (LINEAR)* program [Stokes et al., 2000]. It is classified as a Potentially Hazardous Asteroid (PHA). Its satellite was discovered using radar observations from Goldstone (8560 MHz, 3.5 cm), California, USA and Arecibo Observatory (2380 MHz, 12.6 cm), Puerto Rico by Benner et al. [2007b] during March 27-April 3, 2007. Due to its closest approach to the Earth of only 0.0226 AU around March 31, 2007, a campaign for optical observations in support of radar was set [11] [Warner et al., 2007] and the asteroid was surveilled by several astronomers [Benishek, 2008, Vereshchagina et al., 2009, Hergenrother et al., 2009, Huziak, 2007, Betzler and Novaes, 2009, Klotz and Behrend, 2007, Oey and Krajewski, 2008] from different parts of the world.

Benner et al. [2007a] report a modestly irregular and asymmetric asteroid with a surface with several prominent concavities, possibly including craters, and features along the leading edges that resemble the pronounced ridge seen along the equator of binary asteroid (66391) 1999 KW4.

The diameter of the primary is 1.06 ± 0.05 km [Betzler and Novaes, 2009] and > 0.3 km for the secondary [Benner et al., 2007b]. The maximum orbital distance between the components is at least 1.5 km [Benner et al., 2007b]. The rotation period of the primary is 2.41 ± 0.005 h [Benishek, 2008], and the orbital period of the secondary is estimated in 0.23 d. It has a magnitude $H$= 16.6 ± 0.2 [Betzler and Novaes, 2009] and its geometrical albedo is estimated $p_v$= 0.1.

[11] https://echo.jpl.nasa.gov/asteroids/2006VV2/2006VV2_planning.html

For this asteroid, color indices were measured by Betzler and Novaes [2009], Hergenrother et al. [2009], and Vereshchagina et al. [2009], who reported a strong dependence of the shape of the lightcurve on the color.

This spectrum is from Reddy [2009] (Fig 3.9). Although no taxonomy has been published (in peer reviewed journals), several taxonomies had been proposed before: from Spex data, V [Howell et al., 2008]; from color indices: S type [Hergenrother et al., 2009], A type [Vereshchagina et al., 2009, Vereshchagina, 2011], and V, Q or T type [Betzler and Novaes, 2009].

The best matches are for L, Xe and Ch types with a reliability of 90%. However, this spectrum has good $S/N$ and clearly shows absorption features around 1 and 2 $\mu$m that are shallow for the proposed taxonomies around 1 $\mu$m, and inexistent around 2 $\mu$m. MAST has a feature that allows comparison of the spectrum with different types from Bus-DeMeo taxonomy, using it and after visual inspection looking for good fit of the band positions and shapes, we found that the best matches are for Sr and S type (the best matches do not necessarily correspond to the lowest $\chi^2$ values).

When computing band parameters, the first minimum is at 0.9201 ± 0.0013 $\mu$m, and the second minimum at 1.9498 ± 0.0037 $\mu$m which implies a band separation of 1.0297 $\mu$m. Only this NIR spectrum is available, thus, solely the band minima can be computed for (374851) 2006 VV2.

Comparing the asteroid NIR spectrum with RELAB meteorite database, the best matches are OC/L5 Olivine-Hypersthene meteorite Farmington (ID: MR-MJG-077) Achondrite Ureilite Anomalous Polymict Almahata Sitta #51 chip (ID: MT-PMJ-110), OC H3.4 M-H3.4-2149 (Dhajala H3.4) bulk <125 $\mu$m (ID: DP-JNG-011), OC H5.6 Novosibirsk dark fraction (ID: RS-CMP-049-L), and OC H3.7 ALH85121,11 (H3.7) <45 $\mu$m (ID: MT-PFV-154-A).

### 3.9.6 (399307) 1991 RJ$_2$

(399307) 1991 RJ2, an Amor type near-Earth asteroid, was discovered in September 8, 1991 from Palomar Observatory, California, USA by Helin et al. [1991]. Its companion was discovered in August 27, 2014 by Warner et al. [2015] using lightcurve observations from Palmer Divide Observatory, Colorado Springs, Colorado, USA; PROMPT Telescope, Chile, and Perth Observatory, Australia.

With an absolute magnitude of $H$ = 18.9 [MPC], the primary rotation period is 3.4907 ± 0.0002 h, and the orbital period is 15.917 ± 0.001 h. The estimated diameter of the primary is 0.5 km and the ratio $Ds/Dp$ is > 0.47 ± 0.02. All these data are from Warner et al. [2015].

The NIR spectrum obtained from SMASS (Fig 3.9) shows an spectrum with no features and a positive slope of 0.226212 ± 0.005658 Using `M4AST` Classification tool with $\chi^2$ approach based on Bus-DeMeo taxonomy [DeMeo et al., 2009] the best match is for T type followed by X and Xk types (Fig. 3.5). The reliability of the classification is 80.4%.

Comparing the asteroid NIR spectrum with RELAB meteorite database, the best five matches are for these meteorites: CC/CM2 Migei meteorite (ID: MA-ATB-072), CC/Laser-Irradiated CM Migei 4d 75-125 um meteorite (ID: MA-ATB-065), OC/L6 Pervomaisky meteorite (ID: RS-CMP-064), Sulfide/Troilite Mundrabilla troilite meteorite (ID: MB-CMP-006-P3), and CC/CM2 Murchison meteorite heated at 700C (ID: MB-TXH-064-HD).

### 3.9.7 (399774) 2005 $NB_7$

This asteroid, an Apollo type (PHA), was discovered on July 5, 2005 from Catalina Station, Arizona, USA by the Catalina Sky Survey. Its companion was discovered on April 11, 2008 by Shepard et al. [2008] using radar observations from Arecibo Observatory, Puerto Rico.

With an absolute magnitude of $H$ =18.933 ± 0.545[JPL], the geometric albedo is estimated $p_v$ = 0.2. Primary's rotation period is 3.4883 ± 0.0001 h [Kusnirak et al., 2008], orbital period is 15.267 ± 0.094 h [Vander Haagen, 2008]. The diameter of the primary is 0.5 ± 0.1 km [Shepard et al., 2008] and the ratio $Ds/Dp$ is > 0.32 [Kusnirak et al., 2008]. Somers et al. [2008] already reported this asteroid as Sq in Bus Taxonomy and Gietzen et al. [2012] had already studied a Spex NIR spectrum and classify it as an Sq type in Bus DeMeo scheme.

The NIR spectrum shows clearly an absorption around 0.9 $\mu$m and a slightly shallow absorption around 2$\mu$m. The best match is for Sq type followed by S and Q types (Fig. 3.5). The reliability of the classification is 82.9%. However, the band parameters could not be computed with the tool, by means of a polynomial adjustment we estimate 0.95 $\mu$m for the first minimum.

Comparing the asteroid NIR spectrum with RELAB meteorite database, the best matches are for different type of meteorites: OC/L6 Chateau Renard (L6) <125 $\mu$m pellet irradiated with 5 mJ + 10 mJ + 20 mJ laser (ID: OC-TXH-011-D35), Igneous/Shergottite EETA79001,73 (ID: LM-LAM-007-73), CC/C3 Ungrouped LEW85332,48 (ID: MT-EKT-017), OC/LL6 Appley Bridge (LL6) chip pulse-laser irradiated with 20 mJ x 2 (ID: OC-TXH-012-A40), and OC/L5 Tsarev 15384,3-2 (ID: RS-CMP-065-T).

2005 NB7 has been previously identified as Sq type in Gietzen et al. [2012] with SpeX data using the Modified Gaussian Model [MGM, Sunshine and Pieters, 1993].

### 3.9.8 1994 XD

The NIR spectrum (Fig. 3.5) shows clearly an absorption around 0.9$\mu$m. The best match for this feature is for S type, followed by Cgh and Ch types, which absorption is shallow at that wavelength. The reliability of the classification is 80.4%.

When computing band parameters, the first minimum is prominent at 0.9196±0.0027 $\mu$m, and the second, less noticeable minimum is at 1.7824±0.1305$\mu$m, this implies a band separation of 0.8628$\mu$m,. Only this NIR spectrum is available, thus, solely the band minima can be computed

for 1994 XD.

Comparing the asteroid NIR spectrum with RELAB meteorite database, the best five matches are for these meteorites: OC/H5 Barwise (ID: MR-MJG-036), OC/L3.1 LEW86018,71 (L3.1) <45 $\mu$m (ID: MT-PFV-130-A), OC/L5 M-L5-15 (Aribba) bulk <125 $\mu$m (ID: DP-JNG-017), OC/LL3 Krymka dark powder (ID: RS-CMP-063-D), and OC/L5 Blackwell (ID: MT-HYM-081).

### 3.9.9 2007 $DT_{103}$

The best matches for this spectrum (Fig. 3.5) are for Q, Sq, and S types. From all of these, Q-type matches beautifully. When computing band parameters, the first minimum is prominent at 0.9670 ± 0.0047 $\mu$m, and the second, less noticeable minimum, is at 1.9652 ± 0.0128 $\mu$m, this implies a band separation of 0.9982$\mu$m,

Comparing the asteroid NIR spectrum with RELAB meteorite database, the best fits for the spectrum were for: Laser-Irradiated Ordinary Chondrite Chateau Renard (L6) chip pulse-laser irradiated with 20 mJ x 4 (Sample ID: OC-TXH-011-A80), Achondrite Almahata Sitta #44 125-500 $\mu$m (Sample ID: MT-PMJ-108-B), Ordinary Chondrite Y-74442 (Sample ID: MB-TXH-086-A), Ordinary Chondrite Appley Bridge (LL6) chip pulse-laser irradiated with 20 mJ x 2 (Sample ID: OC-TXH-012-A40), and Ordinary Chondrite Y-74646 (Sample ID: MB-TXH-085-B). From all these meteorites, the best match for a meteorite spectrum is for Almahata Sitta.

This asteroid was already classified as a potential Q-type in DeMeo et al. [2014].

### 3.9.10 (8306) Shoko

From our analysis of this spectrum (Fig. 3.5), Shoko is a Q-type; Sq and S are also proposed, this classification has a reliability of 80.4%. When computing band parameters, the first minimum is at 0.9873±0.0085 $\mu$m, and the second minimum is at 2.0344±0.0078 $\mu$m, this implies a band separation of 1.0471 $\mu$m.

Comparing the asteroid NIR spectrum with RELAB meteorite database, the best fits for the spectra were for ordinary chondrites: Quenggouk (Sample ID: MR-MJG-042), Jelica (Sample ID: MR-MJG-072), Greenwell Springs (Sample ID: TB-TJM-075), Chateau Renard (L6) chip pulse-laser irradiated with 20 mJ energy (Sample ID: OC-TXH-011-A20), and NWA1799 (LL5) <250 $\mu$m (Sample ID: OC-SXS-026-D).

Polishook et al. [2014] classified Shoko as Sq-type using PCA on NIR spectrum obtained at IRTF/SpeX, completing the visible part with BVRI colors. From that analysis Shoko presents a fresh surface.

### 3.9.11 (185851) 2000 $DP_{107}$

Color indices has been measured by Pravec et al. [2000] (U-B): 0.278, (B-V): 0.70, (V-R): 0.388 ± 0.013, (B-R): 1.088 ± 0.019, (V-I): 0.717 and Dandy et al. [2003] (B-V):0.667 ± 0.033 (V-R): 0.405 ± 0.019, (V-I): 0.687 ± 0.024, (V-Z): 0.799 ± 0.056.

The best proposed matches are for Xk, Cg, Cb, Ch, and K types (Fig. 3.5), a classification with a reliability of 80.4%. From inspection, there is an absorption band not considered in X or C types. Thus, the most resemblance is to K type with thermal effect.

Comparing the asteroid NIR spectrum with RELAB meteorite database, the best fits for the spectra are: Carbonaceous Chondrite PCA02012 (Sample ID: PH-D2M-044), Ordinary Chondrite Gorlovka (Sample ID: RS-CMP-048), Ordinary Chondrite Orvinio Clast & Melt (Sample ID: MP-DTB-028-C), Carbonaceous Chondrite MET00426 (Sample ID: PH-D2M-055), and Achondrite Almahata Sitta #4 chip lighter face (Sample ID: MT-PMJ-093). From all these the best match between spectra is for meteorite Gorlovka.

Previous classifications are: C-type from color indices [Pravec et al., 2000, Dandy et al., 2003] and from Yang et al. [2003] X-type based on visible spectrum and albedo.

We concatenate the visible spectrum from Yang et al. [2003] with the NIR spectrum. After performing the match with RELAB database found these samples: Allende 700C (Sample ID: MB-TXH-063-HD), Tsarev >300 um (ground) (Sample ID: MA-ATB-053), Orvinio Clast & Melt (Sample ID: MP-DTB-028-C), DaG 1042,05 <125 um (Sample ID: LM-H1T-052-C), and Abee 700C (Sample ID: MT-TXH-040-D). From these the best match is for Tsarev meteorite.

### 3.9.12 2014 $WZ_{120}$

The NIR spectrum (Fig. 3.5) shows clearly absorptions around 1 $\mu$m and 2$\mu$m. The best match for this features is for Sv type, followed by Sr and S types. The reliability of the classification is 80.4%.

When computing band parameters, the first minimum is prominent at 0.9255 ± 0.0007 $\mu$m, the second minimum is at 1.8468 ± 0.0128$\mu$m, this implies a band separation of 0.9213 $\mu$m. Only this NIR spectrum is available, thus, solely the band minima can be computed.

Comparing the asteroid NIR spectrum with RELAB database, all the best five matches are for ordinary chondrites and all but Lancon meteorite, which is a H6 Olivine-Bronzite, are subtype H5. These are the meteorites: Ehole chip irradiated with pulse laser at 20 mJ energy x 2 (ID: OC-TXH-006-A40), Zhovtnevyi (ID: MR-MJG-041), Allegan (ID: TB-TJM-125), Magombedze (ID: TB-TJM-108), and Lancon (ID: MR-MJG-033).

### 3.9.13 (410777) 2009 FD

The NIR data (Fig. 3.5), although noisy, shows an overall featureless spectrum. The best matches proposed for this spectrum are for the C complex: C, Cb and Cg types (Fig. 3.5). The reliability of the classification is 82.9%.

Comparing the asteroid NIR spectrum with RELAB database, the five best matches are: KLE98300,33 (EH3) <25$\mu$m (ID: MT-PFV-122-B), Y-82162,79 <125 $\mu$m (ID: MB-CMP-019-A), Almahata Sitta #4 chip lighter face (ID: MT-PMJ-093), EET96135,20 (EH4/5) <45$\mu$m (ID: MT-PFV-120-A) and El-Quss Abu Said (CM2) <125$\mu$m (ID: MP-KHO-131-A).

This asteroid is considered as C-type from visible colors in Spoto et al. [2014] .

### 3.9.14 (452561) 2005 AB

This asteroid is classified inside C-complex with a reliability of 80.45%, the most akin to Cb, C, and Xk taxons (Fig. 3.5). The asteroid exhibit a thermal tail toward 2.5$\mu$m which can help us to estimate its geometrical albedo based on thermal excess approach [Rivkin et al., 2005]. Our computation of the thermal excess parameter gives a value of 0.224 ± 0.011. The asteroid was observed at a distance around 1.1 a.u. having a phase angle around 50°. The computed value of geometrical albedo 0.06 ± 0.02, which makes it compatible with low albedo taxons (C, P, T or D).

Comparing the asteroid NIR spectrum with RELAB database, the five best matches are: Almahata Sitta (ID: MT-PMJ-098), Rose City (ID: MR-MJG-079), Abee 900C (ID: MT-TXH-040-F), Y-74659 TXH (ID: MB-TXH-087-C), and Murchison (ID: MH-FPF-052-A). Of all these, the one that resembles more 2005 AB spectrum considering thermal emission, is Rose City meteorite, an ordinary chondrite. This is similar to the comparison made by Fieber-Beyer et al. [2015] of

asteroid 2007 LE.

### 3.9.15 (162000) 1990 OS

The spectrum (Fig. 3.5) is limited to the visible, that wavelength interval already shows the typical S-type curve. We find that the taxonomic types that better fits this spectrum are S, Sv, and L types. The reliability of the classification is 21.9% (low because of the small range considered). Even though, from inspection of this classification, the match that resembles best the spectrum of the asteroid is S type.

Comparing the asteroid visible spectrum with RELAB database, the five best matches are diverse: AC/Angrite Sahara 99555 (ID: TB-TJM-057), Si/Ol ALHA77005 olivine (+ px?) (ID: DD-MDD-009), CC/CV3 Leoville (ID: MR-MJG-120), CC/CK5-6 EET87860,14 (ID: LM-LAM-012), and Iron/IAB Silicate inclusion Campo de Cielo SI (ID: TB-TJM-059). This is understandable due to the limited data range.

### 3.9.16 (66063) 1998 $RO_1$

The best match is for S type -which fits very well the spectrum- followed by Sr and Sv types (Fig. 3.5). The reliability of the classification is 80.4%.

When computing band parameters, the first minimum is at 0.9221 ± 0.0031 $\mu$m, and the second minimum is at 1.8525 ± 0.0229 $\mu$m, this implies a band separation of 0.9304 $\mu$m.

Comparing the asteroid NIR spectrum with RELAB meteorite database, the best fits for the spectra were all for ordinary chondrites: OC/L5 Malakal (Sample ID: TB-TJM-109), OC/L3 Y-74191 (Sample ID: MB-TXH-084-A), OC/L6 Paranaiba (Sample ID: MB-CMP-010-L), OC/L6 Kuttippuram (Sample ID: TB-TJM-098), and OC/L5 Mirzapur (Sample ID: TB-TJM-111).

## 3.10 Discussion

In total, we have now 24 more binaries characterized taxonomically, representing an increase of 21% of known taxonomy classifications in the binary population, obtained with Spex/IRTF. The analysis of all spectra was done with `M4AST` online tool. In this analysis we look at the taxonomy of the asteroids using $\chi^2$ method with Bus-DeMeo taxonomy system [DeMeo et al., 2009] and meteorite analogues using $\chi^2$ method with spectra from RELAB database. Ephemeris circumstances from IRTF telescope allowed us to observe very different taxonomic types of asteroids.

Having now the taxonomies of more binaries, we can look into the amount of each class of binaries among the whole population, to see if we can identify some trend, like which is more abundant (Fig. 3.10). This sample of binary asteroids is dominated by S, X and C type

Table 3.5 – Synthesis of asteroids characterized during this work with no previous taxonomy. These are all small asteroids. In the table are presented: dynamical type (DT), absolute magnitude (H), geometric albedo ($p_v$), diameter in Km (D), previous taxonomy, assigned taxonomy from this work, meteorite class and meteorite analogue. Physical characteristics of the binary asteroids: absolute magnitude, albedo, diameter, previous taxonomical class, this work taxonomical class, suitable meteorite analogue class, and best match analogue.

| Asteroid | DT | $H$ | $p_v$ | $D$ | Prev Tax | Our Tax | Meteorite class |
|---|---|---|---|---|---|---|---|
| (2691) Sersic | IMB | 13.4 | 0.261 ± 0.062 | 5 ± 0.11 | - | Sr | OC/LL4 |
| (4383) Suruga | MB | 12.9 | 0.320 ± 0.038 | 6.33 ± 0.09 | V | V | AC/AHOW |
| (7187) Isobe | HUN | 6.05 ±1.46 | 13.89 | 0.134 ±0.104 | - | K | AC/UAP |
| (8373) Stephengould | MC | 13.8 | - | ~5.29 | - | D | Mixture/10/90 |
| (76818) 2000 RG 79 | HUN | 13.7 | 0.43 | ~3.6 | - | Xe | enstatite chondrite |
| (190208) 2006 AQ | AMO | 18.1 | - | 1.06 | - | K, Cg | Ign/She |
| (348400) 2005 $JF_{21}$ | AMO | 17.1 | ~0.59 | 0.3 | - | V | AC/HED |
| (399307) 1991 $RJ_2$ | AMO | 18.9 | - | ~0.5 | - | T | CC/CM2 |
| 1994 XD | APO | 19.11 | - | 0.6 ± 0.15 | - | S | OC/H5 |
| 2014 $WZ_{120}$ | APO | 20.44 ± 0.36 | - | ~0.3 | - | Sv | OC/H5 |
| (410777) 2009 FD | APO | 22.1 | - | 0.15 | - | C | EC/EH3 |
| (452561) 2005 AB | AMO | 17.5 | 0.03 | >1.9 | - | Xk | OC/H5 |
| (162000) 1990 OS | APO | 19.3 | - | 0.3 ± 0.02 | - | S | AC/Angrite |
| (66063) 1998 $RO_1$ | ATE | 18.1 | 0.14 ±0.06 | 0.8± 0.15 | - | S | OC/L5 |
| (88710) 2001 $SL_9$ | APO | 17.6 | - | ~0.8 | Sr, Q | Sr | OC/LL4 |
| (162483) 2000 $PJ_5$ | ATE | 18.41± 0.05 | 0.2 ± 0.05 | ~0.6 ± 0.1 | O, Q | Q | OC/H4 |
| (374851) 2006 $VV_2$ | APO | 16.6 ± 0.2 | - | 1.06 ± 0.05 | V,S,A Q,T | L, Xe, Ch | OC/L5 |
| (399774) 2005 $NB_7$ | APO | 18.933 ±0.545 | - | 0.5±0.1 | Sq | S Sq, S, Q | OC/L6 |
| 2007 $DT_{103}$ | APO | 19.2 | - | 0.3 | Q | Q, Sq, S | AC/UAP |
| (8306) Shoko | MB | 4.9 | - | 3.21 | Sq | Q Sq S | OC/H4 |
| (185851) 2000 $DP_{107}$ | APO | 18.2 | 0.15 ± 0.065 | 0.8 ± 0.16 | C, X, Sq | K, Xk Cg | OC/H3-4 |
| (153591) 2001 $SN_{263}$ | AMO | 16.861 ± 0.805 | 0.048 ± 0.015 | 2.6 | B | C Cb | AC/Ureillite AP |
| (285263) 1998 $QE_2$ | AMO | 17.07 ± 0.67 | 0.05 ± 0.03 | 3.2 ± 0.3 | Ch | X, T, D | CC/CM2 |
| (481532) 2007 LE | APO | 19.7 | - | 0.5 | S | D | Stony Iron/Pallasite |

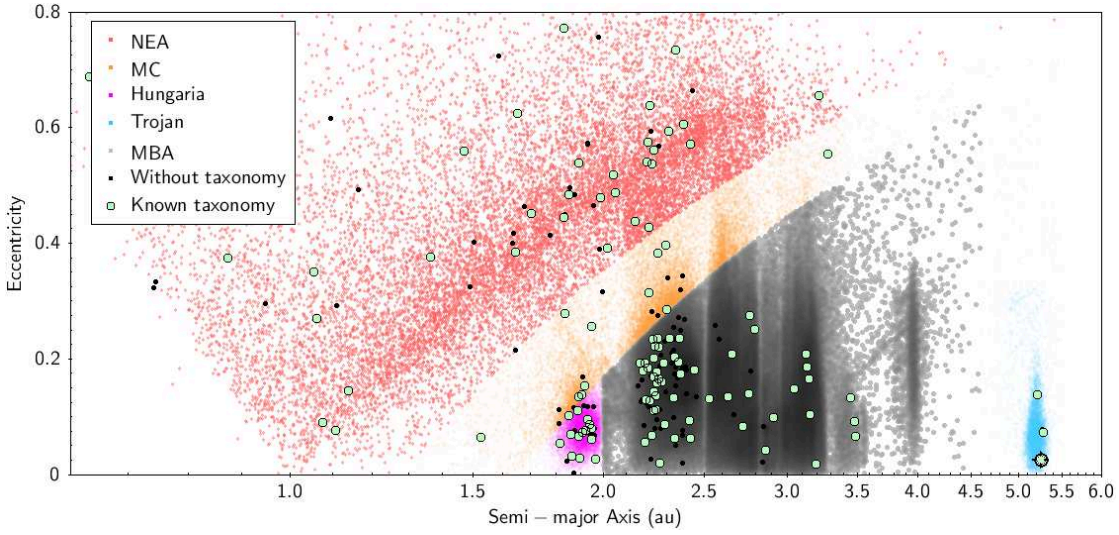


Figure 3.8 – Plot of binaries with known taxonomy (light green dots), and all-binary population (black dots) among the total asteroid population on the background.

as expected considering the binaries we characterized spectroscopically are mainly small asteroids in the near Earth space, Hungaria region, and inner belt.

To determine if a taxonomic class (or several) is prominent among binaries, we compare our sample to the population of near-Earth and Mars-crosser asteroids analyzed by Carry et al. [2016]. These authors indeed showed that the distribution of taxonomic classes was similar among NEAs and inner belt asteroids, in the size range we consider here. We thus compare the taxonomic distribution among binary asteroids with their corresponding background population (Fig. 3.11).

The distribution is flat for most classes but A, Q, and X. Asteroids belonging to the A class are scarce in both the inner belt space and main belt. These results are thus based on very low number statistics. The estimation of the uncertainty is still ongoing but we deem that this over representation of A type among binaries is an artifact and not significant.

Similarly, the over representation of X types is likely a selection effect. Indeed, a significant fraction of binary asteroids are located among Hungarias because they were discovered by B. Warner's observing program dedicated to Hungarias. Photometric and spectroscopic surveys showed X type to be dominant among Hungarias [e.g., Gradie and Tedesco, 1982, Bell et al., 1989, DeMeo and Carry, 2013, Cañada-Assandri et al., 2015]. Moreover, the spectra of X types are mostly featureless, and noisy spectra of low contrast classes such as K or L types that could be misclassified as X types, artificially increasing the representation of X types.

By contrast, the fraction of Q types, 2.5 times more frequent than S types seems real. Finding a high fraction of Q types among small binaries was even to be expected. The most likely formation mechanism of these binaries is indeed rotational fission induced by YORP spin-up [Fig. 1.7, Walsh et al., 2008, Pravec et al., 2010, Walsh and Jacobson, 2015].

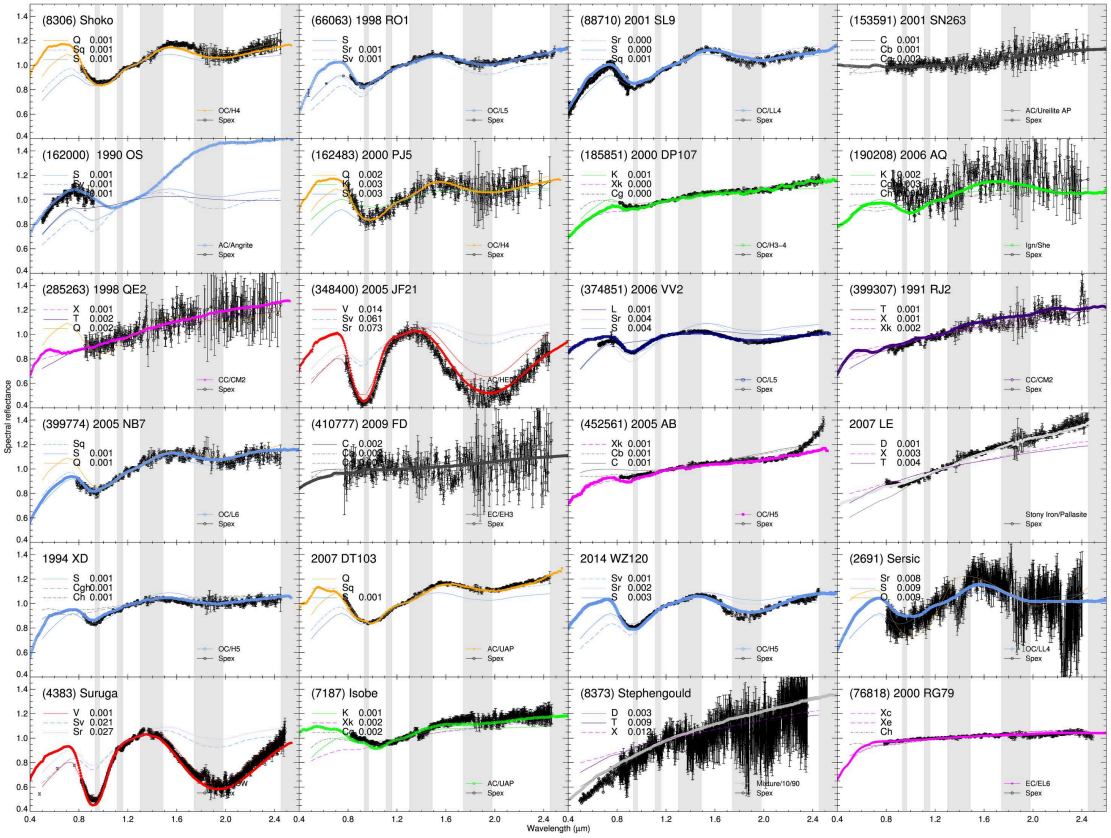


Figure 3.9 – Spectra of all SMASS binaries worked in this thesis.

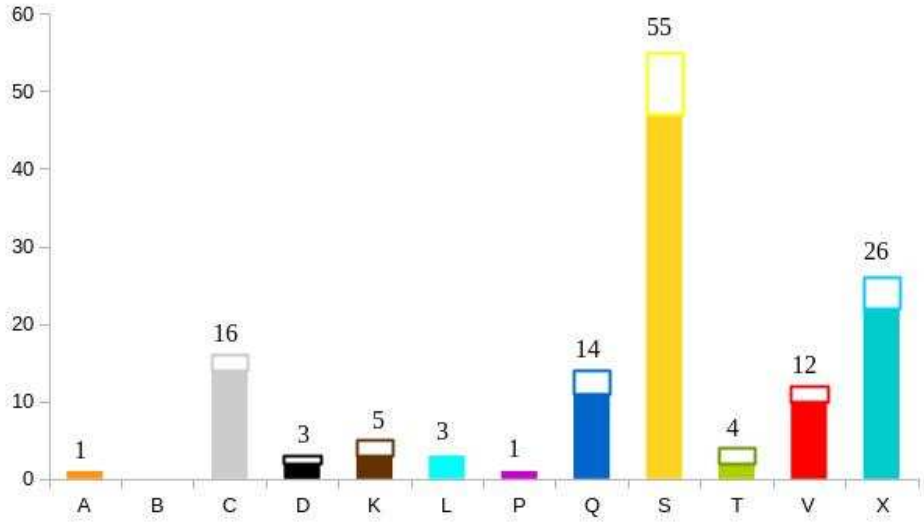


Figure 3.10 – Distribution of taxonomic classes among binary asteroids. Open bars correspond to the new classifications done within this PhD.

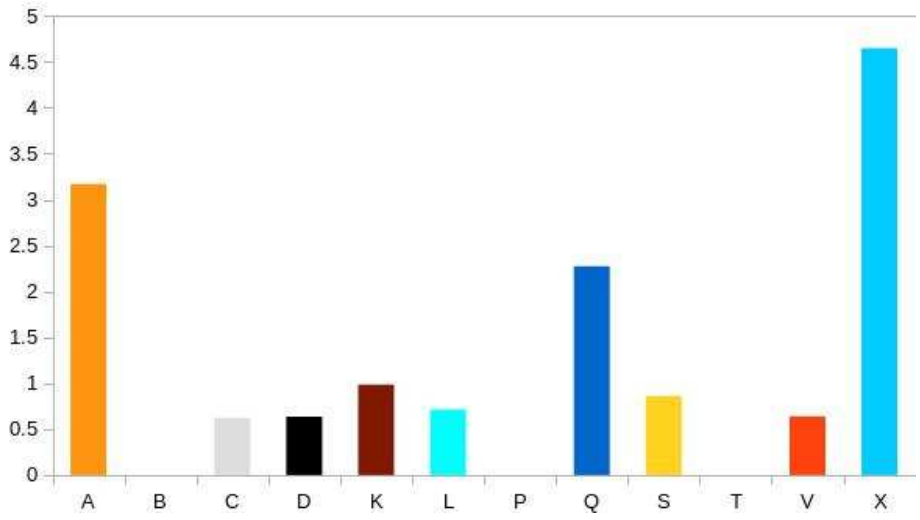


Figure 3.11 – Ratio of the distributions of taxonomic classes among binaries over the background population [Taken from Carry et al., 2016]. Excess of A and X types are deemed spurious (see text), but that of Q/S appears genuine.

# 4 A new taxonomy based on NIR photometry

## 4.1 Rationale for a taxonomy based on NIR colors

### 4.1.1 Introduction

The way a bright source is detected depends on the detector, the natural one for us humans is the retina in our eyes, which is more sensitive to certain wavelengths than others, and varies among different individuals. The same happens with silver emulsions, CCDs and so on. In other words, the magnitude of a bright object depends on the detector. For this reason, we must indicate how the detection was made. The way to quantify a color of a star or an asteroid is by the difference between the magnitudes of the object in two specific wavelengths; this is know as a *Color index* or *Color* for short.

The first indications that asteroids were geologically diverse came from photometric measurements in the 1920s, with the discovery of color differences among asteroids. Bobrovnikoff [1929] found that Ceres was bluer than Vesta, which means that Ceres was reflecting more high-energy radiation than Vesta.

By the beginning of the 1970's the measurement of spectral reflectivity of asteroids with higher resolution became possible, this technique is called spectrophotometry. Observations of the surfaces of asteroids indicated a wide variety of compositional types. [McCord et al., 1970] [McCord and Chapman, 1975a,b]. Little by little, the wavelength ranges were widening.

Spectroscopy became a better technique once CCDs became available, replacing photographic plates. With reflectance spectroscopy, the ratio of reflected sunlight to incident sunlight is determined as a function of wavelength. This is the most widely applied asteroid characterization technique. One advantage is that spectroscopy does not require photometric conditions, as spectrophotometry.

Colors can be considered as super low resolution spectrum. The interesting part is that it has a higher $SNR$ for much shorter integration time, the drawback is precisely, the low resolution $R_\lambda = \lambda/\Delta\lambda$ ($\Delta\lambda$ is the spectral resolution).

### 4.1.2 Large surveys as data sources

Although asteroid taxonomy alone is not sufficient to make meaningful mineralogical inferences, the analysis of the classes distribution in the main belt can help to highlight regions and objects that deserve further investigation for, by instance, do target selection and statistical studies.

Several efforts have been made to understand the composition of the main belt of asteroids with the aims to have insights on the formation and evolution of the Solar System [Chapman et al., 1975, Gradie and Tedesco, 1982, Bus, 1999, Bus and Binzel, 2002, Mothé-Diniz et al., 2003]. The most recent publications presented a bias-corrected color-based taxonomy of asteroids in SDSS data to study the distribution of material in the asteroid belt according to mass, rather than number, to more accurately represent the total material in the belt [DeMeo and Carry, 2013, 2014].

The usefulness of a taxonomic scheme is proportional to the number of objects it potentially can classify. Currently are known more than 700,000 asteroids, and a million or so asteroids greater than 1 km are expected to exist in the belt according to Bottke et al. [2005]. Because several surveys detecting asteroids increase steadily the number of discovered asteroids, it is urgent to continue with this efforts in classifying asteroids.

The advantage of developing taxonomies from large photometric surveys, is that they can provide observations for much more objects than what can be obtained from spectroscopy and dedicated observing programs.

One of the large surveys that provided colors of asteroids is the Eight-Color Asteroid Survey (ECAS) Zellner et al. [1985] that obtained visible reflection spectra for 589 asteroids. In the case of spectroscopic surveys there are: the Small Main-Belt Spectroscopic Survey (SMASS) [Xu et al., 1995, Bus, 1999, Burbine and Binzel, 2002, Bus and Binzel, 2002] which measured visible spectra for 1447 asteroids; the Small Solar System Objects Spectroscopic Survey, or $S^3OS^2$ [Lazzaro et al., 1997, 2004] that observed 820 asteroids. All these information led to a better understanding of minor planets. However, the results of these dedicated surveys are heavily biased towards the closest, largest, and brightest asteroids, distorting our overall picture of the asteroid belt.

In the case of large, non dedicated minor body surveys, asteroids are eventually registered in the field of view, so in order to identify the contaminators of the desired targets (stars, galaxies, extragalactic objects) it is important to discriminate the *moving objects*. Thus, as part of large surveys, we can have asteroid data as a by-product.

This is the case of the *Sloan Digital Sky Survey* (SDSS) primarily designed for observations of extragalactic objects, with the SDSS Moving Object Catalog made by [Ivezić et al., 2002], that identified over 100,000 unique asteroids in five photometric bands over visible wavelengths.

Most recently, the *Visible and Infrared Survey Telescope for Astronomy* (VISTA), a 4m wide field

survey telescope at Paranal Observatory. VISTA is equipped with the biggest near-infrared imaging camera (VIRCAM) operating at the 0.8-2.3$\mu$m [Sutherland et al., 2015], and among other surveys, is conducting the VISTA Hemisphere Survey (VHS[1]), currently being the largest survey conducted by the VISTA telescope. In this case, Popescu et al. [2016] developed a dedicated pipeline and a catalog of moving objects called MOVIS (Moving Objects VISTA Survey) to identify Solar System objects. In their article, Popescu et al. [2016] identified already the clustering of asteroids in color-color space, and Licandro et al. [2017] have studied the V-type candidates in MOVIS catalog.

### 4.1.3 Motivation

We attempt to derive a new classification scheme for VISTA/VHS asteroid colors that is compatible with previous taxonomies based on spectroscopic data, mainly with Bus-DeMeo et al. [2009], which includes visible and NIR spectra, a range that covers important features to discriminate among taxonomic classes. Like previously made by Carvano et al. [2010] and DeMeo and Carry [2013] with SDSS visible data; but in the case of VISTA, taking advantage that in this survey we have NIR photometry, which allows to break degeneracy among taxonomic classes, in particular among silicate rich composition (S-complex). As an example, in Fig. 4.1 the average spectra for four classes are displayed, very similar if we look only the visible part of the spectra, and definitely different if we add the NIR wavelengths.

It is reasonable to define the class boundaries in a non- supervised classification (e.g. using PCA or hierarchical clustering) in order not to bias by human intervention the classification of a large data set like MOVIS. But although incomplete, our best knowledge about asteroid mineralogy comes from relating asteroid spectral taxonomic classes to meteorite spectral classes -which are samples of asteroids, thoroughly studied in laboratories- we found it is most consistent to study MOVIS low resolution data with Bus-DeMeo et al. [2009] taxonomy -the current standard- which in turn has been developed using PCA and was developed striving to be consistent with previous classifications, being an extension of the Bus asteroid taxonomy into the near-infrared. Thus, we can put MOVIS results in context with the findings from decades of research.

## 4.2 Definition of a new taxonomic scheme for NIR colors

### 4.2.1 Method

The methodology is based on the large database VISTA/VHS. We derived templates of the main taxonomic classes according to DeMeo et al. [2009] taxonomy, and use them to classify the asteroid observations.

VHS obtain images of the entire southern hemisphere using four filters in the NIR region: $Y$, $J$,

[1] http://www.vista-vhs.org/

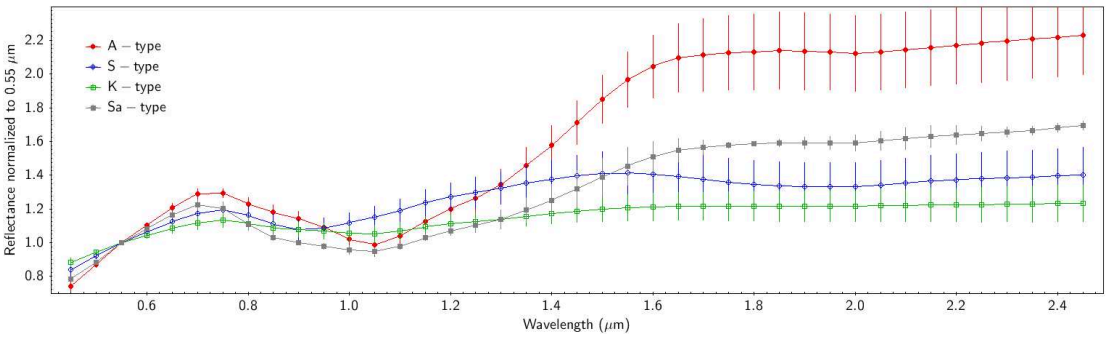


Figure 4.1 – Reflectance spectra of some degeneracy classes with error barrs. Based on visible wavelengths only, A, S, K and Sa classes can hardly be distinguished. When added the NIR part of the spectra, the classes can be discriminated.

$H$ and $Ks$ [Cross et al., 2012]. The band centers of these filters are located at 1.02, 1.25, 1.65 and 2.15 $\mu$m respectively (Fig. 2.18) Similarly as with SDSS, this filter set was designed for minimum superposition, and together cover a wide part of the spectral interval from 0.8 to 2.7 $\mu$m, an important range to detect diagnostic features in asteroids (Fig. 2.18). In particular, the 1 and 2 $\mu$m absorption band, diagnostic of olivine and pyroxenes assemblages, which is the prime separator of taxonomy since the earliest taxonomies in the 1970s [Chapman et al., 1975, Bowell et al., 1978].

### 4.2.2 Data retrieval

Data was collected from MOVIS catalog [Popescu et al., 2016] available online[2] in three catalogues: MOVIS-D (detections catalog), MOVIS-M (magnitudes catalog), and MOVIS-C (colors catalog). We only use MOVIS-C in this work. It has the colors for a total of 39,947 Solar System objects, in which the majority corresponds to asteroids. It includes 52 NEAs, 325 Mars Crossers, 515 Hungaria asteroids, 38,428 main-belt asteroids, 146 Cybele asteroids, 147 Hilda asteroids, 270 Trojans, 13 comets, 12 Kuiper Belt objects and Neptune with four of its satellites.

To ensure the quality of data, we remove observations that seemed unreliable (the catalog has flags relevant to photometry). We do not consider objects that were detected only with one filter. After the selection criteria we kept 7,579 asteroids out of 34,991 objects. We apply cuts in the photometry selecting error in magnitude < 0.05. From initial inspection we saw that the majority of the data was in $J$,$H$, and $K$ filters.

We define subsets based on the distribution on color uncertainty and construct cumulative normalized histograms to define the limits of the valid sample (Fig. 4.2). This is something empiric and chosen from the linearity of the histogram, its a trade-off between a large sample and a high $SNR$ required for taxonomic classification. The maximum uncertainty defined

[2] http://cdsarc.u-strasbg.fr/viz-bin/Cat

from all histograms are: $Y-H=0.10$, $Y-J=0.075$, $Y-Ks=0.125$, $J-H=0.125$, $J-Ks=0.15$, $H-Ks=0.15$.

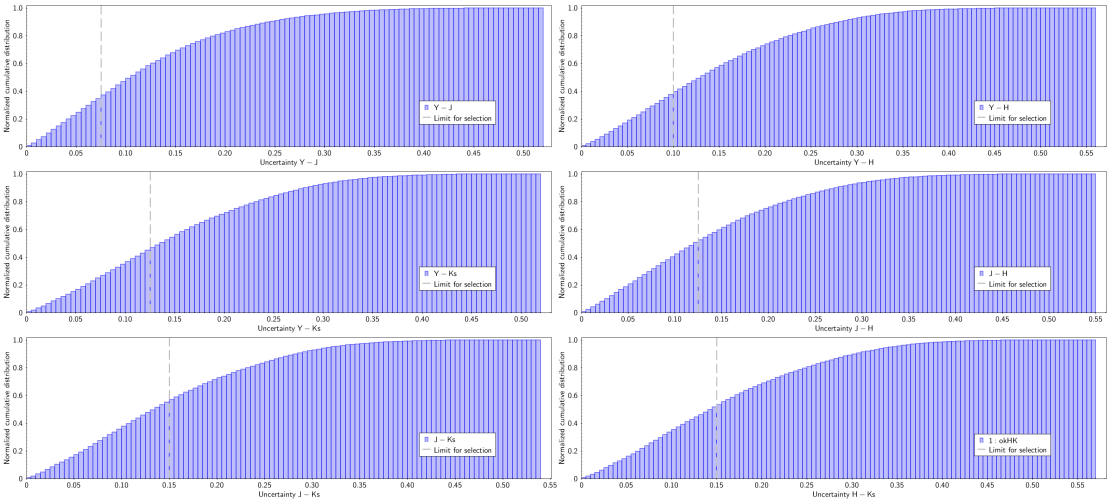


Figure 4.2 – Cumulative normalized histogram in $Y-J$, $Y-H$, $Y-Ks$, $J-H$, $J-Ks$, and $H-Ks$ colors. Vertical line in each histogram is the maximum allowed uncertainty, that define the valid sample.

The catalog does not have images in all the filters. We use always the maximum number of available colors. The degrees of freedom $Dof$ are the total number of filters used -1. We have a maximum of 4 filters with different number of colors: 3, or 2 or 1.

### 4.2.3 Learning sample

We construct a learning sample using Bus-DeMeo et al. [2009] taxonomy with the VNIR reflectance spectra of the 371 asteroids that were used to create the Bus-DeMeo taxonomy, and convert it to VISTA colors. For this, we take Bus-DeMeo reflectance and multiply it with the VISTA filter transmission curves (Fig. 2.18), and take the integral, obtaining their fluxes and errors on flux. In this way we obtain colors for all the pair of filters: $Y-J$, $Y-H$, $Y-Ks$, $J-H$, $J-Ks$, $H-Ks$ in reflectance. But because with MOVIS we have colors, not reflectance, we have to add the colors of the Sun, somehow following the reversed path described in Fig.2.20.

$$F_1 - F_2 = -2.5log\left(\frac{f_1}{f_2}\right) + (F_1 - F_2)_\odot \tag{4.1}$$

where $F_1$ and $F_2$ are magnitudes in two filters, $(F_1-F_2)_\odot$, is the color of the Sun with this pair of filters, and $f_1$, $f_2$ are the fluxes in each filter. The reflectance is the spectrum divided by the spectrum of the Sun (reflectance = spectrum/spectrum$_\odot$).

Similar studies [Carvano et al., 2010, DeMeo and Carry, 2013] using SDSS data took solar colors from Holmberg et al. [2006], who derived color estimates for the Sun in 2MASS and other photometric systems (Johnson–Cousins, Tycho, Strömgren, and SDSS) but not VISTA, besides, they did not consider the $Y$ filter.

To determine the colors of the Sun in VISTA photometric system, we used the advantages that offers the Virtual Observatory (VO) (Sec. 2.2.8). We made a TAP[3] query on VISTA survey catalogue archive for 1500 stars that have similar colors to the Sun (within ±0.1 magnitude from Holmberg et al. [2006] Solar color values).

Then, with VOSED[4] [Solano et al., 2007] of the SVO[5] we retrieved the photometry of these stars from many surveys (SDSS, 2MASS, Herschel, Hipparcos, etc.) and using VOSA (SED Analyzer, Bayo et al. [2008]) adjusted a synthetic stellar model called `NextGen` [Kurucz, 1979, Allard et al., 1997, Baraffe et al., 1997, 1998, Hauschildt et al., 1999] on the photometry; obtaining effective temperature $T_{\rm eff}$, metallicity, and gravity ($\log g$). After that, we select 330 solar twins (stars with same parameters as the sun). But as mentioned before, these stars are in VHS survey, we already had their colors, so we could made histograms for all of them: $Y-J$, $Y-H$, $Y-Ks$, $J-H$, $J-Ks$, $H-Ks$, adjust a gaussian curve and determine mean value and uncertainty ($\mu \pm \sigma$) for each color (Fig. 4.3, Table 4.1). This innovative simple and powerful method can be used to obtain the colors of the Sun for any other photometric system.

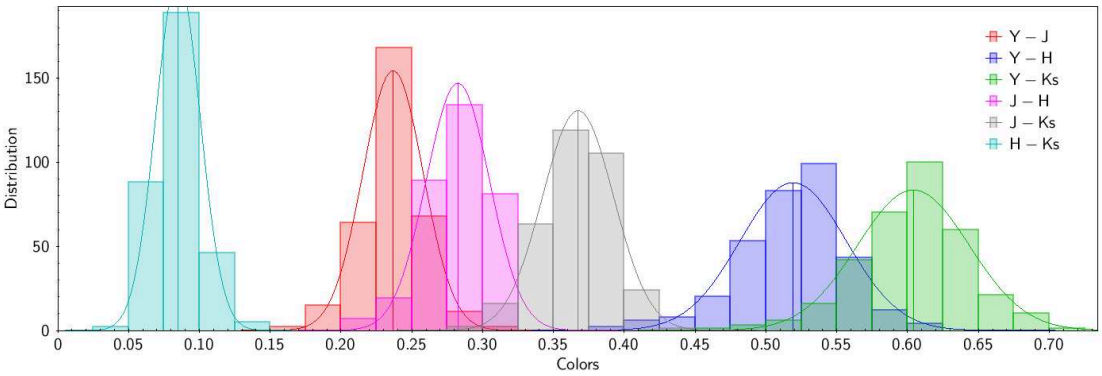


Figure 4.3 – Histograms of 330 solar twins used to obtain the colors of the Sun for the learning sample based on colors from DeMeo taxonomy. Gaussian distributions are adjusted for each color histogram: $Y-J$, $Y-H$, $Y-Ks$, $J-H$, $J-Ks$, $H-Ks$, from that we determine mean value and uncertainty ($\mu \pm \sigma$, Table 4.1).

Once the data parameterization is defined, we proceed with the classification. At the beginning we attempt to use Principal component analysis, but we found that the classification could be achieved in color-color plots using the steps I will describe next.

[3] Table Access Protocol

[4] a Virtual Observatory tool to build and analyze SEDs (Spectral Energy Distributions) developed in the framework of the Spanish VO

[5] Spanish Virtual Observatory, http://sdc.cab.inta-csic.es/vosed/

Table 4.1 – Median $\mu$ and error $\sigma$ values for the colors of the Sun obtained of 330 solar twins observed by VISTA (see text, Fig. 4.3).

| Color | $\mu$ | $\sigma$ |
|---|---|---|
| Y-J | 0.2324 | 0.0163 |
| Y-H | 0.5190 | 0.0314 |
| Y-Ks | 0.6015 | 0.0330 |
| J-H | 0.2835 | 0.0216 |
| J-Ks | 0.3651 | 0.0234 |
| H-Ks | 0.0783 | 0.0150 |

Because from MOVIS we have colors, that means that we have low resolution spectra, and the Bus–DeMeo taxonomy that we use as standard and the learning sample that we are constructing comes from Bus-DeMeo et al. [2009] taxonomy, developed from Visible and NIR spectra, so subtle details are lost. For this reason, instead of considering the 24 classes of Bus-DeMeo et al. [2009], we combine certain of them into their complex: C-, Cb-, Cg-, Cgh-, and Ch- types into C-complex; S-, Sa-, Sq-, Sr-, and Sv- types into S-complex; and X-, Xc-, Xe-, Xk- into X-complex. The classes that are maintained individually are A, B, D, L, K, Q, T, and V. We do not classify the particularly rare R- or O-type defined on a single object each. The list of classes considered in this work is thus: A, B, C, D, K, L, Q, S, T, V, X.

### 4.2.4 Taxonomy scheme

We perform clustering analysis by measuring *distance*[6] to define a metric for the taxonomy scheme. For each class and color combination, we compute the average color, the dispersion, the correlation, and the covariance. Then, in color-color space, we define ellipses with mean values of DeMeo classes as centers of coordinates, ellipse orientations angle $\theta$ are determined by the computed covariance. This maximizes the region that encompasses objects of the same class. Uncertainties $\sigma$ are semimajor and semiminor axis with inclinations (Fig. 4.4), thus the ellipses are tweaked and the clustering of the objects maximized. In this way, we classify the objects by their distance $\mu$ and uncertainties $\sigma$ to all the class centers, and the spread of the class, taking into account correlations between colors.

[6] in color-color space

## 4.3 Spectral classification of asteroids serendipitously observed by VISTA

### 4.3.1 Classification

The probabilities for each object to be in a taxonomic group is defined from its distance to a class center in color-color plots.

$$x' = \frac{xcos\theta - ysin\theta}{\sigma_x} \qquad y' = \frac{xsin\theta + ycos\theta}{\sigma_y} \qquad D = \sqrt{\chi^2} = \sqrt{x'^2 + y'^2} \tag{4.2}$$

Where $x$ and $y$ are any pair of filters, $D = \sqrt{\chi^2}$, is the distance in color-color dimension,

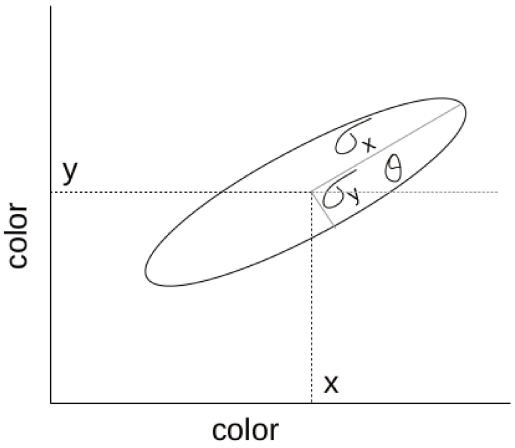


Figure 4.4 – Definition of cluster for classification in color-color space

We compute the cumulative distribution function (CDF) for the $\chi^2$ that corresponds to a gaussian distribution obtained with $Dof$ degrees of freedom, and compute the probability $\mathscr{P}$ that in the $\chi^2$ distribution $\mathscr{P}(x \leq \chi^2)$ , with the integral under the gaussian distribution. Thus, the probability for an object at a given distance of the class, is the integral under the gaussian at this distance.

The classification is represented with a letter assigned for the class, associated with a probability. (Fig. 4.5). If an observation cannot be assigned to any class, it is labeled as unclassified ("U").

The best classification for the object is chosen as the one which have at least 50% probability for all possible classes. In case of lower probability we are not assigning classes for the moment, this is still a work in progress.

Using this tool, I inject the selected MOVIS objects and obtain the following plots in figures (4.5, 4.6), where the clustering of the different classes is remarkable.

When we have only one color (one dimension), we inspect how near to the ends it is, checking for the probability values. If it is in the middle of two classes (50% probability) it cannot be classified. But if it is close to one of the sides -depending of that probability- we can assign a taxonomy (Table 4.2).

Table 4.2 – Assigned taxonomy in case of only one color.

| Color | Inferior | Superior |
|---|---|---|
| $Y-J$ | $<0.25 \rightarrow$ B | $>0.60 \rightarrow$ V |
| $Y-H$ | $<0.45 \rightarrow$ B | $>1.15 \rightarrow$ A |
| $Y-Ks$ | $<0.5 \rightarrow$ B | $>1.30 \rightarrow$ A |
| $J-H$ | $<0.20 \rightarrow$ V | $>0.65 \rightarrow$ A |
| $J-Ks$ | $<0.17 \rightarrow$ V | $>0.80 \rightarrow$ A |
| $H-Ks$ | $>$ -0.03 $\rightarrow$ V | $>0.20 \rightarrow$ D |

### 4.3.2 Validation

In order to asses the quality of the classification scheme, I check the level of success in the taxonomic classification for each class. For this, I follow two paths:

1. I inject DeMeo et al. [2009] objects into the tool.Thus, I am using the learning sample to compare and explore how good the classification tool is. The output is shown in Fig. 4.7 and the fraction of valid classification in Fig. 4.8. As can be seen, there is a very good match for A, B, D and V classes. A and B classes are the most separate groups in color-color space, it is easy to identify them. Also, D and V classes are easily recognizable. In the case of C-complex, it is ~70% positively classified with a slight overlap with X-complex, the K-type overlaps with L and S types, and correspondingly some L types overlaps with K and S types. In case of Q types that are similar to S types, there is also overlap. For the S-type, there is some overlap with Q-type (they have similar spectra differencing mainly by spectral slope) and in less amount with L type. Finally, in the X-complex there is some overlap with C-type asteroids. In the case of T types, the match is not good. That could be because the tool does not work very well discriminating this spectrally featureless class located between the X and D-type in slope. But it is important to take into account that there are only 4 T- type asteroids out of 371 in DeMeo et al. [2009] sample.

2. The other way to check this tool is comparing VISTA results with other sources with known taxonomy. The check I have done was with SDSS objects from DeMeo and Carry [2013] but of course the idea is to compare with all source of taxonomy. This is done as a controlled test: I know the objects that I am injecting in the scheme, and I look

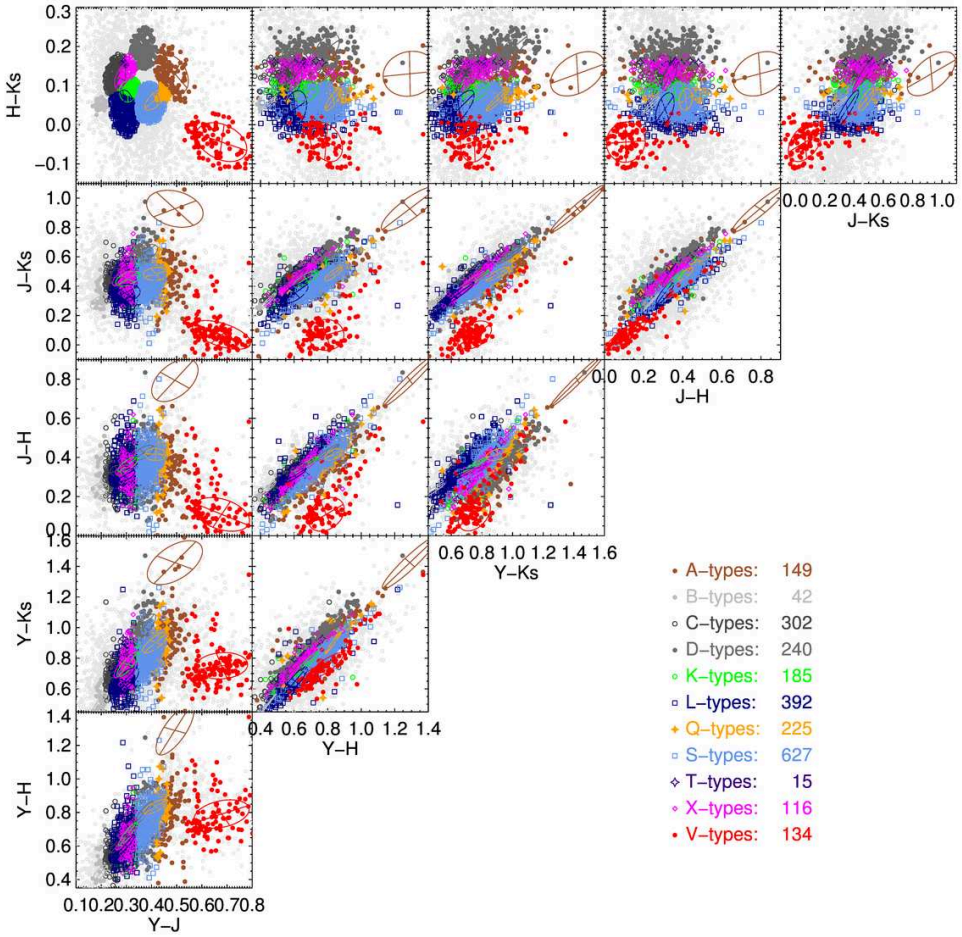


Figure 4.5 – Result of my classification for 2,427 asteroids from VISTA MOVIS catalog [Popescu et al., 2016], displayed in all 15 color-color pair.

for cross-match inspecting how coherent is the proposed scheme. MOVIS classified asteroids in SDSS space is shown in Fig. 4.9. The match is good overall. C-, S-, and V-types are clustered and K- and L- types seems more degenerate. But as good as DeMeo and Carry [2013] work can be, we cannot suppose their others results are 100% accurate. And most important: we have to keep in mind these are different wavelength ranges, SDSS is visible, VISTA is near infrared. With NIR wavelengths the discrimination of classes should be more complete due to the diagnostic features present in this range for several taxonomic classes, especially K,L and S types.

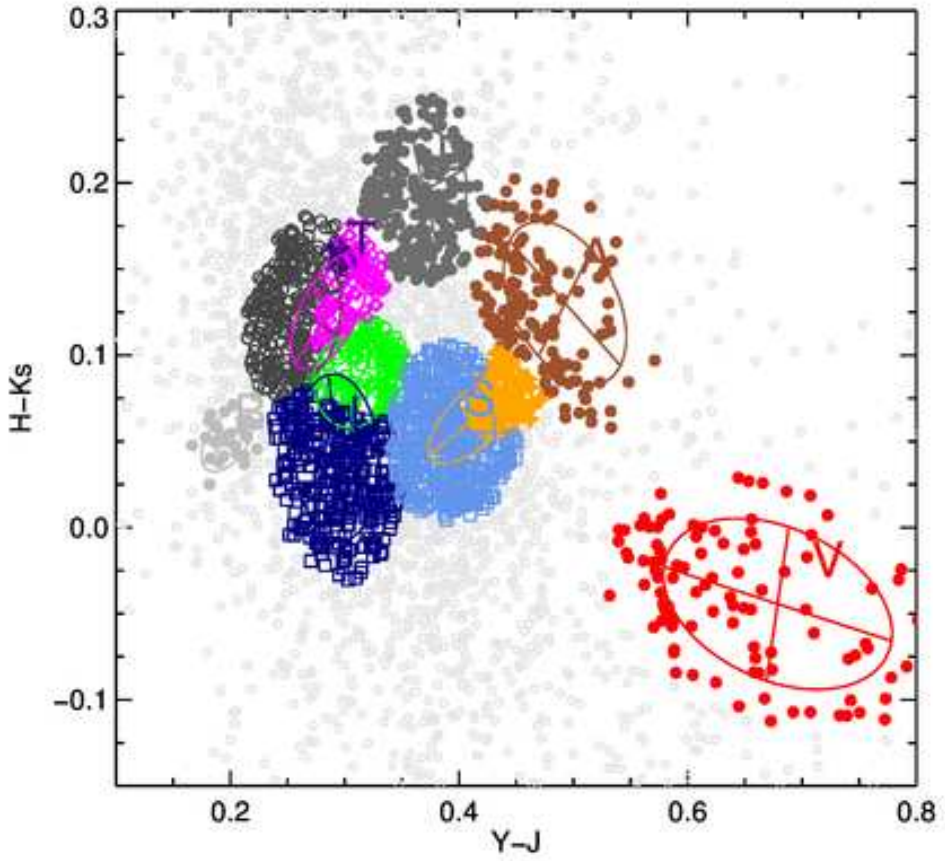


Figure 4.6 – Similar to Fig. 4.5 but for J-Ks vs H-Ks only. Classification cluster around class centers defined from DeMeo et al. [2009] spectra. Asteroids without taxonomy ("U") are displayed as light grey dots in the background.

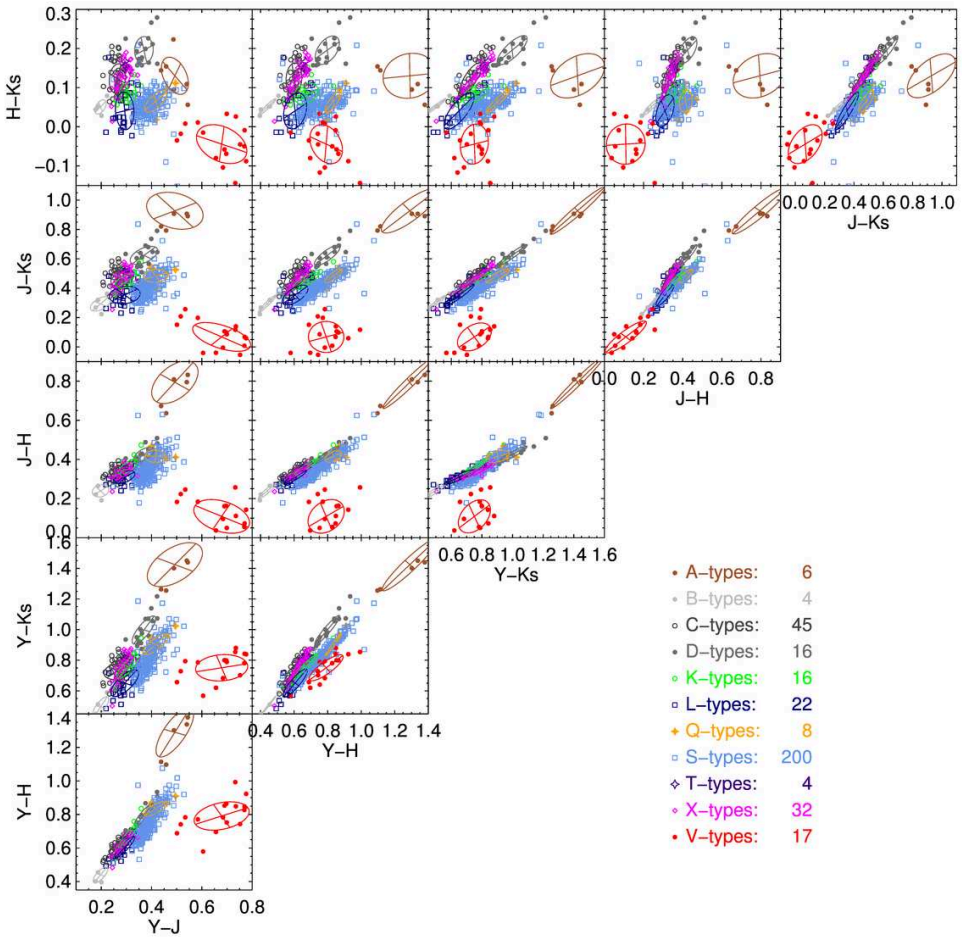


Figure 4.7 – Similar to Fig. 4.5 but using the Bus-DeMeo et al. [2009] 371 asteroid colors as input sample to check the reliability of the classification method.

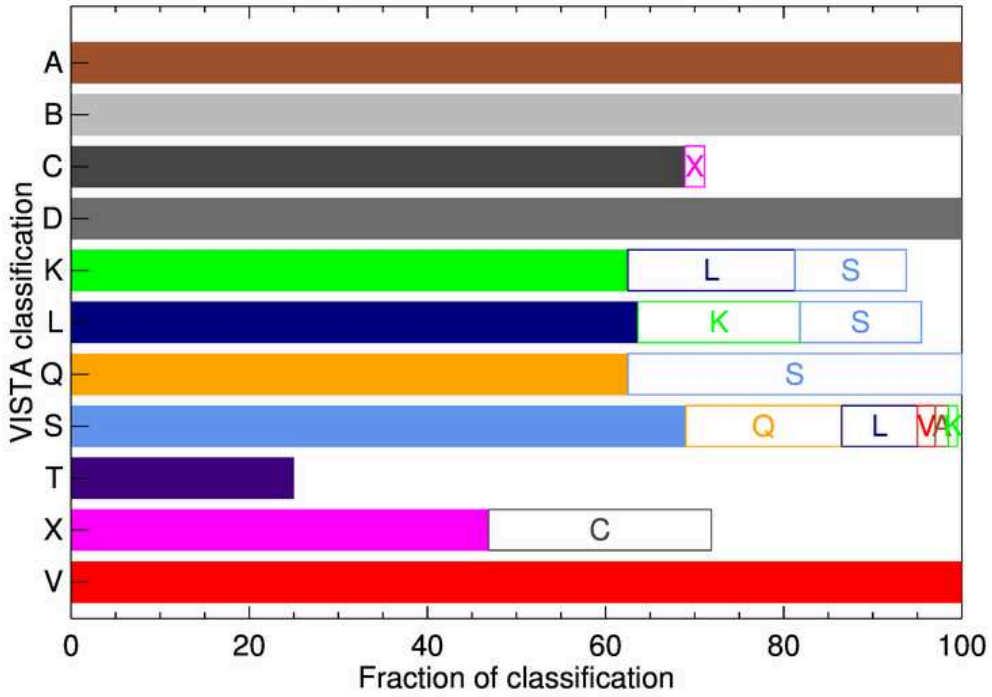


Figure 4.8 – VISTA vs. DeMeo valid fraction of classification. For each class assigned based on VISTA photometry (y-axis) we compute the fraction of appropriate classes (x-axis): solid bar represents correct taxonomical classification taxonomy; open bar represents compatible classification, meaning that the spectral class errors allow to classify in several classes that have similar spectra; remaining space represents incompatible classification, meaning that the spectral class errors are big enough to propose spectral types that are very different. Classification for A, B, D, V classes is successful. On the contrary, T has a poor validation which is natural due to low statistics for this class. The remaining classes presents positive and compatible classifications as well.

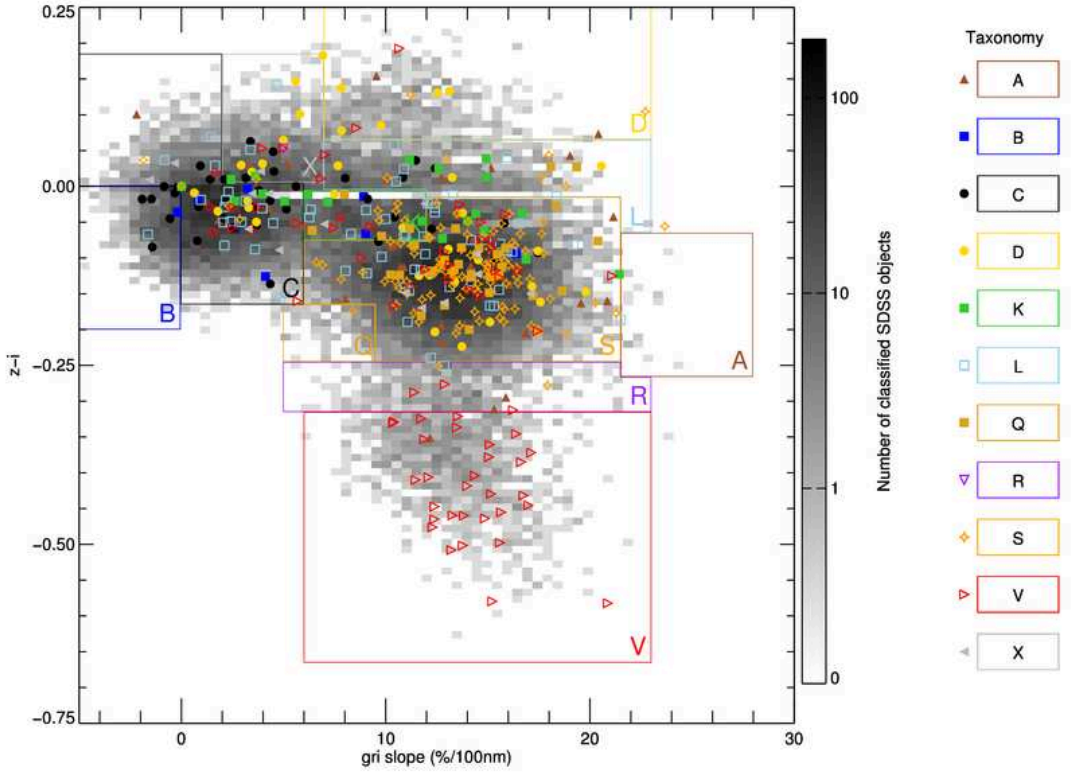


Figure 4.9 – MOVIS-VISTA classified asteroids in SDSS space. This is the match between SDSS and VISTA taxonomies. The colored points are VISTA objects and the rectangles the boundaries for each class defined in DeMeo and Carry [2013].

### 4.3.3 Results

My results are mostly quantitative, improving the statistics in asteroid taxonomy (Fig. 4.5, Fig. 4.6). The number of classified asteroids depends on the threshold on uncertainty used to select the sample.

With this tool, I classified 2,427 asteroids out of 7,579 from MOVIS catalog. The unambiguous classification is the following: A-types are 149, B-types are 42, C-types are 302, D-types are 240, K-types are 185, L-types are 392, Q-types are 225, S-types are 627, T-types are 15, V-types are 134, and X-types are 116. All the other asteroids are assigned a "U" class because we could not assign a class type.

From positive classification, the classes in the total of the sample are: 6% A-types , 1.7% are B-types, 12% are C-types, 10% are D-types, 7.6% are K-types, 16% are L-types, 9% are Q-types, 26% are S-types, 0.6% are T-types, 6% are V-types, and 5% are X-types.

As one would expect, there is a high fraction of S-complex objects. This is consistent with SDSS results [Ivezić et al., 2002, DeMeo and Carry, 2013]. S-type dominates in the Inner Main Belt,

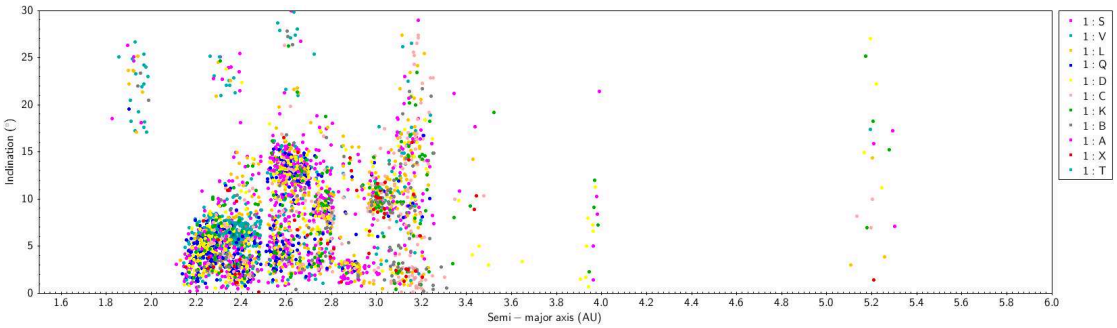


Figure 4.10 – Plot of classified asteroids with VISTA in semimajor axis-vs inclination space.

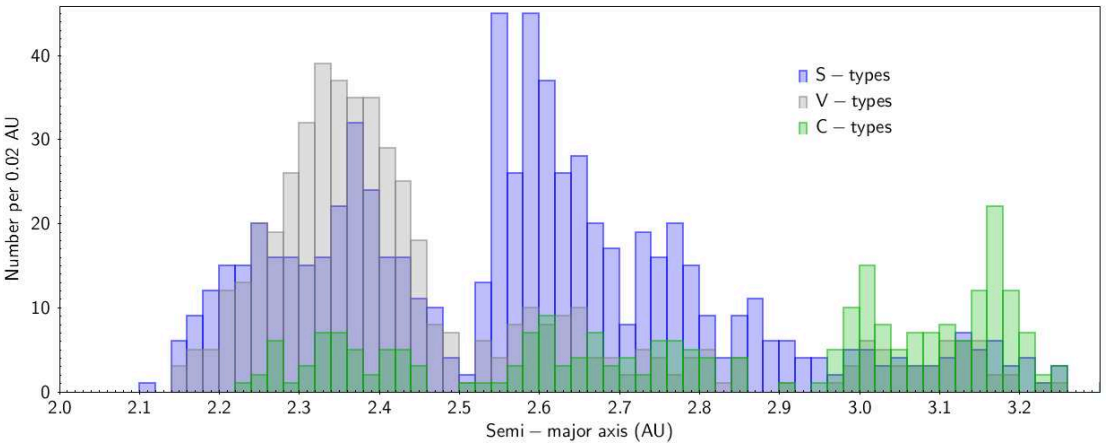


Figure 4.11 – Histogram of the relative distribution of 3 asteroid types (S, V, C) by number, obtained with our taxonomy scheme using MOVIS-VHS objects. It shows a similar trend as the presented in Gradie and Tedesco [1982], in particular the trade off between dominant S in the inner belt and C in the outer belt, and Vesta family in the inner belt.

thus, there are some observing biases: because they are closer to Earth, it is easier to detect them, consequently, smaller asteroids can be detected. S-types are more easily detected also due to their high albedo of ~0.20 [Carvano et al., 2010, DeMeo and Carry, 2013]. This is also consistent with the size-frequency distribution of smaller asteroids [Jedicke et al., 2002].

All the results presented now are preliminary and not bias-corrected. When all the classes found are represented in a plot in the space semi-major-axis vs inclination (Figs. 4.10, 4.11) we found the distribution as in Gradie and Tedesco [1982], which is comforting, and a way to validate our method. We can say that our results are consistent with decades of research (Fig. 4.12) and that we have very promising results.

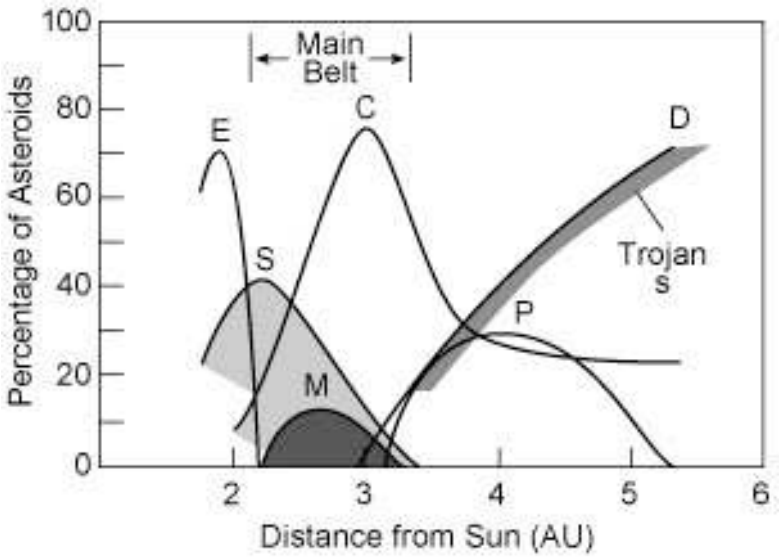


Figure 4.12 – Distribution of compositional types among the asteroids in the asteroid belt, it varies systematically with heliocentric distance, image adapted from Gradie and Tedesco [1982].

### 4.3.4 Conclusions

Taxonomy is the first step to understand the distribution of bodies in the main belt of asteroids, with the aims to have insights on the formation and evolution of the Solar System. Several efforts have been made in the past from spectroscopic studies and from large photometric data analysis but in the visible only, e.g. SDSS, (and in the next future, Gaia when it release data). Now with VISTA, UKIDSS[7], and upcoming ESA Euclid[8]. We have also photometric data of asteroids in the near IR.

Here we have developed a near infrared taxonomic scheme that is compatible with the Bus-DeMeo et al. [2009] taxonomy -the current standard- based in NIR photometry using VISTA colors of asteroids. Our scheme was constructed from a template obtained from Bus-DeMeo et al. [2009] taxonomy. The classification has been validated with asteroids with known taxonomy.

We confirm a trend seen in previous works with taxonomies, the abundance of S-type asteroids in the inner belt. In comparing our results with SDSS, at first glance we can see that the match is satisfying: C-, S-, and V- types are clustered, although K- and L- types seems more degenerate. In this comparison we have to keep in mind that these are different wavelength ranges, SDSS is visible, VISTA is near infrared. With NIR wavelengths the discrimination of classes should be

[7] the next generation near-infrared sky survey, successor to 2MASS, http://www.ukidss.org/

[8] a space mission to map the geometry of the dark Universe, which will produce also a massive legacy of deep images and spectra over at least half of the entire sky with spatial resolution of 0.2 seconds of arc. http://sci.esa.int/euclid/

more complete due to the diagnostic 1$\mu$m and NIR slope features present in this wavelength range for several taxonomic classes (especially S, A, V, Q, K, L). A drawback is that the filter system we use cannot identify easily the 2 $\mu$m band.

The data was retrieved from Popescu et al. [2016] MOVIS-C catalog, which was developed using VISTA-VHS data release 3 (DR3) with 39,947 Solar System objects. The final Data Release is expected to have three times more objects, meaning that the expectations of improving taxonomic research are similar as what has been contributed from SDSS asteroids data.

It is important to highlight the novel way to obtain the colors of the Sun in this work, using VO advantages for search and process data of “solar twin" type stars that are present in VHS survey from all available catalogs. In perspective, compared with Holmberg et al. [2006] who used 9 stars, our sample has 330 solar twins, two orders of magnitude improvement.

As perspectives for future work we can mention:

1. Perform the exploitation of the database, adding new objects from future releases to continue studying the distribution of material in the asteroid belt.

2. Use the joint VIS+NIR photometry in a consistent way to better define and refine the taxonomy of asteroids.

## 4.4 Other Photometric Data

During the time of the thesis I was able to observe from to several facilities. These opportunities allow me to be trained with different instruments and the collection of data if the weather was benevolent.

The photometric data I gathered were colors for taxonomy and light curves for shape and binarity.

I collect light curves and colors for binaries from the Observatoire de Haute-Provence (OHP) (IAU code: 511) in the southeast of France, using the 1.20 m telescope. I also went to the Pic du Midi Observatory (IAU code: 586) in the French Pyrenees and use the 1 meter telescope (T1M) with $ugriz$ SDSS filters. All of the targets were binaries with no taxonomy (Table 4.3).

Also, I was included as Co-Investigator in a large program (Prog. ID 194.C-0207, PI: Pedro Lacerda), a survey for Kuiper Belt Objects (KBOs). In fact, this was the first survey of that kind for small KBOs: magnitude-limited, high-photometric-quality, high-temporal-resolution, multi-band survey of the rotational properties of over 60 Kuiper belt objects. As part of it, I was able to go observe with the New Technology Telescope (NTT, the prototype of active optics.) to La Silla Observatory at the outskirts of the Atacama Desert in Chile in January and July 2016.

This survey heas been conducted in an entirely homogeneous manner (same telescope, same

Table 4.3 – Observation details of binaries at Pic du Midi T1M - January 2017

| | asteroid | filter | exposure |
|---|---|---|---|
| (2044) | Wirt | R | 60 |
| (76818) | 2000 $RG_{79}$ | G | 60 |
| (2486) | Metsahovi | I | 60 |
| (4492) | Debussy | Z | 60 |
| (79472) | Chiorny | R | 60 |
| (4666) | Dietz | G | 60 |
| (2691) | Sersic | I | 60 |
| (3982) | Kastel' | Z | 60 |
| (21436) | Chaoyichi | R | 60 |
| (6244) | Okamoto | G | 60 |
| (2006) | Polonskaya | I | 60 |
| (1338) | Duponta | Z | 60 |
| (9260) | Edwardolson | R | 60 |
| (9783) | Tensho-kan | G | 60 |
| (5477) | Holmes | I | 60 |
| (17365) | 1978 $VF_{11}$ | Z | 60 |
| (31450) | 1999 $CU_9$ | R | 60 |
| (5674) | Wolff | G | 60 |
| (16525) | Shumarinaiko | I | 60 |
| (4272) | Entsuji | Z | 60 |
| (5425) | Vojtech | R | 60 |

observing strategy and data analysis). The survey was proposed to characterize KBOs with the aims to:

1. measure spin periods, and constrain shapes and bulk densities,
2. identify contact binaries or objects with extreme shapes or spins,
3. study surface colour variations, including the presence of surface spots,
4. obtain a sample of absolute magnitudes and optical colours protected from lightcurve variability, and
5. measure solar phase functions for the entire sample.

In order to place constraints on planetesimal accretion mechanisms and time-scales, effects of collisional evolution, the effects of strong early dynamical evolution in our planetary system and also, matching the theme of my current work, allow for comparisons with main-belt asteroids and Trojans.

In this respect, it is important to have in mind that KBO binaries are surprisingly abundant, particularly among Cold Classicals [Noll et al., 2008] and the study of their separations, mass ratios, and surface properties can offer insights into the physics of accretion [Nesvorný et al., 2010] and subsequent evolution.

This participation is also important to broaden my objects of research, having in mind that these are very correlated subjects. Also to stablish and maintain collaboration with other groups besides the French ones, keeping in mind future work from my home institution when back in Peru.

Part of the observing list at La Silla included also a comet: **67P/Churyumov–Gerasimenko**, as part of a campaign of remote observations that supported the European Space Agency's Rosetta mission. My observations were included in a special issue of the *Philosophical Transactions of the Royal Society of London* [Snodgrass et al., 2017] .

# 5 Physical, spectral, and dynamical properties of (107) Camilla's triple system

## 5.1 Introduction

The asteroids orbiting in the main belt, between Mars and Jupiter, are the remnants of the building blocks that accreted to form terrestrial planets, left over from all the dynamical events that shaped our planetary system. If small asteroids (diameter smaller than ≈100 km) are collisionally evolved objects [Morbidelli et al., 2009], larger bodies contain a relatively pristine record of their initial forming conditions.

Decades of photometric and spectroscopic surveys, probing only the composition of the surface, have provided a clear view of the distribution of material in the inner solar system [e.g. Gradie and Tedesco, 1982, DeMeo and Carry, 2014]. They, however, failed to address the original location and time scales for the accretion of these blocks, which are key to understand the processes that occurred in the disk of gas and dust around the young Sun.

Fortunately, these questions can be addressed by studying the internal structure of asteroids: objects formed far from the Sun are expected to be composed by a mixture of rocks and ices, while inner most objects are deemed volatile-free; depending on their formation time scale, the amount of radiogenic heat was different, leading to partial or complete differentiation, or not at all. With the notable exception of asteroids visited by spacecraft, density is the only physical property remotely measurable that constrains internal structure [Scheeres et al., 2015].

Determination of the density relies on the measurement of the mass and the volume, and for that large asteroids with satellites are prime targets [Carry, 2012]. The study of their mutual orbit is currently the most precise method to estimate asteroid's masses, while they usually sustain angular diameters large enough to be spatially resolved by large telescopes, allowing the determination of their volume. Beside, the orbits of the satellites themselves offer a way to probe the gravity field, related to mass distribution inside the asteroid [Berthier et al., 2014].

We focus in the present study on the outer belt asteroid (107) Camilla, discovered in the Cybele region on November 17, 1868 from Madras, India by N. R. Pogson. Its first satellite, *S/2001 (107) 1*, was observed for the first time in March 2001 by Storrs et al. [2001], using the Hubble Space Telescope (HST), and its orbit was first studied by Marchis et al. [2008] using observations

from large ground-based telescopes equipped with adaptive-optic (AO) cameras. Its second satellite, *S/2016 (107) 1*, was discovered in 2016 by our team [Marsset et al., 2016], using the European Southern Observatory (ESO) Very Large Telescope (VLT).
Gathering all the available disk-resolved and high-contrast images from HST and AO cameras, optical lightcurves, stellar occultations, and visible and near-infrared spectra (Section 5.2), we present an extensive study of the dynamics of the system (Section 5.3), of the surface properties of Camilla and its main satellite *S/2001 (107) 1* (Section 5.4), and of Camilla spin and 3-D shape (Section 5.5), all constraining its physical properties (Section 5.6).

## 5.2 Observations

### 5.2.1 Optical lightcurves

We gather the 24 lightcurves used by Torppa et al. [2003] to create a convex 3-D shape model of Camilla[1], compiled from the Uppsala Asteroid Photometric Catalog[2] [Lagerkvist and Magnusson, 2011]. We also retrieve the three lightcurves reported by Polishook [2009]. We complete these observations with additional lightcurves taken by our group. A total of 70 lightcurves observed between 1981 and 2016 (Table A.1) are used in this work.

### 5.2.2 High-angular resolution imaging

We compile here all the high-angular resolution images of (107) Camilla taken with the Hubble Space Telescope (HST) and large ground-based telescopes equipped with adaptive-optics (AO) cameras: Gemini North, ESO VLT, and W. M. Keck, of which only a subset had already been published [Storrs et al., 2001, Marchis et al., 2008]. The images span 15 years, from March 2001 to August 2016.
The images from the VLT were acquired with both the first generation instrument NACO [Lenzen et al., 2003, Rousset et al., 2003] and SPHERE, the second generation extreme-AO instrument designed for exoplanet detection and characterization [Fusco et al., 2006, Beuzit et al., 2008]. The images taken with SPHERE used its IRDIS differential imaging camera [Dohlen et al., 2008] sub-system. Images taken at the Gemini North used NIRI camera [Hodapp et al., 2003], fed by the ALTAIR AO system [Herriot et al., 2000]. Finally, observations at Keck were realized with the NIRC2 camera [van Dam et al., 2004, Wizinowich et al., 2000]. We list in Table A.2 the details of each observation.
The basic data processing (sky subtraction, bad-pixel removal, and flat-field correction) was performed using in-house routines developed in Interactive Data Language (IDL) to reduce AO-imaging data [see Carry et al., 2008, for more details].

[1] Available on DAMIT [Ďurech et al., 2010]:
http://astro.troja.mff.cuni.cz/projects/asteroids3D/
[2] http://asteroid.astro.helsinki.fi/apc/asteroids/

### 5.2.3 High-angular resolution spectro-imaging

In 2015 and 2016, we also used the IRDIFS integral-field spectrograph [Claudi et al., 2008] subsystem of SPHERE at the ESO VLT, aiming at measuring the reflectance spectrum of Camilla satellite *S/2001 (107) 1*. The observations were carried out in the IRDIFS_EXT mode, in which both IRDIS and IRDIFS observe simultaneously. In this set-up, IRDFS covers the wavelength range from 0.95 to 1.65 $\mu$m (YJH bands) at a spectral resolution of ~30 in a $1.7'' \times 1.7''$ field of view (FoV), while IRDIS observes in the dual-band imaging mode [DBI, Vigan et al., 2010] with $K_{12}$, a pair of filters in the $K$ band ($\lambda_{K_1} = 2.110\,\mu$m and $\lambda_{K_2} = 2.251\,\mu$m, ~0.1 $\mu$m bandwidth), within a $11'' \times 11''$ FoV. All observations were performed in the pupil-tracking mode, where the pupil remains fixed while the field orientation varies during the observations. This mode provides the best PSF stability and helps in reducing and subtracting static speckles noise in the images.
For the pre-processing of both the IRDIFS and IRDIS data, we made use of the preliminary release (v0.14.0-2) of the SPHERE Data Reduction and Handling (DRH) software [Pavlov et al., 2008], as well as additional in-house tools written in IDL. We used the DRH for the creation of some of the basic calibrations: master sky frames, master flat-field, IRDIFS spectra positions, initial wavelength calibration and IFU flat-field. Before creating the data cubes, we used IDL routines to subtract the background to each science frame and correct for the bad pixels identified using the master dark and master flat-field DRH products. This step was introduced as a substitute to the bad pixel correction provided by the DRH. Bad pixels were first identified using a sigma-clipping routine, and then corrected performing a bicubic pixel interpolation with the `MASKINTERP` IDL routine. The resulting frames were then injected into the DRH recipe to create the data cubes by interpolating the data spectrally and spatially.

### 5.2.4 Stellar occultations

Eleven stellar occultations by Camilla have been observed in the last decade, mostly by amateur astronomers [see Mousis et al., 2014]. The timings of disappearance and reappearance of the stars, together with the localization of each observing station are compiled by Dunham et al. [2012], and publicly available on the Planetary Data System (PDS[3]). We converted the disappearance and reappearance timings of the occulted stars into segments (called chords) on the plane of the sky, using the location of the observers on Earth and the apparent motion of Camilla following the recipes by Berthier [1999]. Four stellar occultations had multiple chords, while the other events only had one or two positive chords, and provided only little constraints on the size and apparent shape of Camilla. In none of these eleven stellar occultations a secondary event was detected. We list in Table A.3 the detail of the seven events that we used (Fig. 5.7).

[3] http://sbn.psi.edu/pds/resource/occ.html

### 5.2.5 Near-infrared spectroscopy

On November 1, 2010, we observed Camilla over 0.8–2.5 $\mu$m with the near-infrared spectrograph SpeX [Rayner et al., 2003], on the 3-meter NASA IRTF located on Mauna Kea, Hawaii, using the low resolution Prism mode ($R = 100$). We used the standard *nodding* procedure of observation, using alternatively two separated locations of the slit [e.g., Nedelcu et al., 2007] to estimate the sky background. We used Spextool (SPectral EXtraction TOOL), an IDL-based data reduction package written by Cushing et al. [2004] to reduce data obtained with SpeX.

## 5.3 Dynamical properties

### 5.3.1 Data processing

The main challenges in measuring the position and apparent flux of the satellite of an asteroid results from their sub-arcsecond angular separation and high contrast (several magnitudes), combined with non-perfect AO correction. A typical image of a binary asteroid (Fig. 5.1) displays a central peak (the asteroid itself, angularly resolved or not) encompassed by a halo (its diffused light), within which speckle patterns appear. The faintness of these speckles produced by interferences of the incoming light make them very similar in aspect to a small moon with a contrast up to several thousands, and they can be misleading. Speckles, however, present temporal and spatial fluctuations on short timescales, depending on the ambient conditions and AO performances (e.g., seeing, airmass, brightness of the AO reference source). These fluctuations can be used to distinguish genuine satellites from speckles.
As for the direct imaging of exoplanets, it is crucial to substract the halo that surrounds the primary [in a similar way to the digital coronography of Assafin et al., 2008]. Because asteroids are also marginally resolved, their light is not fully coherent, and the speckle pattern is not as stable in time, nor simple, as in the case of a star. The tool we developed consider concentric annuli around the center of light of the primary to evaluate its halo. If the principle is straightforward, great caution was put in the implementation, especially in the computation of the intersection of the annuli with the pixels to allow the use of annuli with a sub-pixel width. The contribution of each pixel to different annuli is thus solved first, and the median flux of each annuli is computed, and subtracted to each pixel accordingly.
The position and flux of the satellite, relative to the primary, is then measured by fitting each time a 2-D Gaussian function to the halo-subtracted image. To estimate the uncertainties on the position and apparent flux of both the primary and the satellites, we use different apertures to fit the 2-D Gaussian function, typically from 5 to 150 pixels for the primary, and 3 to 15 for the satellites. The reported positions and apparent magnitudes (Tables A.4 and A.5) are the average of all fits (after removal of outlier values), and the reported uncertainties are the standard deviations.

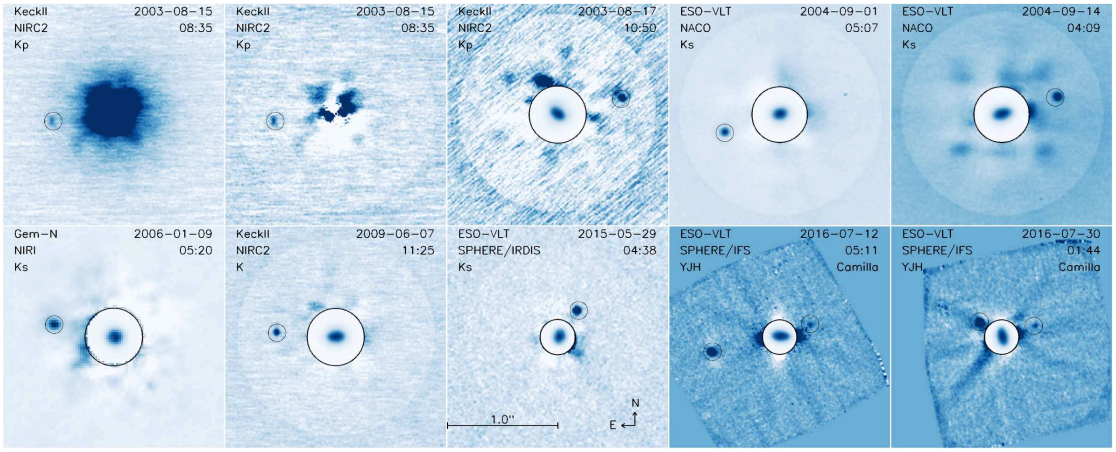


Figure 5.1 – Examples of AO images from Gemini, Keck, and ESO VLT. The first image (August 13, 2003, from Keck) shows a typical image, in which the halo of Camilla dominates the background and makes the satellite hard to detect. The remaining images show the result of the halo subtraction. The inner circles show the original images, in which the elongated shape of Camilla can be guessed.

### 5.3.2 Orbit determination with `Genoid`

We use our algorithm `Genoid` [GENetic Orbit IDentification, Vachier et al., 2012] to determine the orbit of the satellites. `Genoid` is a genetic-based algorithm that relies on a metaheuristic method to find the best-fit (i.e., minimum $\chi^2$) suite of dynamical parameter (semi-major axis, eccentricity, etc) by refining, generation after generation, a grid of test values (called *individuals*).
The first generation is drawn randomly over a very wide range for each parameters, thus avoiding the miss of the global minimum from inadequate initial conditions, which is always a threat in minimization algorithms. For each individual (i.e., set of dynamical parameters), the $\chi^2$ residuals between the observed and predicted positions is computed as

$$\chi^2 = \sum_{i=1}^{N} \left[ \left( \frac{X_{o,i} - X_{c,i}}{\sigma_{x,i}} \right)^2 + \left( \frac{Y_{o,i} - Y_{c,i}}{\sigma_{y,i}} \right)^2 \right] \tag{5.1}$$

where $N$ is the number of observations, and $X_i$ and $Y_i$ are the relative positions between the satellite and Camilla along the right ascension and declination respectively. The indices $o$ and $c$ stand for observed and computed positions, and $\sigma$ are the measurement uncertainties.
A new generation of individuals is drawn by mixing randomly the parameters of individuals with the lowest $\chi^2$ from the former generation, in a survival of the fittest fashion. This way, the entire parameter space is scanned, with the density of evaluation points increasing toward low $\chi^2$ regions along the process. At each generation, we also use the best individual as initial condition to search for the local minimum by gradient descent. The combination of genetic grid-search and gradient descent thus ensures finding *the* best solution.
We then assess the confidence interval of the dynamical parameters by considering all the

individuals providing predictions within 1, 2, and 3 $\sigma$ of the observations. The range spanned by these individuals provide the confidence interval at the corresponding $\sigma$ level for each parameter.
The reliability of `Genoid` has been assessed during a stellar occultation by (87) Sylvia and its satellites Romulus and Remus on January 6, 2013. `Genoid` was used to predict the position of Romulus prior to the event, directing observers to locations specifically to target the satellite. Four different observers observed an occultation by Romulus, which was found only 13.5 km from the position predicted [Berthier et al., 2014].

### 5.3.3 Orbit of *S/2001 (107) 1*

We measured 81 astrometric positions of the satellite *S/2001 (107) 1* relative to Camilla over a span of 15 years, corresponding to 5642 days or 1520 revolutions. The orbit we derive with `Genoid` fits all 81 observed positions of the satellite with a root mean square (RMS) residual of 8.01 milli-arcseconds (mas) only, which corresponds to a sub-pixel accuracy.
*S/2001 (107) 1* orbits Camilla on a circular, prograde, equatorial orbit, in 3.7 days with a semi-major axis of 1242 km. We detail all the parameters of *S/2001 (107) 1*'s orbit in Table 5.1, with their confidence interval taken at 3 $\sigma$. The distribution of residuals between the observed and predicted positions, normalized by the uncertainty on the measured positions, are plotted in Fig. 5.2. The orbit we determine here is qualitatively similar to the one by Marchis et al. [2008], while much better constrained: we fit 81 astrometric positions over 15 years with a RMS residual of 8.01 mas, compared to their fit of 23 positions over less than 3 years with a RMS residual of 22 mas. The much longer time span of observations provides a strict constraint on the orbital period of *S/2001 (107) 1* [$(3.712 \pm 4 \times 10^{-5})$d, compared to $(3.722 \pm 0.003)$d from Marchis et al., 2008, hence 3.2 $\sigma$ away]. As a result, the mass of the system is $(1.10 \pm 0.12) \times 10^{19}$ kg (3 $\sigma$ uncertainty range), about 1% of the mass of Ceres [Carry, 2012], compared with the previous reported value of $(1.12 \pm 0.09) \times 10^{19}$ kg.

### 5.3.4 Orbit of *S/2016 (107) 1*

We measured 11 astrometric positions of the satellite *S/2016 (107) 1* relative to Camilla between 2015 and 2016 , corresponding to 428 days or 502 revolutions. Unfortunately, these observations correspond to only three well-separated epochs: 2015-May-29, 2016-Jul-12, and 2017-Jul-30, providing little constraint on the orbit. The orbit we derive with `Genoid` fits all 11 observed positions of the satellite with a RMS residual of 3.1 mas only.
*S/2016 (107) 1* orbits Camilla on a plane marginally tilted $(9.7 \pm 8.2°)$ with respect to the equator of Camilla and *S/2001 (107) 1*, in 0.85 days with a semi-major axis of 507 km. Its orbit is much more eccentric than *S/2001 (107) 1*'s, with an eccentricity of $0.32^{+0.39}_{-0.32}$ , similarly to the smaller and inner satellites of (45) Eugenia, (87) Sylvia, and (130) Elektra [Marchis et al., 2010, Fang et al., 2012, Berthier et al., 2014, Yang et al., 2016].

We detail all the parameters of its orbit in Table 5.1, with their confidence interval taken at 3 $\sigma$.

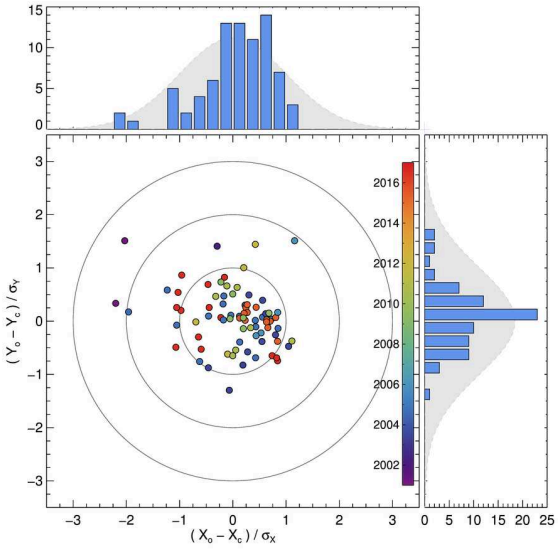


Figure 5.2 – Distribution of residuals between the observed (index o) and predicted (index c) positions, normalized by the uncertainty on the measured positions ($\sigma$), and color-coded by observing epoch. X stands for right ascension and Y for declination. The three large gray circles represent the 1, 2, and 3 $\sigma$ limits. The top panel shows the histogram of residuals along X, and the right panel the residuals along Y. The light gray Gaussian in the background has a standard deviation of 1.

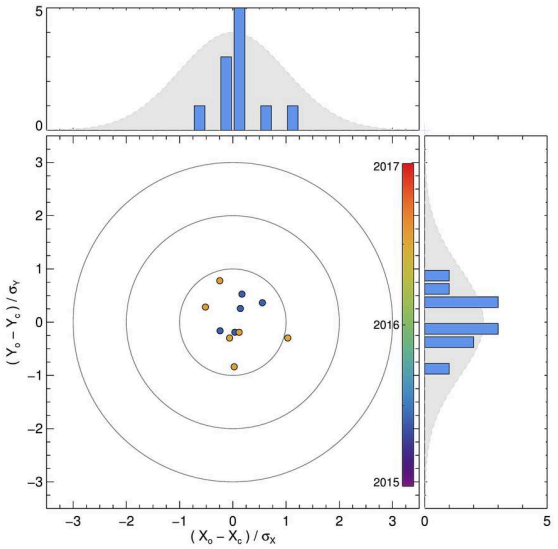


Figure 5.3 – Similar as Fig. 5.2, but for *S/2016 (107) 1*.

Table 5.1 – Orbital elements of the satellites of Camilla *S/2001 (107) 1* and *S/2016 (107) 1*, expressed in EQJ2000, obtained with `Genoid`: orbital period $P$, semi-major axis $a$, eccentricity $e$, inclination $i$, longitude of the ascending node $\Omega$, argument of the pericenter $\varpi$, time of pericenter $t_p$. The number of observations and RMS between predicted and observed positions are also provided. We finally report the derived primary mass $M$, the ecliptic J2000 coordinates of the orbital pole $(\lambda_p, \beta_p)$, the equatorial J2000 coordinates of the orbital pole $(\alpha_p, \delta_p)$, and the angular tilt $(\Lambda)$ with respect to the equator of Camilla. Uncertainties are given at 3-$\sigma$.

| | *S/2001 (107) 1* | | *S/2016 (107) 1* | |
|---|---|---|---|---|
| Observing data set | | | | |
| Number of observations | 81 | | 11 | |
| Time span (days) | 5642 | | 430 | |
| RMS (mas) | 8.0 | | 3.1 | |
| Orbital elements EQJ2000 | | | | |
| $P$ (day) | 3.71234 | ± 0.00004 | 0.8525 | ± 0.0001 |
| $a$ (km) | 1241.7 | ± 47.6 | 507 | ± 104 |
| $e$ | 0.0 | + 0.014 | 0.31 | ±0.39 |
| $i$ (°) | 16.1 | ± 2.2 | 17 | ± 5 |
| $\Omega$ (°) | 140.4 | ± 8.7 | 172 | ± 35 |
| $\varpi$ (°) | 101.2 | ± 45.6 | 252 | ± 49 |
| $t_p$ (JD) | 2452839.64349 | ± 0.462 | 2452836.08215 | ± 0.443 |
| Derived parameters | | | | |
| $M$ ($\times 10^{19}$ kg) | 1.10 | ± 0.12 | | |
| $\lambda_p, \beta_p$ (°) | 73, +53 | ± 4, 2 | 86, +49 | ± 8 |
| $\alpha_p, \delta_p$ (°) | 50, +74 | ± 4, 2 | 87, +25 | ± 8 |
| $\Lambda$ (°) | 0.6 | ± 1.6 | 9.7 | ± 8.2 |

We note, however, than given the very small data set consisting in three epochs only, this orbit for *S/2016 (107) 1* is still preliminary and more observations are required to ascertain its orbit. The distribution of residuals between the observed and predicted positions, normalized by the uncertainty on the measured positions, are plotted in Fig. 5.3.

## 5.4 Surface properties

### 5.4.1 Data processing

We measured the near-infrared spectra of Camilla and its largest satellite *S/2001 (107) 1* on the SPHERE/IRDIFS data. Telluric features were removed, and the reflectance spectra were obtained, by observing the nearby solar type star HD139380.
Similarly to previous sections, the bright halo of Camilla that contaminated the spectrum of the moon was removed. This was achieved by measuring the background at the location of

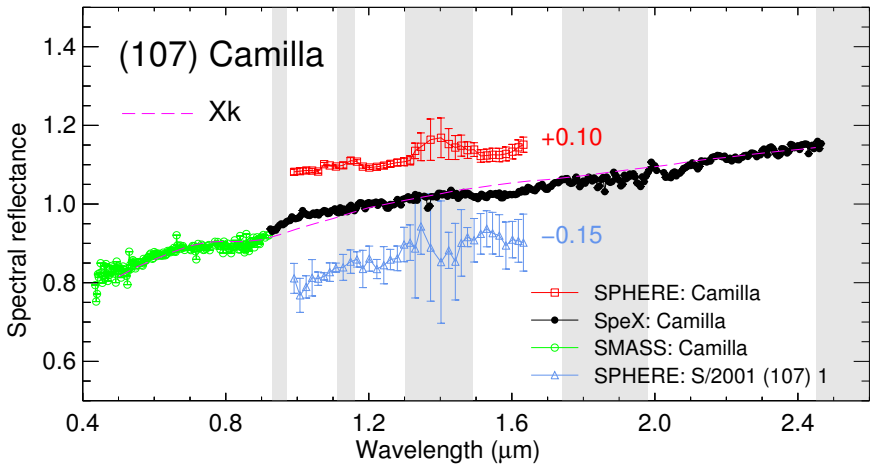


Figure 5.4 – Visible (green), near-infrared spectrum of Camilla from IRTF (deep blue and black dots) and SPHERE (red squares, offset by +0.1), and its moon *S/2001 (107) 1* from SPHERE (blue triangles, offset by -0.15). Gray areas represent the wavelength ranges affected by water vapour in the atmosphere. All spectra were normalize to unity at one micron. Overplot to the IRTF spectra is the Bus-DeMeo Xk class.

the moon for each pixel over a 10×10-pixel region as the median value of the area defined as a 40×1-pixel arc centred on Camilla. To estimate the uncertainty and potential bias on photometry introduced by this method, we performed a number of simulations in which we injected fake companions on the 39 spectral images of the spectro-imaging cube, at separation (≈300 mas) and random position angles from the primary. The simulated sources were modeled as the PSF, from the calibration star images, scaled in contrast.
The halo from Camilla was then removed from these simulated images using the method described above, and the flux of the simulated companion measured by adjusting a 2D-Gaussian profile. Based on a total statistics of 500 simulated companions, we find that the median loss of flux at each wavelength is 11±10%. A spectral gradient is also introduced by our technique, but it is smaller than 0.06±0.07% $\mu$m$^{-1}$. The spectra of Camilla and *S/2001 (107) 1* normalised at 1.1 $\mu$m are shown in Fig. 5.4.

### 5.4.2 Spectrum of (107) Camilla

Camilla was originally classified as a C type based on its visible colors and albedo [Tedesco et al., 1989]. Later on, both Bus and Binzel [2002] and Lazzaro et al. [2004] revised and classified it as X, based on visible spectra. More recently, based on a near-infrared spectrum from NASA IRTF Spex, Lindsay et al. [2015] classified Camilla either Xe or L.
We combine the near-infrared spectrum we acquired at NASA IRTF (Section 5.2.5) with the visible spectrum from SMASS [Bus and Binzel, 2002, Bus and Binzel, 2002] and analyze them with `M4AST`; using the $\chi^2$ metric, we found Camilla to be an Xk-type asteroid (using Bus-DeMeo taxonomic scheme, Fig. 5.4). The low albedo of Camilla [0.059 ± 0.005, taken as the average of

the estimates by Morrison and Zellner, 2007, Tedesco et al., 2002, Ryan and Woodward, 2010, Usui et al., 2011, Masiero et al., 2011] hints at a P-type classification, using the Tedesco et al. [1989] scheme[4].
Although the best spectral match is formally found for an enstatite chondrite EH5 meteorite (Queen Alexandra Range, Antarctica origin, maximum size of 10 $\mu$m), the low albedo of Camilla argues for a different type of analog material. The composition of P-type asteroids is hard, if not impossible, to infer from their visible and near-infrared spectra owing to the lack of absorption bands.

Recently, Vernazza et al. [2015] have shown that anhydrous chondritic porous interplanetary dust particules (IDPs) were likely to originate from D- and P-types asteroids, based on spectroscopic observations in the mid-infrared of outer belt D- and P-type asteroids, including Camilla. The mixture of olivine-rich and pyroxene-rich IDPs they used was compatible with the visible and near-infrared spectrum of Camilla. As such, the surface of Camilla, and more generally of D- and P-types, is very similar to that of comets, as already reported by Emery et al. [2006] from the spectroscopy of Jupiter Trojans in the mid-infrared, revealing the presence of anhydrous silicates.

### 5.4.3 Spectrum of *S/2001 (107) 1*

As visible on Fig. 5.4 the spectrum of *S/2001 (107) 1* is very similar to that of Camilla. No significant difference in slope nor absorption band can be detected. This implies that the two components are spectraly identical from 0.95 to 1.65 $\mu$m within the precision of our measurements. Such a similarity between the components of multiple systems have already been reported for several other main-belt asteroids: (22) Kalliope [Laver et al., 2009], (90) Antiope [Marchis et al., 2011], (130) Elektra [Yang et al., 2016], and (379) Huenna [DeMeo et al., 2011]. Such spectral similarity, together with the main characteristics of the orbit (prograde, equatorial, circular) supports an origin of these satellites, here for *S/2001 (107) 1* in particular, by impact and reaccumulation of material in orbit [see Margot et al., 2015, for a review].

## 5.5 Physical properties

### 5.5.1 Data processing

We used the optical lightcurves at their face value, only converting their heterogeneous formats from many observers to the usual lightcurve inversion format [Ďurech et al., 2010]. The location of observers together with their timings of the disappearance and the reappearance of the star were converted into chords on the plane of the sky, using the recipes from Berthier [1999]. Finally, the 2-D profile of the apparent disk of Camilla was measured on the AO images,

[4] The X-complex is characterized by moderately sloped and featureless spectra, it is compositionally degenerate because it comprises asteroids with different albedos. The Tholen [1984] taxonomy distinguished the X-complex by albedo, breaking it up into the E, M, and P classes that ranged from high to low albedo.

deconvolved using the `Mistral` algorithm [Fusco, 2000, Mugnier et al., 2004] which reliability has been demonstrated elsewhere [Witasse et al., 2006], using the wavelet transform described in Carry et al. [2008], Carry et al. [2010].

### 5.5.2 3-D shape modeling with `KOALA`

We used the multi-data inversion algorithm Knitted Occultation, Adaptive-optics, and Lightcurve Analysis (`KOALA`), which determines the set of rotation period, spin-vector coordinates, and 3-D shape that provide the best fit to all observations simultaneously [Carry et al., 2010].

The `KOALA` algorithm minimizes the total $\chi^2 = \chi^2_{LC} + w_{AO}\,\chi^2_{AO} + w_{Occ}\,\chi^2_{Occ}$ that composes the individual contributions from light curves (LC), profiles from disk-resolved images (AO), and occultation chords (Occ). Adaptive optics and occultation data are weighted with respect to the light-curves with parameters $w_{AO}$ and $w_{Occ}$ respectively. The optimum values of these weights can be objectively obtained following the approach of Kaasalainen [2011].

This method has been spectacularly validated by the images taken by the OSIRIS camera on-board the ESA Rosetta mission during its flyby of the asteroid (21) Lutetia [Sierks et al., 2011]. Before the encounter, the spin and 3-D shape of Lutetia had been determined with `KOALA`, using lightcurves and AO images [Carry et al., 2010]. A comparison of the pre-flyby solution with the OSIRIS images showed that the spin-vector coordinates were accurate to within 2°, and the diameter to within 2%. That is the RMS residuals between the profiles from `KOALA` predictions and OSIRIS images were of only 2 km, for a 98 km-diameter asteroid [Carry et al., 2012].

### 5.5.3 Spin and 3-D shape of (107) Camilla

We used 70 optical lightcurves, 34 profiles from disk-resolved imaging, and 7 stellar occultation events to reconstruct the spin and 3-D shape of Camilla. The model fits very well the entire data set, with mean residuals of only 0.02 mag for the lightcurves (Fig. 5.5), 0.3 pixel for the images (Fig. 5.6), and 0.46 seconds for the stellar occultations (Fig. 5.7).

The rotation period and coordinates of the spin axis (Table 5.2) agree very well with previous results from lightcurve-only inversion and convex shape modeling [Torppa et al., 2003, Ďurech et al., 2011, Hanuš et al., 2016], as well as models obtained by combining lightcurves and smaller subset of present AO data [respectively 3 and 21 epochs, see Hanuš et al., 2013, Hanuš et al., 2017]. The shape of Camilla is far from a sphere, with a strong ellipsoidal elongation along the equator (axes ratio of $1.39 \pm 0.06$ , see Table 5.2). Departures from the ellipsoid are, however, limited, and consist mainly in two large circular basins, reminiscent of impact craters (Fig. 5.8).

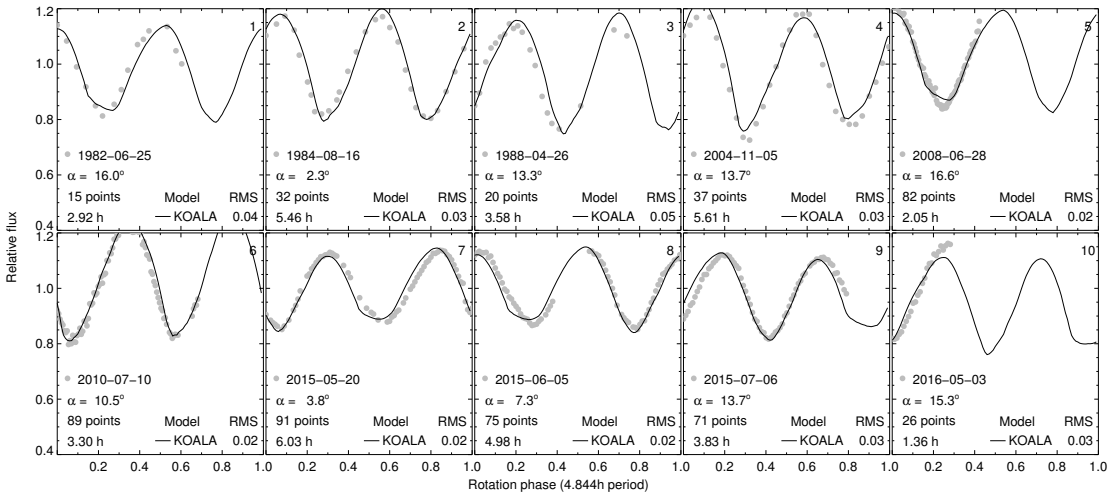


Figure 5.5 – Examples of optical lightcurves of Camilla, compared with the shape model.

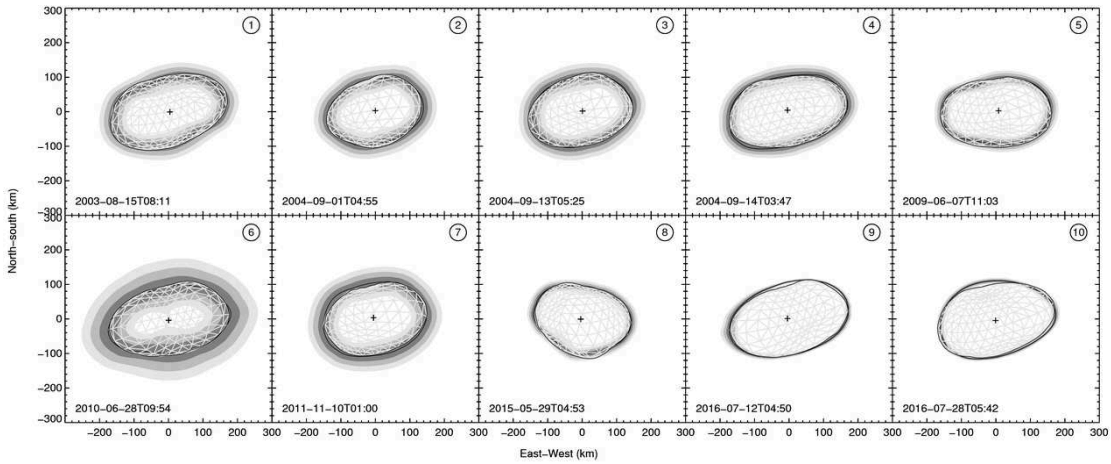


Figure 5.6 – Examples of profiles of Camilla from disk-resolved images, compared with the shape model.

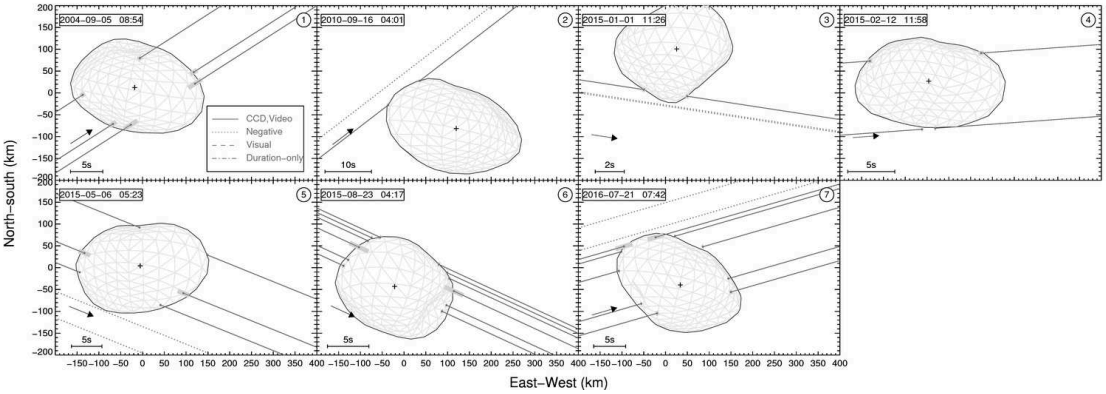


Figure 5.7 – The seven stellar occultations by Camilla, compared with the shape model.

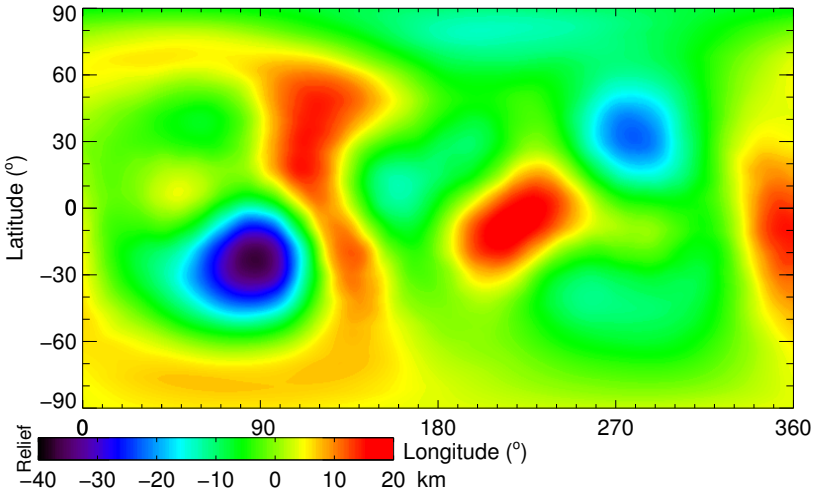


Figure 5.8 – Topographic map of Camilla, with respect to its reference ellipsoid (Table 5.2). The main features are the two deep and circular basins located at (87°,-23°) and (278°,+33°).

The volume-equivalent diameter of Camilla is found to be $254 \pm 12$ km, in perfect agreement with the recent determination by Hanuš et al. [2017] based on a similar data set. Both estimates are high compared to diameter estimates from infrared observations with IRAS, AKARI, or WISE [Tedesco et al., 2004, Ryan and Woodward, 2010, Usui et al., 2011, Masiero et al., 2011, see Table A.6]. However, given the highly elongated shape of Camilla, it is maybe not surprising that disk-integrated mid-infrared radiometry underestimates the diameter.
The agreement of the 3-D models by Hanuš et al. [2017] and developed here with both the disk-resolved images and the stellar occultation timings, providing direct size measurements, indeed argues for Camilla being larger than previously thought. The corresponding volume is $8.6 \pm 0.4 \cdot 10^6$ km$^3$, following $\delta V/V \approx \delta D/D$, because the shape model is not allowed to be simply scaled in size by the data, and the uncertainties are somehow localized [see Kaasalainen and Viikinkoski, 2012, for details].

### 5.5.4 Diameter of *S/2001 (107) 1*

We list in Table A.4 and display in Fig. 5.9 the 65 measured brightness difference with an uncertainty lower than 1 magnitude between Camilla and its largest satellite *S/2001 (107) 1*. We found a normal distribution of measurement, as expected from photon noise, and measure an average magnitude difference of $\Delta m$ = -6.51 ± 0.27 , similar to the value of -6.31 ± 0.68 found by Marchis et al. [2008] on 22 epochs.

Using the diameter of $254 \pm 12$ km for Camilla (Sect. 5.5.3) and assuming *S/2001 (107) 1* has the same albedo as Camilla itself (supported by their spectral similarity, see Section 5.4.3), this magnitude difference implies a size of $12.7 \pm 3.4$ km for *S/2001 (107) 1*, smaller than previously reported.

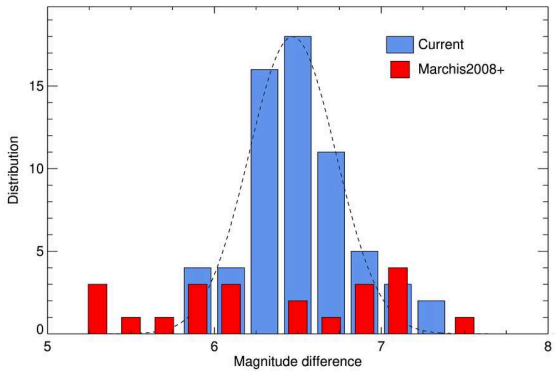


Figure 5.9 – Distribution of the magnitude difference between Camilla and its largest satellite *S/2001 (107) 1*, compared with previous report from Marchis et al. [2008]. The dashed black line represent the normal distribution fit to our results, with a mean and standard deviation of $6.51 \pm 0.27$ .

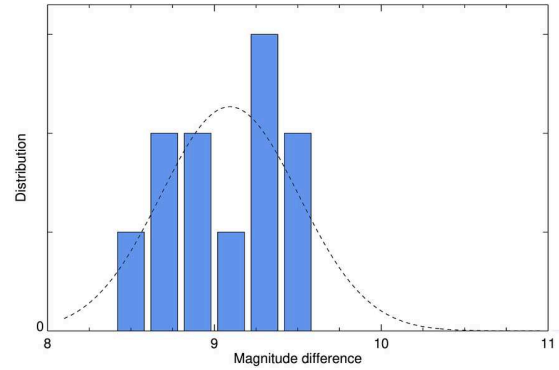


Figure 5.10 – Distribution of the magnitude difference between Camilla and its second satellite *S/2016 (107) 1*. The dashed black line represents the normal distribution fit to our results, with a mean and standard deviation of $9.0 \pm 0.4$ .

Table 5.2 – Sidereal rotation period, spin-vector coordinates (longitude $\lambda$, latitude $\beta$ in ECJ2000), volume-equivalent diameter (D), volume (V), diameters along the principal axis of inertia (a, b, c), and axes ratio of Camilla obtained with KOALA. All uncertainties are reported at 3 $\sigma$.

| Parameter | Value | Unc. | Unit |
|---|---|---|---|
| Period | 4.843927 | $4.10^{-5}$ | hour |
| $\lambda$ | 69.3 | 9.0 | deg. |
| $\beta$ | 56.6 | 7.0 | deg. |
| $T_0$ | 2444636.00000000 | | |
| D | 254.0 | 18.0 | km |
| V | $8.58 \cdot 10^6$ | $6.1 \cdot 10^5$ | $km^3$ |
| a | 347.4 | 18.0 | km |
| b | 250.6 | 18.0 | km |
| c | 193.4 | 18.0 | km |
| a/b | 1.39 | 0.09 | |
| b/c | 1.30 | 0.12 | |

## 5.6 Discussion

### 5.6.1 Density

Using the mass derived from the study of the orbit of *S/2001 (107) 1*, and the volume from the 3-D shape modeling, we infer a density of $1.4 \pm 0.3$ kg.m$^{-3}$ (3 $\sigma$ uncertainty), to be compared with the summary of previous reports at $2.28 \pm 0.87$ kg.m$^{-3}$ (3 $\sigma$ uncertainty) compiled by Carry et al. [2012] from the mass and diameter estimates listed in Tables A.7 and A.6. Without surprise, our result is very similar to the revised density recently published by Hanuš et al. [2017], who found a similar diameter.

This density is consistent with the density of similar-sized asteroids in the outer belt and Trojan space, such as (617) Patroclus and (624) Hektor [Mueller et al., 2010, Marchis et al., 2014]. Without an unambiguous analog compound or meteorite to be used as reference, inferring the internal structure is speculative, but we can nevertheless draw certain limits. Considering the least dense meteorites in our records, the CI carbonaceous chondrites [Consolmagno et al., 2008], implies a porosity of $75 \pm 25$ %, resulting in a macroporosity of $40 \pm 19$ % (a random arrangement of equally sized spheres has minimum macroporosity of 26%). Considering the *second* least dense meteorites in our records, the CM carbonaceous chondrites [Consolmagno et al., 2008], implies an unrealistic porosity of $107 \pm 36$ %, and a macroporosity of $84 \pm 46$ %. This thought experiment shows that Camilla must be made of intrinsically low-density material, such as CI carbonaceous chondrites. Denser materials require more voids in its interior than matter. The low density is also consistent with the presence of ices in its interior, this low density releases some constraints on the density of the silicate phase. In all cases, the presence of fractures and voids can be expected.

### 5.6.2 Craters

We use the topography map (Fig. 5.8) to estimate the volume excavated from Camilla during the collisions that formed the large circular depressions. For each, we estimate the volume as the volume $V_c$ of a paraboloid as $V_c = \frac{\pi}{2} d r^2$, with $d$ the depth of the crater and $r$ its radius.

The deeper crater at (87°, -23°) has a diameter of about 80-90 km for a depth of 13-16 km (16% of diameter), accounting for a volume of 3.4–5.0 × $10^4$ $km^3$, equivalent to a sphere of 40–46 km in diameter. The second largest depression at (278°, +33°) has a diameter of about 70 km and a depth of ≈6 km (i.e., 8% of its diameter), accounting for a volume of 1.2 × $10^4$ $km^3$, equivalent to a sphere of approximately 28 km in diameter.

Either of these excavations can easily account for the volume of material encompassed by the two satellites of Camilla, the diameters of which are $12.7 \pm 3.4$ km for *S/2001 (107) 1* and $4.0 \pm 1.2$ km for *S/2016 (107) 1* (see above). Hence, the formation of these two satellites from one of these two excavations by re-accumulation of material in orbit is probable.

The amount of material ejected by these probable impacts opens the question of a potential dynamical family linked with Camilla. Indeed, we compute that the nearby family of (87) Sylvia encompasses a comparable volume of ≈$10^4$ $km^3$: using the Virtual Observatory tool MP$^3$C [Delbo et al., 2017], we retrieve the family list of members by Milani et al. [2014], and diameter and albedo by WISE [Grav et al., 2012], and compute the sum of all volumes.

Identifying such a family is, however, a complex task. As discussed by Vokrouhlický et al. [2010], the numerous mean-motion resonances with Jupiter and secular $z_1$ resonance [Milani and Knezevic, 1992, 1994] highly perturb the orbit of objects in the vicinity of Camilla, and these authors predict that over 2 Gyr, a family associated with Camilla would have lost 50% of its members. Moreover, the dynamical family related to (87) Sylvia, whose orbit, spectral properties, and albedo are very similar to Camilla's, blurs the picture even further.

It is possible that an ancient family linked with Camilla will be identified once the census of small (H>14) asteroids in the Cybele region grows, and colors of their surfaces will be available.

## 5.7 Conclusions

In the present study, we have acquired and compiled optical lightcurves, stellar occultations, visible and near-infrared spectra, and high-contrast and high-angular-resolution images and spectro-images from the Hubble Space Telescope and large ground-based telescopes (Keck, Gemini, VLT) equipped with adaptive-optics-fed cameras.
Using 81 positions spanning 15 years, we study the dynamics of the largest satellite, *S/2001 (107) 1*, and determine its orbit around Camilla to be circular, equatorial, and prograde. The residuals between our dynamical solution and the observations are 8.0 mas, corresponding to a sub-pixel accuracy. Using 11 positions of the second, smaller satellite *S/2016 (107) 1* we discovered in 2015, we determine a preliminary orbit, marginally tilted from that of *S/2001*

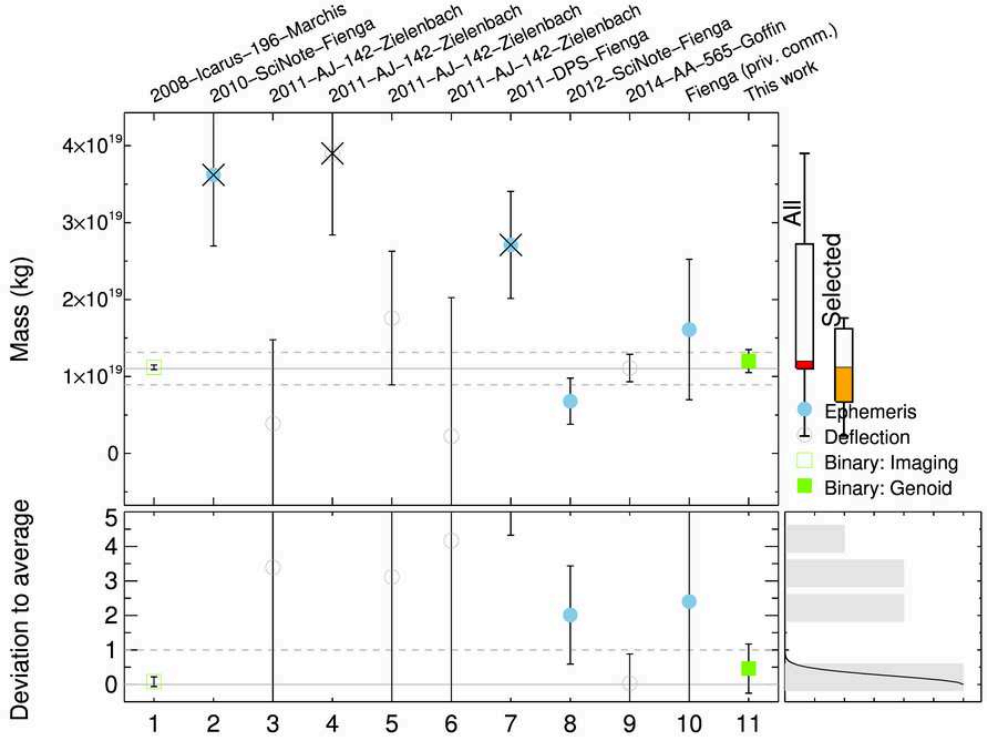


Figure 5.11 – Mass estimates of (107) Camilla gathered from the literature.

*(107) 1* and more eccentric. Predictions of the relative position of the satellite with respect to Camilla, critical for planning stellar occultations for instance, are available to the community through our VO service `Miriade` [5] [Berthier et al., 2008].

From the visible and near-infrared spectrum of Camilla, we classify it as an Xk-type asteroid, in the Bus-DeMeo taxonomy. Considering its low albedo, it would be classified as a P-type in older taxonomic schemes such as Tedesco's. Using VLT/SPHERE integral-field spectrograph, we measure the near-infrared spectrum of the largest satellite, *S/2001 (107) 1*, and compare it with Camilla. No significant difference are found. This together with its orbital parameters argue for a formation of the satellite by excavation from impact, re-accumulation of ejecta in orbit, and circularization by tides.

Using optical lightcurves, profiles from disk-resolved imaging, and stellar occultation events, we determine the spin-vector coordinates and 3-D shape of Camilla. The model fits very well each data set, and reveals two large depressions, reminiscent of impact craters. Either is large enough to be the progenitor of the satellites, and of a dynamical family, considering the comparable size of the nearby family of (87) Sylvia.

[5] http://vo.imcce.fr/

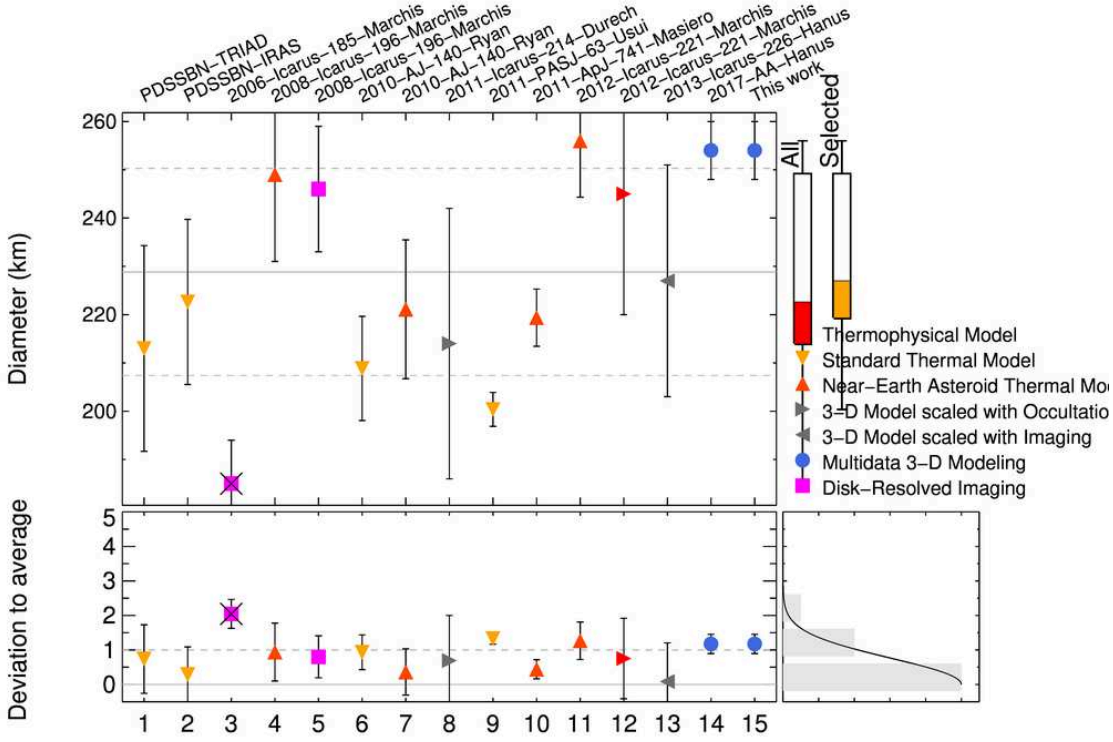


Figure 5.12 – Diameter estimates of (107) Camilla gathered from the literature.

# 6 Conclusions and Perspectives

Asteroids are leftovers of planetary formation, which have primordial information of the processes involved in the formation and evolution of the Solar System. In my PhD I have studied and characterized binary asteroids that serves as the closest laboratories to test properties and processes that are often difficult to probe by other means. With binaries we can obtain masses, and most importantly, densities of asteroids. That gives us information on the composition and structure of these bodies, which helps us to understand how the bodies formed. Information on the interior is something very difficult to acquire otherwise, because the majority of the information we have so far, comes from the surface of these minor bodies.

As part of my investigations I have:

1. Acquired near-infrared spectra of five binary asteroids without known taxonomy using Spex at NASA IRTF. Reduced the data and modeled the spectra to find the taxonomy and mineralogy of these binaries. I also collected 22 spectra of binary asteroids without known taxonomy from the SMASS collaboration database. I perform the modeling, find the best meteorite match from RELAB database and in this case, because I have a larger quantity, I performed a statistical analysis to find the distribution of taxonomy classes among small binaries, finding a predominance of Q-types compared with the S-types, in agreement with a formation of these systems by YORP spin-up and rotational disruption (Ch. 3).

2. Acknowledging the limitations of visible-only data (e.g SMASS and SDSS catalogs), and the difficulties to obtain large amounts of telescope time for acquiring time-consuming spectroscopy, I have worked with a large data set of near-infrared colors from VISTA VHS survey data (Ch. 4). I defined a new taxonomic scheme that will be useful for the community. Applied to VISTA data, this scheme allowed to determine the spectral class of more than 2,000 asteroids. It will open doors thanks to the future data releases from VISTA, and also Euclid and UKIDSS. Although this is a work in progress, I already obtained results that are in accordance to the previous works in the field of asteroid taxonomy, the distribution of asteroid taxonomy in the main belt I determined from

VISTA colors shows similar trends to those in the work by Gradie and Tedesco [1982].

3. I have been trained in stellar occultation detections, which along with radar detection, is a direct way to measure asteroid sizes, shapes and in the cases of binaries, the distance between the bodies (asteroid and satellite).

4. I have studied throughly the binary (107) Camilla (Ch. 5 ), a ~200 km binary asteroid. For Camilla I have collected all available information on AO images, lightcurves, occultations and VNIR spectra to characterize its composition, density and dynamical parameters. Asteroids behave differently according to their size, so to have the big picture on binaries it is important to deal also with large asteroids. This also is important to predict occultations. In fact, the occultation campaigns I have participated in, were all for binaries with large primaries.

Among the important things I learned to acquire information, I learned to make proposals to large telescope facilities: IRTF-Spex, VLT-Xshooter. Three times, I have been granted observing time at international telescopes.

I have observed from small and large telescopes, ~ 35 nights which includes occultations, photomometry, spectroscopy, and mineralogy. I have done the classification of large samples in order to determine physical and dynamical characteristics of binary asteroids using different tools.

Once back in Peru, I will have the task of teaching everything that I learned during this PhD. My long term plans involve forming a Solar System research group with physics students and researchers at my home institution, the Pontificia Universidad Católica del Perú. For that, I will take advantage of my on-going collaboration with european research groups, mainly with Paris Observatory's LESIA & IMCCE.

I plan to continue my research on binary asteroids, searching for more data that can give insights on this important population. I already obtained observing time at IRTF for the coming Semester 2017B for that purpose. An interesting issue is the finding about the Q/S population of small binaries that deserves more investigation and can help to refine the mechanisms that are behind the formation and evolution of these objects.

Building on my experience in observations, I plan to observe binary asteroid to obtain their multi-band photometry, i.e., colors with SDSS filters, and lightcurves, with small telescopes from Peru.

The observation of occultations has already begun via a previous collaboration with Bruno Sicardy's group (LESIA, Paris Observatory), who gave my home institution the kit to perform these observations in 2009. At that time we began with the observations, with emphasis on TNO's. We also received a FRIPON camera to install in Perú. We will be part of the world network for the detection of fireballs and recovery of meteorites. Our targets and duties have broadened.

# A An appendix

## A.1 Asteroid spectra vs meteorites spectra

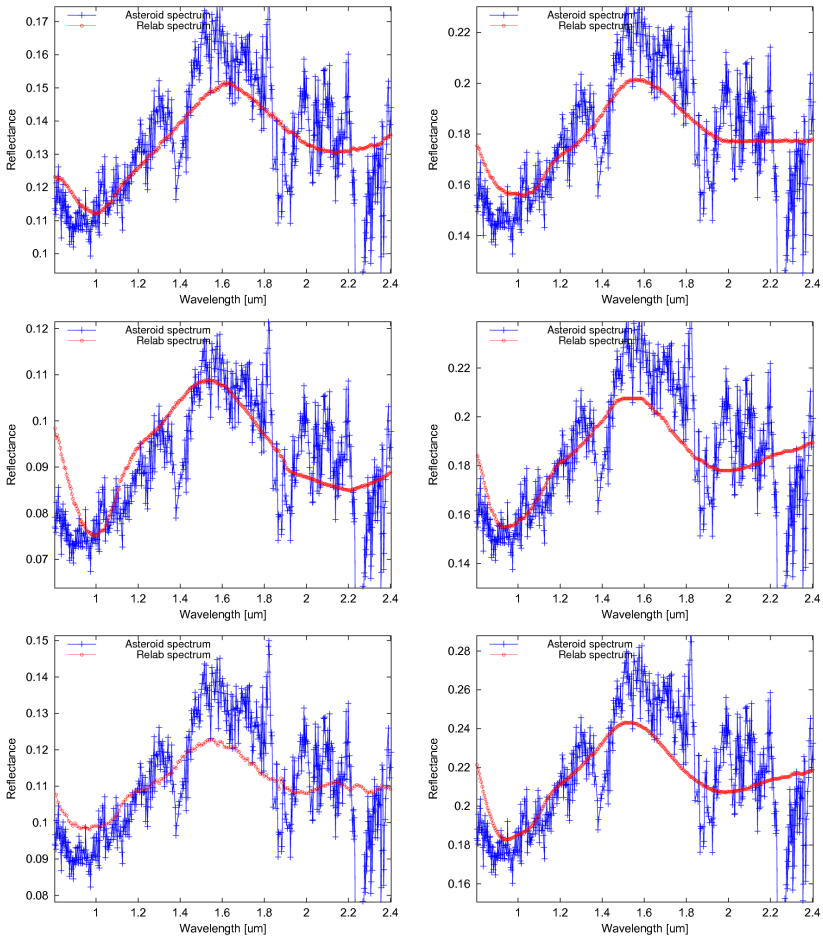


Figure A.1 – Reflectance spectrum of (2691) Sersic and closest matching results from meteorite comparison: a Shergottite Los Angeles (stone 1) (Sample ID MT-JLB-006-C); b LL4 ordinary chondrite Hamlet (Sample ID OC-TXH-002-A20); c Shergottite Los Angeles (Sample ID MT-JFM-005); d LL4 Amphoterite Ordinary Chondrite Soko-Banja (Sample ID MR-MJG-070); e L4 Ordinary Chondrite Barratta (Sample ID MH-CMP-002) and f) L4 Ordinary Chondrite Bjurbole unshaken (Sample ID MP-FPF-027).

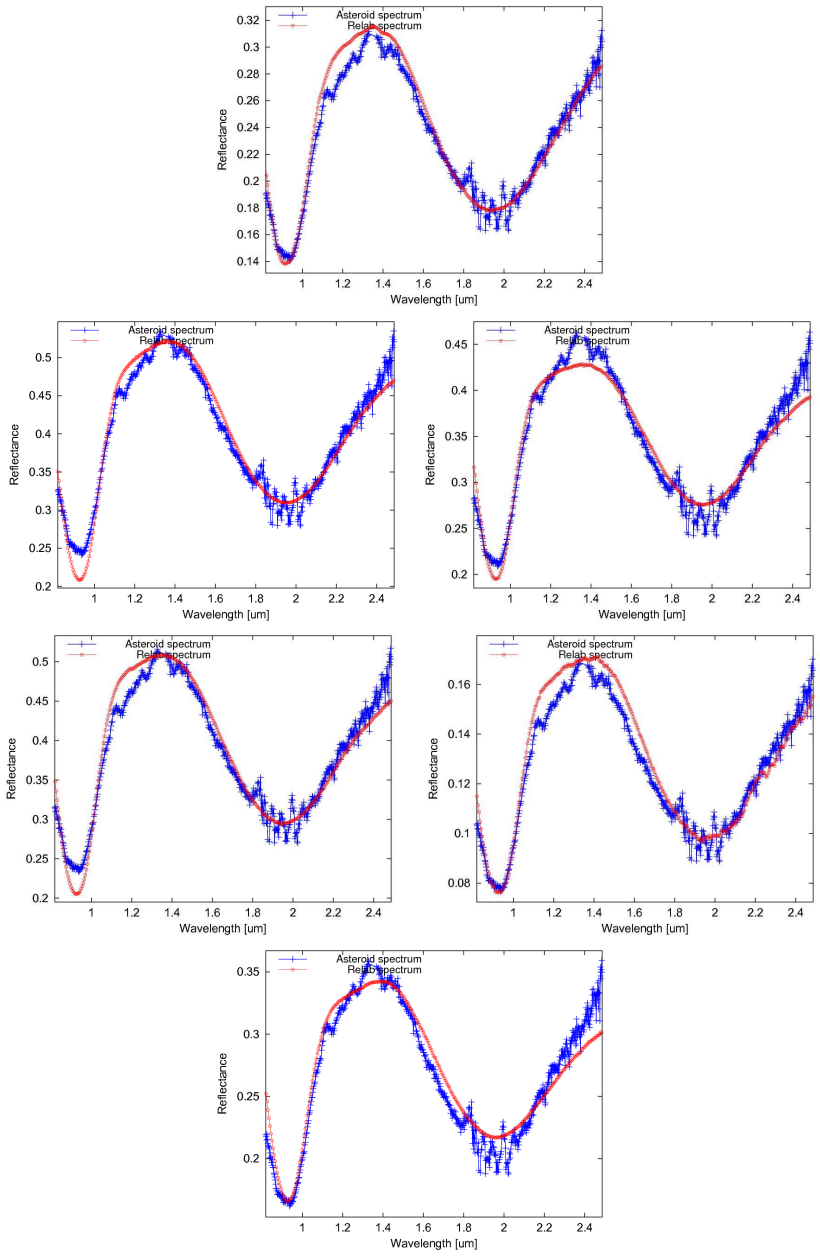


Figure A.2 – Reflectance spectrum of (4383) Suruga and closest matching results from meteorite comparison: a) achondrite Howardite Pavlovka (Sample ID MR-MJG-094); b) achondrite Basaltic HED Howardite Le Teilleul (Sample ID: MP-TXH-093-A); c) achondrite Basaltic HED howardite Frankfort howardite (Sample ID: MP-TXH-085-A); d) achondrite Basaltic HED howardite "Y-7308,142" (Sample ID: MP-TXH-097-A); e) achondrite Basaltic HED Howardite Regolith Breccia, Kapoeta P11410 (Sample ID: SN-CMP-012); and f) achondrite Basaltic HED howardite, "GRO95574,9 (Howardite) <125 um" (Sample ID: MP-TXH-125).

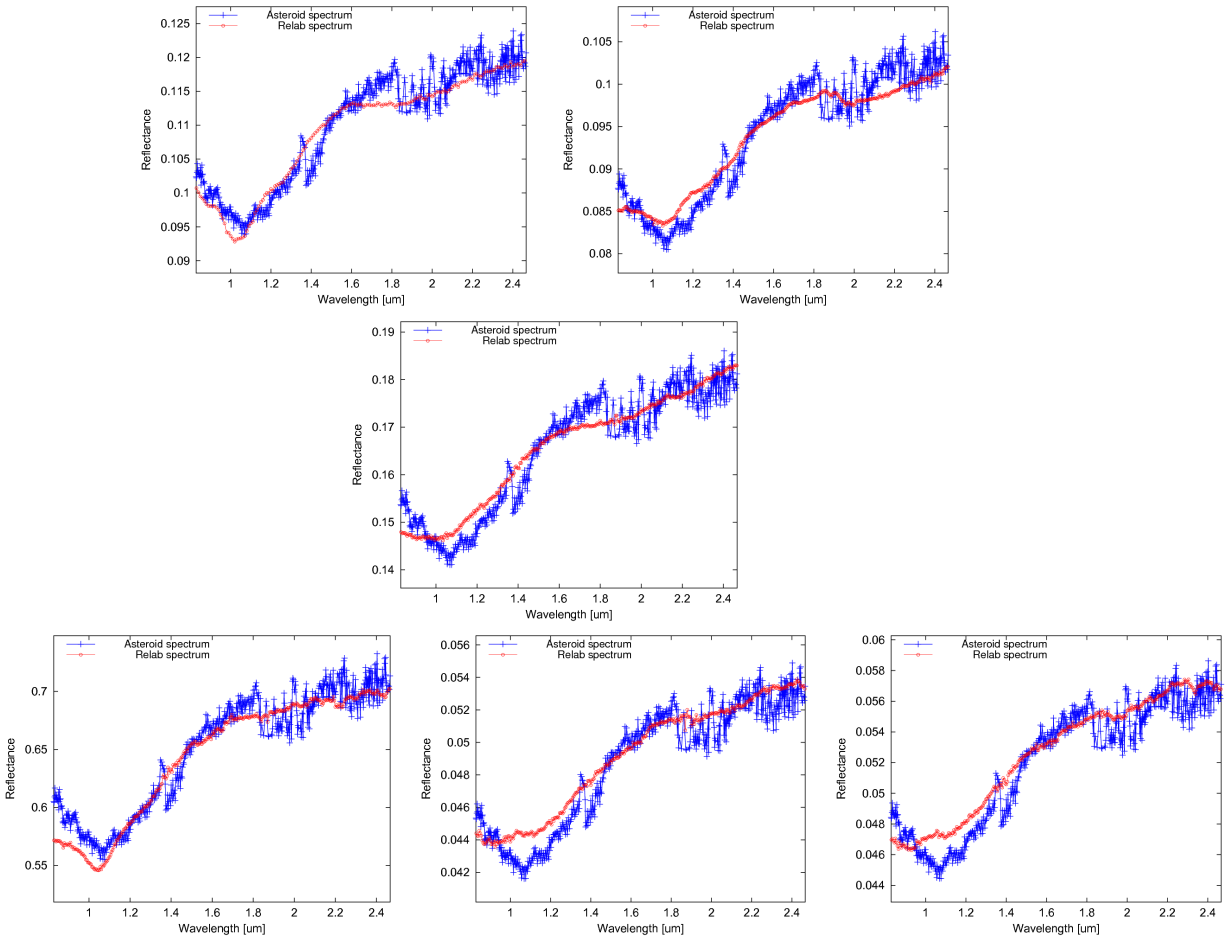


Figure A.3 – Reflectance spectrum of (7187) Isobe and closest matching results from meteorite comparison: a) achondrite Ureilite anomalous polymict Almahata Sitta #4 <125 $\mu$m (Sample ID: MT-PMJ-093-C), b) carbonaceous chondrite Allende: HC-10 dark inclusion (Sample ID: MT-TJM-073), c) ordinary chondrite Tsarev (Sample ID: MA-ATB-053), d) carbonaceous chondrite "LEW87009,16" (Sample ID: LM-LAM-011), e) carbonaceous chondrite "EET90021,10" (Sample ID: MP-TXH-043), and f) carbonaceous chondrite "LEW87148,15" (Sample ID: MP-TXH-016)

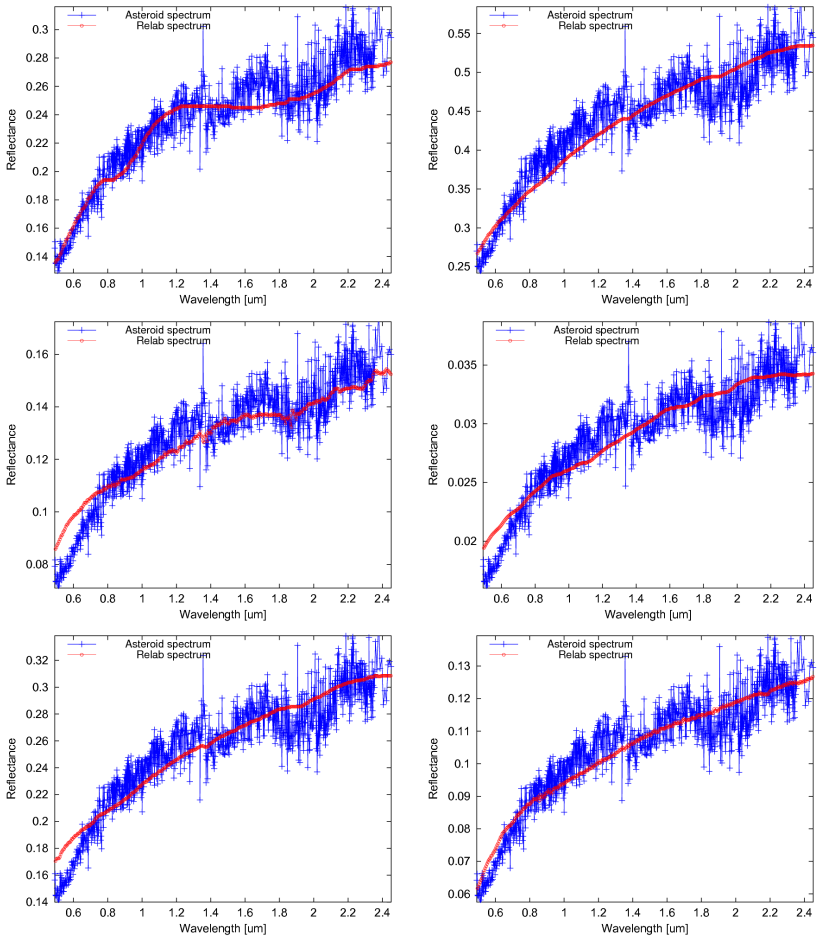


Figure A.4 – Comparison of (8373) Stephengould reflectance spectrum with Relab spectra of different meteorites. (8373) Stephengould spectrum was obtained from concatenation of two spectra, the visible part from de León et al. [2010] and the NIR part from the present work. The closest matching results are for the following meteorites: a) Veramin (Sample ID MR-MJG-084), b) Butler (Sample ID MR-MJG-081), c) Pervomaisky (Sample ID RS-CMP-064), d) Tagish Lake ET01-B (Sample ID MT-MEZ-011), e) Chulafinnee (Sample ID MR-MJG-082) and f) Mundrabilla troilite (Sample ID MB-CMP-006-P2).

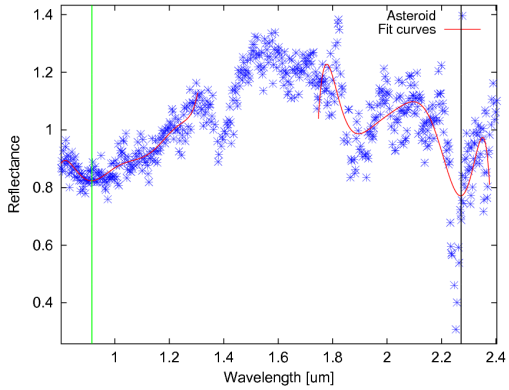


Figure A.5 – Band parameters of (2691) Sersic. Due to poor $S/N$, the analysis of this spectrum is very hard to do. Using `M4Ast` we obtain the first minimum BI at 0.9161±0.0050 $\mu$m, the second minimum BII is at 2.2718±0.0050 $\mu$m, however this part of the data is too nosy to trust that position. There are also spectral variations around 1.45 $\mu$m and 1.9 $\mu$m due to the influence of telluric water that remained after the data reduction.

## A.2 Asteroid Band parameters

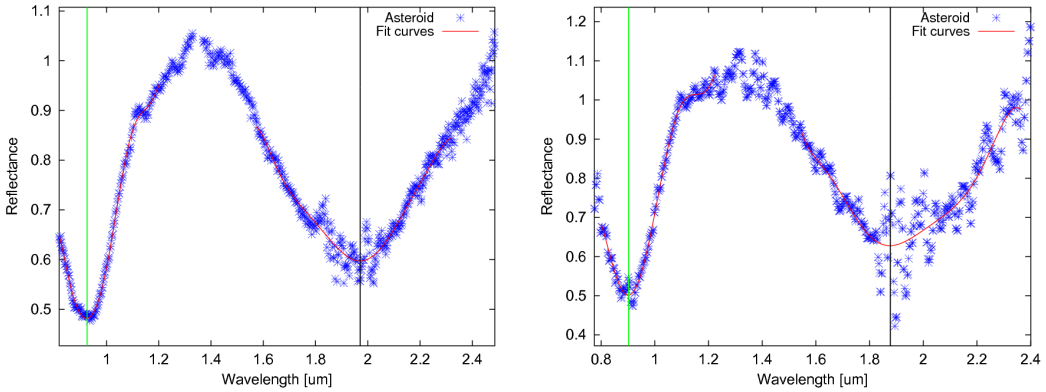


Figure A.6 – Band parameters of (4383) Suruga obtained with `M4Ast` *(Left)* Current work: BI= 0.9254±0.0007$\mu$m and BII= 1.9710±0.0042$\mu$m; *(Right)* de Sanctis et al. [2011] work BI= 0.9023±0.0018 $\mu$m and BII=1.8770±0.0072 $\mu$m. BI position is very similar between the two spectra, for BII the correspondence is not so good due to the noisy data around 1.9$\mu$m in de Sanctis et al. [2011].

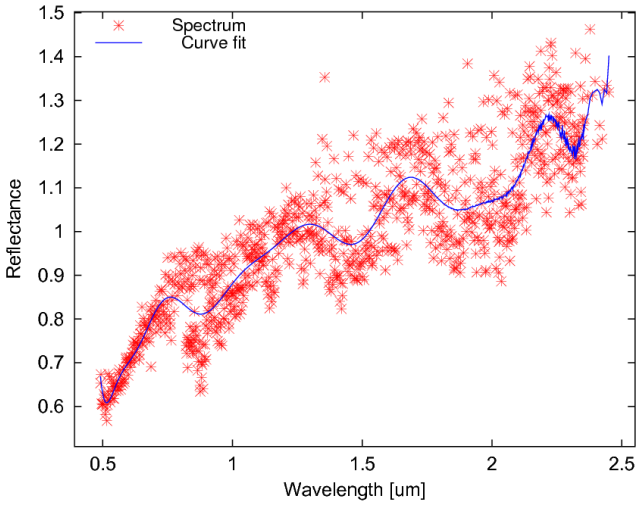


Figure A.7 – Merged spectra and curve fit of visible part of de León et al. [2010] spectrum from 2004 and this work NIR spectrum (2015) for (8373) Stephengould using `M4Ast` tool.

## A.3 (8373) Stephengould spectrum Analysis

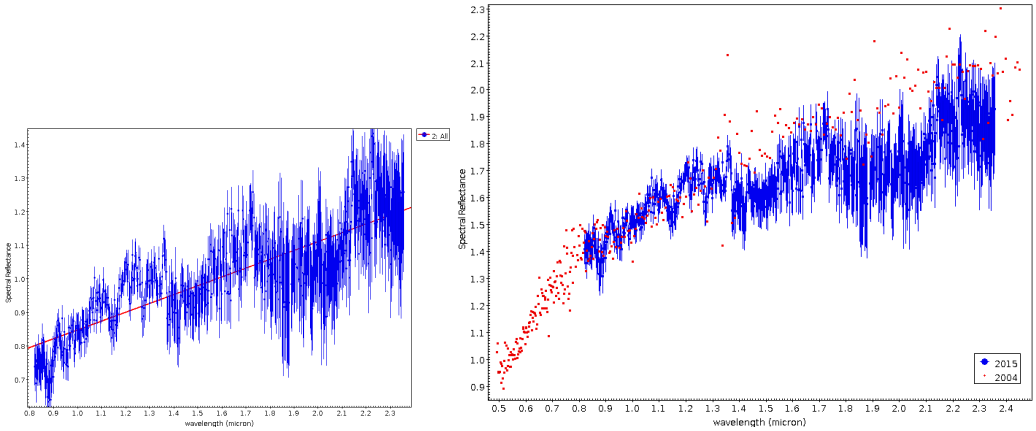


Figure A.8 – *(Left)* (8373) Stephengould linear fit (red) of NIR spectrum points with error bars (blue). Positive slope of 0.2624 with a correlation of 0.8212. *(Right)* superposition of VISNIR spectrum of de León et al. [2010] from 2004 and this work NIR spectrum (2015),

## A.4 Details on the observing data sets of (107) Camilla

We provide here the details for each lightcurve (Table A.1), disk-resolved image (Table A.2), and stellar occultation (Table A.3), as well as the astrometry and photometry of *S/2001 (107) 1* (Table A.4) and *S/2016 (107) 1* (Table A.5)

Table A.1 – Date, duration ($\mathscr{L}$, in hours), number of points ($\mathscr{N}_p$), phase angle ($\alpha$), filter, residual (against the shape model), IAU code, and observers, for each lightcurve.

| | Date | $\mathscr{L}$ (h) | $\mathscr{N}_p$ | $\alpha$ (°) | Filter | RMS (mag) | IAU | Observers |
|---|---|---|---|---|---|---|---|---|
| 1 | 1981-02-01 | 4.0 | 5 | 2.9 | V | 0.035 | 654 | Harris and Young [1989] |
| 2 | 1981-02-02 | 6.2 | 9 | 2.8 | V | 0.030 | 654 | Harris and Young [1989] |
| 3 | 1981-02-04 | 7.7 | 10 | 2.7 | V | 0.030 | 654 | Harris and Young [1989] |
| 4 | 1981-02-05 | 5.6 | 14 | 2.8 | V | 0.015 | 654 | Harris and Young [1989] |
| 5 | 1982-01-09 | 2.4 | 11 | 16.4 | V | 0.024 | 695 | Weidenschilling et al. [1987] |
| 6 | 1982-01-15 | 4.4 | 8 | 16.6 | V | 0.027 | 695 | Weidenschilling et al. [1987] |
| 7 | 1982-05-20 | 4.5 | 19 | 10.6 | V | 0.024 | 695 | Weidenschilling et al. [1987] |
| 8 | 1982-06-23 | 4.6 | 6 | 15.8 | V | 0.035 | 695 | Weidenschilling et al. [1987] |
| 9 | 1982-06-24 | 2.1 | 8 | 15.9 | V | 0.033 | 695 | Weidenschilling et al. [1987] |
| 10 | 1982-06-25 | 2.9 | 15 | 16.0 | V | 0.023 | 695 | Weidenschilling et al. [1987] |
| 11 | 1983-03-27 | 2.0 | 10 | 15.5 | V | 0.046 | 695 | Weidenschilling et al. [1987] |
| 12 | 1983-03-29 | 4.3 | 5 | 15.4 | V | 0.064 | 695 | Weidenschilling et al. [1987] |
| 13 | 1983-05-24 | 4.8 | 35 | 7.6 | V | 0.020 | 695 | Weidenschilling et al. [1987] |
| 14 | 1983-07-03 | 4.7 | 23 | 6.1 | V | 0.015 | 695 | Weidenschilling et al. [1987] |
| 15 | 1984-06-07 | 2.2 | 11 | 14.8 | V | 0.053 | 695 | Weidenschilling et al. [1987] |
| 16 | 1984-06-10 | 4.6 | 10 | 14.5 | V | 0.052 | 695 | Weidenschilling et al. [1987] |
| 17 | 1984-07-05 | 3.0 | 15 | 10.7 | V | 0.068 | 695 | Weidenschilling et al. [1987] |
| 18 | 1984-08-16 | 5.5 | 32 | 2.3 | V | 0.036 | 809 | di Martino et al. [1987] |
| 19 | 1985-10-20 | 4.6 | 21 | 3.0 | V | 0.025 | 695 | Weidenschilling et al. [1987] |
| 20 | 1987-02-06 | 2.7 | 20 | 13.6 | V | 0.029 | 695 | Weidenschilling et al. [1990] |
| 21 | 1987-02-07 | 4.7 | 17 | 13.8 | V | 0.037 | 695 | Weidenschilling et al. [1990] |
| 22 | 1988-04-25 | 4.7 | 15 | 13.1 | V | 0.040 | 695 | Weidenschilling et al. [1990] |
| 23 | 1988-04-26 | 3.6 | 20 | 13.3 | V | 0.034 | 695 | Weidenschilling et al. [1990] |
| 24 | 1988-04-29 | 2.9 | 16 | 13.9 | V | 0.052 | 695 | Weidenschilling et al. [1990] |
| 25 | 2004-09-19 | 6.8 | 15 | 2.0 | C | 0.028 | A14 | L. Bernasconi |
| 26 | 2004-11-05 | 5.6 | 37 | 13.7 | C | 0.052 | A14 | L. Bernasconi |
| 27 | 2008-05-31 | 1.5 | 44 | 13.5 | C | 0.036 | 181 | Polishook [2009] |
| 28 | 2008-06-27 | 1.7 | 63 | 16.6 | C | 0.028 | 181 | Polishook [2009] |
| 29 | 2008-06-28 | 2.0 | 82 | 16.6 | C | 0.023 | 181 | Polishook [2009] |
| 30 | 2010-07-09 | 2.7 | 86 | 10.7 | C | 0.040 | 615 | J. Montier & S. Heterier |

Continued on next page

Table A.1 – continued from previous page

| | Date | $\mathscr{L}$ (h) | $\mathscr{N}_p$ | $\alpha$ (°) | Filter | RMS (mag) | IAU | Observers |
|---|---|---|---|---|---|---|---|---|
| 31 | 2010-07-10 | 3.3 | 89 | 10.5 | C | 0.047 | 517 | F. Reignier |
| 32 | 2010-07-11 | 3.1 | 140 | 10.3 | C | 0.041 | 615 | J. Montier & S. Heterier |
| 33 | 2015-04-20 | 3.6 | 70 | 8.2 | R | 0.022 | 181 | F. Vachier |
| 34 | 2015-04-21 | 5.7 | 108 | 7.9 | R | 0.020 | 181 | F. Vachier |
| 35 | 2015-04-23 | 5.5 | 87 | 7.4 | R | 0.020 | 181 | F. Vachier |
| 36 | 2015-04-24 | 6.6 | 118 | 7.2 | R | 0.015 | 181 | F. Vachier |
| 37 | 2015-05-09 | 1.4 | 24 | 3.9 | R | 0.026 | 181 | F. Vachier |
| 38 | 2015-05-11 | 4.9 | 84 | 3.6 | R | 0.015 | 181 | F. Vachier |
| 39 | 2015-05-12 | 5.8 | 44 | 3.6 | R | 0.022 | 181 | F. Vachier |
| 40 | 2015-05-13 | 5.2 | 85 | 3.5 | R | 0.015 | 181 | F. Vachier |
| 41 | 2015-05-17 | 3.8 | 58 | 3.5 | R | 0.018 | 181 | F. Vachier |
| 42 | 2015-05-18 | 5.8 | 89 | 3.6 | R | 0.013 | 181 | F. Vachier |
| 43 | 2015-05-19 | 5.1 | 61 | 3.7 | R | 0.017 | 181 | F. Vachier |
| 44 | 2015-05-20 | 6.0 | 91 | 3.8 | R | 0.015 | 181 | F. Vachier |
| 45 | 2015-05-21 | 5.8 | 106 | 4.0 | R | 0.016 | 181 | F. Vachier |
| 46 | 2015-05-22 | 5.4 | 98 | 4.1 | R | 0.015 | 181 | F. Vachier |
| 47 | 2015-05-23 | 6.3 | 102 | 4.3 | R | 0.016 | 181 | F. Vachier |
| 48 | 2015-05-24 | 1.0 | 14 | 4.5 | R | 0.014 | 181 | F. Vachier |
| 49 | 2015-05-26 | 1.9 | 36 | 4.9 | R | 0.018 | 181 | F. Vachier |
| 50 | 2015-06-03 | 3.6 | 68 | 6.8 | R | 0.016 | 181 | F. Vachier |
| 51 | 2015-06-03 | 5.5 | 251 | 6.8 | V | 0.020 | 517 | D. Romeuf |
| 52 | 2015-06-04 | 4.2 | 76 | 7.0 | R | 0.017 | 181 | F. Vachier |
| 53 | 2015-06-05 | 5.0 | 75 | 7.3 | R | 0.016 | 181 | F. Vachier |
| 54 | 2015-06-05 | 4.9 | 274 | 7.3 | V | 0.020 | 517 | D. Romeuf |
| 55 | 2015-06-09 | 3.2 | 59 | 8.3 | R | 0.020 | 181 | F. Vachier |
| 56 | 2015-06-10 | 3.0 | 38 | 8.5 | R | 0.019 | 181 | F. Vachier |
| 57 | 2015-06-11 | 1.4 | 27 | 8.7 | R | 0.024 | 181 | F. Vachier |
| 58 | 2015-06-17 | 5.4 | 98 | 10.1 | R | 0.020 | 181 | F. Vachier |
| 59 | 2015-06-20 | 28.2 | 376 | 10.7 | R | 0.019 | 586 | S. Fauvaud |
| 60 | 2015-06-22 | 5.8 | 104 | 11.2 | R | 0.046 | 181 | F. Vachier |
| 61 | 2015-06-23 | 2.2 | 40 | 11.4 | R | 0.029 | 181 | F. Vachier |
| 62 | 2015-06-25 | 4.7 | 88 | 11.8 | R | 0.021 | 181 | F. Vachier |
| 63 | 2015-06-26 | 3.8 | 70 | 12.0 | R | 0.022 | 181 | F. Vachier |
| 64 | 2015-07-06 | 3.8 | 71 | 13.7 | R | 0.020 | 181 | F. Vachier |
| 65 | 2016-04-30 | 1.1 | 19 | 15.5 | R | 0.026 | 181 | F. Vachier |
| 66 | 2016-05-02 | 1.3 | 25 | 15.4 | R | 0.046 | 181 | F. Vachier |
| 67 | 2016-05-03 | 1.4 | 26 | 15.3 | R | 0.036 | 181 | F. Vachier |
| 68 | 2016-05-05 | 1.5 | 28 | 15.2 | R | 0.044 | 181 | F. Vachier |

Continued on next page

Table A.1 – continued from previous page

| | Date | $\mathscr{L}$ (h) | $\mathscr{N}_p$ | $\alpha$ (°) | Filter | RMS (mag) | IAU | Observers |
|---|---|---|---|---|---|---|---|---|
| 69 | 2016-05-08 | 1.7 | 32 | 15.0 | R | 0.051 | 181 | F. Vachier |
| 70 | 2016-05-09 | 1.0 | 9 | 14.9 | R | 0.021 | 181 | F. Vachier |

Table A.2 – Date, mid-observing time (UTC), heliocentric distance ($\Delta$) and range to observer ($r$), phase angle ($\alpha$), apparent size ($\Theta$), longitude ($\lambda$) and latitude ($\beta$) of the subsolar and subobserver points (SSP, SEP).

| | Date | UTC | $\Delta$ (AU) | $r$ (AU) | $\alpha$ (°) | $\Theta$ ($''$) | $\mathrm{SEP}_\lambda$ (°) | $\mathrm{SEP}_\beta$ (°) | $\mathrm{SSP}_\lambda$ (°) | $\mathrm{SSP}_\beta$ (°) |
|---|---|---|---|---|---|---|---|---|---|---|
| 1 | 2003-06-06 | 12:54:27 | 3.74 | 2.97 | 11.3 | 0.127 | 29.3 | 9.9 | 19.9 | 16.5 |
| 2 | 2003-08-15 | 08:35:22 | 3.75 | 2.87 | 8.5 | 0.119 | 42.5 | 14.6 | 51.3 | 13.7 |
| 3 | 2003-08-17 | 10:50:07 | 3.75 | 2.88 | 9.0 | 0.117 | 268.3 | 14.8 | 277.5 | 13.6 |
| 4 | 2009-06-07 | 10:29:13 | 3.68 | 2.71 | 5.0 | 0.111 | 333.0 | 17.7 | 330.2 | 22.0 |
| 5 | 2009-06-07 | 10:54:07 | 3.68 | 2.71 | 5.0 | 0.114 | 302.2 | 17.7 | 299.3 | 22.0 |
| 6 | 2009-06-07 | 11:25:55 | 3.68 | 2.71 | 5.0 | 0.124 | 262.8 | 17.7 | 259.9 | 22.0 |
| 7 | 2009-08-16 | 06:47:01 | 3.71 | 3.14 | 14.1 | 0.099 | 307.3 | 21.1 | 322.3 | 20.2 |
| 8 | 2010-06-28 | 10:19:28 | 3.74 | 3.04 | 12.6 | 0.116 | 227.0 | -0.9 | 217.0 | 6.9 |
| 9 | 2003-07-15 | 07:32:49 | 3.75 | 2.75 | 3.3 | 0.188 | 337.0 | 11.8 | 337.6 | 15.0 |
| 10 | 2004-09-01 | 05:07:38 | 3.66 | 2.67 | 3.7 | 0.107 | 128.4 | -8.1 | 125.5 | -5.9 |
| 11 | 2004-09-01 | 05:17:22 | 3.66 | 2.67 | 3.7 | 0.118 | 116.4 | -8.1 | 113.4 | -5.9 |
| 12 | 2004-09-01 | 05:33:49 | 3.66 | 2.67 | 3.7 | 0.078 | 96.0 | -8.1 | 93.0 | -5.9 |
| 13 | 2004-09-01 | 05:54:54 | 3.66 | 2.67 | 3.7 | 0.157 | 69.9 | -8.1 | 66.9 | -5.9 |
| 14 | 2004-09-01 | 06:03:54 | 3.66 | 2.67 | 3.7 | 0.159 | 58.7 | -8.1 | 55.8 | -5.9 |
| 15 | 2004-09-01 | 08:25:33 | 3.66 | 2.67 | 3.6 | 0.156 | 243.2 | -8.1 | 240.3 | -5.9 |
| 16 | 2004-09-01 | 08:06:42 | 3.66 | 2.67 | 3.7 | 0.129 | 266.6 | -8.1 | 263.7 | -5.9 |
| 17 | 2004-09-03 | 06:51:57 | 3.66 | 2.66 | 3.1 | 0.129 | 31.5 | -7.9 | 29.1 | -6.0 |
| 18 | 2004-09-04 | 09:02:35 | 3.66 | 2.66 | 2.7 | 0.129 | 245.8 | -7.7 | 243.7 | -6.0 |
| 19 | 2004-09-05 | 04:28:19 | 3.66 | 2.66 | 2.5 | 0.137 | 241.7 | -7.6 | 239.8 | -6.1 |
| 20 | 2004-09-06 | 03:35:30 | 3.66 | 2.65 | 2.2 | 0.100 | 323.3 | -7.5 | 321.7 | -6.1 |
| 21 | 2004-09-07 | 02:20:10 | 3.66 | 2.65 | 1.9 | 0.126 | 72.8 | -7.4 | 71.4 | -6.2 |
| 22 | 2004-09-08 | 06:41:20 | 3.65 | 2.65 | 1.5 | 0.119 | 125.5 | -7.2 | 124.4 | -6.2 |
| 23 | 2004-09-11 | 04:34:26 | 3.65 | 2.65 | 0.6 | 0.130 | 331.2 | -6.9 | 330.8 | -6.4 |
| 24 | 2004-09-13 | 03:42:51 | 3.65 | 2.65 | 0.2 | 0.142 | 67.5 | -6.6 | 67.6 | -6.5 |
| 25 | 2004-09-13 | 05:47:28 | 3.65 | 2.65 | 0.2 | 0.126 | 273.1 | -6.6 | 273.3 | -6.5 |
| 26 | 2004-09-14 | 04:09:30 | 3.65 | 2.65 | 0.4 | 0.138 | 50.6 | -6.5 | 51.1 | -6.6 |
| 27 | 2004-09-14 | 07:06:44 | 3.65 | 2.65 | 0.5 | 0.139 | 191.1 | -6.5 | 191.5 | -6.6 |

Continued on next page

Table A.2 – continued from previous page

| | Date | UTC | $\Delta$ (AU) | $r$ (AU) | $\alpha$ (°) | $\Theta$ ($''$) | $SEP_\lambda$ (°) | $SEP_\beta$ (°) | $SSP_\lambda$ (°) | $SSP_\beta$ (°) |
|---|---|---|---|---|---|---|---|---|---|---|
| 28 | 2004-09-14 | 07:14:31 | 3.65 | 2.65 | 0.5 | 0.133 | 181.4 | -6.5 | 181.9 | -6.6 |
| 29 | 2004-09-15 | 04:18:34 | 3.65 | 2.65 | 0.7 | 0.140 | 55.6 | -6.4 | 56.3 | -6.6 |
| 30 | 2004-09-15 | 04:26:55 | 3.65 | 2.65 | 0.7 | 0.134 | 45.2 | -6.4 | 45.9 | -6.6 |
| 31 | 2004-09-16 | 04:48:18 | 3.65 | 2.65 | 1.1 | 0.134 | 35.0 | -6.2 | 35.9 | -6.7 |
| 32 | 2004-10-07 | 02:12:52 | 3.64 | 2.72 | 7.4 | 0.141 | 208.5 | -3.8 | 214.7 | -7.8 |
| 33 | 2004-10-08 | 02:22:37 | 3.64 | 2.73 | 7.6 | 0.136 | 212.7 | -3.7 | 219.2 | -7.8 |
| 34 | 2004-10-08 | 04:47:21 | 3.64 | 2.73 | 7.7 | 0.153 | 33.5 | -3.6 | 39.9 | -7.8 |
| 35 | 2004-10-20 | 00:39:21 | 3.63 | 2.83 | 10.6 | 0.117 | 176.7 | -2.6 | 185.5 | -8.5 |
| 36 | 2011-09-29 | 05:21:18 | 3.52 | 2.57 | 5.6 | 0.147 | 202.6 | -17.5 | 196.8 | -16.7 |
| 37 | 2011-11-08 | 03:21:35 | 3.50 | 2.59 | 7.7 | 0.131 | 278.0 | -13.5 | 284.3 | -18.4 |
| 38 | 2011-11-10 | 01:22:04 | 3.50 | 2.61 | 8.2 | 0.134 | 98.6 | -13.4 | 105.4 | -18.5 |
| 39 | 2015-05-29 | 04:38:45 | 3.58 | 2.61 | 5.4 | 0.120 | 345.4 | 19.5 | 349.4 | 23.5 |
| 40 | 2015-05-29 | 04:51:26 | 3.58 | 2.61 | 5.4 | 0.118 | 329.7 | 19.5 | 333.7 | 23.5 |
| 41 | 2015-05-29 | 05:07:36 | 3.58 | 2.61 | 5.5 | 0.120 | 309.7 | 19.5 | 313.7 | 23.5 |
| 42 | 2015-05-29 | 05:15:12 | 3.58 | 2.61 | 5.5 | 0.122 | 300.3 | 19.5 | 304.2 | 23.5 |
| 43 | 2015-05-29 | 05:25:54 | 3.58 | 2.61 | 5.5 | 0.125 | 287.0 | 19.5 | 291.0 | 23.5 |
| 44 | 2015-05-29 | 05:28:58 | 3.58 | 2.61 | 5.5 | 0.126 | 283.2 | 19.5 | 287.2 | 23.5 |
| 45 | 2015-05-29 | 05:32:04 | 3.58 | 2.61 | 5.5 | 0.127 | 279.4 | 19.5 | 283.4 | 23.5 |
| 46 | 2016-07-02 | 08:49:12 | 3.72 | 2.74 | 5.2 | 0.149 | 150.4 | 11.4 | 147.8 | 15.9 |
| 47 | 2016-07-02 | 08:56:24 | 3.72 | 2.74 | 5.2 | 0.158 | 141.5 | 11.4 | 138.9 | 15.9 |
| 48 | 2016-07-02 | 09:03:36 | 3.72 | 2.74 | 5.2 | 0.152 | 132.6 | 11.4 | 130.0 | 15.9 |
| 49 | 2016-07-12 | 05:06:10 | 3.72 | 2.72 | 3.4 | 0.140 | 228.2 | 12.1 | 228.4 | 15.5 |
| 50 | 2016-07-12 | 05:13:32 | 3.72 | 2.72 | 3.4 | 0.142 | 219.0 | 12.1 | 219.3 | 15.5 |
| 51 | 2016-07-12 | 05:20:55 | 3.72 | 2.72 | 3.4 | 0.137 | 209.9 | 12.1 | 210.1 | 15.5 |
| 52 | 2016-07-28 | 05:52:47 | 3.72 | 2.74 | 4.8 | 0.139 | 69.3 | 13.5 | 74.1 | 14.8 |
| 53 | 2016-07-28 | 05:59:03 | 3.72 | 2.74 | 4.8 | 0.139 | 61.6 | 13.5 | 66.4 | 14.8 |
| 54 | 2016-07-28 | 06:05:21 | 3.72 | 2.74 | 4.8 | 0.140 | 53.8 | 13.5 | 58.6 | 14.8 |
| 55 | 2016-07-30 | 01:39:02 | 3.72 | 2.75 | 5.2 | 0.128 | 56.1 | 13.7 | 61.4 | 14.8 |
| 56 | 2016-07-30 | 01:46:07 | 3.72 | 2.75 | 5.2 | 0.129 | 47.3 | 13.7 | 52.6 | 14.8 |
| 57 | 2016-07-30 | 01:53:12 | 3.72 | 2.75 | 5.2 | 0.130 | 38.6 | 13.7 | 43.8 | 14.8 |
| 58 | 2016-08-11 | 00:14:23 | 3.72 | 2.81 | 8.1 | 0.124 | 356.1 | 14.8 | 4.4 | 14.2 |
| 59 | 2016-08-11 | 00:20:33 | 3.72 | 2.81 | 8.1 | 0.123 | 348.4 | 14.8 | 356.7 | 14.2 |
| 60 | 2016-08-11 | 02:43:24 | 3.72 | 2.81 | 8.1 | 0.125 | 171.5 | 14.8 | 179.8 | 14.2 |
| 61 | 2016-08-11 | 02:50:31 | 3.72 | 2.81 | 8.1 | 0.127 | 162.6 | 14.8 | 171.0 | 14.2 |
| 62 | 2016-08-11 | 02:57:41 | 3.72 | 2.81 | 8.1 | 0.126 | 153.8 | 14.8 | 162.1 | 14.2 |

Table A.3 – Date, number of positive and negative chords ($\#_p$ and $\#_n$), average uncertainty in seconds ($\sigma_s$) and kilometers ($\sigma_k$), and RMS residuals with seconds, kilometers, and expressed in amount of standard deviation.

| | Date | UT (h) | $\#_p$ | $\#_n$ | $\sigma_s$ (s) | $\sigma_k$ (km) | RMS$_s$ (s) | RMS$_k$ (km) | RMS$_\sigma$ ($\sigma$) |
|---|---|---|---|---|---|---|---|---|---|
| 1 | 2004-09-05 | 08:54 | 3 | 0 | 0.73 | 17.831 | 0.860 | 32.358 | 3.277 |
| 2 | 2010-09-16 | 04:01 | 1 | 1 | 0.05 | 0.267 | 0.066 | 0.995 | 1.318 |
| 3 | 2015-01-01 | 11:26 | 1 | 2 | 0.22 | 2.445 | 0.017 | 0.975 | 0.077 |
| 4 | 2015-02-12 | 11:58 | 2 | 0 | 0.20 | 6.728 | 1.230 | 22.304 | 8.171 |
| 5 | 2015-05-06 | 05:23 | 3 | 4 | 0.33 | 3.831 | 0.389 | 13.324 | 13.219 |
| 6 | 2015-08-23 | 04:17 | 6 | 5 | 0.15 | 4.994 | 0.072 | 8.039 | 2.362 |
| 7 | 2016-07-21 | 07:42 | 5 | 5 | 0.56 | 5.060 | 0.579 | 18.920 | 3.067 |
| 0 | Average | – | 3 | 2 | 0.32 | 5.880 | 0.459 | 13.845 | 4.499 |

Table A.4 – Astrometry of *S/2001 (107) 1*. Date, mid-observing time (UTC), telescope, camera, filter, astrometry ($X$ is aligned with Right Ascension, and $Y$ with Declination, and $o$ and $c$ indices stand for observed and computed positions), and photometry (magnitude difference $\Delta M$ with uncertainty $\delta M$).

| Date | UTC | Tel. | Cam. | Filter | $X_o$ (mas) | $Y_o$ (mas) | $X_{o-c}$ (mas) | $Y_{o-c}$ (mas) | $\sigma$ (mas) | $\Delta M$ (mag) | $\delta M$ (mag) |
|---|---|---|---|---|---|---|---|---|---|---|---|
| 2001-03-01 | 05:48:13.0 | HST | ACS | F439W | -573 | -84 | -22 | 3 | 10.00 | 0.00 | 0.00 |
| 2001-03-01 | 06:00:12.9 | HST | ACS | F791W | -565 | -70 | -20 | 15 | 10.00 | 0.00 | 0.00 |
| 2002-05-08 | 10:46:01.0 | Keck | NIRC2 | Kp | 472 | -189 | -2 | 14 | 9.94 | 6.34 | 1.50 |
| 2003-06-06 | 14:03:06.0 | Keck | NIRC2 | Ks | 402 | -214 | -4 | -8 | 9.94 | 6.53 | 1.18 |
| 2003-06-06 | 14:08:23.2 | Keck | NIRC2 | Ks | 406 | -213 | 1 | -8 | 9.94 | 7.18 | 0.45 |
| 2003-06-06 | 14:13:30.3 | Keck | NIRC2 | Ks | 402 | -218 | 0 | -12 | 9.94 | 6.31 | 0.23 |
| 2003-07-15 | 07:32:50.5 | VLT | NACO | H | -540 | 216 | 6 | 8 | 27.00 | 6.56 | 0.02 |
| 2003-07-15 | 07:37:26.2 | VLT | NACO | H | -536 | 222 | 8 | 13 | 27.00 | 6.34 | 0.14 |
| 2003-08-14 | 08:43:13.1 | Keck | NIRC2 | H | -249 | 232 | 10 | -4 | 9.94 | 6.88 | 1.94 |
| 2003-08-14 | 10:35:08.0 | Keck | NIRC2 | H | -183 | 227 | 5 | -3 | 9.94 | 5.04 | 3.68 |
| 2003-08-15 | 08:35:22.2 | Keck | NIRC2 | Kp | 554 | -62 | 7 | -2 | 9.94 | 6.67 | 0.18 |
| 2003-08-15 | 08:39:27.2 | Keck | NIRC2 | Kp | 550 | -66 | 2 | -5 | 9.94 | 6.62 | 0.31 |
| 2003-08-17 | 10:50:08.0 | Keck | NIRC2 | Kp | -568 | 146 | 5 | 3 | 9.94 | 6.55 | 1.21 |
| 2003-08-17 | 10:53:39.3 | Keck | NIRC2 | Kp | -567 | 144 | 6 | 1 | 9.94 | 6.39 | 0.66 |
| 2004-09-01 | 05:07:38.3 | VLT | NACO | Ks | 504 | -164 | 7 | 1 | 13.24 | 6.06 | 0.31 |
| 2004-09-01 | 05:17:22.2 | VLT | NACO | H | 510 | -165 | 8 | 0 | 13.24 | 6.34 | 0.24 |
| 2004-09-01 | 08:06:43.4 | VLT | NACO | Ks | 576 | -169 | 11 | -1 | 13.24 | 6.98 | 0.43 |
| 2004-09-03 | 06:51:57.5 | VLT | NACO | Ks | -623 | 166 | -25 | 2 | 13.24 | 6.76 | 0.70 |
| 2004-09-05 | 04:28:20.2 | VLT | NACO | Ks | 624 | -163 | 9 | 0 | 13.24 | 6.73 | 0.09 |

Continued on next page

Table A.4 – continued from previous page

| Date | UTC | Tel. | Cam. | Filter | $X_o$ (mas) | $Y_o$ (mas) | $X_{o-c}$ (mas) | $Y_{o-c}$ (mas) | $\sigma$ (mas) | $\Delta M$ (mag) |
|---|---|---|---|---|---|---|---|---|---|---|
| 2004-09-08 | 06:41:20.2 | VLT | NACO | Ks | 211 | -120 | 5 | -9 | 13.24 | 6.95 |
| 2004-09-11 | 04:34:26.2 | VLT | NACO | Ks | -539 | 87 | -8 | -10 | 13.24 | 7.09 |
| 2004-09-13 | 03:42:52.5 | VLT | NACO | Ks | 470 | -75 | 1 | 1 | 13.24 | 7.23 |
| 2004-09-13 | 05:47:28.2 | VLT | NACO | Ks | 386 | -46 | -16 | 7 | 13.24 | 6.08 |
| 2004-09-14 | 04:09:30.3 | VLT | NACO | Ks | -500 | 153 | -13 | -1 | 13.24 | 6.59 |
| 2004-09-15 | 04:18:34.3 | VLT | NACO | Ks | -321 | 35 | -2 | 4 | 13.24 | 6.28 |
| 2004-09-15 | 04:26:56.5 | VLT | NACO | H | -315 | 36 | -2 | 6 | 13.24 | 7.30 |
| 2004-10-07 | 02:02:03.0 | VLT | NACO | Ks | -540 | 123 | 1 | -5 | 13.24 | 8.49 |
| 2004-10-08 | 02:22:38.3 | VLT | NACO | Ks | 356 | -106 | 5 | 0 | 13.24 | 8.22 |
| 2004-10-08 | 04:47:21.2 | VLT | NACO | Ks | 435 | -125 | 5 | -1 | 13.24 | 7.07 |
| 2004-10-20 | 00:39:22.2 | VLT | NACO | Ks | 553 | -136 | 9 | 0 | 13.24 | 6.55 |
| 2004-11-02 | 07:36:13.0 | Gemini | NIRI | Kp | -344 | 88 | -3 | 0 | 21.90 | 6.49 |
| 2004-11-02 | 07:38:36.9 | Gemini | NIRI | Kp | -340 | 90 | 0 | 2 | 21.90 | 6.40 |
| 2004-11-05 | 08:09:18.1 | Gemini | NIRI | Kp | -538 | 138 | -9 | 2 | 21.90 | 5.95 |
| 2005-12-21 | 09:05:51.5 | Gemini | NIRI | Ks | 684 | 0 | 11 | -4 | 21.90 | 6.53 |
| 2006-01-01 | 10:17:12.1 | Gemini | NIRI | Ks | 651 | -35 | 9 | -5 | 21.90 | 6.71 |
| 2006-01-09 | 05:20:11.1 | Gemini | NIRI | Ks | 557 | 116 | 18 | 3 | 21.90 | 5.86 |
| 2006-01-16 | 05:16:51.5 | Gemini | NIRI | Ks | 619 | -17 | 25 | 33 | 21.90 | 5.85 |
| 2009-06-07 | 10:29:14.1 | Keck | NIRC2 | H | 510 | 54 | 1 | -1 | 9.94 | 6.56 |
| 2009-06-07 | 10:32:18.1 | Keck | NIRC2 | H | 511 | 55 | 1 | 0 | 9.94 | 6.49 |
| 2009-06-07 | 10:54:08.0 | Keck | NIRC2 | Kp | 516 | 55 | -2 | 7 | 9.94 | 6.23 |
| 2009-06-07 | 11:23:04.0 | Keck | NIRC2 | Kp | 530 | 44 | 0 | 5 | 9.94 | 6.56 |
| 2009-06-07 | 11:25:56.5 | Keck | NIRC2 | Kp | 530 | 39 | 0 | 0 | 9.94 | 6.66 |
| 2009-08-16 | 06:47:02.0 | Keck | NIRC2 | FeII | -36 | 239 | 6 | 1 | 9.94 | 6.99 |
| 2010-08-15 | 08:07:02.0 | Gemini | NIRI | Kp | -421 | 182 | -2 | 14 | 21.90 | 5.84 |
| 2010-08-15 | 08:16:53.5 | Gemini | NIRI | Kp | -412 | 181 | 1 | 13 | 21.90 | 6.40 |
| 2010-08-28 | 08:49:11.1 | Gemini | NIRI | Kp | 379 | -189 | 0 | -14 | 21.90 | 6.05 |
| 2010-08-28 | 08:54:01.0 | Gemini | NIRI | Kp | 378 | -186 | 1 | -11 | 21.90 | 6.52 |
| 2010-09-02 | 06:45:32.3 | Gemini | NIRI | Kp | -588 | 157 | -7 | 10 | 21.90 | 6.02 |
| 2010-10-31 | 05:58:48.4 | Gemini | NIRI | Kp | -271 | -8 | 24 | -8 | 21.90 | 6.67 |
| 2010-10-31 | 06:03:23.2 | Gemini | NIRI | Kp | -290 | -2 | 7 | -2 | 21.90 | 6.87 |
| 2011-09-27 | 05:04:41.0 | VLT | NACO | H | -287 | 236 | 2 | 13 | 13.24 | 6.39 |
| 2011-09-29 | 05:21:18.1 | VLT | NACO | H | 440 | -217 | -1 | -8 | 13.24 | 7.04 |
| 2011-11-08 | 03:21:35.3 | VLT | NACO | H | -438 | -61 | -9 | 0 | 13.24 | 6.66 |
| 2011-11-10 | 01:22:04.0 | VLT | NACO | H | 386 | 93 | 5 | 19 | 13.24 | 7.35 |
| 2015-05-29 | 04:38:46.4 | VLT | SPHERE | YJH | -184 | 237 | 6 | -2 | 7.40 | 6.28 |
| 2015-05-29 | 04:38:46.4 | VLT | SPHERE | Ks | -188 | 240 | 2 | 0 | 12.26 | 6.29 |
| 2015-05-29 | 04:51:27.2 | VLT | SPHERE | YJH | -176 | 239 | 4 | 0 | 7.40 | 6.30 |

Continued on next page

Table A.4 – continued from previous page

| Date | UTC | Tel. | Cam. | Filter | $X_o$ (mas) | $Y_o$ (mas) | $X_{o-c}$ (mas) | $Y_{o-c}$ (mas) | $\sigma$ (mas) | $\Delta M$ (mag) | $\delta M$ (mag) |
|---|---|---|---|---|---|---|---|---|---|---|---|
| 2015-05-29 | 04:51:27.2 | VLT | SPHERE | Ks | -180 | 241 | 1 | 0 | 12.26 | 6.26 | 0.09 |
| 2015-05-29 | 05:07:36.3 | VLT | SPHERE | YJH | -164 | 241 | 5 | 0 | 7.40 | 6.35 | 0.09 |
| 2015-05-29 | 05:07:36.3 | VLT | SPHERE | Ks | -166 | 245 | 3 | 3 | 12.26 | 6.26 | 0.06 |
| 2015-05-29 | 05:15:13.1 | VLT | SPHERE | YJH | -157 | 242 | 5 | 0 | 7.40 | 6.43 | 0.30 |
| 2015-05-29 | 05:15:13.1 | VLT | SPHERE | Ks | -158 | 245 | 5 | 3 | 12.26 | 6.35 | 0.17 |
| 2015-05-29 | 05:25:55.5 | VLT | SPHERE | Ks | -152 | 245 | 3 | 2 | 12.26 | 6.36 | 0.16 |
| 2015-05-29 | 05:28:59.5 | VLT | SPHERE | YJH | -148 | 243 | 4 | 0 | 7.40 | 6.49 | 0.16 |
| 2015-05-29 | 05:28:59.5 | VLT | SPHERE | Ks | -150 | 247 | 3 | 3 | 12.26 | 6.34 | 0.08 |
| 2015-05-29 | 05:32:04.0 | VLT | SPHERE | YJH | -146 | 243 | 4 | 0 | 7.40 | 6.51 | 0.17 |
| 2015-05-29 | 05:32:04.0 | VLT | SPHERE | Ks | -148 | 245 | 2 | 1 | 12.26 | 6.42 | 0.09 |
| 2016-07-02 | 08:47:22.2 | VLT | SPHERE | YJH | -279 | -90 | -7 | -3 | 7.40 | 6.68 | 0.28 |
| 2016-07-12 | 05:04:19.4 | VLT | SPHERE | YJH | 601 | -129 | -7 | 1 | 7.40 | 6.55 | 0.19 |
| 2016-07-12 | 05:11:41.7 | VLT | SPHERE | YJH | 601 | -130 | -7 | 1 | 7.40 | 6.51 | 0.06 |
| 2016-07-12 | 05:19:03.9 | VLT | SPHERE | YJH | 601 | -129 | -7 | 4 | 7.40 | 6.49 | 0.03 |
| 2016-07-28 | 05:50:56.0 | VLT | SPHERE | YJH | -208 | -138 | 5 | -4 | 7.40 | 6.96 | 0.24 |
| 2016-07-28 | 05:57:12.3 | VLT | SPHERE | YJH | -212 | -137 | 6 | -5 | 7.40 | 7.10 | 0.06 |
| 2016-07-28 | 06:03:30.1 | VLT | SPHERE | YJH | -216 | -135 | 6 | -5 | 7.40 | 7.07 | 0.19 |
| 2016-07-30 | 01:37:12.1 | VLT | SPHERE | YJH | 192 | 141 | -1 | 0 | 7.40 | 6.90 | 0.20 |
| 2016-07-30 | 01:44:17.2 | VLT | SPHERE | YJH | 194 | 135 | -4 | -3 | 7.40 | 6.78 | 0.23 |
| 2016-07-30 | 01:51:22.2 | VLT | SPHERE | YJH | 199 | 135 | -4 | -2 | 7.40 | 6.65 | 0.44 |
| 2016-08-11 | 00:18:43.4 | VLT | SPHERE | YJH | 579 | -159 | -7 | 6 | 7.40 | 6.18 | 0.07 |
| 2016-08-11 | 02:41:34.1 | VLT | SPHERE | YJH | 559 | -189 | -3 | 5 | 7.40 | 6.54 | 0.23 |
| 2016-08-11 | 02:48:41.5 | VLT | SPHERE | YJH | 560 | -189 | -1 | 6 | 7.40 | 6.43 | 0.08 |
| 2016-08-11 | 02:55:50.8 | VLT | SPHERE | YJH | 556 | -194 | -3 | 1 | 7.40 | 6.43 | 0.07 |
| | | | | | | Average | 1 | 1 | 18 | 6.50 | 0.48 |
| | | | | | | Standard deviation | 8 | 7 | 7 | 0.28 | 0.63 |

Table A.5 – Astrometry of *S/2016 (107) 1*. Date, mid-observing time (UTC), telescope, camera, filter, astrometry ($X$ is aligned with Right Ascension, and $Y$ with Declination, and $o$ and $c$ indices stand for observed and computed positions), and photometry (magnitude difference $\Delta M$ with uncertainty $\delta M$).

| Date | UTC | Tel. | Cam. | Filter | $X_o$ (mas) | $Y_o$ (mas) | $X_{o-c}$ (mas) | $Y_{o-c}$ (mas) | $\sigma$ (mas) | $\Delta M$ (mag) | $\delta M$ (mag) |
|---|---|---|---|---|---|---|---|---|---|---|---|
| 2015-05-29 | 04:38:46.4 | VLT | SPHERE | YJH | 87 | 140 | 1 | 1 | 7.40 | 8.95 | 1.40 |
| 2015-05-29 | 04:51:27.2 | VLT | SPHERE | YJH | 102 | 141 | 4 | 2 | 7.40 | 8.65 | 0.25 |

Continued on next page

Table A.5 – continued from previous page

| Date | UTC | Tel. | Cam. | Filter | $X_o$ (mas) | $Y_o$ (mas) | $X_{o-c}$ (mas) | $Y_{o-c}$ (mas) | $\sigma$ (mas) | $\Delta M$ (mag) | $\delta M$ (mag |
|---|---|---|---|---|---|---|---|---|---|---|---|
| 2015-05-29 | 05:07:36.3 | VLT | SPHERE | YJH | 111 | 137 | -1 | -1 | 7.40 | 8.43 | 1.5 |
| 2015-05-29 | 05:15:13.1 | VLT | SPHERE | YJH | 121 | 142 | 1 | 3 | 7.40 | 8.66 | 0.6 |
| 2015-05-29 | 05:32:04.0 | VLT | SPHERE | YJH | 135 | 136 | 0 | -1 | 7.40 | 8.83 | 1.5 |
| 2016-07-12 | 05:04:19.4 | VLT | SPHERE | YJH | -271 | 115 | 7 | -2 | 7.40 | 9.16 | 0.8 |
| 2016-07-12 | 05:11:41.7 | VLT | SPHERE | YJH | -275 | 113 | 0 | -6 | 7.40 | 9.53 | 1.2 |
| 2016-07-12 | 05:19:03.9 | VLT | SPHERE | YJH | -272 | 119 | 0 | -2 | 7.40 | 9.34 | 0.9 |
| 2016-07-30 | 01:37:12.1 | VLT | SPHERE | YJH | -295 | 104 | -1 | 5 | 7.40 | 9.32 | 0.3 |
| 2016-07-30 | 01:44:17.2 | VLT | SPHERE | YJH | -295 | 103 | -3 | 2 | 7.40 | 9.23 | 0.2 |
| 2016-07-30 | 01:51:22.2 | VLT | SPHERE | YJH | -288 | 102 | 0 | -1 | 7.40 | 9.53 | 1.6 |
| | | | | | | Average | 0 | 0 | 10 | 9.05 | 0.9 |
| | | | | | | Standard deviation | 3 | 3 | 0 | 0.32 | 0.5 |

## A.5 Previous determinations of mass and diameter of (107) Camilla

Table A.6 – The diameter estimates ($\mathscr{D}$) of (107) Camilla collected in the literature. For each, the uncertainty, method, selection flag, and bibliographic reference are reported. The methods are IM: Disk-Resolved Imaging, KOALA: Multidata 3-D Modeling, LCIMG: 3-D Model scaled with Imaging, LCOCC: 3-D Model scaled with Occultation, NEATM: Near-Earth Asteroid Thermal Model, STM: Standard Thermal Model, TPM: Thermophysical Model.

| # | $\mathscr{D}$ (km) | $\delta\mathscr{D}$ (km) | Method | Sel. | Reference |
|---|---|---|---|---|---|
| 1 | 213.00 | 21.30 | STM | ✓ | Morrison and Zellner [2007] |
| 2 | 222.62 | 17.10 | STM | ✓ | Tedesco et al. [2004] |
| 3 | 185.00 | 9.00 | IM | ✗ | Marchis et al. [2006] |
| 4 | 249.00 | 18.00 | NEATM | ✓ | Marchis et al. [2008] |
| 5 | 246.00 | 13.00 | IM | ✓ | Marchis et al. [2008] |
| 6 | 208.85 | 10.79 | STM | ✓ | Ryan and Woodward [2010] |
| 7 | 221.10 | 14.37 | NEATM | ✓ | Ryan and Woodward [2010] |
| 8 | 214.00 | 28.00 | LCOCC | ✓ | Ďurech et al. [2011] |
| 9 | 200.37 | 3.51 | STM | ✓ | Usui et al. [2011] |
| 10 | 219.37 | 5.94 | NEATM | ✓ | Masiero et al. [2011] |
| 11 | 256.00 | 11.67 | NEATM | ✓ | Marchis et al. [2012] |
| 12 | 245.00 | 25.00 | TPM | ✓ | Marchis et al. [2012] |
| 13 | 227.00 | 24.00 | LCIMG | ✓ | Hanuš et al. [2013] |
| 14 | 254.00 | 6.00 | KOALA | ✓ | Hanuš et al. [2017] |
| 15 | 254.00 | 6.00 | KOALA | ✓ | This work |
| | 228.83 | 21.45 | Average | | |

Table A.7 – The mass estimates ($\mathscr{M}$) of (107) Camilla collected in the literature. For each, the uncertainty, method, selection flag, and bibliographic reference are reported. The methods are BGENO: Binary: Genoid, BIMG: Binary: Imaging, DEFL: Deflection, EPHEM: Ephemeris.

| # | Mass ($\mathscr{M}$) (kg) | Method | Sel. | Reference |
|---|---|---|---|---|
| 1 | $(1.12 \pm 0.03) \times 10^{19}$ | BIMG | ✓ | Marchis et al. [2008] |
| 2 | $(3.62 \pm 0.92) \times 10^{19}$ | EPHEM | ✗ | Fienga et al. [2010] |
| 3 | $3.88^{+10.90}_{-3.88} \times 10^{18}$ | DEFL | ✓ | Zielenbach [2011] |
| 4 | $(3.90 \pm 1.06) \times 10^{19}$ | DEFL | ✗ | Zielenbach [2011] |
| 5 | $(17.60 \pm 8.69) \times 10^{18}$ | DEFL | ✓ | Zielenbach [2011] |
| 6 | $2.25^{+18.00}_{-2.25} \times 10^{18}$ | DEFL | ✓ | Zielenbach [2011] |
| 7 | $(2.71 \pm 0.70) \times 10^{19}$ | EPHEM | ✗ | Fienga et al. [2011] |
| 8 | $(6.79 \pm 3.00) \times 10^{18}$ | EPHEM | ✓ | Fienga et al. [2013] |
| 9 | $(11.10 \pm 1.79) \times 10^{18}$ | DEFL | ✓ | Goffin [2014] |
| 10 | $(16.10 \pm 9.13) \times 10^{18}$ | EPHEM | ✓ | Fienga (priv. comm.) |
| 11 | $(1.20 \pm 0.15) \times 10^{19}$ | BGENO | ✓ | This work |
| | $(11.03 \pm 2.11) \times 10^{18}$ | Average | | |

# Bibliography

F. Allard, P. H. Hauschildt, D. R. Alexander, and S. Starrfield. Model Atmospheres of Very Low Mass Stars and Brown Dwarfs. *Annual Review of Astronomy and Astrophysics*, 35:137–177, 1997. doi: 10.1146/annurev.astro.35.1.137.

E. Asphaug and W. Benz. Density of comet Shoemaker-Levy 9 deduced by modelling breakup of the parent 'rubble pile'. *Nature*, 370:120–124, July 1994. doi: 10.1038/370120a0.

M. Assafin, R. P. Campos, R. Vieira Martins, D. N. da Silva Neto, J. I. B. Camargo, and A. H. Andrei. Instrumental and digital coronagraphy for the observation of the Uranus satellites' upcoming mutual events. *Planetary and Space Science*, 56:1882–1887, November 2008. doi: 10.1016/j.pss.2007.05.030.

I. Baraffe, G. Chabrier, F. Allard, and P. H. Hauschildt. Evolutionary models for metal-poor low-mass stars. Lower main sequence of globular clusters and halo field stars. *Astronomy & Astrophysics*, 327:1054–1069, November 1997.

I. Baraffe, G. Chabrier, F. Allard, and P. H. Hauschildt. Evolutionary models for solar metallicity low-mass stars: mass-magnitude relationships and color-magnitude diagrams. *Astronomy & Astrophysics*, 337:403–412, September 1998.

M. A. Barucci, M. T. Capria, A. Coradini, and M. Fulchignoni. Classification of asteroids using G-mode analysis. *Icarus*, 72:304–324, November 1987. doi: 10.1016/0019-1035(87)90177-1.

A. Bayo, C. Rodrigo, D. Barrado Y Navascués, E. Solano, R. Gutiérrez, M. Morales-Calderón, and F. Allard. VOSA: virtual observatory SED analyzer. An application to the Collinder 69 open cluster. *Astronomy & Astrophysics*, 492:277–287, December 2008. doi: 10.1051/0004-6361:200810395.

R. Behrend, L. Bernasconi, R. Roy, A. Klotz, F. Colas, P. Antonini, R. Aoun, K. Augustesen, E. Barbotin, N. Berger, H. Berrouachdi, E. Brochard, A. Cazenave, C. Cavadore, J. Coloma, V. Cotrez, S. Deconihout, C. Demeautis, J. Dorseuil, G. Dubos, R. Durkee, E. Frappa, F. Hormuth, T. Itkonen, C. Jacques, L. Kurtze, A. Laffont, M. Lavayssière, J. Lecacheux, A. Leroy, F. Manzini, G. Masi, D. Matter, R. Michelsen, J. Nomen, A. Oksanen, P. Pääkkönen, A. Peyrot, E. Pimentel, D. Pray, C. Rinner, S. Sanchez, K. Sonnenberg, S. Sposetti, D. Starkey, R. Stoss, J.-P. Teng, M. Vignand, and N. Waelchli. Four new binary minor planets: (854) Frostia, (1089)

Tama, (1313) Berna, (4492) Debussy. *Astronomy and Astrophysics*, 446:1177–1184, February 2006. doi: 10.1051/0004-6361:20053709.

J. F. Bell, D. R. Davis, W. K. Hartmann, and M. J. Gaffey. Asteroids - The big picture. *Asteroids II*, pages 921–945, 1989.

I. N. Belskaya and V. G. Shevchenko. Opposition Effect of Asteroids. *Icarus*, 147:94–105, September 2000. doi: 10.1006/icar.2000.6410.

M. Belton and R. Carlson. 1993 (243) 1. *IAU Circular*, 5948, March 1994.

M. J. S. Belton, C. R. Chapman, P. C. Thomas, M. E. Davies, R. Greenberg, K. Klaasen, D. Byrnes, L. D'Amario, S. Synnott, T. V. Johnson, A. McEwen, W. J. Merline, D. R. Davis, J.-M. Petit, A. Storrs, J. Veverka, and B. Zellner. Bulk density of asteroid 243 Ida from the orbit of its satellite Dactyl. *Nature*, 374:785–788, April 1995. doi: 10.1038/374785a0.

V. Benishek. CCD Photometry of Seven Asteroids at the Belgrade Astronomical Observatory. *Minor Planet Bulletin*, 35:28–30, March 2008.

L. A. Benner, M. W. Busch, M. C. Nolan, S. J. Ostro, J. D. Giorgini, R. Rose, J. S. Jao, G. J. Black, L. M. Carter, M. A. Slade, R. F. Jurgens, and A. A. Hine. Radar Images Of Binary Near-earth Asteroid 2006 VV2. In *AAS/Division for Planetary Sciences Meeting Abstracts #39*, volume 39 of *Bulletin of the American Astronomical Society*, page 432, October 2007a.

L. A. M. Benner, S. J. Ostro, J. D. Giorgini, M. W. Busch, R. Rose, M. A. Slade, R. F. Jurgens, M. C. Nolan, A. A. Hine, G. J. Black, and L. M. Carter. 2006 VV_2. *IAU Circular*, 8826, April 2007b.

J. Berthier. Principe de réduction des occultations stellaires. *Notes scientifique et techniques du Bureau des longitudes*, S064, 1999.

J. Berthier, F. Vachier, W. Thuillot, P. Fernique, F. Ochsenbein, F. Genova, V. Lainey, and J.-E. Arlot. SkyBoT, a new VO service to identify Solar System objects. In C. Gabriel, C. Arviset, D. Ponz, and S. Enrique, editors, *Astronomical Data Analysis Software and Systems XV*, volume 351 of *Astronomical Society of the Pacific Conference Series*, page 367, July 2006.

J. Berthier, D. Hestroffer, B. Carry, J. Ďurech, P. Tanga, M. Delbo, and F. Vachier. A Service of Position and Physical Ephemerides Computation Dedicated to the Small Bodies of the Solar System. *LPI Contributions*, 1405:8374, Jul. 2008.

J. Berthier, D. Hestroffer, B. Carry, F. Vachier, V. Lainey, N. V. Emelyanov, W. Thuillot, J.-E. Arlot, and I. Ephemerides Service. Miriade: A Service for Solar Sytem Ojects Ephemerides in the VO Framework. In *European Planetary Science Congress 2009*, page 676, September 2009.

J. Berthier, F. Vachier, F. Marchis, J. Ďurech, and B. Carry. Physical and dynamical properties of the main belt triple Asteroid (87) Sylvia. *Icarus*, 239:118–130, September 2014. doi: 10.1016/j.icarus.2014.05.046.

A. S. Betzler and A. B. Novaes. Observations of V-type Binary Near-Earth Asteroids 2006 VV2 and 2008 BT18. *Minor Planet Bulletin*, 36:94–96, July 2009.

J.-L. Beuzit, M. Feldt, K. Dohlen, D. Mouillet, P. Puget, F. Wildi, L. Abe, J. Antichi, A. Baruffolo, P. Baudoz, A. Boccaletti, M. Carbillet, J. Charton, R. Claudi, M. Downing, C. Fabron, P. Feautrier, E. Fedrigo, T. Fusco, J.-L. Gach, R. Gratton, T. Henning, N. Hubin, F. Joos, M. Kasper, M. Langlois, R. Lenzen, C. Moutou, A. Pavlov, C. Petit, J. Pragt, P. Rabou, F. Rigal, R. Roelfsema, G. Rousset, M. Saisse, H.-M. Schmid, E. Stadler, C. Thalmann, M. Turatto, S. Udry, F. Vakili, and R. Waters. SPHERE: a 'Planet Finder' instrument for the VLT. In *Society of Photo-Optical Instrumentation Engineers (SPIE) Conference Series*, volume 7014 of *Society of Photo-Optical Instrumentation Engineers (SPIE) Conference Series*, page 701418, July 2008. doi: 10.1117/12.790120.

S. Bilir, S. Karaali, and S. Tunçel. Absolute magnitudes for late-type dwarf stars for Sloan photometry. *Astronomische Nachrichten*, 326:321–331, June 2005. doi: 10.1002/asna.200510358.

R. P. Binzel. Advances in Understanding physical properties of small bodies. In *Asteroids, Comets, and Meteors: ACM 2017*, Asteroid Comets and Meteors Conference, April 2017.

R. P. Binzel and S. Xu. Chips off of asteroid 4 Vesta - Evidence for the parent body of basaltic achondrite meteorites. *Science*, 260:186–191, April 1993. doi: 10.1126/science.260.5105.186.

R. P. Binzel, A. S. Rivkin, J. S. Stuart, A. W. Harris, S. J. Bus, and T. H. Burbine. Observed spectral properties of near-Earth objects: results for population distribution, source regions, and space weathering processes. *Icarus*, 170:259–294, August 2004. doi: 10.1016/j.icarus.2004.04.004.

M. Birlan, M. A. Barucci, P. Vernazza, M. Fulchignoni, R. P. Binzel, S. J. Bus, I. Belskaya, and S. Fornasier. Near-IR spectroscopy of asteroids 21 Lutetia, 89 Julia, 140 Siwa, 2181 Fogelin and 5480 (1989YK8), potential targets for the Rosetta mission; remote observations campaign on IRTF. *New Astronomy*, 9:343–351, June 2004. doi: 10.1016/j.newast.2003.12.005.

M. Birlan, P. Vernazza, M. Fulchignoni, M. A. Barucci, P. Descamps, R. P. Binzel, and S. J. Bus. Near infra-red spectroscopy of the asteroid 21 Lutetia. I. New results of long-term campaign. *Astronomy & Astrophysics*, 454:677–681, August 2006. doi: 10.1051/0004-6361:20054460.

M. Birlan, M. Popescu, L. Irimiea, and R. Binzel. M4AST - A Tool for Asteroid Modelling. In *AAS Division for Planetary Sciences Meeting Abstracts*, volume 48 of *AAS Division for Planetary Sciences Meeting Abstracts*, page 325.17, October 2016.

N. T. Bobrovnikoff. The spectra of minor planets. *Lick Observatory Bulletin*, 14:18–27, 1929. doi: 10.5479/ADS/bib/1929LicOB.14.18B.

W. F. Bottke and H. J. Melosh. Formation of asteroid satellites and doublet craters by planetary tidal forces. *Nature*, 381:51–53, May 1996a. doi: 10.1038/381051a0.

W. F. Bottke, M. C. Nolan, R. Greenberg, and R. A. Kolvoord. Velocity distributions among colliding asteroids. *Icarus*, 107:255–268, February 1994. doi: 10.1006/icar.1994.1021.

W. F. Bottke, D. D. Durda, D. Nesvorný, R. Jedicke, A. Morbidelli, D. Vokrouhlický, and H. Levison. The fossilized size distribution of the main asteroid belt. *Icarus*, 175:111–140, May 2005. doi: 10.1016/j.icarus.2004.10.026.

W. F. Bottke, Jr. and H. J. Melosh. Binary Asteroids and the Formation of Doublet Craters. *Icarus*, 124:372–391, December 1996b. doi: 10.1006/icar.1996.0215.

E. Bowell, C. R. Chapman, J. C. Gradie, D. Morrison, and B. Zellner. Taxonomy of asteroids. *Icarus*, 35:313–335, September 1978. doi: 10.1016/0019-1035(78)90085-4.

F. Braga-Ribas, B. Sicardy, J. L. Ortiz, C. Snodgrass, F. Roques, R. Vieira-Martins, J. I. B. Camargo, M. Assafin, R. Duffard, E. Jehin, J. Pollock, R. Leiva, M. Emilio, D. I. Machado, C. Colazo, E. Lellouch, J. Skottfelt, M. Gillon, N. Ligier, L. Maquet, G. Benedetti-Rossi, A. R. Gomes, P. Kervella, H. Monteiro, R. Sfair, M. El Moutamid, G. Tancredi, J. Spagnotto, A. Maury, N. Morales, R. Gil-Hutton, S. Roland, A. Ceretta, S.-H. Gu, X.-B. Wang, K. Harpsøe, M. Rabus, J. Manfroid, C. Opitom, L. Vanzi, L. Mehret, L. Lorenzini, E. M. Schneiter, R. Melia, J. Lecacheux, F. Colas, F. Vachier, T. Widemann, L. Almenares, R. G. Sandness, F. Char, V. Perez, P. Lemos, N. Martinez, U. G. Jørgensen, M. Dominik, F. Roig, D. E. Reichart, A. P. Lacluyze, J. B. Haislip, K. M. Ivarsen, J. P. Moore, N. R. Frank, and D. G. Lambas. A ring system detected around the Centaur (10199) Chariklo. *Nature*, 508:72–75, April 2014. doi: 10.1038/nature13155.

D. T. Britt, D. K. Yeomans, K. R. Housen, and G. J. Consolmagno. Asteroid Density, Porosity, and Structure. *Asteroids III*, pages 485–500, March 2002.

R. Brunetto, P. Vernazza, S. Marchi, M. Birlan, M. Fulchignoni, V. Orofino, and G. Strazzulla. Modeling asteroid surfaces from observations and irradiation experiments: The case of 832 Karin. *Icarus*, 184:327–337, October 2006. doi: 10.1016/j.icarus.2006.05.019.

T. H. Burbine and R. P. Binzel. Small Main-Belt Asteroid Spectroscopic Survey in the Near-Infrared. *Icarus*, 159:468–499, October 2002. doi: 10.1006/icar.2002.6902.

S. J. Bus. *Compositional structure in the asteroid belt: Results of a spectroscopic survey*. PhD thesis, MASSACHUSETTS INSTITUTE OF TECHNOLOGY, January 1999.

S. J. Bus and R. P. Binzel. Phase II of the Small Main-Belt Asteroid Spectroscopic Survey: The Observations. *Icarus*, 158:106–145, July 2002. doi: 10.1006/icar.2002.6857.

S. J. Bus and R. P. Binzel. Phase II of the Small Main-Belt Asteroid Spectroscopic Survey. A Feature-Based Taxonomy. *Icarus*, 158:146–177, July 2002. doi: 10.1006/icar.2002.6856.

S. J. Bus, F. Vilas, and M. A. Barucci. Visible-Wavelength Spectroscopy of Asteroids. *Asteroids III*, pages 169–182, March 2002.

M. Cañada-Assandri, R. Gil-Hutton, and A. O. Ribeiro. The Hungaria population: A comparison between sub-groups. *Planetary and Space Science*, 105:60–64, January 2015. doi: 10.1016/j.pss.2014.11.004.

B. Carry. Density of asteroids. *Planetary and Space Science*, 73:98–118, December 2012. doi: 10.1016/j.pss.2012.03.009.

B. Carry, C. Dumas, M. Fulchignoni, W. J. Merline, J. Berthier, D. Hestroffer, T. Fusco, and P. Tamblyn. Near-infrared mapping and physical properties of the dwarf-planet Ceres. *Astronomy & Astrophysics*, 478:235–244, January 2008. doi: 10.1051/0004-6361:20078166.

B. Carry, C. Dumas, M. Kaasalainen, J. Berthier, W. J. Merline, S. Erard, A. Conrad, J. D. Drummond, D. Hestroffer, M. Fulchignoni, and T. Fusco. Physical properties of (2) Pallas. *Icarus*, 205:460–472, February 2010. doi: 10.1016/j.icarus.2009.08.007.

B. Carry, M. Kaasalainen, C. Leyrat, W. J. Merline, J. D. Drummond, A. R. Conrad, H. A. Weaver, P. M. Tamblyn, C. R. Chapman, C. Dumas, F. Colas, J. C. Christou, E. Dotto, D. Perna, S. Fornasier, L. Bernasconi, R. Behrend, F. Vachier, A. Kryszczynska, M. Polinska, M. Fulchignoni, R. Roy, R. Naves, R. Poncy, and P. Wiggins. Physical properties of the ESA Rosetta target asteroid (21) Lutetia. II. Shape and flyby geometry. *Astronomy & Astrophysics*, 523:A94, nov 2010. doi: 10.1051/0004-6361/201015074.

B. Carry, M. Kaasalainen, W. J. Merline, T. G. Müller, L. Jorda, J. D. Drummond, J. Berthier, L. O'Rourke, J. Ďurech, M. Küppers, A. R. Conrad, C. Dumas, H. Sierks, and the OSIRIS TeamPSS. Koala shape modeling technique validated at (21) lutetia by esa rosetta mission. *Planetary and Space Science*, 66:200–212, 2012. doi: dx.doi.org/10.1016/j.pss.2011.12.018.

B. Carry, E. Solano, S. Eggl, and F. E. DeMeo. Spectral properties of near-Earth and Mars-crossing asteroids using Sloan photometry. *Icarus*, 268:340–354, April 2016. doi: 10.1016/j.icarus.2015.12.047.

J. M. Carvano, P. H. Hasselmann, D. Lazzaro, and T. Mothé-Diniz. SDSS-based taxonomic classification and orbital distribution of main belt asteroids. *Astronomy & Astrophysics*, 510:A43, February 2010. doi: 10.1051/0004-6361/200913322.

C. R. Chapman, D. Morrison, and B. Zellner. Surface properties of asteroids - A synthesis of polarimetry, radiometry, and spectrophotometry. *Icarus*, 25:104–130, May 1975. doi: 10.1016/0019-1035(75)90191-8.

R. U. Claudi, M. Turatto, R. G. Gratton, J. Antichi, M. Bonavita, P. Bruno, E. Cascone, V. De Caprio, S. Desidera, E. Giro, D. Mesa, S. Scuderi, K. Dohlen, J. L. Beuzit, and P. Puget. SPHERE IFS: the spectro differential imager of the VLT for exoplanets search. In *Ground-based and Airborne Instrumentation for Astronomy II*, volume 7014 of *Society of Photo-Optical Instrumentation Engineers (SPIE) Conference Series*, page 70143E, July 2008. doi: 10.1117/12.788366.

E. A. Cloutis, M. J. Gaffey, T. L. Jackowski, and K. L. Reed. Calibrations of phase abundance, composition, and particle size distribution for olivine-orthopyroxene mixtures from reflectance spectra. *Journal of Geophysical Research*, 91:11, October 1986. doi: 10.1029/JB091iB11p11641.

E. A. Cloutis, P. Hudon, C. S. Romanek, J. L. Bishop, V. Reddy, M. J. Gaffey, and P. S. Hardersen. Spectral reflectance properties of ureilites. *Meteoritics and Planetary Science*, 45:1668–1694, October 2010. doi: 10.1111/j.1945-5100.2010.01065.x.

G. Consolmagno, D. Britt, and R. Macke. The significance of meteorite density and porosity. *Chemie der Erde / Geochemistry*, 68:1–29, April 2008. doi: 10.1016/j.chemer.2008.01.003.

N. J. G. Cross, R. S. Collins, R. G. Mann, M. A. Read, E. T. W. Sutorius, R. P. Blake, M. Holliman, N. C. Hambly, J. P. Emerson, A. Lawrence, and K. T. Noddle. The VISTA Science Archive. *Astronomy & Astrophysics*, 548:A119, December 2012. doi: 10.1051/0004-6361/201219505.

C. Cunningham. *Early Investigations of Ceres and the Discovery of Pallas*. Springer International Publishing, 2016.

C. J. Cunningham. 211-YEAR-OLD MYSTERY SOLVED: CREATOR OF THE WORD "ASTEROID" REVEALED. In *AAS/Division for Planetary Sciences Meeting Abstracts*, volume 45 of *AAS/Division for Planetary Sciences Meeting Abstracts*, page 108.02, October 2013.

M. C. Cushing, W. D. Vacca, and J. T. Rayner. Spextool: A Spectral Extraction Package for SpeX, a 0.8-5.5 Micron Cross-Dispersed Spectrograph. *Publications of the Astronomical Society of the Pacific*, 116:362–376, April 2004. doi: 10.1086/382907.

C. L. Dandy, A. Fitzsimmons, and S. J. Collander-Brown. Optical colors of 56 near-Earth objects: trends with size and orbit. *Icarus*, 163:363–373, June 2003. doi: 10.1016/S0019-1035(03)00087-3.

J. de León, J. Licandro, M. Serra-Ricart, N. Pinilla-Alonso, and H. Campins. Observations, compositional, and physical characterization of near-Earth and Mars-crosser asteroids from a spectroscopic survey. *Astronomy & Astrophysics*, 517:A23, July 2010. doi: 10.1051/0004-6361/200913852.

M. C. de Sanctis, A. Migliorini, F. Luzia Jasmin, D. Lazzaro, G. Filacchione, S. Marchi, E. Ammannito, and M. T. Capria. Spectral and mineralogical characterization of inner main-belt V-type asteroids. *Astronomy & Astrophysics*, 533:A77, September 2011. doi: 10.1051/0004-6361/201117136.

M. Delbo, P. Tanga, B. Carry, C. Ordenovic, and P. Bottein. Mp$^3$c: The minor planet physical properties catalogue. *ACM*, 2017.

F. E. DeMeo and B. Carry. The taxonomic distribution of asteroids from multi-filter all-sky photometric surveys. *Icarus*, 226:723–741, September 2013. doi: 10.1016/j.icarus.2013.06.027.

F. E. DeMeo and B. Carry. Solar System evolution from compositional mapping of the asteroid belt. *Nature*, 505:629–634, January 2014. doi: 10.1038/nature12908.

F. E. DeMeo, R. P. Binzel, S. M. Slivan, and S. J. Bus. An extension of the Bus asteroid taxonomy into the near-infrared. *Icarus*, 202:160–180, July 2009. doi: 10.1016/j.icarus.2009.02.005.

F. E. DeMeo, B. Carry, F. Marchis, M. Birlan, R. P. Binzel, S. J. Bus, P. Descamps, A. Nedelcu, M. Busch, and H. Bouy. A spectral comparison of (379) Huenna and its satellite. *Icarus*, 212: 677–681, Apr 2011. doi: 10.1016/j.icarus.2011.02.002.

F. E. DeMeo, R. P. Binzel, B. Carry, D. Polishook, and N. A. Moskovitz. Unexpected D-type interlopers in the inner main belt. *Icarus*, 229:392–399, February 2014. doi: 10.1016/j.icarus.2013.11.026.

F. E. DeMeo, C. M. O. Alexander, K. J. Walsh, C. R. Chapman, and R. P. Binzel. The Compositional Structure of the Asteroid Belt. *Asteroids IV*, pages 13–41, 2015. doi: 10.2458/azu_uapress_9780816532131-ch002.

M. di Martino, V. Zappala, G. de Sanctis, and S. Cacciatori. Photoelectric photometry of 17 asteroids. *Icarus*, 69:338–353, feb 1987. doi: 10.1016/0019-1035(87)90110-2.

K. Dohlen, M. Langlois, M. Saisse, L. Hill, A. Origne, M. Jacquet, C. Fabron, J.-C. Blanc, M. Llored, M. Carle, C. Moutou, A. Vigan, A. Boccaletti, M. Carbillet, D. Mouillet, and J.-L. Beuzit. The infra-red dual imaging and spectrograph for SPHERE: design and performance. In *Society of Photo-Optical Instrumentation Engineers (SPIE) Conference Series*, volume 7014 of *Society of Photo-Optical Instrumentation Engineers (SPIE) Conference Series*, page 70143, July 2008. doi: 10.1117/12.789786.

D. W. Dunham, D. Herald, E. Frappa, T. Hayamizu, J. Talbot, and B. Timerson. Asteroid Occultations. NASA Planetary Data System, 2012. EAR-A-3-RDR-OCCULTATIONS-V10.0.

T. L. Dunn, T. H. Burbine, W. F. Bottke, and J. P. Clark. Mineralogies and source regions of near-Earth asteroids. *Icarus*, 222:273–282, January 2013. doi: 10.1016/j.icarus.2012.11.007.

D. D. Durda, W. F. Bottke, B. L. Enke, W. J. Merline, E. Asphaug, D. C. Richardson, and Z. M. Leinhardt. The formation of asteroid satellites in large impacts: results from numerical simulations. *Icarus*, 170:243–257, July 2004. doi: 10.1016/j.icarus.2004.04.003.

J. Ďurech, M. Kaasalainen, D. Herald, D. Dunham, B. Timerson, J. Hanuš, E. Frappa, J. Talbot, T. Hayamizu, B. D. Warner, F. Pilcher, and A. Galád. Combining asteroid models derived by lightcurve inversion with asteroidal occultation silhouettes. *Icarus*, 214:652–670, August 2011. doi: 10.1016/j.icarus.2011.03.016.

J. P. Emery, D. P. Cruikshank, and J. van Cleve. Thermal emission spectroscopy (5.2 38 $\mu$m) of three Trojan asteroids with the Spitzer Space Telescope: Detection of fine-grained silicates. *Icarus*, 182:496–512, June 2006. doi: 10.1016/j.icarus.2006.01.011.

J. Fang, J.-L. Margot, and P. Rojo. Orbits, Masses, and Evolution of Main Belt Triple (87) Sylvia. *Astronomical Journal*, 144:70, August 2012. doi: 10.1088/0004-6256/144/2/70.

S. K. Fieber-Beyer, M. J. Gaffey, W. F. Bottke, and P. S. Hardersen. Potentially hazardous Asteroid 2007 LE: Compositional link to the black chondrite Rose City and Asteroid (6) Hebe. *icarus*, 250:430–437, April 2015. doi: 10.1016/j.icarus.2014.12.021.

A. Fienga, H. Manche, P. Kuchynka, J. Laskar, and M. Gastineau. INPOP10a. *Scientific Notes*, 2010.

A. Fienga, P. Kuchynka, J. Laskar, H. Manche, and M. Gastineau. Asteroid mass determinations with INPOP planetary ephemerides. *EPSC-DPS Joint Meeting 2011*, page 1879, October 2011.

A. Fienga, H. Manche, J. Laskar, M. Gastineau, and A. Verma. INPOP new release: INPOP10e. *ArXiv e-prints*, January 2013.

M. Florczak, M. A. Barucci, A. Doressoundiram, D. Lazzaro, C. A. Angeli, and E. Dotto. A Visible Spectroscopic Survey of the Flora Clan. *Icarus*, 133:233–246, June 1998. doi: 10.1006/icar.1998.5928.

G. Foderà Serio, A. Manara, and P. Sicoli. Giuseppe Piazzi and the Discovery of Ceres. *Asteroids III*, pages 17–24, 2002.

S. Fornasier, I. Belskaya, M. Fulchignoni, M. A. Barucci, and C. Barbieri. First albedo determination of 2867 Steins, target of the Rosetta mission. *Astronomy & Astrophysics*, 449:L9–L12, April 2006. doi: 10.1051/0004-6361:20064913.

M. Fulchignoni, M. Birlan, and M. Antonietta Barucci. The Extension of the G-Mode Asteroid Taxonomy. *Icarus*, 146:204–212, July 2000. doi: 10.1006/icar.2000.6381.

T. Fusco. *Correction Partielle Et Anisoplanétisme En Optique*. PhD thesis, Université de Nice Sophia-Antipolis, 2000.

T. Fusco, G. Rousset, J.-F. Sauvage, C. Petit, J.-L. Beuzit, K. Dohlen, D. Mouillet, J. Charton, M. Nicolle, M. Kasper, P. Baudoz, and P. Puget. High-order adaptive optics requirements for direct detection of extrasolar planets: Application to the SPHERE instrument. *Optics Express*, 14:7515, 2006. doi: 10.1364/OE.14.007515.

M. J. Gaffey, T. H. Burbine, J. L. Piatek, K. L. Reed, D. A. Chaky, J. F. Bell, and R. H. Brown. Mineralogical variations within the S-type asteroid class. *Icarus*, 106:573, December 1993. doi: 10.1006/icar.1993.1194.

M. J. Gaffey, E. A. Cloutis, M. S. Kelley, and K. L. Reed. Mineralogy of Asteroids. *Asteroids III*, pages 183–204, March 2002.

G. Galilei. *Sidereus nuncius magna, longeque admirabilia spectacula pandens lunae facie, fixis innumeris, lacteo circulo, stellis nebulosis, ... Galileo Galileo : nuper a se reperti beneficio sunt observata in apprime vero in quatuor planetis circa Iovis stellam disparibus intervallis, atque periodis, celeritate mirabili circumvolutis ... atque Medicea sidera nuncupandos decrevit*. Thomas Baglionum, 1610. doi: 10.3931/e-rara-695.

T. Gehrels. Physical studies of minor planets. *NASA Special Publication*, 267, 1971.

T. Gehrels, J. D. Drummond, and N. A. Levenson. The absence of satellites of asteroids. *Icarus*, 70:257–263, May 1987. doi: 10.1016/0019-1035(87)90133-3.

K. M. Gietzen, C. H. S. Lacy, D. R. Ostrowski, and D. W. G. Sears. IRTF observations of S complex and other asteroids: Implications for surface compositions, the presence of clinopyroxenes, and their relationship to meteorites. *Meteoritics and Planetary Science*, 47:1789–1808, November 2012. doi: 10.1111/maps.12013.

M. Gillon, A. H. M. J. Triaud, B.-O. Demory, E. Jehin, E. Agol, K. M. Deck, S. M. Lederer, J. de Wit, A. Burdanov, J. G. Ingalls, E. Bolmont, J. Leconte, S. N. Raymond, F. Selsis, M. Turbet, K. Barkaoui, A. Burgasser, M. R. Burleigh, S. J. Carey, A. Chaushev, C. M. Copperwheat, L. Delrez, C. S. Fernandes, D. L. Holdsworth, E. J. Kotze, V. Van Grootel, Y. Almleakey, Z. Benkhaldoun, P. Magain, and D. Queloz. Seven temperate terrestrial planets around the nearby ultracool dwarf star TRAPPIST-1. *Nature*, 542:456–460, February 2017. doi: 10.1038/nature21360.

B. J. Gladman, F. Migliorini, A. Morbidelli, V. Zappala, P. Michel, A. Cellino, C. Froeschle, H. F. Levison, M. Bailey, and M. Duncan. Dynamical lifetimes of objects injected into asteroid belt resonances. *Science*, 277:197–201, 1997. doi: 10.1126/science.277.5323.197.

E. Goffin. Astrometric asteroid masses: a simultaneous determination. *Astronomy & Astrophysics*, 565:A56, May 2014. doi: 10.1051/0004-6361/201322766.

P. Goldreich, Y. Lithwick, and R. Sari. Formation of Kuiper-belt binaries by dynamical friction and three-body encounters. *Nature*, 420:643–646, December 2002. doi: 10.1038/nature01227.

R. Gomes, H. F. Levison, K. Tsiganis, and A. Morbidelli. Origin of the cataclysmic Late Heavy Bombardment period of the terrestrial planets. *Nature*, 435:466–469, May 2005. doi: 10.1038/nature03676.

J. Gradie and E. Tedesco. Compositional structure of the asteroid belt. *Science*, 216:1405–1407, June 1982. doi: 10.1126/science.216.4553.1405.

T. Grav, A. K. Mainzer, J. Bauer, J. Masiero, T. Spahr, R. S. McMillan, R. Walker, R. Cutri, E. Wright, P. R. Eisenhardt, E. Blauvelt, E. DeBaun, D. Elsbury, T. Gautier, S. Gomillion, E. Hand, and A. Wilkins. WISE/NEOWISE Observations of the Hilda Population: Preliminary Results. *Astrophysical Journal*, 744:197, January 2012. doi: 10.1088/0004-637X/744/2/197.

Josef Hanuš, Matti Viikinkoski, Franck Marchis, Josef Durech, Mikko Kaasalainen, Marco Delbo', David Herald, Eric Frappa, Tsutomu Hayamizu, S. Kerr, Steve Preston, Brad Timerson, David Dunham, and John Talbot. Volumes and bulk densities of forty asteroids from adam shape modeling. *Astronomy & Astrophysics*, 2017.

J. Hanuš, F. Marchis, and J. Ďurech. Sizes of main-belt asteroids by combining shape models and Keck adaptive optics observations. *Icarus*, 226:1045–1057, September 2013. doi: 10.1016/j.icarus.2013.07.023.

J. Hanuš, J. Ďurech, D. A. Oszkiewicz, R. Behrend, B. Carry, M. Delbo, O. Adam, V. Afonina, R. Anquetin, P. Antonini, L. Arnold, M. Audejean, P. Aurard, M. Bachschmidt, B. Baduel, E. Barbotin, P. Barroy, P. Baudouin, L. Berard, N. Berger, L. Bernasconi, J.-G. Bosch, S. Bouley, I. Bozhinova, J. Brinsfield, L. Brunetto, G. Canaud, J. Caron, F. Carrier, G. Casalnuovo, S. Casulli, M. Cerda, L. Chalamet, S. Charbonnel, B. Chinaglia, A. Cikota, F. Colas, J.-F. Coliac, A. Collet, J. Coloma, M. Conjat, E. Conseil, R. Costa, R. Crippa, M. Cristofanelli, Y. Damerdji, A. Debackère, A. Decock, Q. Déhais, T. Déléage, S. Delmelle, C. Demeautis, M. Dróżdż, G. Dubos, T. Dulcamara, M. Dumont, R. Durkee, R. Dymock, A. Escalante del Valle, N. Esseiva, R. Esseiva, M. Esteban, T. Fauchez, M. Fauerbach, M. Fauvaud, S. Fauvaud, E. Forné, C. Fournel, D. Fradet, J. Garlitz, O. Gerteis, C. Gillier, M. Gillon, R. Giraud, J.-P. Godard, R. Goncalves, H. Hamanowa, H. Hamanowa, K. Hay, S. Hellmich, S. Heterier, D. Higgins, R. Hirsch, G. Hodosan, M. Hren, A. Hygate, N. Innocent, H. Jacquinot, S. Jawahar, E. Jehin, L. Jerosimic, A. Klotz, W. Koff, P. Korlevic, E. Kosturkiewicz, P. Krafft, Y. Krugly, F. Kugel, O. Labrevoir, J. Lecacheux, M. Lehký, A. Leroy, B. Lesquerbault, M. J. Lopez-Gonzales, M. Lutz, B. Mallecot, J. Manfroid, F. Manzini, A. Marciniak, A. Martin, B. Modave, R. Montaigut, J. Montier, E. Morelle, B. Morton, S. Mottola, R. Naves, J. Nomen, J. Oey, W. Ogłoza, M. Paiella, H. Pallares, A. Peyrot, F. Pilcher, J.-F. Pirenne, P. Piron, M. Polińska, M. Polotto, R. Poncy, J. P. Previt, F. Reignier, D. Renauld, D. Ricci, F. Richard, C. Rinner, V. Risoldi, D. Robilliard, D. Romeuf, G. Rousseau, R. Roy, J. Ruthroff, P. A. Salom, L. Salvador, S. Sanchez, T. Santana-Ros, A. Scholz, G. Séné, B. Skiff, K. Sobkowiak, P. Sogorb, F. Soldán, A. Spiridakis, E. Splanska, S. Sposetti, D. Starkey, R. Stephens, A. Stiepen, R. Stoss, J. Strajnic, J.-P. Teng, G. Tumolo, A. Vagnozzi, B. Vanoutryve, J. M. Vugnon, B. D. Warner, M. Waucomont, O. Wertz, M. Winiarski, and M. Wolf. New and updated convex shape models of asteroids based on optical data from a large collaboration network. *Astronomy & Astrophysics*, 586: A108, February 2016. doi: 10.1051/0004-6361/201527441.

P. S. Hardersen, M. J. Gaffey, and P. A. Abell. Mineralogy of Asteroid 1459 Magnya and implications for its origin. *Icarus*, 167:170–177, January 2004. doi: 10.1016/j.icarus.2003.09.022.

A. W. Harris and J. W. Young. Asteroid lightcurve observations from 1979-1981. *Icarus*, 81: 314–364, oct 1989. doi: 10.1016/0019-1035(89)90056-0.

P. H. Hauschildt, F. Allard, and E. Baron. The NextGen Model Atmosphere Grid for 3000$\leqslant$=$T_{eff}$$\leqslant$=10,000 K. *The Astrophysical Journal*, 512:377–385, February 1999. doi: 10.1086/306745.

E. Helin, P. Rose, T. Gehrels, K. Lawrence, S. Cohen, J. V. Scotti, and B. G. Marsden. 1991 RJ2. *IAU Circular*, 5357, October 1991.

E. F. Helin, S. H. Pravdo, D. L. Rabinowitz, and K. J. Lawrence. Near-Earth Asteroid Tracking (NEAT) Program. *Annals of the New York Academy of Sciences*, 822:6, May 1997. doi: 10.1111/j.1749-6632.1997.tb48329.x.

C. W. Hergenrother, R. J. Whiteley, and E. J. Christensen. Photometric Observations of Five Near-Earth Asteroids: (31221) 1998 BP26, (96315) 1997 AP10, (164184) 2004 BF68, 2006 VV2, and 2006 XY. *Minor Planet Bulletin*, 36:16–18, January 2009.

G. Herriot, S. Morris, A. Anthony, D. Derdall, D. Duncan, J. Dunn, A. W. Ebbers, J. M. Fletcher, T. Hardy, B. Leckie, A. Mirza, C. L. Morbey, M. Pfleger, S. Roberts, P. Shott, M. Smith, L. K. Saddlemyer, J. Sebesta, K. Szeto, R. Wooff, W. Windels, and J.-P. Veran. Progress on Altair: the Gemini North adaptive optics system. In P. L. Wizinowich, editor, *Adaptive Optical Systems Technology*, volume 4007 of *Society of Photo-Optical Instrumentation Engineers (SPIE) Conference Series*, pages 115–125, July 2000.

W. Herschel. Observations on the Two Lately Discovered Celestial Bodies. *Philosophical Transactions of the Royal Society of London Series I*, 92:213–232, 1802.

K. W. Hodapp, J. B. Jensen, E. M. Irwin, H. Yamada, R. Chung, K. Fletcher, L. Robertson, J. L. Hora, D. A. Simons, W. Mays, R. Nolan, M. Bec, M. Merrill, and A. M. Fowler. The Gemini Near-Infrared Imager (NIRI). *Publications of the Astronomical Society of the Pacific*, 115: 1388–1406, December 2003. doi: 10.1086/379669.

J. Holmberg, C. Flynn, and L. Portinari. The colours of the Sun. *Monthly Notices of the Royal Astronomical Society*, 367:449–453, April 2006. doi: 10.1111/j.1365-2966.2005.09832.x.

E. S. Howell, C. Magri, R. J. Vervack, M. C. Nolan, Y. Fernandez, and A. S. Rivkin. Thermal Infrared Observations of Several Near-Earth Asteroids. In *AAS/Division for Planetary Sciences Meeting Abstracts #40*, volume 40 of *Bulletin of the American Astronomical Society*, page 436, September 2008.

S. B. Howell. *Handbook of CCD Astronomy*. Cambridge University Press, March 2006.

R. Huziak. Ramblings of a Variable-Star Addict: Precise Measurements for Earth-Crossing Asteroid 2006 VV2. *Journal of the Royal Astronomical Society of Canada*, 101:165, August 2007.

Ž. Ivezić, S. Tabachnik, R. Rafikov, R. H. Lupton, T. Quinn, M. Hammergren, L. Eyer, J. Chu, J. C. Armstrong, X. Fan, K. Finlator, T. R. Geballe, J. E. Gunn, G. S. Hennessy, G. R. Knapp, S. K. Leggett, J. A. Munn, J. R. Pier, C. M. Rockosi, D. P. Schneider, M. A. Strauss, B. Yanny, J. Brinkmann, I. Csabai, R. B. Hindsley, S. Kent, D. Q. Lamb, B. Margon, T. A. McKay, J. A. Smith, P. Waddel, D. G. York, and SDSS Collaboration. Solar System Objects Observed in the Sloan Digital Sky Survey Commissioning Data. *The Astronomical Journal*, 122:2749–2784, November 2001. doi: 10.1086/323452.

Ž. Ivezić, R. H. Lupton, M. Jurić, S. Tabachnik, T. Quinn, J. E. Gunn, G. R. Knapp, C. M. Rockosi, and J. Brinkmann. Color Confirmation of Asteroid Families. *The Astronomical Journal*, 124: 2943–2948, November 2002. doi: 10.1086/344077.

Ž. Ivezić, M. Juric, R. H. Lupton, S. Tabachnik, T. Quinn, and SDSS Collaboration. SDSS Moving Object Catalog V3.0. *NASA Planetary Data System*, 124, August 2010.

S. A. Jacobson and D. J. Scheeres. Dynamics of rotationally fissioned asteroids: Source of observed small asteroid systems. *Icarus*, 214:161–178, July 2011. doi: 10.1016/j.icarus.2011.04.009.

S. A. Jacobson, F. Marzari, A. Rossi, D. J. Scheeres, and D. R. Davis. Effect of rotational disruption on the size-frequency distribution of the Main Belt asteroid population. *mnras*, 439:L95–L99, March 2014. doi: 10.1093/mnrasl/slu006.

E. Jagoutz and H. Wanke. SR and Nd isotopic systematics of Shergotty meteorite. *Geochimica et Cosmochimica Acta*, 50:939–953, June 1986. doi: 10.1016/0016-7037(86)90375-3.

R. Jedicke, J. Larsen, and T. Spahr. Observational Selection Effects in Asteroid Surveys. *Asteroids III*, pages 71–87, 2002.

W. R. Johnston. Binary Minor Planets V7.0. *NASA Planetary Data System*, 219, June 2014.

W. R. Johnston. Binary Minor Planets V9.0. *NASA Planetary Data System*, 244, July 2016.

M. Juric, Z. Ivezic, R. Lupton, and SDSS Collaboration. The SDSS Moving Object Catalog, Asteroid Data Release 4. In *American Astronomical Society Meeting Abstracts*, volume 39 of *Bulletin of the American Astronomical Society*, page 828, December 2007.

M. Kaasalainen. Maximum compatibility estimates and shape reconstruction with boundary curves and volumes of generalized projections. *Inverse Problems and Imaging*, 5(1):37–57, Feb 2011.

M. Kaasalainen and M. Viikinkoski. Shape reconstruction of irregular bodies with multiple complementary data sources. *Astronomy and Astrophysics*, 543:A97, July 2012. doi: 10.1051/0004-6361/201219267.

J. Kepler. *Ioannis Keppleri harmonices mundi libri V : quorum primus harmonicus ... quartus metaphysicus, psychologicus et astrologicus geometricus ... secundus architectonicus ... tertius proprie ... quintus astronomicus & metaphysicus ... : appendix habet comparationem huius operis cum harmonices Cl. Ptolemaei libro III cumque Roberti de Fluctibus ... speculationibus harmonicis, operi de macrocosmo & microcosmo insertis.* Johann Planck, 1619. doi: 10.3931/e-rara-8723.

J. Kepler, N. Copernicus, M. Mästlin, and J. Schöner. *Prodromus dissertationum cosmographicarum, continens mysterium causis coelorum numeri, magnitudinis, motuumque periodicorum genuinis cosmographicum, de admirabili proportione orbium coelestium,*

*deque & propriis, demonstratum, per quinque regularia corpora geometrica*. Georgius Gruppenbachius, 1596. doi: 10.3931/e-rara-445.

A. Klotz and R. Behrend. Courbes de rotation d'astéroïdes et de comètes, CdR, 2007. URL https://obswww.unige.ch/~behrend/page5cou.html#06v02v.

A. Klotz, R. Delmas, D. Marchais, M. Pujol, and C. Jasinski. The AudeLA software. In *Astronomical Society of India Conference Series*, volume 7 of *Astronomical Society of India Conference Series*, page .15, 2012.

N. Krugly, R. Behrend, P. Pravec, K. Hornoch, P. Kusnirak, A. Galad, P. Veres, R. Crippa, F. Manzini, M. Audejean, L. Bernasconi, N. Gaftonyuk, B. D. Warner, I. Molotov, and L. Elenin. (8373) Stephengould. *Central Bureau Electronic Telegrams*, 2193, March 2010.

P. Kuchynka and W. M. Folkner. A new approach to determining asteroid masses from planetary range measurements. *Icarus*, 222:243–253, January 2013. doi: 10.1016/j.icarus.2012.11.003.

R. L. Kurucz. Model atmospheres for G, F, A, B, and O stars. *Astrophysical Journal Supplement*, 40:1–340, May 1979. doi: 10.1086/190589.

P. Kusnirak, P. Pravec, A. Galad, L. Kornos, W. Cooney, J. Gross, and D. Terrell. 2005 NB_7. *Central Bureau Electronic Telegrams*, 1383, May 2008.

C.-I. Lagerkvist and P. Magnusson. Asteroid Photometric Catalog V1.1. EAR-A-3-DDR-APC-LIGHTCURVE-V1.1. NASA Planetary Data System, 2011.

C. Laver, I. de Pater, F. Marchis, M. Ádámkovics, and M. H. Wong. Component-resolved near-infrared spectra of the (22) Kalliope system. *Icarus*, 204:574–579, December 2009. doi: 10.1016/j.icarus.2009.07.002.

M. Lazzarin, S. Marchi, M. A. Barucci, M. Di Martino, and C. Barbieri. Visible and near-infrared spectroscopic investigation of near-Earth objects at ESO: first results. *icarus*, 169:373–384, June 2004. doi: 10.1016/j.icarus.2003.12.023.

M. Lazzarin, S. Marchi, S. Magrin, and J. Licandro. Spectroscopic investigation of near-Earth objects at Telescopio Nazionale Galileo. *MNRAS*, 359:1575–1582, June 2005. doi: 10.1111/j.1365-2966.2005.09006.x.

M. Lazzarin, S. Magrin, and S. Marchi. SINEO: Spectroscopic Investigation of Near Earth Objects. *Memorie della Societa Astronomica Italiana Supplementi*, 12:20, 2008.

D. Lazzaro, C. A. Angeli, M. Florczak, A. Betzler, M. A. Barucci, and M. Fulchignoni. Small Solar System Objects Spectroscopic Survey: First Results. In *AAS/Division for Planetary Sciences Meeting Abstracts #29*, volume 29 of *Bulletin of the American Astronomical Society*, page 975, July 1997.

D. Lazzaro, C. A. Angeli, J. M. Carvano, T. Mothé-Diniz, R. Duffard, and M. Florczak. $S^3OS^2$: the visible spectroscopic survey of 820 asteroids. *Icarus*, 172:179–220, November 2004. doi: 10.1016/j.icarus.2004.06.006.

R. Lenzen, M. Hartung, W. Brandner, G. Finger, N. N. Hubin, F. Lacombe, A.-M. Lagrange, M. D. Lehnert, A. F. M. Moorwood, and D. Mouillet. NAOS-CONICA first on sky results in a variety of observing modes. *SPIE*, 4841:944–952, 2003.

H. F. Levison, W. F. Bottke, M. Gounelle, A. Morbidelli, D. Nesvorný, and K. Tsiganis. Contamination of the asteroid belt by primordial trans-Neptunian objects. *Nature*, 460:364–366, July 2009. doi: 10.1038/nature08094.

H. F. Levison, A. Morbidelli, K. Tsiganis, D. Nesvorný, and R. Gomes. Late Orbital Instabilities in the Outer Planets Induced by Interaction with a Self-gravitating Planetesimal Disk. *The Astronomical Journal*, 142:152, November 2011. doi: 10.1088/0004-6256/142/5/152.

J. Licandro, M. Popescu, D. Morate, and J. de León. V-type candidates and Vesta family asteroids in the Moving Objects VISTA (MOVIS) catalogue. *Astronomy & Astrophysics*, 600: A126, April 2017. doi: 10.1051/0004-6361/201629465.

S. S. Lindsay, F. Marchis, J. P. Emery, J. E. Enriquez, and M. Assafin. Composition, mineralogy, and porosity of multiple asteroid systems from visible and near-infrared spectral data. *Icarus*, 247:53–70, February 2015. doi: 10.1016/j.icarus.2014.08.040.

S. D. Lord. A new software tool for computing Earth's atmospheric transmission of near- and far-infrared radiation. Technical report, NASA, December 1992.

F. Marchis, M. Kaasalainen, E. F. Y. Hom, J. Berthier, J. Enriquez, D. Hestroffer, D. Le Mignant, and I. de Pater. Shape, size and multiplicity of main-belt asteroids. *Icarus*, 185(1):39–63, Aug. 2006.

F. Marchis, P. Descamps, M. Baek, A. W. Harris, M. Kaasalainen, J. Berthier, D. Hestroffer, and F. Vachier. Main belt binary asteroidal systems with circular mutual orbits. *Icarus*, 196(1): 97–118, Jul. 2008. doi: 10.1016/j.icarus.2008.03.007.

F. Marchis, V. Lainey, P. Descamps, J. Berthier, M. Van Dam, I. de Pater, B. Macomber, M. Baek, D. Le Mignant, H. B. Hammel, M. Showalter, and F. Vachier. A dynamical solution of the triple asteroid system (45) Eugenia. *Icarus*, 210:635–643, December 2010. doi: 10.1016/j.icarus.2010.08.005.

F. Marchis, J. E. Enriquez, J. P. Emery, J. Berthier, P. Descamps, and F. Vachier. The origin of (90) Antiope from component-resolved near-infrared spectroscopy. *Icarus*, 213:252–264, May 2011. doi: 10.1016/j.icarus.2011.02.011.

F. Marchis, J. E. Enriquez, J. P. Emery, M. Mueller, M. Baek, J. Pollock, M. Assafin, R. Vieira Martins, J. Berthier, F. Vachier, D. P. Cruikshank, L. F. Lim, D. E. Reichart, K. M. Ivarsen, J. B.

Haislip, and A. P. LaCluyze. Multiple asteroid systems: Dimensions and thermal properties from spitzer space telescope and ground-based observations. *Icarus*, 221:1130–1161, November 2012. doi: 10.1016/j.icarus.2012.09.013.

F. Marchis, J. Durech, J. Castillo-Rogez, F. Vachier, M. Cuk, J. Berthier, M. H. Wong, P. Kalas, G. Duchene, M. A. van Dam, H. Hamanowa, and M. Viikinkoski. The Puzzling Mutual Orbit of the Binary Trojan Asteroid (624) Hektor. *Astrophysical Journal*, 783:L37, March 2014. doi: 10.1088/2041-8205/783/2/L37.

J. L. Margot, M. C. Nolan, L. A. M. Benner, S. J. Ostro, R. F. Jurgens, M. A. Slade, J. D. Giorgini, and D. B. Campbell. SATELLITES OF MINOR PLANETS. *IAU Circular*, 7503, October 2000.

J.-L. Margot, P. Pravec, P. Taylor, B. Carry, and S. Jacobson. Asteroid Systems: Binaries, Triples, and Pairs. *Asteroids IV*, pages 355–374, 2015.

M. Marsset, B. Carry, B. Yang, F. Marchis, P. Vernazza, C. Dumas, J. Berthier, and F. Vachier. S/2016 (107) 1. *IAU Circular*, 9282, August 2016.

P. Martinez, J. Kolb, M. Sarazin, and A. Tokovinin. On the Difference between Seeing and Image Quality: When the Turbulence Outer Scale Enters the Game. *The Messenger*, 141:5–8, September 2010.

J. R. Masiero, A. K. Mainzer, T. Grav, J. M. Bauer, R. M. Cutri, J. Dailey, P. R. M. Eisenhardt, R. S. McMillan, T. B. Spahr, M. F. Skrutskie, D. Tholen, R. G. Walker, E. L. Wright, E. DeBaun, D. Elsbury, T. Gautier, IV, S. Gomillion, and A. Wilkins. Main Belt Asteroids with WISE/NEOWISE. I. Preliminary Albedos and Diameters. *The Astrophysical Journal*, 741:68, November 2011. doi: 10.1088/0004-637X/741/2/68.

J. R. Masiero, A. K. Mainzer, T. Grav, J. M. Bauer, R. M. Cutri, C. Nugent, and M. S. Cabrera. Preliminary Analysis of WISE/NEOWISE 3-Band Cryogenic and Post-cryogenic Observations of Main Belt Asteroids. *The Astrophysical Journal Letters*, 759:L8, November 2012. doi: 10.1088/2041-8205/759/1/L8.

J. R. Masiero, F. E. DeMeo, T. Kasuga, and A. H. Parker. Asteroid Family Physical Properties. *Asteroids IV*, pages 323–340, 2015.

T. B. McCord and C. R. Chapman. Asteroids: Spectral reflectance and color characteristics. *The Astrophysical Journal*, 195:553–562, January 1975a. doi: 10.1086/153355.

T. B. McCord and C. R. Chapman. Asteroids - Spectral reflectance and color characteristics. II. *The Astrophysical Journal*, 197:781–790, May 1975b. doi: 10.1086/153565.

T. B. McCord, J. B. Adams, and T. V. Johnson. Asteroid Vesta: Spectral Reflectivity and Compositional Implications. *Science*, 168:1445–1447, June 1970. doi: 10.1126/science.168.3938.1445.

F. M. McEachern, M. Ćuk, and S. T. Stewart. Dynamical evolution of the Hungaria asteroids. *Icarus*, 210:644–654, December 2010. doi: 10.1016/j.icarus.2010.08.003.

W. J. Merline, L. M. Close, C. Dumas, C. R. Chapman, F. Roddier, F. Menard, D. C. Slater, G. Duvert, C. Shelton, T. Morgan, and D. W. Dunham. S/1998 (45) 1. *IAU Circular*, 7129, March 1999.

W. J. Merline, L. M. Close, C. Dumas, J. C. Shelton, F. Menard, C. R. Chapman, and D. C. Slater. Discovery of Companions to Asteroids 762 Pulcova and 90 Antiope by Direct Imaging. In *AAS/Division for Planetary Sciences Meeting Abstracts #32*, volume 32 of *Bulletin of the American Astronomical Society*, page 1017, October 2000.

W. J. Merline, S. J. Weidenschilling, D. D. Durda, J.-L. Margot, P. Pravec, and A. D. Storrs. Asteroids Do Have Satellites. *Asteroids III*, pages 289–312, 2002.

A. Milani and Z. Knezevic. Asteroid proper elements and secular resonances. *Icarus*, 98: 211–232, August 1992. doi: 10.1016/0019-1035(92)90091-K.

A. Milani and Z. Knezevic. Asteroid proper elements and the dynamical structure of the asteroid main belt. *Icarus*, 107:219–254, February 1994. doi: 10.1006/icar.1994.1020.

A. Milani, A. Cellino, Z. Knežević, B. Novaković, F. Spoto, and P. Paolicchi. Asteroid families classification: Exploiting very large datasets. *Icarus*, 239:46–73, September 2014. doi: 10.1016/j.icarus.2014.05.039.

A. Morbidelli, H. F. Levison, K. Tsiganis, and R. Gomes. Chaotic capture of Jupiter's Trojan asteroids in the early Solar System. *Nature*, 435:462–465, May 2005. doi: 10.1038/nature03540.

A. Morbidelli, W. F. Bottke, D. Nesvorný, and H. F. Levison. Asteroids were born big. *Icarus*, 204:558–573, Dec 2009. doi: 10.1016/j.icarus.2009.07.011.

F. Moreno, F. J. Pozuelos, B. Novaković, J. Licandro, A. Cabrera-Lavers, B. Bolin, R. Jedicke, B. J. Gladman, M. T. Bannister, S. D. J. Gwyn, P. Vereš, K. Chambers, S. Chastel, L. Denneau, H. Flewelling, M. Huber, E. Schunová-Lilly, E. Magnier, R. Wainscoat, C. Waters, R. Weryk, D. Farnocchia, and M. Micheli. The Splitting of Double-component Active Asteroid P/2016 J1 (PANSTARRS). *The Astrophysical Journal Letters*, 837:L3, March 2017. doi: 10.3847/2041-8213/aa6036.

D. Morrison and B. Zellner. TRIAD Radiometric Diameters and Albedos. NASA Planetary Data System, 2007. EAR-A-COMPIL-5-TRIADRAD-V1.0.

N. A. Moskovitz, M. Willman, T. H. Burbine, R. P. Binzel, and S. J. Bus. A spectroscopic comparison of HED meteorites and V-type asteroids in the inner Main Belt. *Icarus*, 208: 773–788, August 2010. doi: 10.1016/j.icarus.2010.03.002.

T. Mothé-Diniz, J. M. á. Carvano, and D. Lazzaro. Distribution of taxonomic classes in the main belt of asteroids. *Icarus*, 162:10–21, March 2003. doi: 10.1016/S0019-1035(02)00066-0.

S. Mottola, G. Hahn, P. Pravec, and L. Sarounova. S/1997 (3671) 1. *IAU Circular*, 6680, June 1997.

O. Mousis, R. Hueso, J.-P. Beaulieu, S. Bouley, B. Carry, F. Colas, A. Klotz, C. Pellier, J.-M. Petit, P. Rousselot, M. Ali-Dib, W. Beisker, M. Birlan, C. Buil, A. Delsanti, E. Frappa, H. B. Hammel, A. C. Levasseur-Regourd, G. S. Orton, A. Sánchez-Lavega, A. Santerne, P. Tanga, J. Vaubaillon, B. Zanda, D. Baratoux, T. Böhm, V. Boudon, A. Bouquet, L. Buzzi, J.-L. Dauvergne, A. Decock, M. Delcroix, P. Drossart, N. Esseiva, G. Fischer, L. N. Fletcher, S. Foglia, J. M. Gómez-Forrellad, J. Guarro-Fló, D. Herald, E. Jehin, F. Kugel, J.-P. Lebreton, J. Lecacheux, A. Leroy, L. Maquet, G. Masi, A. Maury, F. Meyer, S. Pérez-Hoyos, A. S. Rajpurohit, C. Rinner, J. H. Rogers, F. Roques, R. W. Schmude, B. Sicardy, B. Tregon, M. Vanhuysse, A. Wesley, and T. Widemann. Instrumental methods for professional and amateur collaborations in planetary astronomy. *Experimental Astronomy*, 38:91–191, November 2014. doi: 10.1007/s10686-014-9379-0.

M. Mueller, F. Marchis, J. P. Emery, A. W. Harris, S. Mottola, D. Hestroffer, J. Berthier, and M. di Martino. Eclipsing binary Trojan asteroid Patroclus: Thermal inertia from Spitzer observations. *Icarus*, 205:505–515, February 2010. doi: 10.1016/j.icarus.2009.07.043.

L. M. Mugnier, T. Fusco, and J.-M. Conan. MISTRAL: a Myopic Edge-Preserving Image Restoration Method, with Application to Astronomical Adaptive-Optics-Corrected Long-Exposure Images. *Journal of the Optical Society of America A*, 21(10):1841–1854, Oct. 2004.

C. D. Murray and S. F. Dermott. *Solar system dynamics*. University of Cambridge, 1999.

S. P. Naidu, L. A. M. Benner, M. Brozovic, J. D. Giorgini, C. J. Jao, C. G. Lee, L. G. Snedeker, K. J. Lawrence, M. W. Busch, and A. Lacluyze. ((348400) 2005 JF_21. *Central Bureau Electronic Telegrams*, 4139, August 2015.

T. Nakamura, T. Noguchi, M. Tanaka, M. E. Zolensky, M. Kimura, A. Tsuchiyama, A. Nakato, T. Ogami, H. Ishida, M. Uesugi, T. Yada, K. Shirai, A. Fujimura, R. Okazaki, S. A. Sandford, Y. Ishibashi, M. Abe, T. Okada, M. Ueno, T. Mukai, M. Yoshikawa, and J. Kawaguchi. Itokawa Dust Particles: A Direct Link Between S-Type Asteroids and Ordinary Chondrites. *Science*, 333:1113, August 2011. doi: 10.1126/science.1207758.

D. A. Nedelcu, M. Birlan, P. Vernazza, P. Descamps, R. P. Binzel, F. Colas, A. Kryszczynska, and S. J. Bus. Near infra-red spectroscopy of the asteroid 21 Lutetia. II. Rotationally resolved spectroscopy of the surface. *Astronomy & Astrophysics*, 470:1157–1164, aug 2007. doi: 10.1051/0004-6361:20066944.

D. Nesvorný, A. Morbidelli, D. Vokrouhlický, W. F. Bottke, and M. Brož. The Flora Family: A Case of the Dynamically Dispersed Collisional Swarm? *Icarus*, 157:155–172, May 2002. doi: 10.1006/icar.2002.6830.

D. Nesvorný, A. N. Youdin, and D. C. Richardson. Formation of Kuiper Belt Binaries by Gravitational Collapse. *Astronomical Journal*, 140:785–793, September 2010. doi: 10.1088/0004-6256/140/3/785.

T. Nimura, T. Hiroi, M. Ohtake, Y. Ueda, M. Abe, and A. Fujiwara. An Attempt of Restricting Olivine Bands in the Modified Gaussian Model. In S. Mackwell and E. Stansbery, editors,

*37th Annual Lunar and Planetary Science Conference*, volume 37 of *Lunar and Planetary Science Conference*, March 2006.

M. C. Nolan, J.-L. Margot, E. S. Howell, L. A. M. Benner, S. J. Ostro, R. F. Jurgens, J. D. Giorgini, and D. B. Campbell. 2000 UG_11. *IAU Circular*, 7518, November 2000.

Keith S. Noll, William M. Grundy, Denise C. Stephens, Harold F. Levison, and Susan D. Kern. Evidence for two populations of classical transneptunian objects: The strong inclination dependence of classical binaries. *Icarus*, 194(2):758 – 768, 2008. ISSN 0019-1035. doi: http://dx.doi.org/10.1016/j.icarus.2007.10.022. URL http://www.sciencedirect.com/science/article/pii/S0019103507005854.

J. Oey and R. Krajewski. Lightcurve Analysis of Asteroids from Kingsgrove and Other Collaborating Observatories in the First Half of 2007. *Minor Planet Bulletin*, 35:47–48, June 2008.

J. Oey, P. Pravec, P. Kusnirak, N. Morales, A. Thirouin, J. Pollock, D. E. Reichart, K. M. Ivarsen, J. B. Haislip, and A. Lacluyze. (2691) Sersic. *Central Bureau Electronic Telegrams*, 2766, July 2011.

S. J. Ostro, J.-L. Margot, M. C. Nolan, L. A. M. Benner, R. F. Jurgens, and J. D. Giorgini. 2000 DP107. *IAU Circular*, 7496, September 2000.

Alex H. Parker, Zeljko Ivezic, Mario Juric, Robert H. Lupton, Michael D. Sekora, and Adam F. Kowalski. The Size Distributions of Asteroid Families in the SDSS Moving Object Catalog 4. *Icarus*, 198:138–155, 2008. doi: 10.1016/j.icarus.2008.07.002.

A. Pavlov, O. Möller-Nilsson, M. Feldt, T. Henning, J.-L. Beuzit, and D. Mouillet. SPHERE data reduction and handling system: overview, project status, and development. In *Advanced Software and Control for Astronomy II*, volume 7019 of *SPIE*, page 701939, July 2008. doi: 10.1117/12.789110.

D. Perna, E. Dotto, S. Ieva, M. A. Barucci, F. Bernardi, S. Fornasier, F. De Luise, E. Perozzi, A. Rossi, E. Mazzotta Epifani, M. Micheli, and J. D. P. Deshapriya. Grasping the Nature of Potentially Hazardous Asteroids. *The Astronomical Journal*, 151:11, January 2016. doi: 10.3847/0004-6256/151/1/11.

C. M. Pieters. Strength of mineral absorption features in the transmitted component of near-infrared reflected light - First results from RELAB. *Journal of Geophysical Research*, 88: 9534–9544, November 1983. doi: 10.1029/JB088iB11p09534.

D. Polishook. Lightcurves for Shape Modeling Obtained at the Wise Observatory. *Minor Planet Bulletin*, 36:119–120, July 2009.

D. Polishook and N. Brosch. Photometry of Aten asteroids—More than a handful of binaries. *Icarus*, 194:111–124, March 2008. doi: 10.1016/j.icarus.2007.09.022.

D. Polishook, N. Moskovitz, R. P. Binzel, F. E. DeMeo, D. Vokrouhlický, J. Žižka, and D. Oszkiewicz. Observations of fresh and weathered surfaces on asteroid pairs and their implications on the rotational-fission mechanism. *Icarus*, 233:9–26, May 2014. doi: 10.1016/j.icarus.2014.01.014.

M. Popescu, M. Birlan, and D. A. Nedelcu. Modeling of asteroid spectra - M4AST. *Astronomy & Astrophysics*, 544:A130, August 2012. doi: 10.1051/0004-6361/201219584.

M. Popescu, J. Licandro, D. Morate, J. de León, D. A. Nedelcu, R. Rebolo, R. G. McMahon, E. Gonzalez-Solares, and M. Irwin. Near-infrared colors of minor planets recovered from VISTA-VHS survey (MOVIS). *Astronomy & Astrophysics*, 591:A115, June 2016. doi: 10.1051/0004-6361/201628163.

P. Pravec and G. Hahn. Two-Period Lightcurve of 1994 AW $_1$: Indication of a Binary Asteroid? *Icarus*, 127:431–440, June 1997. doi: 10.1006/icar.1997.5703.

P. Pravec and A. W. Harris. Fast and Slow Rotation of Asteroids. *Icarus*, 148:12–20, November 2000. doi: 10.1006/icar.2000.6482.

P. Pravec and A. W. Harris. Binary asteroid population. 1. Angular momentum content. *Icarus*, 190:250–259, Sep 2007. doi: 10.1016/j.icarus.2007.02.023.

P. Pravec and A. W. Harris. Binary asteroid population. 1. Angular momentum content. *Icarus*, 190:250–259, September 2007. doi: 10.1016/j.icarus.2007.02.023.

P. Pravec, L. Sarounova, M. Wolf, S. Mottola, and F. Lahulla. 1996 FG_3. *IAU Circular*, 7074, December 1998a.

P. Pravec, M. Wolf, and L. Šarounová. Occultation/Eclipse Events in Binary Asteroid 1991 VH. *Icarus*, 133:79–88, May 1998b. doi: 10.1006/icar.1998.5890.

P. Pravec, P. Kusnirak, M. Hicks, B. Holliday, and B. Warner. 2000 DP_107. *IAU Circular*, 7504, October 2000.

P. Pravec, P. Kusnirak, and B. Warner. 2001 SL_9. *IAU Circular*, 7742, November 2001.

P. Pravec, P. Kusnirak, B. Warner, R. Behrend, A. W. Harris, A. Oksanen, D. Higgins, R. Roy, C. Rinner, C. Demeautis, F. van den Abbeel, A. Klotz, N. Waelchli, T. Alderweireldt, V. Cotrez, and L. Brunetto. 1937 UB (Hermes). *IAU Circular*, 8233, October 2003.

P. Pravec, P. Scheirich, P. Kušnirák, L. Šarounová, S. Mottola, G. Hahn, P. Brown, G. Esquerdo, N. Kaiser, Z. Krzeminski, D. P. Pray, B. D. Warner, A. W. Harris, M. C. Nolan, E. S. Howell, L. A. M. Benner, J.-L. Margot, A. Galád, W. Holliday, M. D. Hicks, Y. N. Krugly, D. Tholen, R. Whiteley, F. Marchis, D. R. DeGraff, A. Grauer, S. Larson, F. P. Velichko, W. R. Cooney, R. Stephens, J. Zhu, K. Kirsch, R. Dyvig, L. Snyder, V. Reddy, S. Moore, Š. Gajdoš, J. Világi, G. Masi, D. Higgins, G. Funkhouser, B. Knight, S. Slivan, R. Behrend, M. Grenon, G. Burki, R. Roy, C. Demeautis, D. Matter, N. Waelchli, Y. Revaz, A. Klotz, M. Rieugné, P. Thierry,

V. Cotrez, L. Brunetto, and G. Kober. Photometric survey of binary near-Earth asteroids. *Icarus*, 181:63–93, March 2006. doi: 10.1016/j.icarus.2005.10.014.

P. Pravec, D. Vokrouhlický, D. Polishook, D. J. Scheeres, A. W. Harris, A. Galád, O. Vaduvescu, F. Pozo, A. Barr, P. Longa, F. Vachier, F. Colas, D. P. Pray, J. Pollock, D. Reichart, K. Ivarsen, J. Haislip, A. Lacluyze, P. Kušnirák, T. Henych, F. Marchis, B. Macomber, S. A. Jacobson, Y. N. Krugly, A. V. Sergeev, and A. Leroy. Formation of asteroid pairs by rotational fission. *Nature*, 466:1085–1088, August 2010. doi: 10.1038/nature09315.

P. Pravec, P. Scheirich, D. Vokrouhlický, A. W. Harris, P. Kušnirák, K. Hornoch, D. P. Pray, D. Higgins, A. Galád, J. Világi, Š. Gajdoš, L. Kornoš, J. Oey, M. Husárik, W. R. Cooney, J. Gross, D. Terrell, R. Durkee, J. Pollock, D. E. Reichart, K. Ivarsen, J. Haislip, A. LaCluyze, Y. N. Krugly, N. Gaftonyuk, R. D. Stephens, R. Dyvig, V. Reddy, V. Chiorny, O. Vaduvescu, P. Longa-Peña, A. Tudorica, B. D. Warner, G. Masi, J. Brinsfield, R. Gonçalves, P. Brown, Z. Krzeminski, O. Gerashchenko, V. Shevchenko, I. Molotov, and F. Marchis. Binary asteroid population. 2. Anisotropic distribution of orbit poles of small, inner main-belt binaries. *Icarus*, 218: 125–143, March 2012. doi: 10.1016/j.icarus.2011.11.026.

P. Pravec, P. Scheirich, P. Kušnirák, K. Hornoch, A. Galád, S. P. Naidu, D. P. Pray, J. Világi, Š. Gajdoš, L. Kornoš, Y. N. Krugly, W. R. Cooney, J. Gross, D. Terrell, N. Gaftonyuk, J. Pollock, M. Husárik, V. Chiorny, R. D. Stephens, R. Durkee, V. Reddy, R. Dyvig, J. Vraštil, J. Žižka, S. Mottola, S. Hellmich, J. Oey, V. Benishek, A. Kryszczyńska, D. Higgins, J. Ries, F. Marchis, M. Baek, B. Macomber, R. Inasaridze, O. Kvaratskhelia, V. Ayvazian, V. Rumyantsev, G. Masi, F. Colas, J. Lecacheux, R. Montaigut, A. Leroy, P. Brown, Z. Krzeminski, I. Molotov, D. Reichart, J. Haislip, and A. LaCluyze. Binary asteroid population. 3. Secondary rotations and elongations. *Icarus*, 267:267–295, March 2016. doi: 10.1016/j.icarus.2015.12.019.

T. H. Prettyman, D. W. Mittlefehldt, N. Yamashita, D. J. Lawrence, A. W. Beck, W. C. Feldman, T. J. McCoy, H. Y. McSween, M. J. Toplis, T. N. Titus, P. Tricarico, R. C. Reedy, J. S. Hendricks, O. Forni, L. Le Corre, J.-Y. Li, H. Mizzon, V. Reddy, C. A. Raymond, and C. T. Russell. Elemental Mapping by Dawn Reveals Exogenic H in Vesta's Regolith. *Science*, 338:242, October 2012. doi: 10.1126/science.1225354.

Rayner. *SpeX Observing Manual*. IRTF NASA Infrared Telescope Facility Institute for Astronomy University of Hawai, March 2015. URL http://irtfweb.ifa.hawaii.edu/~spex/SpeX_manual_20mar15.pdf.

J. T. Rayner, D. W. Toomey, P. M. Onaka, A. J. Denault, W. E. Stahlberger, W. D. Vacca, M. C. Cushing, and S. Wang. SpeX: A Medium-Resolution 0.8-5.5 Micron Spectrograph and Imager for the NASA Infrared Telescope Facility. *Publications of the Astronomical Society of the Pacific*, 115:362–382, March 2003. doi: 10.1086/367745.

V. Reddy. *Mineralogical Survey of near-Earth asteroid population Implications. for impact hazard assessment and sustainability of life on Earth.* PhD thesis, University of North Dakota, Grand Forks, January 2009.

D. C. Richardson, Z. M. Leinhardt, H. J. Melosh, W. F. Bottke, Jr., and E. Asphaug. Gravitational Aggregates: Evidence and Evolution. *Asteroids III*, pages 501–515, March 2002.

A. S. Rivkin, R. P. Binzel, and S. J. Bus. Constraining near-Earth object albedos using near-infrared spectroscopy. *Icarus*, 175:175–180, May 2005. doi: 10.1016/j.icarus.2004.11.005.

C. T. Rodgers, R. Canterna, J. A. Smith, M. J. Pierce, and D. L. Tucker. Improved u'g'r'i'z' to UBVR$_C$I$_C$ Transformation Equations for Main-Sequence Stars. *The Astronomical Journal*, 132:989–993, September 2006. doi: 10.1086/505864.

G. Rousset, F. Lacombe, P. Puget, N. N. Hubin, E. Gendron, T. Fusco, R. Arsenault, J. Charton, P. Feautrier, P. Gigan, P. Y. Kern, A.-M. Lagrange, P.-Y. Madec, D. Mouillet, D. Rabaud, P. Rabou, E. Stadler, and G. Zins. NAOS, the first AO system of the VLT: on-sky performance. *SPIE*, 4839:140–149, Feb. 2003.

E. L. Ryan and C. E. Woodward. Rectified Asteroid Albedos and Diameters from IRAS and MSX Photometry Catalogs. *Astronomical Journal*, 140:933–943, Oct 2010. doi: 10.1088/0004-6256/140/4/933.

D. J. Scheeres. Stability of Binary Asteroids. *Icarus*, 159:271–283, October 2002. doi: 10.1006/icar.2002.6908.

D. J. Scheeres and S. J. Ostro. Regolith Mechanics on Binary Asteroids. In *AAS/Division for Planetary Sciences Meeting Abstracts #36*, volume 36 of *Bulletin of the American Astronomical Society*, page 1185, November 2004.

D. J. Scheeres, L. A. M. Benner, S. J. Ostro, A. Rossi, F. Marzari, and P. Washabaugh. Abrupt alteration of Asteroid 2004 MN4's spin state during its 2029 Earth flyby. *Icarus*, 178:281–283, November 2005. doi: 10.1016/j.icarus.2005.06.002.

D. J. Scheeres, D. Britt, B. Carry, and K. A. Holsapple. Asteroid Interiors and Morphology. *Asteroids IV*, pages 745–766, 2015. doi: 10.2458/azu_uapress_9780816530595-ch038.

M. K. Shepard, M. C. Nolan, L. A. M. Benner, J. D. Giorgini, S. J. Ostro, and C. Magri. 2005 NB_7. *IAU Circular*, 8936, April 2008.

H. Sierks, P. Lamy, C. Barbieri, D. Koschny, H. Rickman, R. Rodrigo, M. F. A'Hearn, F. Angrilli, A. Barucci, J.-L. Bertaux, I. Bertini, S. Besse, B. Carry, G. Cremonese, V. Da Deppo, B. Davidsson, S. Debei, M. De Cecco, J. De Leon, F. Ferri, S. Fornasier, M. Fulle, S. F. Hviid, G. W. Gaskell, O. Groussin, P. J. Gutierrez, L. Jorda, M. Kaasalainen, H. U. Keller, J. Knollenberg, J. R. Kramm, E. Kührt, M. Küppers, L. M. Lara, M. Lazzarin, C. Leyrat, J. L. Lopez Moreno, S. Magrin, S. Marchi, F. Marzari, M. Massironi, H. Michalik, R. Moissl, G. Naletto, F. Preusker, L. Sabau, W. Sabolo, F. Scholten, C. Snodgrass, N. Thomas, C. Tubiana, P. Vernazza, J.-B. Vincent, K.-P. Wenzel, T. Andert, M. Pätzold, and B. P. Weiss. Images of asteroid (21) Lutetia: A remnant planetesimal from the early Solar System. *Science*, 334:487–490, 2011.

C. Snodgrass and B. Carry. Automatic Removal of Fringes from EFOSC Images. *The Messenger*, 152:14–16, June 2013.

C. Snodgrass, M. F. A'Hearn, F. Aceituno, V. Afanasiev, S. Bagnulo, J. Bauer, G. Bergond, S. Besse, N. Biver, D. Bodewits, H. Boehnhardt, B. P. Bonev, G. Borisov, B. Carry, V. Casanova, A. Cochran, B. C. Conn, B. Davidsson, J. K. Davies, J. de León, E. de Mooij, M. de Val-Borro, M. Delacruz, M. A. DiSanti, J. E. Drew, R. Duffard, N. J. T. Edberg, S. Faggi, L. Feaga, A. Fitzsimmons, H. Fujiwara, E. L. Gibb, M. Gillon, S. F. Green, A. Guijarro, A. Guilbert-Lepoutre, P. J. Gutiérrez, E. Hadamcik, O. Hainaut, S. Haque, R. Hedrosa, D. Hines, U. Hopp, F. Hoyo, D. Hutsemékers, M. Hyland, O. Ivanova, E. Jehin, G. H. Jones, J. V. Keane, M. S. P. Kelley, N. Kiselev, J. Kleyna, M. Kluge, M. M. Knight, R. Kokotanekova, D. Koschny, E. A. Kramer, J. J. López-Moreno, P. Lacerda, L. M. Lara, J. Lasue, H. J. Lehto, A. C. Levasseur-Regourd, J. Licandro, Z. Y. Lin, T. Lister, S. C. Lowry, A. Mainzer, J. Manfroid, J. Marchant, A. J. McKay, A. McNeill, K. J. Meech, M. Micheli, I. Mohammed, M. Monguió, F. Moreno, O. Muñoz, M. J. Mumma, P. Nikolov, C. Opitom, J. L. Ortiz, L. Paganini, M. Pajuelo, F. J. Pozuelos, S. Protopapa, T. Pursimo, B. Rajkumar, Y. Ramanjooloo, E. Ramos, C. Ries, A. Riffeser, V. Rosenbush, P. Rousselot, E. L. Ryan, P. Santos-Sanz, D. G. Schleicher, M. Schmidt, R. Schulz, A. K. Sen, A. Somero, A. Sota, A. Stinson, J. M. Sunshine, A. Thompson, G. P. Tozzi, C. Tubiana, G. L. Villanueva, X. Wang, D. H. Wooden, M. Yagi, B. Yang, B. Zaprudin, and T. J. Zegmott. The 67p/churyumov–gerasimenko observation campaign in support of the rosetta mission. *Philosophical Transactions of the Royal Society of London A: Mathematical, Physical and Engineering Sciences*, 375(2097), 2017. ISSN 1364-503X. doi: 10.1098/rsta.2016.0249. URL http://rsta.royalsocietypublishing.org/content/375/2097/20160249.

E. Solano, R. Gutiérrez, A. Delgado, L. M. Sarro, and B. Merín. VOSED: a tool for the characterization of developing planetary systems. *Highlights of Astronomy*, 14:634, August 2007.

J. M. Somers, M. D. Hicks, and K. J. Lawrence. Optical Characterization of Planetary Radar Targets. In *AAS/Division for Planetary Sciences Meeting Abstracts #40*, volume 40 of *Bulletin of the American Astronomical Society*, page 440, September 2008.

F. Spoto, A. Milani, D. Farnocchia, S. R. Chesley, M. Micheli, G. B. Valsecchi, D. Perna, and O. Hainaut. Nongravitational perturbations and virtual impactors: the case of asteroid (410777) 2009 FD. *AAP*, 572:A100, December 2014. doi: 10.1051/0004-6361/201424743.

R. D. Stephens. Asteroids Observed from CS3: 2015 July - September. *Minor Planet Bulletin*, 43:52–56, January 2016.

G. H. Stokes, J. B. Evans, H. E. M. Viggh, F. C. Shelly, and E. C. Pearce. Lincoln Near-Earth Asteroid Program (LINEAR). *Icarus*, 148:21–28, November 2000. doi: 10.1006/icar.2000.6493.

A. Storrs, F. Vilas, R. Landis, E. Wells, C. Woods, B. Zellner, and M. Gaffey. S/2001 (107) 1. *IAU Circular*, 7599:3, March 2001.

K. Y. L. Su, J. M. De Buizer, G. H. Rieke, A. V. Krivov, T. Löhne, M. Marengo, K. R. Stapelfeldt, N. P. Ballering, and W. D. Vacca. The Inner 25 au Debris Distribution in the $\epsilon$ Eri System. *The Astronomical Journal*, 153:226, May 2017. doi: 10.3847/1538-3881/aa696b.

J. M. Sunshine and C. M. Pieters. Estimating modal abundances from the spectra of natural and laboratory pyroxene mixtures using the modified Gaussian model. *Journal of Geophysical Research*, 98:9075–9087, May 1993. doi: 10.1029/93JE00677.

W. Sutherland, J. Emerson, G. Dalton, E. Atad-Ettedgui, S. Beard, R. Bennett, N. Bezawada, A. Born, M. Caldwell, P. Clark, S. Craig, D. Henry, P. Jeffers, B. Little, A. McPherson, J. Murray, M. Stewart, B. Stobie, D. Terrett, K. Ward, M. Whalley, and G. Woodhouse. The Visible and Infrared Survey Telescope for Astronomy (VISTA): Design, technical overview, and performance. *Astronomy & Astrophysics*, 575:A25, March 2015. doi: 10.1051/0004-6361/201424973.

M. V. Sykes, R. M. Cutri, J. W. Fowler, D. J. Tholen, M. F. Skrutskie, S. Price, and E. F. Tedesco. The 2MASS Asteroid and Comet Survey. *Icarus*, 146:161–175, July 2000. doi: 10.1006/icar.2000.6366.

P. Tanga and M. Delbo. Asteroid occultations today and tomorrow: toward the GAIA era. *Astronomy and Astrophysics*, 474:1015–1022, nov 2007. doi: 10.1051/0004-6361:20077470.

E. F. Tedesco, J. G. Williams, D. L. Matson, G. J. Veeder, J. C. Gradie, and L. A. Lebofsky. Three-parameter asteroid taxonomy classifications. *Asteroids II*, pages 1151–1161, 1989.

E. F. Tedesco, P. V. Noah, M. C. Noah, and S. D. Price. The Supplemental IRAS Minor Planet Survey. *Astronomical Journal*, 123:1056–1085, Feb. 2002. doi: 10.1086/338320.

E. F. Tedesco, P. V. Noah, M. C. Noah, and S. D. Price. IRAS Minor Planet Survey. NASA Planetary Data System, 2004. IRAS-A-FPA-3-RDR-IMPS-V6.0.

D. J. Tholen. *Asteroid taxonomy from cluster analysis of photometry.* PhD thesis, University of Arizona, Tucson, September 1984.

B. Timerson, J. Durech, S. Aguirre, L. Benner, D. Blacnhette, D. Breit, S. Campbell, R. Campbell, R. Carlisle, E. Castro, D. Clark, J. Clark, A. Correa, K. Coughlin, S. Degenhardt, D. Dunham, R. Fleishman, R. Frankenberger, P. Gabriel, B. Harris, D. Herald, M. Hicks, G. Hofler, A. Holmes, R. Jones, R. Lambert, G. Lucas, G. Lyzenga, C. Macdougal, P. Maley, W. Morgan, G. Mroz, R. Nolthenius, R. Nugent, S. Preston, C. Rodriguez, R. Royer, P. Sada, E. Sanchez, B. Sanford, R. Sorensen, R. Stanton, R. Venable, M. Vincent, R. Wasson, and E. Wilson. A Trio of Well-Observed Asteroid Occultations in 2008. *Minor Planet Bulletin*, 36:98–100, July 2009.

J. Torppa, M. Kaasalainen, T. Michalowski, T. Kwiatkowski, A. Kryszczyńska, P. Denchev, and R. Kowalski. Shapes and rotational properties of thirty asteroids from photometric data. *Icarus*, 164:346–383, Aug. 2003.

K. Tsiganis, R. Gomes, A. Morbidelli, and H. F. Levison. Origin of the orbital architecture of the giant planets of the Solar System. *Nature*, 435:459–461, May 2005. doi: 10.1038/nature03539.

F. Usui, D. Kuroda, T. G. Müller, S. Hasegawa, M. Ishiguro, T. Ootsubo, D. Ishihara, H. Kataza, S. Takita, S. Oyabu, M. Ueno, H. Matsuhara, and T. Onaka. Asteroid Catalog Using Akari: AKARI/IRC Mid-Infrared Asteroid Survey. *Publications of the Astronomical Society of Japan*, 63:1117–1138, October 2011. doi: 10.1093/pasj/63.5.1117.

J. Ďurech and M. Kaasalainen. Photometric signatures of highly nonconvex and binary asteroids. *Astronomy & Astrophysics*, 404:709–714, June 2003. doi: 10.1051/0004-6361:20030505.

J. Ďurech, V. Sidorin, and M. Kaasalainen. DAMIT: a database of asteroid models. *Astronomy & Astrophysics*, 513:A46, April 2010. doi: 10.1051/0004-6361/200912693.

J. Ďurech, B. Carry, M. Delbo, M. Kaasalainen, and M. Viikinkoski. Asteroid Models from Multiple Data Sources. *Asteroids IV*, pages 183–202, 2015. doi: 10.2458/azu_uapress_9780816532131-ch010.

F. Vachier, J. Berthier, and F. Marchis. Determination of binary asteroid orbits with a genetic-based algorithm. *Astronomy & Astrophysics*, 543:A68, July 2012. doi: 10.1051/0004-6361/201118408.

M. A. van Dam, D. Le Mignant, and B. Macintosh. Performance of the Keck Observatory adaptive-optics system. *Applied Optics*, 43(23):5458–5467, 2004.

G. A. Vander Haagen. Lightcurve of Binary Minor Planet 2005 NB7. *Minor Planet Bulletin*, 35:181–182, October 2008.

I. A. Vereshchagina. Investigation of multiple asteroids 2006 VV2, (45) Eugenia, (90) Antiope, (762) Pulcova, (87) Sylvia, 137170 (1999 HF1). *ArXiv e-prints*, February 2011.

I. A. Vereshchagina, D. L. Gorshanov, A. V. Devyatkin, and P. G. Papushev. Some specific features of light curves of (39) Laetitia, (87) Sylvia, (90) Antiopa, and 2006 VV2 asteroids. *Solar System Research*, 43:291–300, August 2009. doi: 10.1134/S0038094609040030.

P. Vernazza, R. P. Binzel, C. A. Thomas, F. E. DeMeo, S. J. Bus, A. S. Rivkin, and A. T. Tokunaga. Compositional differences between meteorites and near-Earth asteroids. *Nature*, 454:858–860, August 2008. doi: 10.1038/nature07154.

P. Vernazza, R. Brunetto, R. P. Binzel, C. Perron, D. Fulvio, G. Strazzulla, and M. Fulchignoni. Plausible parent bodies for enstatite chondrites and mesosiderites: Implications for Lutetia's fly-by. *Icarus*, 202:477–486, August 2009. doi: 10.1016/j.icarus.2009.03.016.

P. Vernazza, P. Lamy, O. Groussin, T. Hiroi, L. Jorda, P. L. King, M. R. M. Izawa, F. Marchis, M. Birlan, and R. Brunetto. Asteroid (21) Lutetia as a remnant of Earth's precursor planetesimals. *Icarus*, 216:650–659, December 2011. doi: 10.1016/j.icarus.2011.09.032.

P. Vernazza, M. Marsset, P. Beck, R. P. Binzel, M. Birlan, R. Brunetto, F. E. Demeo, Z. Djouadi, C. Dumas, S. Merouane, O. Mousis, and B. Zanda. Interplanetary Dust Particles as Samples of Icy Asteroids. *The Astrophysical Journal*, 806:204, June 2015. doi: 10.1088/0004-637X/806/2/204.

J. Veverka. Small is NOT Dull: Unravelling the Complexity of Surface Processes on Asteroids, Comets and Small Satellites. In *AAS/Division for Planetary Sciences Meeting Abstracts*, volume 45 of *AAS/Division for Planetary Sciences Meeting Abstracts*, page 109.01, October 2013.

A. Vigan, C. Moutou, M. Langlois, D. Mouillet, K. Dohlen, A. Boccaletti, M. Carbillet, I. Smith, A. Ferrari, L. Mugnier, and C. Thalmann. Comparison of methods for detection and characterization of exoplanets with sphere/irdis. In *Proc. SPIE 7735*, volume 7735, pages 77352X–77352X–12, 2010. doi: 10.1117/12.856701.

D. Vokrouhlický, D. Nesvorný, W. F. Bottke, and A. Morbidelli. Collisionally Born Family About 87 Sylvia. *Astronomical Journal*, 139:2148–2158, June 2010. doi: 10.1088/0004-6256/139/6/2148.

K. J. Walsh and S. A. Jacobson. Formation and Evolution of Binary Asteroids. *Asteroids IV*, pages 375–393, 2015. doi: 10.2458/azu_uapress_9780816532131-ch020.

K. J. Walsh, D. C. Richardson, and P. Michel. Rotational breakup as the origin of small binary asteroids. *Nature*, 454:188–191, July 2008. doi: 10.1038/nature07078.

K. J. Walsh, A. Morbidelli, S. N. Raymond, D. P. O'Brien, and A. M. Mandell. A low mass for Mars from Jupiter's early gas-driven migration. *Nature*, 475:206–209, July 2011. doi: 10.1038/nature10201.

B. D. Warner. Lightcurve analysis for numbered asteroids 301, 380, 2867, 8373, 25143, and 31368. *Minor Planet Bulletin*, 31:67–70, September 2004.

B. D. Warner. Lightcurve analysis for asteroids 242, 893, 921, 1373, 1853, 2120, 2448 3022, 6490, 6517, 7187, 7757, and 18108. *Minor Planet Bulletin*, 32:4–7, March 2005.

B. D. Warner. Asteroid Lightcurve Analysis at the Palmer Divide Observatory: September-December 2007. *Minor Planet Bulletin*, 35:67–71, June 2008.

B. D. Warner. Asteroid Lightcurve Analysis at the Palmer Divide Observatory: 2010 December-2011 March. *Minor Planet Bulletin*, 38:142–149, July 2011.

B. D. Warner. Rounding Up the Unusual Suspects. *Minor Planet Bulletin*, 40:36–42, January 2013a.

B. D. Warner. Something Old, Something New: Three Binary Discoveries from the Palmer Divide Observatory. *Minor Planet Bulletin*, 40:119–121, July 2013b.

B. D. Warner. Binary Asteroid Lightcurve Analysis at the CS3-Palmer Divide Station: 2013 June-September. *Minor Planet Bulletin*, 41:54–57, January 2014a.

B. D. Warner. Near-Earth Asteroid Lightcurve Analysis at CS3-Palmer Divide Station: 2013 September-December. *Minor Planet Bulletin*, 41:113–124, April 2014b.

B. D. Warner. A Sextet of Main-belt Binary Asteroid Candidates. *Minor Planet Bulletin*, 42: 60–66, January 2015a.

B. D. Warner. Two New Binaries and Continuing Observations of Hungaria Group Asteroids. *Minor Planet Bulletin*, 42:132–136, April 2015b.

B. D. Warner and R. D. Stephens. Lightcurve Analysis of Two Binary Asteroids: (76818) 2000 RG79 and (185851) 2000 DP107. *Minor Planet Bulletin*, 36:62–63, April 2009.

B. D. Warner, P. Pravec, and D. Pray. (76818) 2000 RG_79. *Central Bureau Electronic Telegrams*, 207, August 2005.

B. D. Warner, A. W. Harris, P. Pravec, M. Kaasalainen, and L. A. M. Benner. Lightcurve Photometry Opportunities April-June 2007. *Minor Planet Bulletin*, 34:50–51, June 2007.

B. D. Warner, P. Pravec, P. Kusnirak, A. W. Harris, W. R. Cooney, Jr., J. Gross, D. Terrell, S. Nudds, J. Vilagi, S. Gajdos, G. Masi, D. P. Pray, R. Dyvig, and V. Reddy. Lightcurves from the Initial Discovery of Four Hungaria Binary Asteroids. *Minor Planet Bulletin*, 38:107–109, April 2011.

B. D. Warner, J. T. Pollock, D. E. Reichart, J. B. Haislip, A. P. LaCluyze, A. Verveer, T. Spuck, and A. W. Harris. (399307) 1991 RJ2: A New NEA Binary Discovery. *Minor Planet Bulletin*, 42: 37–38, January 2015.

S. J. Weidenschilling, C. R. Chapman, D. R. Davis, R. Greenberg, D. H. Levy, and S. Vail. Photometric geodesy of main-belt asteroids. I - Lightcurves of 26 large, rapid rotators. *Icarus*, 70: 191–245, may 1987. doi: 10.1016/0019-1035(87)90131-X.

S. J. Weidenschilling, P. Paolicchi, and V. Zappala. Do asteroids have satellites? *Asteroids II*, pages 643–658, 1989.

S. J. Weidenschilling, C. R. Chapman, D. R. Davis, R. Greenberg, and D. H. Levy. Photometric geodesy of main-belt asteroids. III - Additional lightcurves. *Icarus*, 86:402–447, aug 1990. doi: 10.1016/0019-1035(90)90227-Z.

O. Witasse, J.-P. Lebreton, M. K. Bird, R. Dutta-Roy, W. M. Folkner, R. A. Preston, S. W. Asmar, L. I. Gurvits, S. V. Pogrebenko, I. M. Avruch, R. M. Campbell, H. E. Bignall, M. A. Garrett, H. J. van Langevelde, S. M. Parsley, C. Reynolds, A. Szomoru, J. E. Reynolds, C. J. Phillips, R. J. Sault, A. K. Tzioumis, F. Ghigo, G. Langston, W. Brisken, J. D. Romney, A. Mujunen, J. Ritakari, S. J. Tingay, R. G. Dodson, C. G. M. van't Klooster, T. Blancquaert, A. Coustenis, E. Gendron, B. Sicardy, M. Hirtzig, D. Luz, A. Negrao, T. Kostiuk, T. A. Livengood, M. Hartung, I. de Pater, M. Ádámkovics, R. D. Lorenz, H. G. Roe, E. L. Schaller, M. E. Brown, A. H. Bouchez,

C. A. Trujillo, B. J. Buratti, L. Caillault, T. Magin, A. Bourdon, and C. Laux. Overview of the coordinated ground-based observations of Titan during the Huygens mission. *Journal of Geophysical Research (Planets)*, 111:7–19, Jul 2006. doi: 10.1029/2005JE002640.

Peter L. Wizinowich, D. Scott Acton, Olivier Lai, John Gathright, William Lupton, and Paul J. Stomski, Jr. Performance of the W.M. Keck Observatory Natural Guide Star Adaptive Optic Facility: the first year at the telescope. In *Proc. SPIE 4007*, volume 4007, pages 2–13, 2000. doi: 10.1117/12.390368.

S. Xu, R. P. Binzel, T. H. Burbine, and S. J. Bus. Small main-belt asteroid spectroscopic survey: Initial results. *Icarus*, 115:1–35, May 1995. doi: 10.1006/icar.1995.1075.

B. Yang, J. Zhu, J. Gao, H. T. Zhang, and X. Z. Zheng. Observations of 2000 DP $_{107}$ in NAOC: rotation period and reflectance spectrum. *planss*, 51:411–414, May 2003. doi: 10.1016/S0032-0633(03)00024-2.

B. Yang, Z. Wahhaj, L. Beauvalet, F. Marchis, C. Dumas, M. Marsset, E. L. Nielsen, and F. Vachier. Extreme ao observations of two triple asteroid systems with sphere. *Astrophysical Journal Letter*, 820:L35, April 2016. doi: 10.3847/2041-8205/820/2/L35.

F. Yoshida and T. Nakamura. Subaru Main Belt Asteroid Survey (SMBAS)—Size and color distributions of small main-belt asteroids. *Planetary and Space Science*, 55:1113–1125, June 2007. doi: 10.1016/j.pss.2006.11.016.

B. Zellner, D. J. Tholen, and E. F. Tedesco. The eight-color asteroid survey - Results for 589 minor planets. *Icarus*, 61:355–416, March 1985. doi: 10.1016/0019-1035(85)90133-2.

W. Zielenbach. Mass Determination Studies of 104 Large Asteroids. *Astronomical Journal*, 142:120–128, October 2011. doi: 10.1088/0004-6256/142/4/120.

## Résumé

Les astéroïdes binaires représentent un laboratoire naturel pour recueillir des informations cruciales sur les petits corps du Système Solaire, fournissant un aperçu des mécanismes de formation et d'évolution de ces objets. Leur caractérisation physique nous aide à comprendre les processus qui ont pris part à la formation et l'évolution des planétesimaux dans le Système Solaire. Les caractéristiques qui sont évaluées dans ce travail sont: masse, taille, forme, rotation, densité, composition et taxonomie. L'une des plus importantes caractéristiques que l'on puisse obtenir avec les objets binaires est leur masse grâce à l'interaction gravitationnelle mutuelle. Avec masse et taille du corps, nous pouvons déterminer sa densité, qui peut nous donner un aperçu de sa structure interne.

Exploration de données a été faite à partir d'images à haute résolution angulaire du HST et télescopes avec OA (VLT/NACO, VLT/SPHERE, Gemini/NIRI, Keck/NIRC2) dans le VIS+NIR. Ayant réduit images et mesuré positions des satellites de nombreuses époques, l'algorithme Genoid est utilisé pour déterminer l'orbite de compagnons et la masse du corps central. Ceci est utile pour améliorer éphémérides des satellites, qui à leur tour seront utiles pour prédire des occultations, cette technique étant la plus fructueuse pour l'observation des objets de faible diamètre du Système Solaire. Pour déterminer taille et forme, l'algorithme KOALA d'inversion multidonnées est utilisé.

En photométrie, courbes de lumiere et couleurs SDSS ont été obtenues depuis le T1m au Pic du Midi et de 1.20m de l'OHP dans le but de déterminer et affiner leurs propriétés. J'ai egalement acquis à distance des spectres d'astéroïdes binaires en utilisant le spectrographe Spex sur le télescope IRTF de 3m au Mauna Kea (Hawaii), afin de déterminer leur taxonomie pour la première fois.

J'ai fait le modelisation de spectres de binaires sans taxonomie dans la base de données MIT-UH-IRTF. Ce plus grand échantillon, j'ai la comparez avec la population du NEAs et de MCs, en trouvant une prédominance Q/S. Cela est consistant avec la formation de binaires petits par effet YORP et perturbation rotationnelle.

Finalement, j'ai développé une classification taxonomique basée sur la photométrie large bande dans l'IR, et je l'ai appliquée aux données de 30,000 astéroïdes provenant du survey VHS par le télescope VISTA.

## Mots Clés

astéroïdes, propietes, spectra, taxonomie

## Abstract

Binary asteroids represent a natural laboratory to gather crucial information on small bodies of the Solar System, providing an overview of the formation and evolution mechanisms of these objects. Their physical characterization can constrain the processes that took part in the formation and evolution of planetessimals in the Solar System. The characteristics assessed in this work are: mass, size, shape, spin, density, surface composition, and taxonomy.

One of the most important characteristics that can be obtained of binaries is their mass through their mutual gravitational interaction. From the mass and the size of the asteroid we determine its density, which provides insight on its internal structure.

For this purpose, data mining has been done for high-angular resolution images from HST and ground-based telescopes equipped with AO (VLT/-NACO, VLT/SPHERE, Gemini/NIRI, Keck/NIRC2) in VIS+NIR. Having reduced the images and determined the satellite positions for over many epochs, the algorithm Genoid is used to determine the orbit of the companion, and mass of the primary. This improves the ephemerides of binary companions, which in turn allows to detect occultations, being this technique the most fruitful for observing small diameter Solar System objects. For size and shape determination, KOALA multidata inversion algorithm is used.

Concerning photometry, light curves and SDSS colors have been obtained from T1M at Pic du Midi & 1.20m telescope at OHP, aiming at determining and refining their properties. I remotely acquired spectra of binary asteroids using Spex/IRTF system based on 3m at Mauna Kea (Hawaii), to determine their taxonomic class for the first time. Additionally, I collected spectra of small binaries from the SMASS collaboration database, modelled it, and found their taxonomy. I compare the now larger sample of classified binaries to the population of NEAs and Mars Crossers, and found a predominance of Q/S types. This is in agreement with a formation by YORP spin-up and rotational disruption.

Finally, I developed a taxonomic classification for asteroids in general, based on infrared large band photometry, and applied it to 30,000 asteroids from VHS survey at the ESO's telescope VISTA.

## Keywords

minor planets, asteroids, properties, asteroids techniques, spectra, taxonomy